Volume 6 Issue 1 (2020) · ISSN 2424-7723

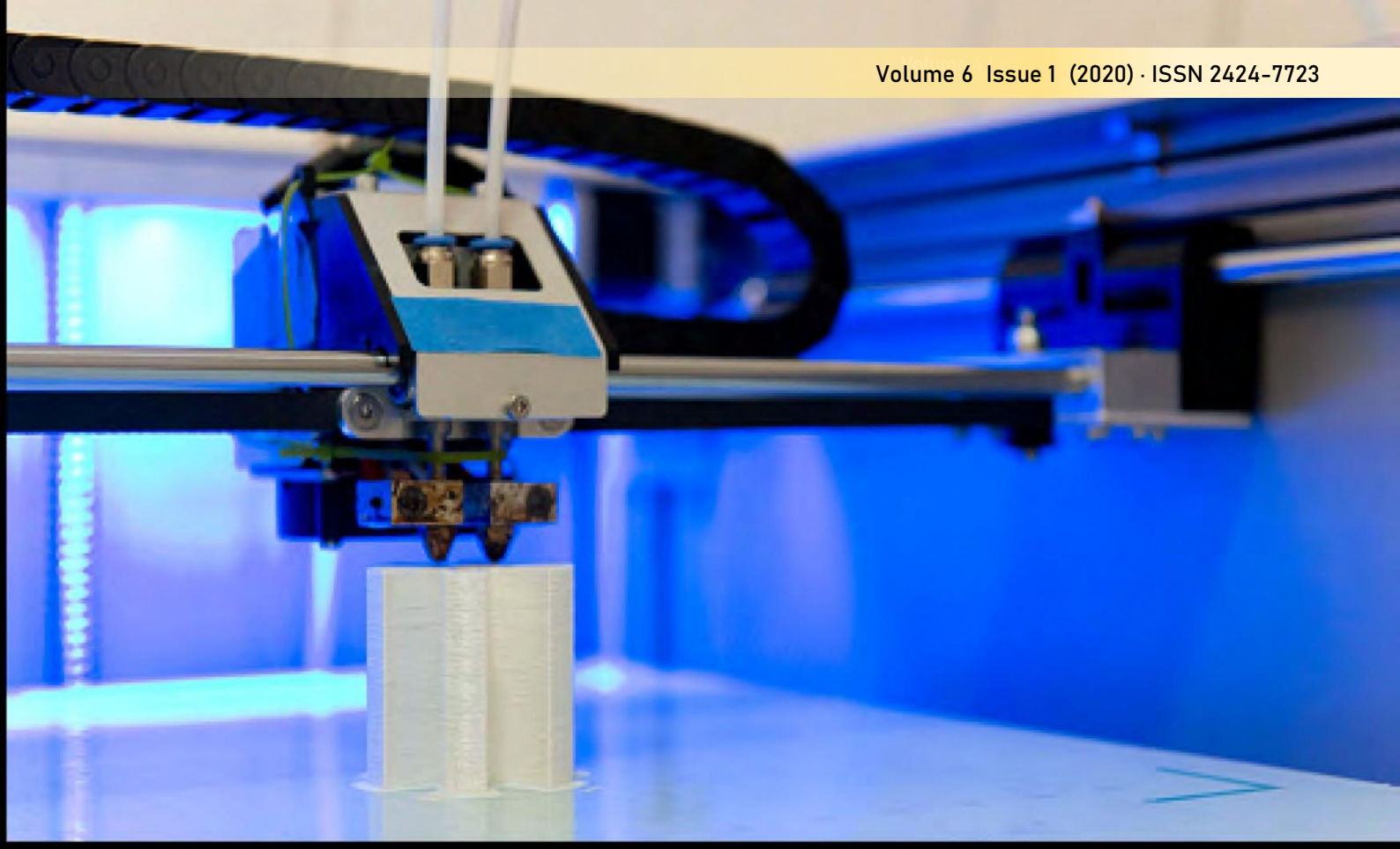

INTERNATIONAL JOURNAL OF BIOPRINTING

WHIOCE PUBLISHING PTE. LTD.
PROVIDING
FIRST-CLASS SCIENTIFIC INFORMATION
FOR TOP SCHOLARS

Volume 6 Issue 1 • 2020
ISSN 2424-7723 (print) ISSN 2424-8002 (online)

INTERNATIONAL JOURNAL OF BIOPRINTING

Editor-in-Chief

Chee Kai Chua

Singapore University of Technology and Design, Singapore

WHIOCE PUBLISHING PTE. LTD.

Volume 6 | Issue 1 | 2020 | Page 1 – 111 |

International Journal of Bioprinting

https://ijb.whioce.com/index.php/int-j-bioprinting

CONTENTS

EDITORIAL

Publication Trends in 3D Bioprinting and 3D Food Printing

Editor-in-Chief: Chee Kai Chua

Engineering Product Development Pillar, Singapore University of Technology and Design, 8 Somapah Road, Singapore 487372, Singapore

http://dx/doi.org/10.18063/ijb.v6i1.257

In the past two decades, major advances have been made in the field of three-dimensional (3D) bioprinting[1-3]. The term "three-dimensional (3D) bioprinting" is defined as "the use of computer-aided transfer processes for patterning and assembling living and non-living materials with a prescribed 2D or 3D organization in order to produce bioengineered structures serving in regenerative medicine, pharmacokinetic, and basic cell biology studies"[4-7]. As opposed to conventional tissue engineering approaches, 3D bioprinting allows scalable and reproducible deposition of bioinks (biomaterials, living cells, and growth factors) with the use of highly advanced and automated additive manufacturing platforms. Complex bioengineered constructs can be fabricated by depositing bioinks, layer by layer, with precise control of the spatial arrangement of these functional components[4,8].

The printing techniques for 3D bioprinting are commonly categorized into these five major categories[4]: (a) Extrusion, (b) stereolithography, (c) inkjet, (d) laser-assisted, and (e) microvalve-based bioprinting. Hence, these keywords[4], "bioprinting technique – extrusion, stereolithography, inkjet, laser assisted, or microvalve based" + "biomaterials" + "cells," are used to search for bioprinting related technical publications from Web of Science. Data have shown that research related to bioprinting has clearly grown exponentially since the year 2000 and the number of bioprinting related technical publications has been increasing steadily in the past 5 years (**Figure 1**).

According to a comprehensive market survey by Roots Analysis[9], there are currently more than 70 bioprinters available which are either commercialized or under development, and more than 60% of these bioprinters utilize the extrusion technology for material deposition. It can be observed from **Figure 1** that the extrusion-based printing technique remains to be the most widely used method in bioprinting, in which its popularity can be largely attributed to its fast printing speed, wide acceptance range of printable materials[4], and also the wide availability of commercial extrusion-based bioprinters. Moreover, each printing technique has its own merits and the selection of suitable printing techniques for bioprinting is application dependent.

Moving over to 3D food printing, 3D food printing remains an emerging field as compared to 3D bioprinting. The use of food materials with additive manufacturing technology, or commonly known as 3D food printing[10-12], has captivated the commercial sector for the past decade with potential convenience of low-cost food customization and precise nutrition control. In recent years, 3D food printing related research is gaining momentum with increased attention from the academic field and its technical publications has also increased significantly (**Figure 2**).

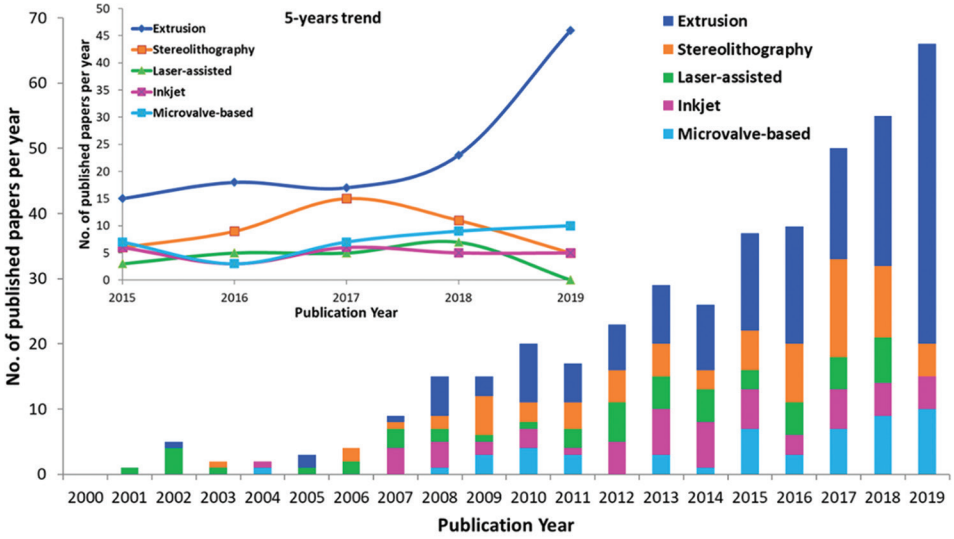

Figure 1. Detailed breakdown of the number of publications for each bioprinting technique (extrusion, stereolithography, laser assisted, inkjet, and microvalve based) from the publication year 2000 to 2019; inset: 5 years publication trend from the year 2015 to 2019. Adapted from Ng *et al*.

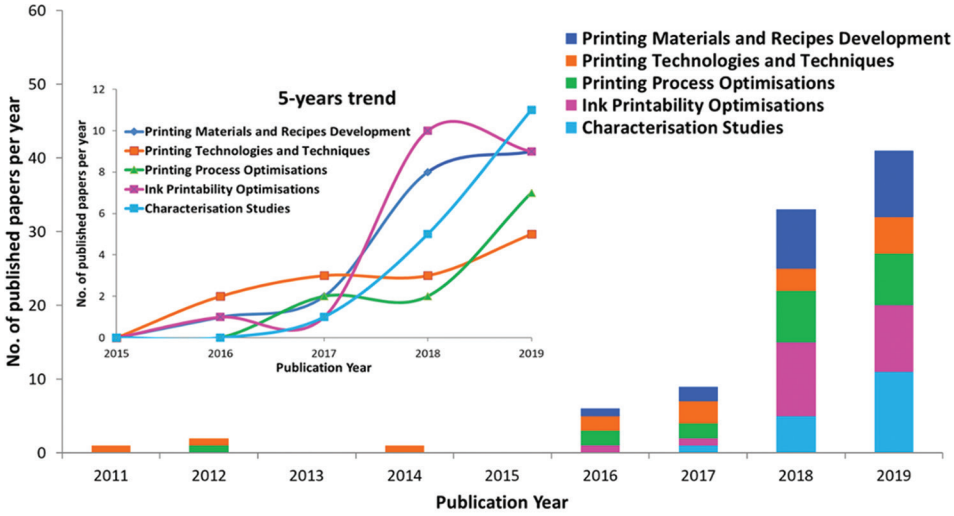

Figure 2. Detailed breakdown of the number of publications for each 3D food printing classification (printing materials and recipes development, printing technologies and techniques, printing process optimizations, ink printability optimizations, and characterization studies) from the publication year 2011 to 2019; inset: 5 years publication trend from the year 2015 to 2019.

The keyword "3D food printing" is used to search for 3D food printing related technical publications from Web of Science. These publications are categorized into these five different categories of 3D food printing research: (a) Printing materials and recipes development, (b) printing technologies and techniques, (c) printing process optimizations, (d) ink printability optimizations, and (e) characterization studies.

It is evident that the novelty of 3D food printing research now is not just about constructing edible structures with additive manufacturing technologies[10]. In fact, more focus is emphasized on gaining a better understanding on developing

new printing materials and recipes, optimizing the printing process and inks' printability, and characterizing the 3D printed foods. Nevertheless, public acceptance, palatability, and food safety are also some of the critical areas for research to make 3D-printed foods available to the public for consumption in the near future.

References

1. An J, Teoh JE, Suntornnond R, *et al*., 2015, Design and 3D Printing of Scaffolds and Tissues. *Engineering,* 1(2):261–8.
2. Lee, JM, Sing SL, Zhou M, *et al*., 2018, 3D Bioprinting Processes: A Perspective on Classification and Terminology. *Int J Bioprinting*, 4:1–5. DOI: 10.18063/ijb.v4i2.151.
3. Pei DZ, 2018, 3D Neural Tissue Models: From Spheroids to Bioprinting. *Biomaterials*, 154:113–33.
4. Ng WL, Chua CK, Shen YF, 2019, Print Me An Organ! Why We Are Not There Yet. *Prog Polym Sci*, 97:101145. DOI: 10.1016/j.progpolymsci.2019.101145.
5. Guillemot F, Mironov V, Nakamura M, 2010, Bioprinting is Coming of Age: Report from the International Conference on Bioprinting and Biofabrication in Bordeaux (3B'09). *Biofabrication*, 2(1):010201. DOI: 10.1088/1758-5082/2/1/010201.
6. Liu H, Zhou H, Lan H, 2017, Organ Regeneration: Integration Application of Cell Encapsulation and 3D Bioprinting. *Virtual Phys Prototyp*, 12(4):279–89. DOI: 10.1080/17452759.2017.1338065.
7. Jang TS, Jung HD, Pan MH, *et al*., 2018, 3D Printing of Hydrogel Composite Systems: Recent Advances in Technology for Tissue Engineering. *Int J Bioprinting*, 4(1):126.
8. Zhuang P, Ng WL, An J, *et al*., 2019, Layer-By-Layer Ultraviolet Assisted Extrusion-Based (UAE) Bioprinting of Hydrogel Constructs with High Aspect Ratio for Soft Tissue Engineering Applications. *PLOS One*, 14(6):e0216776. DOI: 10.1371/journal.pone.0216776.
9. 3D Bioprinting: Technologies, Products and Key Application Areas. 2nd ed. pp2018-2035. Available from: <https://www.rootsanalysis.com/reports/view_document/3d-bioprinting-technologies-products-and-key-application-areas-2nd-edition-2018-2035/182.html>. [Last accessed on 2020 Jan 20].
10. Voon SL, An J, Wong G, *et al*., 2019, 3D Food Printing: A Categorised Review of Inks and Their Development. *Virtual Phys Prototyp*, 14(3):203–18.
11. Sun J, Peng Z, Yan L, *et al*., 2015, 3D Food Printing An Innovative Way of Mass Customization in Food Fabrication. *Int J Bioprinting*, 1:27–38. DOI: 10.18063/ijb.2015.01.006.
12. Tan C, Toh W, Wong G, *et al*., 2018, Extrusion-Based 3D Food Printing Materials and Machines. *Int J Bioprinting*, 4:143.

PERSPECTIVE ARTICLE

A Perspective on Using Machine Learning in 3D Bioprinting

Chunling Yu[1], Jingchao Jiang[2*]

[1]Faculty of Maritime and Transportation, Ningbo University, Ningbo 315211, China

[2]Department of Mechanical Engineering, University of Auckland, Auckland 1010, New Zealand

Abstract: Recently, three-dimensional (3D) printing technologies have been widely applied in industry and our daily lives. The term 3D bioprinting has been coined to describe 3D printing at the biomedical level. Machine learning is currently becoming increasingly active and has been used to improve 3D printing processes, such as process optimization, dimensional accuracy analysis, manufacturing defect detection, and material property prediction. However, few studies have been found to use machine learning in 3D bioprinting processes. In this paper, related machine learning methods used in 3D printing are briefly reviewed and a perspective on how machine learning can also benefit 3D bioprinting is discussed. We believe that machine learning can significantly affect the future development of 3D bioprinting and hope this paper can inspire some ideas on how machine learning can be used to improve 3D bioprinting.

Keywords: 3D printing, Bioprinting, Machine learning

***Corresponding Author:** Jingchao Jiang, Department of Mechanical Engineering, University of Auckland, Auckland 1010, New Zealand; jjia547@aucklanduni.ac.nz

Received: November 24, 2019; ***Accepted:*** December 23, 2019; ***Published Online:*** January 24, 2020

Citation: Yu C, Jiang J, 2020, A perspective on using machine learning in 3D bioprinting. *Int J Bioprint*, 6(1):253. DOI: 10.18063/ijb.v6i1.253

1 Introduction

Currently, three-dimensional (3D) printing technologies have been widely applied in many fields, including aerospace, medicine, industry, and esthetic[1-3]. The process of 3D printing starts from the bottom to the top of a product in a point-by-point and layer-by-layer manner[4-8]. It is an additive process that adds materials gradually until the whole part is fabricated. **Figure 1a** shows a typical extrusion-based 3D printing process to manufacture a component. 3D bioprinting is a process that uses 3D printing-like technologies to fabricate biomedical parts that consist of biomaterials, growth factors and cells, with the aim of maximally imitating natural tissue characteristics[9-11]. The fabrication process of 3D bioprinting is similar to 3D printing that uses a layer-by-layer method to deposit materials[12-14]. The raw materials used in 3D bioprinting are bio-inks, rather than polymer, metal or ceramic in traditional 3D printing processes[15]. 3D bioprinting can create tissue-like structures that can be utilized in tissue or medical engineering fields.

Currently, there are five major bioprinting techniques available, including stereolithography-based, inkjet, extrusion-based, and laser-assisted bioprinting. The details of these techniques have been described[16]. Among them, extrusion-based bioprinting is the most common technique. **Figure 1b** shows the typical three extrusion-based bioprinting processes. The difference among them is the type of force that can be either air pressure (pneumatic dispensing), direct

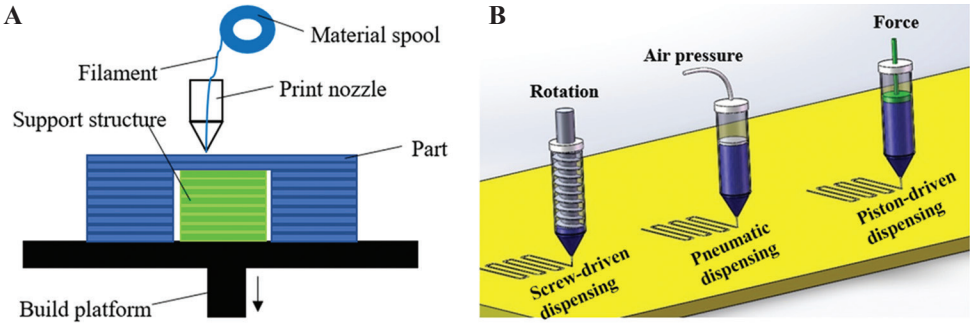

Figure 1. Typical three-dimensional printing process (a) and extrusion-based bioprinting methods (b).

force (piston-driven dispensing), or rotation (screw-driven dispensing).

Machine learning is an emerging technology that can optimize systems through smarter and effective use of products, materials, and services. In terms of 3D printing processes, machine learning can lead to a reduction of fabrication time, minimized cost, and increased quality. In literature, machine learning has already been applied to process optimization[17-21], dimensional accuracy analysis[22-25], manufacturing defect detection[26-28], and material property prediction[29-32]. However, machine learning has not been applied in 3D bioprinting yet. In this paper, the perspective on how machine learning can help to improve 3D bioprinting is discussed. Related machine learning used in 3D printing will be briefly reviewed for illustrating its effects on 3D bioprinting. We believe that machine learning can significantly affect the future development of 3D bioprinting and hope this paper can inspire some ideas on how machine learning can be used to improve 3D bioprinting.

2 Machine learning

Machine learning is one of today's most rapidly growing technical fields. It is a subset of artificial intelligence, mainly focusing on the designing of systems. Machine learning allows these designed systems to learn and make predictions based on the previous experience which is data in terms of machines. **Figure 2** shows a typical machine learning process. The data in the training set needs to be trained first by the algorithm. During the training process, the parameters in the algorithm will be improved and then generate a machine learning model. Using the updated machine learning parameters, it can then predict the results with new input data. The most commonly used machine learning methods include supervised learning[33], unsupervised learning[34], and reinforcement learning[35].

In supervised learning, the training data are a collection of x, y form pairs, and the objective is to get the predicted result $y^{\wedge}$ in response to a query x. x, y can be more than one element that will be expressed as a vector in machine learning. Currently, supervised learning has been used in spam classification of email, medical diagnosis systems for patients and face recognition over images.

In unsupervised learning, the input data are unlabeled data which are different from supervised learning. Algorithms will automatically learn and extract the features of the input data and then divide them into different clusters. The aim of unsupervised learning is to model the underlying distribution or structure of the input data for learning more about the data. Currently, unsupervised learning has been applied in market segmentation for targeting appropriate customers, clustering documents based on content, image division, and anomaly or fraud detection in banking companies.

In reinforcement learning, the information from the training data fed into algorithms is intermediate between unsupervised and supervised learning. Instead of indicating the correct output for a given input in supervised learning, the training data are assumed to provide only an indication as to whether an action is correct or not. Currently, reinforcement

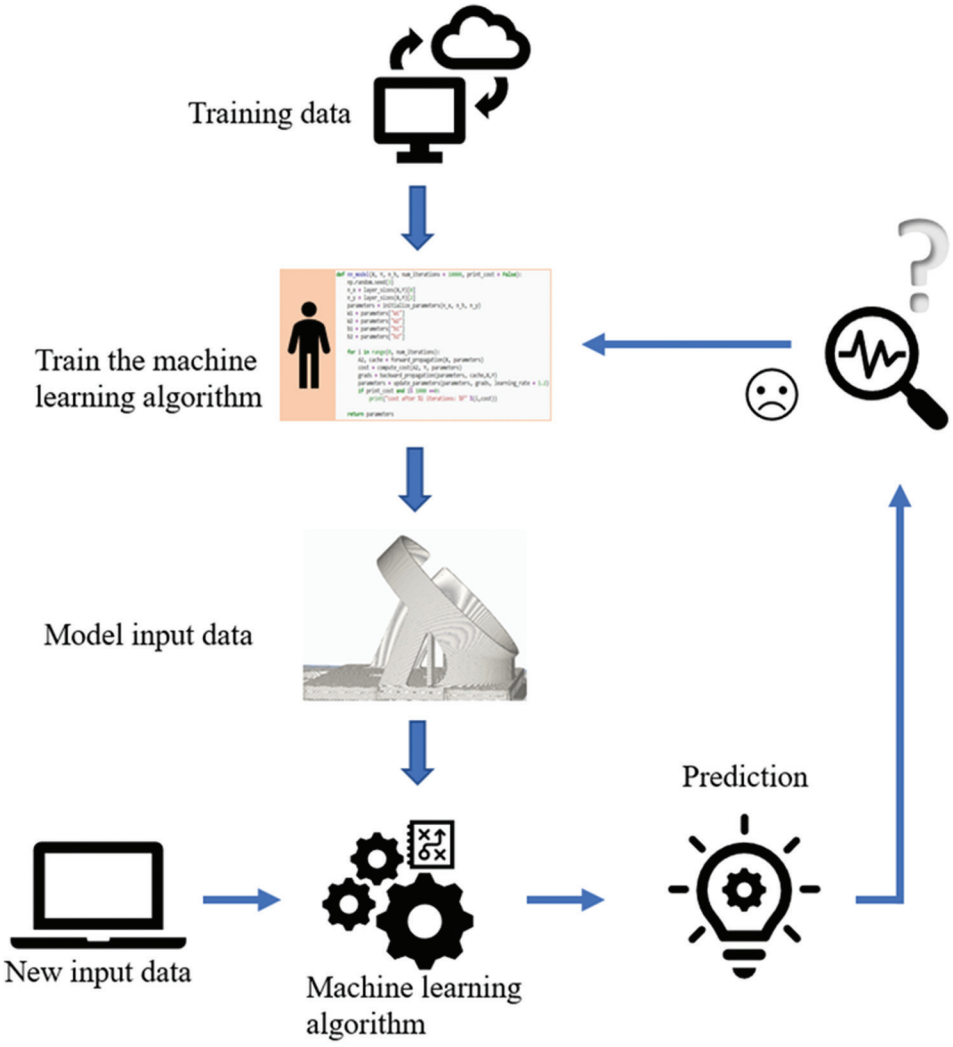

Figure 2. A typical machine learning process.

learning has been used in aircraft control, robot motion control, traffic light control, web system configuration, and games (e.g., AlphaGo).

In addition to these three learning paradigms, some new machine learning methods have also been developed, such as semi-supervised learning. More details can be found in a review paper on machine learning[36]. There are many algorithms available in each machine learning method; the main specific techniques in each method are listed in **Table 1**. Some of these specific techniques have been applied in 3D printing. In the next section, machine learning used in 3D printing processes will be briefly reviewed and the corresponding inspirations for 3D bioprinting will be proposed.

Table 1. Main specific techniques in each machine learning method

Machine learning methods	Main specific techniques
Supervised learning	Decision trees, logistic regression, decision forests, support vector machines, kernel machines, Bayesian classifiers
Unsupervised learning	k-means, generative adversarial networks, expectation-maximization algorithm, Hebbian Learning, self-organizing map, adaptive resonance theory
Reinforcement learning	Monte Carlo, Q-learning, Soft Actor-Critic, proximal policy optimization, Trust Region Policy Optimization, Deep Q-Network, deep deterministic policy gradient

3 Perspective on using machine learning in bioprinting

Machine learning has been integrated into 3D printing processes in many ways to improve applications, including process optimization, dimensional accuracy analysis, manufacturing defect detection, and material property prediction. However, machine learning has not been applied in 3D bioprinting yet. In this section, the perspective on how machine learning can help to improve 3D bioprinting will be illustrated.

3.1 Process optimization

In traditional 3D printing processes, Aoyagi *et al*.[17] proposed a method to construct a process map for 3D printing using a support vector machine. This method can predict a process condition that is effective for manufacturing a product with low pore density. Menon *et al*.[18] used hierarchical machine learning to simultaneously optimize material, process variables, and formulate 3D printing of silicone elastomer through freeform reversible embedding. He *et al*.[19] investigated using different machine learning techniques for modeling and predicting the proper printing speed in a vat photopolymerization process (Continuous Liquid Interface Production). In their study, siamese network model has the highest accuracy. In a previous study, the convolutional neural network (CNN) was applied to enable the angular re-orientation of a projector within a fringe projection system in real-time without re-calibrating the system[20]. In addition, a conceptual framework on combining mathematical modeling and machine learning to evaluate and optimize parameters in Powder Bed Fusion processes was proposed by Baturynska *et al*.[21]

In 3D bioprinting, similarly, machine learning can be used for improving the fabrication process, such as predicting process conditions and optimizing process parameters. Taking extrusion-based bioprinting as an example, it is now able to stably fabricate organoids using low-concentration gelatin-methacryloyl with the help of electrostatic attraction[37]. However, what are the best values of these parameters? This still can be further explored using machine learning. **Figure 3** shows an example case of using neural networks to improve the bioprinting process. The variables are the inputs influencing the objective results (e.g., cell damage, cost, and time). In the case here, voltage, gas, nozzle size, pressure, etc., can be fed into the neural network for training. Corresponding outputs (cell damage, cost, time, etc.) need to be provided to tune machine learning parameters. Once the algorithm is done, new input data can be used for performance evaluation.

3.2 Manufacturing defect detection

In the traditional 3D printing process, Scime and Beuth[26] used computer vision techniques and unsupervised machine learning to identify *in situ* melt pool signatures indicative of flaw formation in a laser powder bed fusion process. Caggiano *et al*.[27] developed a machine learning method to timely recognize metal material defects in Selective Laser Melting processes. Images obtained from the layer-by-layer manufacturing process are analyzed through a bi-stream deep CNN for identifying defects. Zhang *et al*.[28] described a CNN strategy for monitoring porosity in laser additive manufacturing (AM) processes. The melt-pool data were gained through a high-speed digital camera for in-process sensing. Then, the data were analyzed by their developed neural network.

In 3D bioprinting, similarly, machine learning can be used to detect defects such as wrong

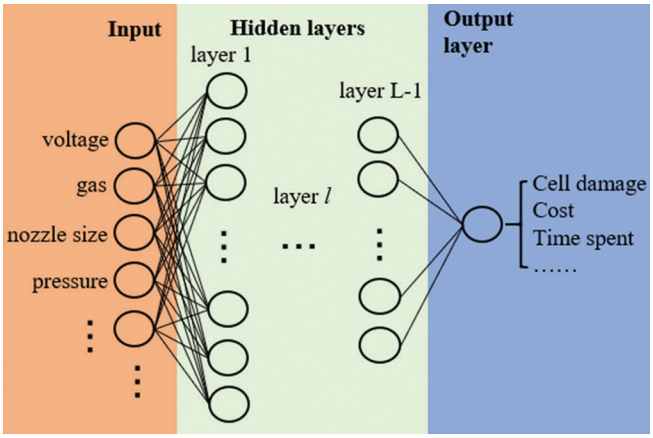

Figure 3. Example neural network for process optimization in three-dimensional bioprinting.

positioned cells, curved layers, and microstructure errors in a fabrication process which can monitor the whole bioprinting process. **Figure 4** shows an example of using CNN to detect flaws, errors, or defects in 3D bioprinting. The input data can be the images from high-quality cameras during the bioprinting process. Then, the data are analyzed by the CNN model to predict a defect or other objectives.

3.3 Dimensional accuracy analysis

In the traditional 3D printing process, Francis and Bian[22] developed a deep learning method that can accurately predict the distortion of parts in laser-based AM. Similarly, Khanzadeh *et al*.[23] proposed an unsupervised machine learning approach (self-organizing map) to quantify the geometric deviations of additively manufactured parts in fused filament fabrication processes. In addition, Zhu *et al*.[24] also developed a strategy coupled with machine learning to address the modeling of shape deviations in AM. Tootooni *et al*.[25] compared six machine learning techniques (sparse representation, k-nearest neighbors, neural network, naïve Bayes, support vector machine, and decision tree) with regard to the accuracy of predicting dimensional variation in fused deposition modeling (FDM) printed parts. Based on their study, the sparse representation approach has the best classification performance.

In 3D bioprinting, similarly, machine learning can be used for analyzing the accuracy of fabricated bio-parts. For example, the tissue-engineered scaffolds are generally very complex because they supporting cell growth in an expected way to achieve corresponding functions. If the accuracy can be analyzed by machine learning in advance, the final fabricated bio-parts can then be guaranteed in good quality. The process is similar, as shown in **Figure 4**, while the input data are different.

3.4 Material property design or prediction

In traditional 3D printing, Gu *et al*.[29] proposed a machine learning-enabled method to design hierarchical composites for fabrication, trained with a database of enough structures from finite element analysis. Hamel *et al*.[30] presented a machine learning method to design active composite structures where target shape shifting responses can be achieved in a 4D printing process. Li *et al*.[31] proposed a predictive modeling method with machine learning that can predict the surface roughness of FDM printed parts with high accuracy. Currently, Jiang *et al*.[32] used backpropagation neural network to analyze and predict printable bridge length[38] in FDM processes.

Similarly, machine learning can also be used to design or analyze material properties in 3D bioprinting process. For example, tissue-engineered scaffolds are very important in 3D bioprinting, whose structures should be carefully designed for successful cell growth and function achievement. For example, if we want to bioprint an organ in the future, the scaffolds should have the specific structure for the successful growth of cells to form a functional organ. In the case here, what kind of complex scaffold structure is the most suitable? How the properties (e.g., density and strength) of the scaffolds will influence the printed organ function? If machine learning can be used to generate these qualified

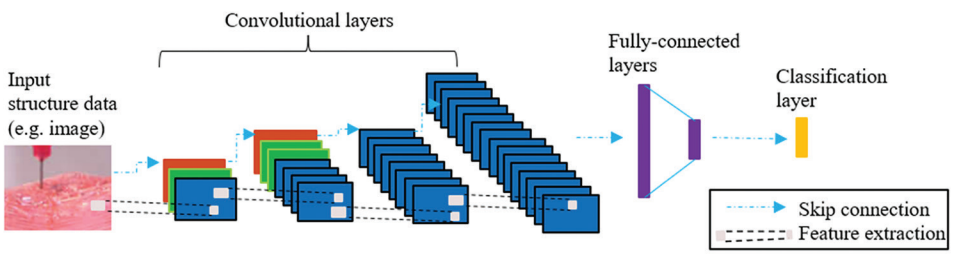

Figure 4. An example of using machine learning (convolutional neural network) in three-dimensional bioprinting.

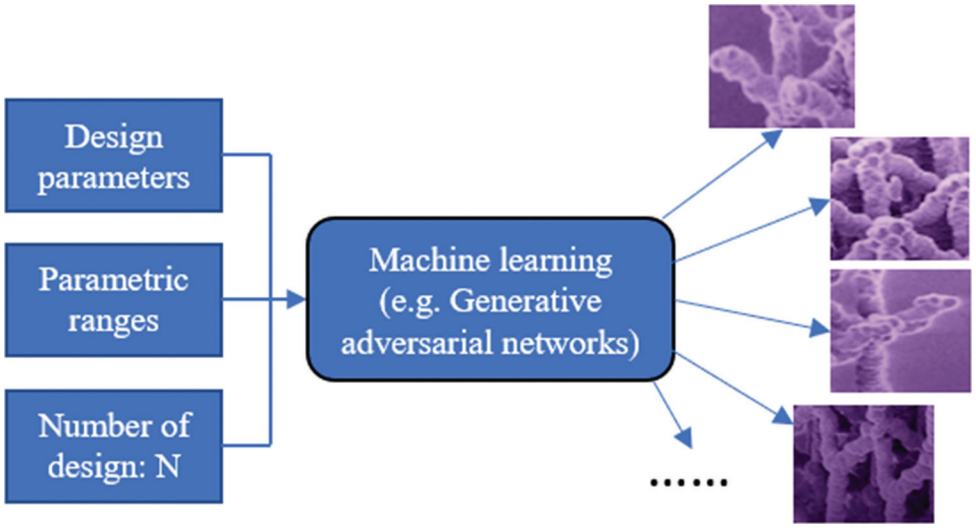

Figure 5. An example of using machine learning to design scaffolds for three-dimensional bioprinting.

scaffolds with different functions, the timescale for developing biomedical or tissue engineering coupled with bioprinting can be largely reduced in the future. Most importantly, machine learning may be able to generate some unexpected novel structures that can better support cell growth and functionalization than ever before. **Figure 5** shows an example of using machine learning (e.g., generative design method) to generate a lot of qualified scaffolds for being chosen or tested in 3D bioprinting. Once the design variables and their corresponding range values are provided, the number of expected generated scaffolds can then be set. With many options generated by machine learning, the scaffolds can then be tested for different objectives.

Another example is that machine learning can be used to design better combinations of materials at different concentrations for bioprinting. Currently, researchers have blended different gels such as collagen or hyaluronic acid to enhance mechanical and degradation properties. However, experiments on testing combinations of materials at different concentrations are a time-consuming and expensive process. Thus, if machine learning can be used to predict the temporal or structural impact of cell proliferation and extracellular matrix deposition on the tissue construct, machine learning will be an effective tool to develop or design novel biomaterials or bioprinting techniques.

4 Conclusions

Machine learning has been widely applied in 3D printing for optimizing its performance and applications. However, few studies have been reported on using machine learning in 3D bioprinting processes. The reason for this may be due to the lack of data of bioprinting as machine learning needs enough data to do predictions and optimizations. While in traditional 3D printing, it has much more data than 3D bioprinting. Another reason is that 3D bioprinting is still new compared with 3D printing, and the bioprinting technique itself still has many challenges to be solved. However, we believe that bioprinting will benefit a lot from machine learning in the future. In this paper, a perspective on how machine learning can be used in bioprinting is proposed and illustrated. Specifically, machine learning can be used to optimize the process of bioprinting, improve or analyze dimensional accuracy, defect detection, and material property design.

Acknowledgments

This research is sponsored by K.C.Wong Magna Fund in Ningbo University.

References

1. Ng WL, Yeong WY, 2019, The Future of Skin Toxicology Testing 3D Bioprinting Meets Microfluidics. *Int J Bioprinting*,

5:237. DOI: 10.18063/ijb.v5i2.1.237.

2. Jiang J, Weng F, Gao S, *et al*., 2019, A Support Interface Method for Easy Part Removal in Direct Metal Deposition. *Manuf Lett*, 20:30–3. DOI: 10.1016/j.mfglet.2019.04.002.
3. Liu J, Gaynor AT, Chen S, *et al.*, 2018, Current and Future Trends in Topology Optimization for Additive Manufacturing. *Struct Multidiscipl Optim,* 57:2457–83. DOI: 10.1007/s00158-018-1994-3.
4. Jiang J, Xu X, Stringer J, 2018, Support Structures for Additive Manufacturing: A Review. *J Manuf Mater Process*, 2:64. DOI: 10.3390/jmmp2040064.
5. Jiang J, Xu X, Stringer J, 2019, Optimisation of Multi-part Production in Additive Manufacturing for Reducing Support Waste. *Virtual Phys Prototyp*, 14:219–28. DOI: 10.1080/17452759.2019.1585555.
6. Weng F, Gao S, Jiang J, *et al.*, 2019, A Novel Strategy to Fabricate Thin 316L Stainless Steel Rods by Continuous Direct Metal Deposition in Z Direction. *Addit Manuf*, 27:474–81. DOI: 10.1016/j.addma.2019.03.024.
7. Jiang J, Xu X, Stringer J, 2018, A New Support Strategy for Reducing Waste in Additive Manufacturing. In: The 48th International Conference on Computers and Industrial Engineering (CIE 48). Curran Associates, Inc., Auckland. pp. 1–7.
8. Jiang J, Stringer J, Xu X, *et al*., 2018, A Benchmarking Part for Evaluating and Comparing Support Structures of Additive Manufacturing. In: 3rd International Conference on Progress in Additive Manufacturing (Pro-AM 2018). Singapore. pp. 196–202.
9. Lv S, Nie J, Gao Q, *et al*., 2019, Micro/Nanofabrication of Brittle Hydrogels Using 3D Printed Soft Ultrafine Fiber Molds for Damage-free Demolding. *Biofabrication*. DOI: 10.1088/1758-5090/ab57d8.
10. Nie J, Gao Q, Wang Y, *et al.*, 2018, Vessel-on-a-chip with Hydrogel-Based Microfluidics. *Small*, 14:1802368. DOI: 10.1002/smll.201802368.
11. An J, Chua CK, Mironov V, 2016, A Perspective on 4D Bioprinting. *Int J Bioprinting*, 2:3–5. DOI: 10.18063/IJB.2016.01.003.
12. Jiang J, Xu X, Stringer J, 2019, Optimization of Process Planning for Reducing Material Waste in Extrusion Based Additive Manufacturing. *Robot Comput Integr Manuf*, 59:317–25. DOI: 10.1016/j.rcim.2019.05.007.
13. Jiang J, Stringer J, Xu X, *et al.*, 2018, Investigation of Printable Threshold Overhang Angle in Extrusion-based Additive Manufacturing for Reducing Support Waste. *Int J Comput Integr Manuf*, 31:961–9. DOI: 10.1080/0951192X.2018.1466398.
14. Jiang J, Lou J, Hu G, 2019, Effect of Support on Printed Properties in Fused Deposition Modelling Processes. *Virtual Phys Prototyp*, 14:308–15. DOI: 10.1080/17452759.2019.1568835.
15. Ng WL, Chua CK, Shen YF, 2019, Print Me An Organ! Why We Are Not There Yet. *Prog Polym Sci*, 97:101145. DOI: 10.1016/j.progpolymsci.2019.101145.
16. Derakhshanfar S, Mbeleck R, Xu K, *et al.*, 2018, 3D Bioprinting for Biomedical Devices and Tissue Engineering: A Review of Recent Trends and Advances. *Bioact Mater*, 3:144–56. DOI: 10.1016/j.bioactmat.2017.11.008.
17. Aoyagi K, Wang H, Sudo H, *et al*., 2019, Simple Method to Construct Process Maps for Additive Manufacturing Using a Support Vector Machine. *Addit Manuf*, 27:353–62. DOI: 10.1016/j.addma.2019.03.013.
18. Menon A, Póczos B, Feinberg AW, *et al*., 2019, Optimization of Silicone 3D Printing with Hierarchical Machine Learning. *3D Print Addit Manuf*, 6:181–9. DOI: 10.1089/3dp.2018.0088.
19. He H, Yang Y, Pan Y, 2019, Machine Learning for Continuous Liquid Interface Production: Printing Speed Modelling. *J Manuf Syst*, 50:236–46. DOI: 10.1016/j.jmsy.2019.01.004.
20. Stavroulakis P, Chen S, Delorme C, *et al.*, 2019, Rapid Tracking of Extrinsic Projector Parameters in Fringe Projection Using Machine Learning. *Opt Lasers Eng*, 114:7–14. DOI: 10.1016/j.optlaseng.2018.08.018.
21. Baturynska I, Semeniuta O, Martinsen K, 2018, Optimization of Process Parameters for Powder Bed Fusion Additive Manufacturing by Combination of Machine Learning and Finite Element Method: A Conceptual Framework. In: Procedia CIRP. Elsevier B.V., Heidelberg. pp. 227–32. DOI: 10.1016/j.procir.2017.12.204.
22. Francis J, Bian L, 2019, Deep Learning for Distortion Prediction in Laser-Based Additive Manufacturing Using Big Data. *Manuf Lett*, 20:10–4. DOI: 10.1016/j.mfglet.2019.02.001.
23. Khanzadeh M, Rao P, Jafari-Marandi R, *et al.*, 2018, Quantifying Geometric Accuracy with Unsupervised Machine Learning: Using Self-Organizing Map on Fused Filament Fabrication Additive Manufacturing Parts. *J Manuf Sci Eng*, 140:301011. DOI: 10.1115/1.4038598.
24. Zhu Z, Anwer N, Huang Q, *et al*., 2018, Machine Learning in Tolerancing for Additive Manufacturing. *CIRP Ann*, 67:157–60. DOI: 10.1016/j.cirp.2018.04.119.
25. Tootooni MS, Dsouza A, Donovan R, *et al.*, 2017, Classifying the Dimensional Variation in Additive Manufactured Parts from Laser-Scanned Three-Dimensional Point Cloud Data

Using Machine Learning Approaches. *J Manuf Sci Eng*, 139:091005. DOI: 10.1115/1.4036641.

26. Scime L, Beuth J, 2019, Using Machine Learning to Identify *in situ* Melt Pool Signatures Indicative of Flaw Formation in a Laser Powder Bed Fusion Additive Manufacturing Process. *Addit Manuf*, 25:151–65. DOI: 10.1016/j.addma.2018.11.010.
27. Caggiano A, Zhang J, Alfieri V, *et al.*, 2019, Machine Learning-based Image Processing for On-Line Defect Recognition in Additive Manufacturing. *CIRP Ann*, 68:451–4. DOI: 10.1016/j.cirp.2019.03.021.
28. Zhang B, Liu S, Shin YC, 2019, In-Process Monitoring of Porosity During Laser Additive Manufacturing Process. *Addit Manuf*, 28:497–505. DOI: 10.1016/j.addma.2019.05.030.
29. Gu GX, Chen CT, Richmond DJ, *et al*, 2018, Bioinspired Hierarchical Composite Design Using Machine Learning: Simulation, Additive Manufacturing, and Experiment. *Mater Horizons*, 5:939–45. DOI: 10.1039/c8mh00653a.
30. Hamel CM, Roach DJ, Long KN, *et al.,* 2019, Machine-Learning Based Design of Active Composite Structures for 4D Printing. *Smart Mater Struct*, 28:065005. DOI: 10.1088/1361-665X/ab1439.
31. Li Z, Zhang Z, Shi J, *et al*., 2019, Prediction of Surface Roughness in Extrusion-Based Additive Manufacturing with Machine Learning. *Robot Comput Integr Manuf*, 57:488–95. DOI: 10.1016/j.rcim.2019.01.004.
32. Jiang J, Hu G, Li X, *et al.*, 2019, Analysis and Prediction of Printable Bridge Length in Fused Deposition Modelling Based on Back Propagation Neural Network. *Virtual Phys Prototyp*, 14:253–66. DOI: 10.1080/17452759.2019.1576010.
33. Caruana R, Niculescu-Mizil A, 2006, An Empirical Comparison of Supervised Learning Algorithms. In: ACM International Conference Proceeding Series. ACM, Pittsburgh. pp. 161–8. DOI: 10.1145/1143844.1143865.
34. Francis L, 2014, Unsupervised Learning. In: Predictive Modeling Applications in Actuarial Science. Predictive Modeling Techniques. Vol. 1. Cambridge University Press, Philadelphia, PA.
35. Arulkumaran K, Deisenroth MP, Brundage M, *et al*., 2017, Deep Reinforcement Learning: A Brief Survey. *IEEE Signal Process Mag*, 34:26–38. DOI: 10.1109/msp.2017.2743240.
36. Jordan MI, Mitchell TM, 2015, Machine Learning: Trends, Perspectives, and Prospects. *Science*, 349:255–60.
37. Xie M, Gao Q, Zhao H, *et al*., 2019, Electro-Assisted Bioprinting of Low-Concentration GelMA Microdroplets. *Small*, 15:1804216. DOI: 10.1002/smll.201804216.
38. Jiang J, Stringer J, Xu X, 2019, Support Optimization for Flat Features via Path Planning in Additive Manufacturing. *3D Print Addit Manuf*, 6:171–9. DOI: 10.1089/3dp.2017.0124.

REVIEW ARTICLE

Digital Light Processing Based Three-dimensional Printing for Medical Applications

Jiumeng Zhang[1], Qipeng Hu[2], Shuai Wang[1], Jie Tao[1], Maling Gou[1]*

[1]State Key Laboratory of Biotherapy and Cancer Center, West China Hospital, Sichuan University, Chengdu, Sichuan 610065, China

[2]Department of Thoracic Oncology, West China Hospital of Sichuan University, 610041, Chengdu, Sichuan, China

Abstract: An additive manufacturing technology based on projection light, digital light processing (DLP), three-dimensional (3D) printing, has been widely applied in the field of medical products production and development. The precision projection light, reflected by a digital micromirror device of million pixels instead of one focused point, provides this technology both printing accuracy and printing speed. In particular, this printing technology provides a relatively mild condition to cells due to its non-direct contact. This review introduces the DLP-based 3D printing technology and its applications in medicine, including precise medical devices, functionalized artificial tissues, and specific drug delivery systems. The products are particularly discussed for their significance in medicine. This review indicates that the DLP-based 3D printing technology provides a potential tool for biological research and clinical medicine. While, it is faced to the challenges of scale-up of its usage and waiting period of regulatory approval.

Keywords: Digital light processing, Three-dimensional print, Medical devices, Tissue engineering, Pharmacy

***Corresponding Author:** Maling Gou, State Key Laboratory of Biotherapy and Cancer Center, West China Hospital, Sichuan University, and Collaborative Innovation Center for Biotherapy, Chengdu, Sichuan 610065, China; goumaling@scu.edu.cn.

Received: September 13, 2019; ***Accepted:*** October 29, 2019; ***Published Online:*** November 28, 2019

Citation: Zhang J, Hu Q, Wang S, *et al*., 2020, Digital light processing based 3D printing for medical applications. *Int J Bioprint*, 6(1):242. DOI: 10.18063/ijb.v6i1.242

1 Introduction

Three-dimensional (3D) printing, a rapidly emerging technology, can construct products with complex geometric features by depositing materials according to the digital files[1-3]. This neoteric technology provides a rapid manufacturing method to fabricate medical products that are usually complex and urgent. In addition, 3D printing can fabricate customized products with complex accurate structure at comparatively low costs, especially in personalized medical application. This has important implications for a unique patient[4]. Therefore, 3D printing technology has profoundly impacted biomedicine for fabricating various complex and personalized medical products. In the meanwhile, the application of these products continues to grow rapidly. The latest forecast is that the global market for medical products manufactured through 3D printing will reach nearly 26 billion dollars by 2022, while the market related to bio-printing will exceed 1.3 billion dollars[3].

Digital light processing (DLP)-based 3D printing is utilizing projection light to polymerize materials to obtain the pre-designed structures[5]. Compared with other 3D printing methods, such as extrusion-based 3D printing technology and inkjet-based 3D printing technology, this technology has significant advantages in printing resolution, efficiency, and working condition. Hence, it can give many good

features to the products. The medical models have fine shape and physical property for simulating human body. Additionally, favorable structures can be integrated into implants to promote tissue regeneration. Besides, artificial tissues and organs are built with precise bionic structure and high cell viability. Last but not least, customized drug delivery system can provide a nuanced solution to controlled release, accurate drug dosages, and minimally invasive delivery[6-10].

This review introduces the DLP-based 3D printing technology and its applications in medical field. The principle and characteristics of DLP printing technology are introduced. Then, the main applications demonstrate the influence of DLP-based 3D printing to medicine (**Figure 1**). Finally, this review culminates with the limitations of existing techniques and future research directions.

2 DLP-based 3D printing

2.1 DLP-based 3D printing technology

The concept of 3D printing is first described in 1986 by Charles[11]. The method, named stereolithography, sequentially print many layers by ultraviolet light to create 3D structures. With the development of additive manufacturing technology and material science, various 3D printing methods have emerged. There are two common types of 3D printing methods: The nozzle-based and the light-based 3D printing. The nozzle-based 3D printing includes extrusion printing and inkjet printing. In these printing methods, the printed materials are extruded or jetted and deposited onto the platform. The light-based 3D printing includes DLP printing, laser assisted printing, selective laser melting (SLM), and selective laser sintering (SLS). The DLP and laser assisted printing methods apply photopolymerization reactions. During the process of SLM and SLS, material powders are melted and reshaped at the high temperature created by laser. These 3D printing platforms have significant differences in printing mechanism, speed, material selection, and resolution[12,13]. **Table 1** compares the DLP printing with other 3D techniques used in the medical field.

DLP-based 3D printing technology comes from the image projection technology developed by Texas Instruments in the 1980s[5]. This method uses a set of chipsets based on optical micro-electromechanical technology to process working light sources to photosensitive materials (**Figure 1**). The main functional part is a digital micro mirror device (DMD) which consists of a group of micron-sized, controllable mirrors. The mirrors rotate to control the path of light and then project it onto the photosensitive resin during working. The ordinary arrays have a large number of mirrors, from nearly a million mirrors to more than 2 million. On the other hand, the pixel spacing of the micromirror is only a few microns or a dozen microns. The resolution of the DLP-based 3D printing depends on the projection plane adjusted by DMD and lens. Thus, the DLP printing technique has a relatively high resolution, which is usually at the micron scale[12]. Furthermore, the printing conditions are mild for cells. In general, the printing process without high temperature, pressure, and shear stress caused by the nozzle is suitable for printing living tissues or organs with

Table 1. Comparison of various 3D printing methods in the medical field[12,14,15].

Properties	Materials	Printing process	Resolution (μm)	Speed	Cell viability
Nozzle based printing					
Extrusion	Thermoplastic polymer	Serial (line by line)	50	Slow (μm/s)	40-80%
Inkjet	Thermoplastic polymer	Serial (drop by drop)	50	Medium (mm/s)	＞85%
Light based printing					
DLP	Photosensitive polymer	Continue Plane (layer by layer)	6	Fast (mm^3/s)	85-95%
Laser assisted	Photosensitive polymer	Serial (dot by dot)	~1	Medium (mm/s)	＞85%
SLM/SLS	Metals and alloys powder, ceramic and polymer	Serial (dot by dot)	80	slow (μm/s)	—

little cell damage. When light is projected onto the resin using DLP technology, instead of being restricted to a spot like the laser-assisting 3D printing, the entire layer is printed immediately. Hence, this technology allows fast printing[5,12].

2.2 The advancements of DLP-based 3D printing

During the past decade, the printing accuracy which is, a key indicator of 3D printing technology, has improved greatly. The accuracy improvement is related to the printing equipment, materials, and process parameters. When DLP 3D printing technology was first invented in 2006, the researchers manufactured constructs that have 20 μm microstructure[12]. In 2013, Yi *et al*. fabricated constructs with various topologies. In fact, the resolution of DLP 3D printing partially depends on the material chosen. When the 3D constructs are printed using polyethylene glycol diacrylate (PEGDA MW = 700 da) solely, the XY resolution of the constructs can reach nearly 6 by 6 μm. Meanwhile, the resolution is about 17 μm with bioink containing 10% gelatin-methacrylate (GelMA) and 3 × 10^6 cells/mL[16]. Dai *et al*. used a high precision DMD (each micromirror is 10.8 μm) to build the projection-based 3D printing platform. This platform can fabricate multiscale vascular channels, ranging from the main trunk channel (> 1100 μm wide) to the relatively small branch channel (up to 17 μm wide)[17]. Saha *et al*. combined the advantages of two-photon lithography (TPL) and DLP printing and developed a femtosecond projection TPL (FP-TPL) technique. By this method, complex 3D structures maintaining sub-500-nm features can be printed rapidly[18].

Besides accuracy, many methods were applied to improve printing speed. These methods greatly improve printing efficiency and ensure cell viability during tissue construction[19]. In 2015, John *et al*. modified the technique and created a continuous liquid interface fabrication method. The continuous liquid interface in this study is realized through the oxygen-permeating region under the printing platform, which forms a persistent liquid interface between the oxygen-permeating region and the photopolymerization region of the material, in which the material cannot conduct photopolymerization. When the average thickness of each layer is set at 50–100 μm, this method can manufacture a 3D structure with 5 cm high in <10 min[20]. Recently, a faster DLP 3D printing method, computed axial lithography, has been

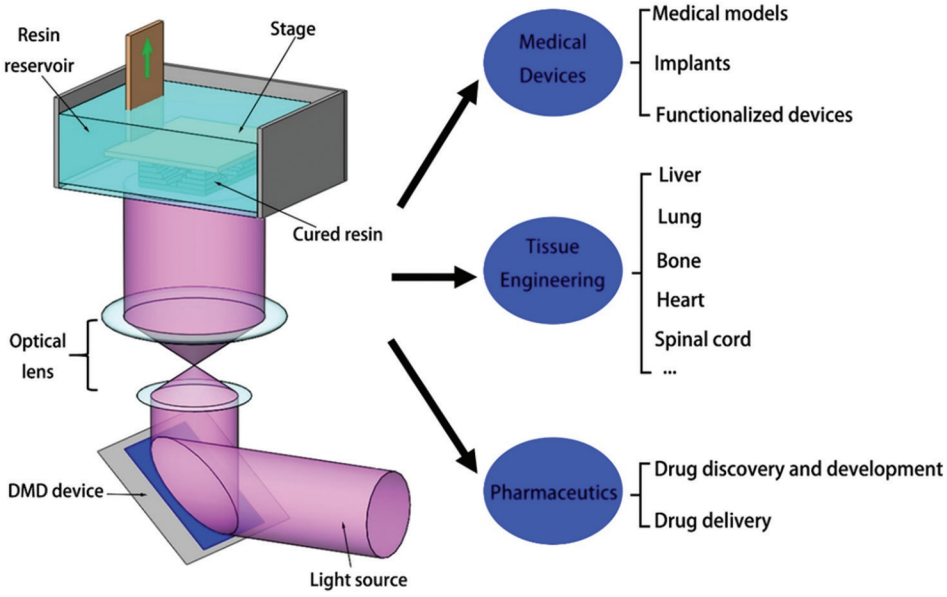

Figure 1. This schematic diagram shows the working principle and related application fields related to, DLP based 3D printing technology.

developed[21]. In this manufacturing system, light is reflected onto the photosensitive material in the form of a 2D image. When different plane images are projected onto the material from different angles, the energy generated by the multi-angle superposition exposure will cause the material to converge into the originally designed 3D structure. This technology can be scaled up to a relatively large additive manufacturing volume and is order of magnitude faster than conventional 3D printing methods.

To design products with ideal performance, the selection of appropriate materials has become an important requirement. Materials for DLP printing are photosensitive polymers that can polymerize from liquid into solid when exposed to light. The physical and chemical properties of traditional photosensitive polymers limit their applications. Most of them are incompatible with cells. What is more, the monomers and its vapors are also harmful to humans. Hence, researchers have manifolded the materials used for DLP-based 3D printing. Due to the biocompatibility and good polymerization effect, PEGDA and GelMA are widely used inks for bioprinting. Soon *et al.* modified silk fibroin with glycidyl methacrylate to get SF-based bioink-methyl acrylate (SiL-MA). This polymerized SiL-MA hydrogel has the characteristics of high tensile strength, which is available to suture. In addition, SiL-MA hydrogels produced by DLP 3D printing have remarkable biocompatibility, which gives the hydrogel a broad application prospect in the field of tissue engineering[22]. Many components can be mixed in the liquid printed materials to obtain functionalized constructs. The addition of piezoelectric $BaTiO_3$ nanoparticles and electric silver nanoparticles to ink can give the products the functions of piezoelectricity and electroconductibility, respectively. Ceramic and glass products can be sintered with printing inks combining ceramic fillers or silicate[23,24]. These improvements made this manufacturing method more competitive in fabricating medical products.

Given the favorable properties of printing speed, accuracy, and materials, DLP 3D printing has great value in the rapid fabrication of precision personalized products.

3 Medical devices

A medical device is an important tool that can benefit the patient by helping health-care providers diagnose and treat patients, assisting patients to overcome sickness or disease, and improving their quality of life[25]. The 3D printing technology has been widely applied in fabricating specific medical devices based on patients' disease. According to the statistics, the U.S. Food and Drug Administration (FDA) has approved at least 85 3D printed medical devices up to 2015[26]. These products including medical models, personalized implants, and functionalized devices.

3.1 Medical models

The solid 3D model can remedy the limitation of medical imaging technology that can only transform the information of patients' lesions into visual graphics and display them to doctors and patients. These 3D models are tangible objects that can be operated by hand and can directly reflect patients' conditions, providing more intuitive and convenient means for clinical medical teaching, diagnosis, and surgical planning. The 3D printing technology provides a method that can use the graphic information to create patient-specific anatomical 3D medical models[27]. So far, a series of medical models have been manufactured by various 3D printing technologies, such as skull, heart, pelvis, blood vessel, and tumor, which are beneficial to surgery assistance, disease analysis, and teaching demonstration[28,29].

Due to the fast printing speed of DLP-based 3D printing, doctors no longer have to wait for long hours to prepare 3D models of patients' pathological organs. In the clinical treatment of various acute diseases, such as cerebral hemorrhage, cerebral infarction, and myocardial infarction, the effective treatment window period is only a few hours, requiring the doctor to prepare the patient's surgical plan within a few minutes. On the premise of ensuring printing accuracy (~100 μm), polymeric models, up to tens of centimeters, in size can be produced in minutes[20]. This characteristic can meet the time requirement of clinical treatments of the above acute disease models. Compared with other 3D printing technologies, the DLP

printing platform can flexibly set a series of manufacturing parameters, including printing time, light intensity, and even the wavelength of light. Kuang *et al.* designed a special grayscale light DLP 3D printing technology. This method utilizes a grayscale light to print the material that can be two-stage curing into a 3D structure that can be printed with relatively high precision and has remarkable changes in mechanical strength gradient. A bionic 3D structure with both soft muscle and hard bone was created by this printing technique (**Figure 2A**). When pressed lightly, the muscles are easily squeezed out of shape. However, in the process of pressing the muscles, the hard bones remain stable[6]. An other group fabricated spine-shaped phantom for stereotactic body radiation therapy and oral cavity model for orthodontics (**Figure 2B and C**)[30,31].

In addition to the benefits of surgical assistance and disease analysis, DLP 3D printed disease model is also applicable to the teaching of clinical medicine, especially the basic subjects of medical education such as human body and pathological anatomy. For example, this technology can quickly print personalized zirconia material dental teaching model, this personalized teaching model has sufficient dimensional accuracy, and maintains clinical-pathological oral deformity so that students can get an intuitive impression of oral malformation disease[32,33].

3.2 Implants

The field of *in vivo* medical devices that can be printed with DLP-based 3D printers mainly includes biodegradable or non-degradable human implants made of various materials, such as metals,

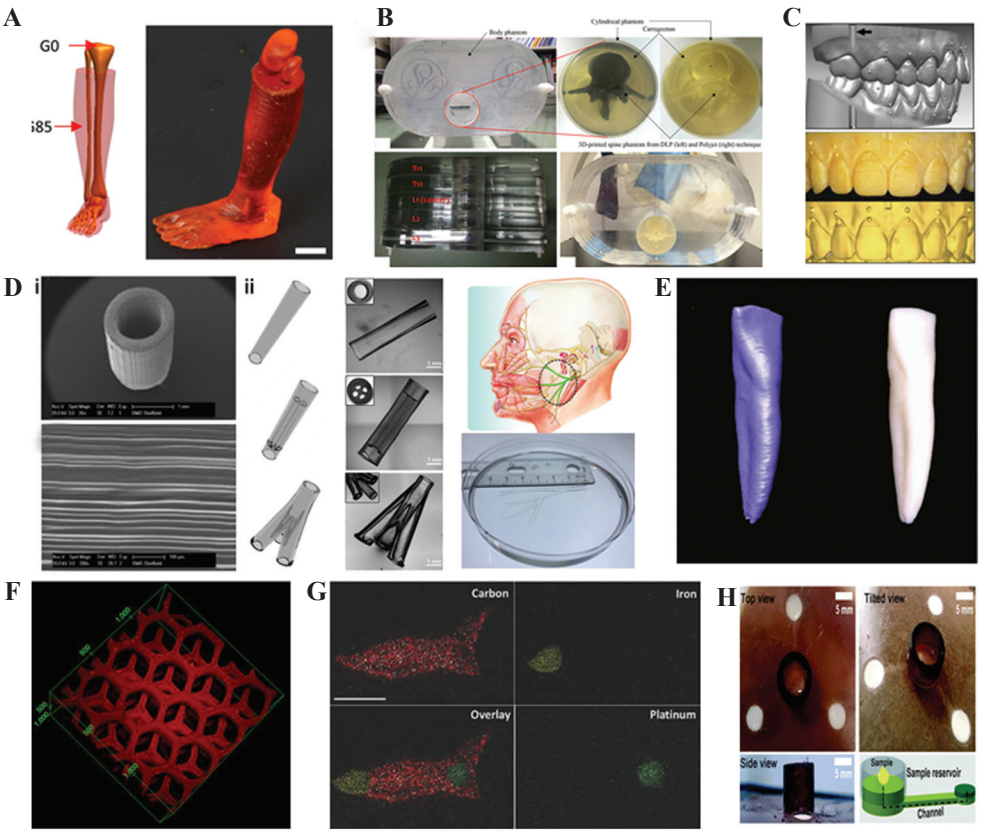

Figure 2. Digital light processing 3D printed medical devices: (A) A limb with soft "muscle" and stiff "bone"[6], (B) spine-shaped phantom[32]. (C) Oral cavity model[33], (D) (i) nerve conduit with microchannels[7]; (ii) a range of nerve conduits[34], (E) zirconia dental implant[35], (F) detoxification device[8], (G) toxin sensor[36], (H) blood senor for measuring glucose, cholesterol, and triglycerides[37].

ceramics, and polymers. These implants are used to replace or repair the injuries *in vivo*. First, the shapes of the implants are well-matched with the injury parts. Then, the printed microstructure can guide the regeneration of injured tissues.

3.2.1 Biodegradable implants

Biodegradable implants refer to a series of medical implants that can be gradually degraded by the human body with the change of time and other conditions after implantation and finally replaced by human original tissues. Many biodegradable materials, such as alginate, cellulose, extracellular matrix (ECM), and collagen, have been developed and applied in DLP 3D printing. Christopher *et al*. used the DMD device that can print in micron scale to obtain nerve conduits with parallel microchannels (**Figure 2D i**). The light is reflected by the 20 μm size mirrors of the device. This translates the 2D image into a 3D microstructure that is identical to the micron array of mirrors. The microstructure can guide Schwann cell-directed migration. Tao *et al*. created similar nerve conduits encapsulating nanoparticles. The drugs loaded in nanoparticles can further improve the regeneration of injured nerve[38]. For treating different injury sites, Zhu *et al*. have utilized this technique to create a series of nerve conduits, such as conduits with microchannels and even bionic conduits that are beneficial to nerve repair in humans (**Figure 2D ii**)[34].

3.2.2 Non-biodegradable implants

DLP 3D printed implants play an important role in stomatology, brain surgery, ent (ear, nose and throat), thoracic surgery, and other surgical operations. Reham *et al*. reported that they used DLP technology to fabricate a customized zirconia implant and evaluated its related physical properties (**Figure 2E**). In this study, they evaluated the precision size, surface morphology, and physical properties of printed zirconia implants[39]. The results show that this printed custom implant has a precision size similar to the reference model and competitive bending strength (943 MPa), which can be compared with grinding zirconia (800–1000 MPa). In addition, DLP technology can also quickly print photosensitive resin materials. These resin materials have been widely used as a filling materials in stomatology due to the characteristics of low viscosity, curing and shrinking, fast processing rate, small swelling, and high wet strength[35].

3.3 Functionalized devices

Besides satisfying shapes and microstructures of DLP printed 3D models and implants, it can add specific functions to medical devices. These devices take the fixability to combine materials and structures to achieve their functions. Due to the efficiency and high accuracy of DLP printing, it only takes a short time to fabricate medical devices with powerful functions.

In 2014, Gou *et al*. loaded the printed hydrogel with polydiacetylene (PDA) nanoparticles to construct a detoxification device (**Figure 2F**). The lobule-like microstructures allow efficient contact between toxins and the 3D devices. At the same time, detoxification particles in the hydrogel can trap and attract toxins while sensing them. It turns out that the printed detoxification hydrogel device can effectively remove certain toxins from aqueous solutions[8]. The combination of PDA nanoparticles and 3D printed hydrogels not only act as a detoxification device but also a toxin sensor in solutions. When the nanoparticles bind to the toxin, the ordered π-conjugated chain structure on the particle surface is disrupted, triggering a fluorescent radiation reaction that makes it easy to detect the presence of the toxin. Zhu *et al*. printed swimming microfish encapsulated PDA, iron oxide, and platinum nanoparticles (**Figure 2G**). The microfish can be chemically powered and magnetically guided. They took the fluorescence intensity change of PDA as an indicator to evaluate the detoxification efficiency of hydrogels and the concentration of toxins in solution[36]. Recently, a 3D paper-based microfluidics analysis device (3D-μPAD) has been reported for *in vitro* diagnosis (**Figure 2H**). The 3D-μPAD is produced by a DLP 3D printer using a material called photoluminescent liquid resin, which is printed on both sides of the paper in one go, with no additional assembly required.

This 3D-μPAD could be used to measure glucose, cholesterol, and triglycerides in human blood[40].

4. Tissue engineering

Tissue engineering aims at improving or replacing biological functions to improve clinical procedures for repairing damaged tissues and organs[41]. The 3D bioprinting allows cells, materials, and biological factors reasonably distributed in the construct. It provides a new method for building artificial tissue[2]. DLP-based 3D printing has a great advantage in bioprinting for its mild printing condition. It causes little damage to functional components, including cells, biological factors, and biomaterials[42]. The DLP 3D bioprinting technology has been applied to construct a range of tissues and organs, such as liver, cardiac, vascularized, and cancer models. In the following part, some typical applications are discussed in detail[8,43-45].

4.1 Liver

The liver is the largest internal organ and gland in the human body. Many important physiological functions are performed by it, which include bile secretion, detoxification, drug metabolism, and producing serum proteins. So, hepatic diseases have significant influence on patient. Actually, the liver has a certain degree of self-regeneration ability. However, many severe diseases, such as hepatocellular carcinoma and cirrhosis, can reduce or even eliminate the regenerative ability of the liver. For these patients, a common treatment is transplanting a new healthy liver to replace the old one. There is forecast predicting that the demand for liver transplantation will increase by 23% in the next two decades. Aside from the high cost of surgery, donors and their availabilities are very limited[46]. Thus, the artificial liver has wide application prospects.

In the past decades, people have been trying to obtain artificial liver tissue. However, due to the complex structure and various cell types, it is hard to construct an artificial liver with multiple functions. The bioprinting technology has promoted the development of engineered liver tissue. It can fabricate the interwoven networks such as bile duct, lymphatic, and vessels in the natural liver. DLP-based 3D printing technology has the potential of accurately patterning cells and biomaterials and maintaining high activity. Taking advantage of this technology, engineered livers' constructs are more precise with increasing structural and functional complexity[47].

Ma *et al*. used a DLP-based 3D printer to obtain a 3D triculture hepatic model. The model consists of many micro hexagonal structures and encapsulated three kinds of cells, including human induced pluripotent stem cells (hiPSC)-hematopoietic progenitor cells (HPCs), human umbilical vein endothelial cells (HUVECs), and adipose-derived stem cells. (**Figure 3A i**)[48]. By characterizing the cell morphology, the liver-specific gene expression levels, metabolic product, and cytochrome P450 (CYP) induction, they found that the hiPSC-HPCs in the hepatic models are very similar to hepatic cells in human body. The results indicated that the microstructure and supporting cells can promote the maturation of hiPSC-HPCs and maintain their functions. Zhu *et al*. fabricated a relatively simple model that encapsulated HUVECs and HepG2 (**Figure 3A ii**)[47]. Grigoryan *et al*. used DLP printing technique to fabricate artificial liver with functional intravascular topologies[9]. Compared with tissues containing single hepatocyte, the vascularized liver containing hepatocyte aggregates showed 60 times activity of the albumin promoter. Furthermore, the DLP 3D printed vascularized liver tissues appeared better integration with host after implanted *in vivo*.

4.2 Lung

Lung is one of the main functional organs of the respiratory system. The function of lung is to extract and transfer oxygen into human blood and release carbon dioxide to the air. However, human lungs have no regenerative capacity. Constructing artificial lung to replace diseased lung is the only alternative to treat patients with severe lung diseases[49]. They are faced with the same problems as liver disease patients. Therefore, the construction of artificial lung is one of the best solutions.

The lung contacts air and blood at the same time. Thus, it takes huge challenges to construct

a satisfying artificial lung. The 3D printing has helped fabricate lung tissue analog[49]. Lenke *et al*. designed a lung model to simulate air-blood barrier architecture (**Figure 3B**). The model consisted of two layers: The endothelial layer containing HUVEC and A549 cells and thin Matrigel layer[50]. They have not evaluated the functional of the printed membrane model. However, natural lungs are 3D and can "breathe". Grigoryan *et al*. added a nontoxic light blocker to improve the z-resolution of DLP 3D printing and fabricated vascularized alveolar model topologies[9]. The alveolar model showed two major functions of lung tissues that are blood flowing and air exchanging. Circulating moist 10 kPa, 0.5 Hz oxygen gas, the distension of the structures, and the shape changes of the concave airway regions could be found. In the meantime, they perfuse the deoxygenated red blood cells (RBCs) at the blood vessel inlet. Then, they saw the RBCs became clear after passing through the vessels adjacent to airway. In this work, the high precision of DLP 3D printing lent them the ability to fabricate 3D entangled networks in organs.

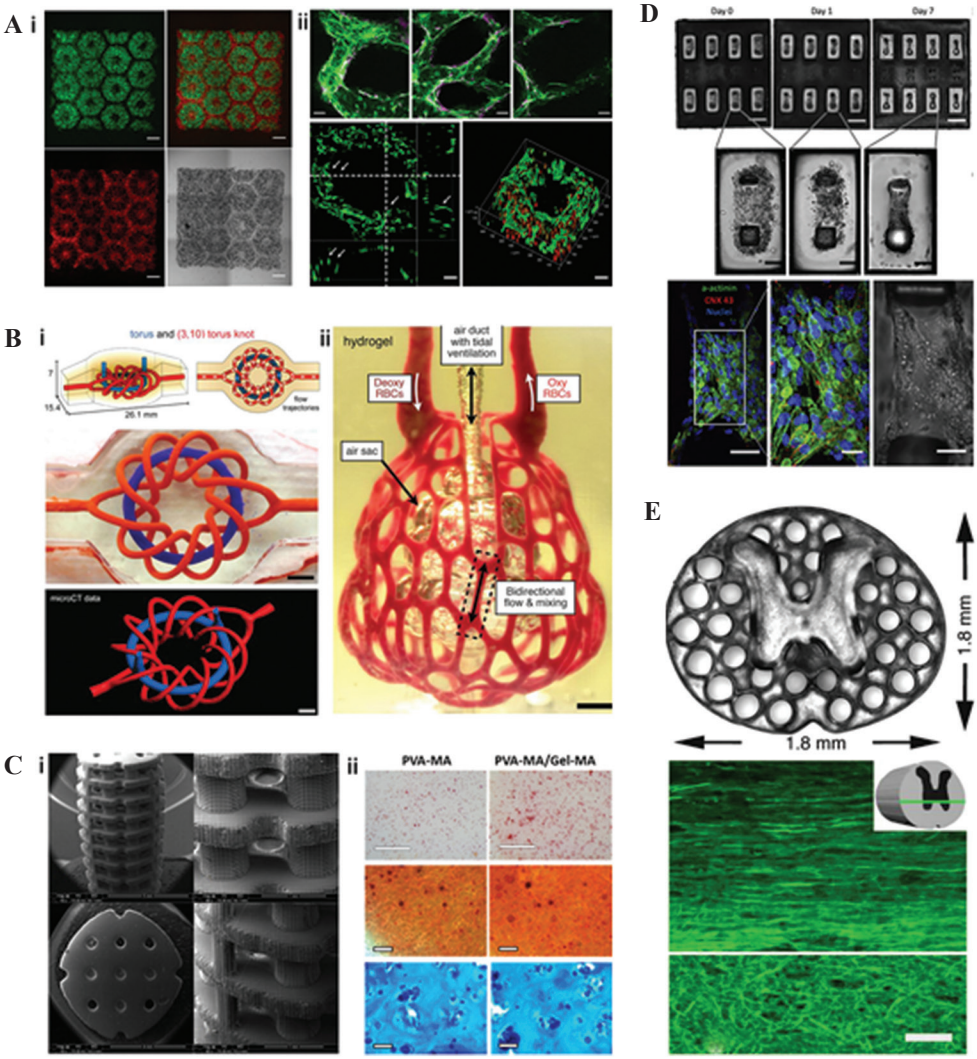

Figure 3. Digital light processing 3D printing of artificial tissues: (A) (i) Hepatic structure containing human induced pluripotent stem cells (hiPSC)-hematopoietic progenitor cells (green) and supporting cells (red)[48]; (ii) endothelial network of prevascularized hepatic tissue[47], (B) (i) multivascular network; (ii) vascularized lung tissue[9], (C) (i) bone tissue engineering scaffold[51]; (ii) staining of cells encapsulated in bone tissue engineering hydrogel[52], (D) hiPSC-derived cardiac tissue on force gauge[53], (E) spinal cord and its horizontal section[54].

4.3 Bone

Bone is a dynamic vascularized tissue that can repair and remodel itself without leaving scars[55]. However, for critical size bone defects, bone replacement or surgical intervention is usually required[56]. Besides the autograft and allografts, the implant made by biocompatible metal or ceramic is an alternative to repair the injured bone. However, the inert implant will slowly break down with time. Therefore, active bone tissue is considered as an ideal implant to replace the injured part[14,57]. The 3D bioprinting allows precise bone scaffolds to be fabricated and a variety of cells arranged in the scaffolds to form bionic bone constructs.

The bone tissue engineering scaffolds are required to fit the defect site, allow transport of nutrient and growth factor, and degrade over time. DLP 3D printing has demonstrated a very important prospect to construct these scaffolds. Dean *et al*. took advantage of the high accuracy of DLP 3D printing to fabricate tissue-engineered bone scaffolds (**Figure 3C i**) [51]. The printed microstructure improved the adhesion, proliferation, and maturation of the cells. The degradation velocity of the scaffolds can also be adjusted by the microstructure. Recently, Lim *et al*. encapsulated mesenchymal stem cells (MSCs) in hydrogels to obtain bone or cartilage tissues[52]. They developed a new bioink by combining methacrylate polyvinyl alcohol (PVA-MA) and GelMA. Using this bioink and a DLP 3D printer, they printed some biologically relevant scaffolds with precise microstructures. The MSCs encapsulated in printed hydrogels maintain high viability (≈90%) after 21 days of culture. Through staining analysis, osteogenic differentiation, and cartilage-specific ECM were observed in the 3D printed hydrogel (**Figure 3C ii**). The result indicated potential applications of DLP 3D printing and the bioink in bone tissue engineering.

4.4 Heart

Cardiovascular diseases are the foremost cause of death over the world. The heart-valve replacement is a common treatment for valvular heart diseases. There are two kinds of artificial heart valves, including mechanical valves and biological valves (autograft and allograft). The mechanical valves lead to the risk of thrombus. The autograft implantation is a complex surgery that requires cutting the other part of the patient. On the other hand, the allograft always causes an immune response. In addition, the biological valves may fail more than 10 years after implantation[58,59]. Thus, a new strategy is necessary to be developed to fabricate artificial myocardium replacements.

Some studies have been carried out to develop 3D cardiac tissue *in vitro*. However, the cardiomyocyte is usually seeded on or encapsulated in a simple 3D scaffold in these studies[60]. It is very easy to culture cardiomyocyte and maintains its viability *in vitro*. However, the key point of fabricating artificial cardiac tissue is obtaining biomimetic structures and promoting cardiomyocyte orientation alignment. Liu *et al*. blended human embryonic stem cell-derived cardiomyocytes (hESC-CMs) into 3D pattern hydrogel constructs by a DLP-based 3D printer (**Figure 3D**)[61]. The DLP-based 3D printing technology allowed hESC-CMs to mimic the multilayered aligned myocardium. Meanwhile, they printed a customizable cantilever-based force detector to measure the force from the artificial cardiac model. Further to this, they encapsulated a specific hESC line that is sensitive to calcium. Then, they can detect the calcium transient of the cardiac model. Recently, this group used DLP-based 3D printing technology to obtain artificial cardiac tissue and detect the expression of mature cardiac marker genes. The work will promote the development of artificial cardiac tissue[53].

4.5 Spinal cord

The spinal cord, together with the brain, is called the central nervous system (CNS). It is a cylindrical structure and consists of nerve fibers and associated tissues. In USA, there are more than 50,000 people who are suffering from the diseases of spinal cord injury (SCI). Due to the importance of CNS, SCI causes significant influence on patients and is hard

to cure. Recently, the artificial spinal cord shows great potential in assisting SCI repair[54,62,63].

The 3D printing technology allows the fabrication of personalized scaffolds that are matched with the patients' injured sites. The microstructure can promote SCI repair by stimulating, guiding, and aligning axon. However, due to the complex inner structure of the spinal cord, it is difficult to construct a spinal cord structure in detail[62]. The technology of DLP 3D printing provides a method to manufacture such complex and precise structures. Using this rapid 3D printing technology, Koffler *et al*. printed 3D biomimetic hydrogel scaffolds suitable for rodent spinal cord size in several seconds (**Figure 3E**)[54]. The printed scaffolds can encapsulate the neuronal progenitor cells (NPCs) and promote axonal regeneration. After implanting the bionic scaffold to replace the injured site, the damaged axons regenerated and entered to the scaffold and synapsed with NPCs. The NPCs extended to and synapsed with the host spinal cord below the injury. The scaffold formed a new "contact" across the entire spinal cord and improved the recovery of the function of spinal cord. The artificial spinal cord tissue can be extended to human spinal cord size and fit to any shapes.

The 3D bioprinting has been widely used in fabricating various tissues and organs. Inkjet and extrusion bioprinters are good methods to solve part of the problems in tissue engineering. However, these two methods also have limitations. First, they are nozzle-based 3D printing technology. Due to the small aperture of the nozzle, used to deliver bio-ink, cells will be stressed and damaged during passing through the nozzle. Next, the printing resolution is limited by the aperture of the nozzle, which is usually bigger than 50 μm. Finally, the printing speed of these methods is not very high. Cells would subside to the bottom of the printing ink in the process of printing[16,64,65]. DLP 3D bioprinting is a rapid, precise and mild printing method. The printing speed is approximately ~1000× times faster than the traditional nozzle printers[16]. The X- and Y-resolutions can reach 6 μm. Thus, DLP 3D bioprinting has advantages in fabricating living tissues with complex and miniscule structure, such as liver, lung and other vascularized tissues.

5 Pharmacy

The 3D printing technology can be used in all phases of pharmacy research, including drug discovery, development, and delivery[66]. Despite the continuous improvement of detection equipment and technology, achievement in discovery and development require a long time and high cost, which are mainly reflected in screening drugs from a large number of candidates and researching their absorption, metabolization, toxicity, etc. As described in the previous section, the DLP 3D printed tissue or organ or disease model can simulate the real situation of human body. It can be used to discover and develop drugs *in vitro* and replace part animal experiments[42]. High-accuracy 3D printing allows the fabrication of pharmaceutical preparations with fine structures, and control the position and dose of drugs precisely.

5.1 Drug discovery and development

In the early stage of drug development, 3D printing products have important applications in early and high throughput drug screening due to their complex bionic structure and good repeatability[67]. It is difficult to get a satisfying result by applying traditional 2D and 3D disease models for drug screening. These disease models lack bionic structures, vascular networks, and complex microenvironments. In the section of tissue engineering, it has been discussed that DLP-based 3D printing can build complicated vascularized tissues, which can also be used in fabricating disease models correspond to those in the human body. If these models were applied in drug screening, the results might be more accurate. On the cover glass, an alginate loaded gel chip loaded with *Escherichia coli* was printed on the cover glass as a platform for high-throughput screening of micro drugs[68]. Three drops of the antibiotic mixture (penicillin/streptomycin, antifungal agent, and kanamycin sulfate) were added to evaluate the bioactivity, function,

and antibacterial activity of antibiotics. Thus, DLP-based 3D printing provides a rapid method for disease modeling. Especially for precision medicine, high throughput drug screening is very important. The disease model based on patient's cell can get an accurate screening result. Besides drug screening, the researches of cancer models can provide new solutions for cancer therapy.

Developing a drug, it is required to study its absorption, metabolization, excretion, optimal dosage, and toxicity. Most measurements are carried out in the traditional 2D monolayer culture system, which cannot simulate the natural 3D tissue microenvironment. Hence, the results are greatly different between the *in vivo* and *in vitro* tests[69]. Artificial tissue fabricated by 3D printing can simulate the state of the tissue *in vivo* more effectively and can quickly and cheaply carry out pharmacological, toxicological, and pharmacokinetic studies, so as to reduce the losses caused by pharmacodynamic, and toxicity problems found only in animal or clinical trials[14,70]. The 3D printed liver and kidney tissues have been applied to testing drug metabolism. For example, Ma *et al.* studied drug metabolism by their printed hepatic model. Treating the biomimetic hepatic model with an inducer, they characterized the expression levels of CYP which includes several key enzymes for drug metabolism. They found significant increases in three key enzymes. The positive response indicated that the inducer can be cleared by liver.

5.2 Drug delivery

As a manufacturing technology, DLP-based 3D printing technology can also be used in the preparation of the drug delivery system with customized dosages, shapes, sizes, and release ways. In 2015, the FDA approved a 3D-printed drug to accurately control the structure and dosage of the drug. Through 3D printing technology, the tablet is constructed in microporous structures, which will dissolve immediately after oral administration. Patients who have difficulties in swallowing can easily take the tablet[71]. This technology also encourages the development of 3D printed drug delivery system. The delivery system can also mix or print multi-drug layers to control drug release. Adding drugs at fixed points on drug delivery vectors can control the time of drug release to achieve the purpose of accelerating or delaying drug release. Printing different drug layers can make drugs release at intervals according to their structural characteristics. Changing 3D printing can make drug release at intervals according to their structural characteristics[72]. The filling degree of the printed preparation can accurately customize personalized drugs containing different dosages. Liu *et al.* fabricated microhydrogels with predesigned shapes and sizes to carry drugs. The microhydrogels are small enough to be injected through a 1-mL syringe in a noninvasive way[10]. Tao *et al.* encapsulated PDA nanoparticles into the microhydrogels (**Figure 4A**). Then, the microhydrogels are injected into the location of bacterial infection to improve tissue recovery[73]. The 3D printed implants can act as drug delivery systems. The 3D printed post-operative filler of drug-loaded gene drugs for patients with glioma, which can continuously release drugs to eliminate residual tumor cells and avoid recurrence of tumors[74]. Xu *et al*. encapsulated RGFP966 nanoparticle into 3D printed nerve conduits to improve nerve regeneration and repair (**Figure 4B**)[75]. Taking theophylline as the model drug, Hossam *et al.* used PEGDA at various concentrations to fabricate tablets (**Figure 4C**). Then, they studied the release of theophylline from the printed tablets. The DLP-based 3D printing is flexible in fabricating personalized drug delivery systems by changing printed structure, polymer concentration, and printer parameters, including light intensity and wavelength and exposure time. Therefore, this printing technology has great potential in fabricating personalized drugs[44].

Taking advantage of DLP-based 3D printing technology, printed products can significantly save the drug discovery time and cost and accelerate the accuracy of drug screening. Meanwhile, the printed tissues or cancer models formed by the patient's own cells could be used for precision medicine. Last but not least, the DLP-based 3D printed drugs or drug carriers can be designed with specific structures, precise dosages, and personalized release ways.

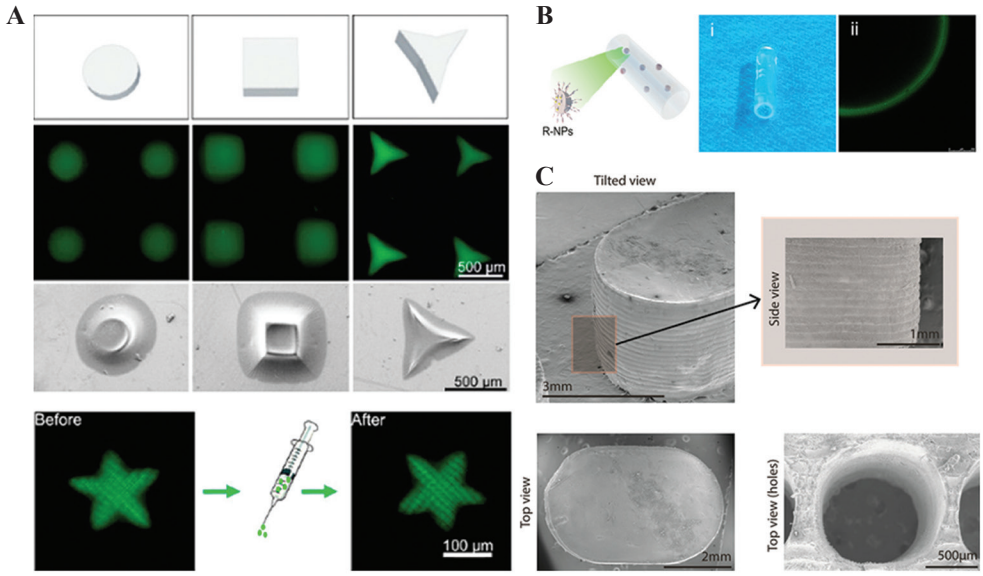

Figure 4. DLP 3D printing of drug delivery system: (A) A range of injectable microhydrogels encapsulating drugs[73], (B) functionalized nerve conduits[75], (C) microstructure of 3D printed tablets[44].

6 Challenges and future perspectives

As one of the 3D printing techniques, DLP-based 3D printing inherits the advantages of fabricating complex personalized productions. Meanwhile, this technique has its own characteristics of high precision, fast speed, and mild condition. Thus, on the basis of conventional medical applications, DLP-based 3D printing can improve the accuracy and cell livability of the fabricated products. As a result, the medical models manufactured by DLP 3D printing can better simulate the real states or locate implants. The devices with precision structures are more sensitive. The microstructures of tissues can be accurately built to obtain engineered tissues and organs for organ transplantation, disease research, and drug development. Furthermore, DLP 3D printing can manufacture predesigned microstructures of pharmaceutical and accurately control the position and doses of drugs.

The printing equipment and materials are the foundation of applications in medicine, which are increasingly developed. Some breakthroughs have been made. Continuous liquid interface printing improved the resolution and speed of DLP 3D printing[20]. Using tomographic reconstruction can fabricate a volumetric construct at once[21]. Metal, glass, and ceramic products can be obtained through printing and sintering. More and more materials are developed in DLP-based 3D printing[76]. For example, the materials include functionalized materials, initiator-free materials, and non-toxic initiators. Although DLP 3D printing technology has made advancements, it still takes some deficiencies[12]. The materials choice is limited to only photosensitive polymers. Many excellent materials cannot be printed directly. They are required to be combined with photosensitive polymer or chemical modified by photosensitive groups. To accelerate the photopolymerization, photoinitiator, mostly having toxicity, is required to be added in the mixed inks. When the light is projected from top-down in DLP-based 3D printer, the materials are not extruded by nozzles, but pre-filled the container. It may raise the concerns of materials wastage and cost increases. With the development of 3D printing technology, there will be more equipment and materials emerging in the future. There is forced onto the cells as well when the printing platform is lowered or the platform is separated from the printed surface. The repeated lifting of printing platform should be avoided or reduced during printing. More studies are required to reduce the separating force between

the platform and the printed surface. Meanwhile, more clinical researches and improved law systems are required to regulate the use of 3D printed products. The clinical researches would provide a good foundation for making the rules. These, the rules could guide doctors or researchers to use 3D printing technology for medical applications.

Author contributions

J. Z. and Q. H. are co-first authors, who contributed equally to this work. S. W., J. T. and M.G. gave advice and discussion. M. G. supervised the project. All authors read and approved the final manuscript.

Conflict of interest

No conflict of interest was reported by the authors.

Acknowledgments

This work was supported by the Key Research and Development Projects of People's Liberation Army (BWS17J036), 1·3·5 project for disciplines of excellence, West China Hospital, Sichuan University (ZYJC18017) and the Science and Technology Project of Chengdu (2018-CY02-00041-GX).

References

1. Kang HW, Lee SJ, Ko IK, *et al.*, 2016, A 3D Bioprinting System to Produce Human-Scale Tissue Constructs with Structural Integrity. *Nat Biotechnol*, 34(3):312–9. DOI: 10.1038/nbt.3413.
2. Murphy SV, Atala A, 2014, 3D Bioprinting of Tissues and Organs. *Nat Biotechnol*, 32(8): 773–85. DOI: 10.1038/nbt.2958.
3. Ricles JCC, Di Prima M, Oh SS, 2018, Regulating 3D-Printed Medical Products. *Sci Transl Med*, 10(461):6.
4. Rybicki FJ, 2018, Medical 3D Printing and the Physician-Artist. *Lancet*, 391(10121):651–2. DOI: 10.1016/s0140-6736(18)30212-5.
5. Lu Y, Mapili G, Suhali G, *et al.*, 2006, A Digital Micro-Mirror Device-Based System for the Microfabrication of Complex, Spatially Patterned Tissue Engineering Scaffolds. *J Biomed Mater Res A*, 77(2):396–405. DOI: 10.1002/jbm.a.30601.
6. Kuang X, Wu J, Chen K, *et al.*, 2019, Grayscale Digital Light Processing 3D Printing for Highly Functionally Graded Materials. *Sci Adv*, 5(5):eaav5790. DOI: 10.1126/sciadv.aav5790.
7. Pateman CJ, Harding AJ, Glen A, *et al.*, 2015, Nerve Guides Manufactured from Photocurable Polymers to Aid Peripheral Nerve Repair. *Biomaterials*, 49:13. DOI: 10.1016/j.biomaterials.2015.01.055.
8. Gou M, Qu X, Zhu W, *et al.*, 2014, Bio-Inspired Detoxification Using 3D-Printed Hydrogel Nanocomposites. *Nat Commun*, 5:3774. DOI: 10.1038/ncomms4774.
9. Grigoryan B, Paulsen SJ, Corbett DC, *et al.*, 2019, Multivascular Networks and Functional Intravascular Topologies Within Biocompatible Hydrogels. *Science*, 364:8.
10. Liu X, Tao J, Liu J, *et al.*, 2019, 3D Printing Enabled Customization of Functional Microgels. *ACS Appl Mater Interfaces*, 11(13):12209–15. DOI: 10.1021/acsami.8b18701.
11. Hull CW, Spence ST, Lewis CW, *et al.*, 1998, Stereolithographic Curl Reduction. *US, US 5772947 A*.
12. Ngo TD, Kashani A, Imbalzano G, *et al.*, 2018, Additive Manufacturing (3D Printing): A Review of Materials, Methods, Applications and Challenges. *Compos Part B*, 143:172–96. DOI: 10.1016/j.compositesb.2018.02.012.
13. Ligon SC, Liska R, Stampfl J, *et al.*, 2017, Polymers for 3D Printing and Customized Additive Manufacturing. *Chem Rev*, 117(15):10212–90. DOI: 10.1021/acs.chemrev.7b00074.
14. Vijayavenkataraman S, Yan WC, Lu WF, *et al.*, 2018, 3D Bioprinting of Tissues and Organs for Regenerative Medicine. *Adv Drug Deliv Rev*, 132:296–332. DOI: 10.1016/j.addr.2018.07.004.
15. Zhu W, Ma X, Gou M, *et al.*, 2016, 3D Printing of Functional Biomaterials for Tissue Engineering. *Curr Opin Biotechnol*, 40:103–12. DOI: 10.1016/j.copbio.2016.03.014.
16. Soman P, Chung PH, Zhang AP, *et al.*, 2013, Digital Microfabrication of User-Defined 3D Microstructures in Cell-Laden Hydrogels. *Biotechnol Bioeng*, 110(11):3038–47. DOI: 10.1002/bit.24957.
17. Xue D, Wang Y, Zhang J, *et al.*, 2018, Projection-Based 3D Printing of Cell Patterning Scaffolds with Multiscale Channels. *ACS Appl Mater Interfaces*, 10(23):19428–35. DOI: 10.1021/acsami.8b03867.
18 Saha SK, Wang D, Nguyen VH, *et al*., 2019, Scalable Submicrometer Additive Manufacturing. *Science*, 366(6461):105-109. DOI: 10.1126/science.aax8760.
19. Bernal PN, Delrot P, Loterie D, *et al.*, 2019, Volumetric Bioprinting of Complex Living-Tissue Constructs Within Seconds. *Adv Mater*, 31:e1904209. DOI: 10.1002/adma.201904209.

20. Tumbleston JR, Shirvanyants D, Ermoshkin N*, et al.*, 2015, Continuous Liquid Interface Production of3D Objects. *Science*, 347:5.
21. Kelly BE, Bhattacharya I, Heidari H*, et al.*, 2019, Volumetric Additive Manufacturing Via Tomographic Reconstruction. *Science*, 8(363):1075–9.
22. Kim SH, Yeon YK, Lee JM*, et al.*, 2018, Precisely Printable and Biocompatible Silk Fibroin Bioink for Digital Light Processing 3D Printing. *Nat Commun*, 9(1):1620. DOI: 10.1038/s41467-018-03759-y.
23. Kim K, Zhu W, Qu X*, et al.*, 2014, 3D Optical Printing of Piezoelectric Nanoparticle-Polymer Composite Materials. *ACS Nano*, 8:8.
24. Fantino E, Chiappone A, Roppolo I*, et al.*, 2016, 3D Printing of Conductive Complex Structures with In Situ Generation of Silver Nanoparticles. *Adv Mater*, 28(19):3712–7. DOI: 10.1002/adma.201505109.
25. US Food and Drug Administration, is the Product A Medical Device? Available from: https://www.fda.gov/medical-devices/classify-your-medical-device/product-medical-device.
26. Rindelaub JD, Baird Z, Lindner BA*, et al.*, 2019, Identifying Extractable Profiles from 3D Printed Medical Devices. *PLoS One*, 14(5):e0217137. DOI: 10.1371/journal.pone.0217137.
27. Pashuck ET, Stevens M, 2016, From Clinical Imaging to Implantation of 3D Printed Tissues. *Nat Biotechnol*, 34(3):295–6. DOI: 10.1038/nbt.3503.
28. Tack P, Victor J, Gemmel P*, et al.*, 2016, 3D-Printing Techniques in a Medical Setting: A Systematic Literature Review. *Biomed Eng Online*, 15(1):115. DOI: 10.1186/s12938-016-0236-4.
29. Paul GM, Amin R, Wen P, *et al*., 2018, Medical Applications for 3D Printing: Recent Developments. *Mo Med*, 115(1):75–81.
30. Kim MJ, Lee SR, Lee MY*, et al.*, 2017, Characterization of 3D Printing Techniques: Toward Patient Specific Quality Assurance Spine-Shaped Phantom for Stereotactic Body Radiation Therapy. *PLoS One*, 12(5):e0176227. DOI: 10.1371/journal.pone.0176227.
31. Kim SY, Shin YS, Jung HD*, et al.*, 2018, Precision and Trueness of Dental Models Manufactured with Different 3-Dimensional Printing Techniques. *Am J Orthod Dentofacial Orthop*, 153(1):144–53. DOI: 10.1016/j.ajodo.2017.05.025.
32. Hohne C, Schmitter M, 2019, 3D Printed Teeth for the Preclinical Education of Dental Students. *J Dent Educ*, 83:1100–6. DOI: 10.21815/jde.019.103.
33. Brown GB, Currier GF, Kadioglu O*, et al.*, 2018, Accuracy of 3-Dimensional Printed Dental Models Reconstructed from Digital Intraoral Impressions. *Am J Orthod Dentofacial Orthop*, 154(5):733–9. DOI: 10.1016/j.ajodo.2018.06.009.
34. Zhu W, Tringale KR, Woller SA*, et al.*, 2018, Rapid Continuous 3D Printing of Customizable Peripheral Nerve Guidance Conduits. *Mater Today*, 21(9):951–9. DOI: 10.1016/j.mattod.2018.04.001.
35. Moin DA, Wismeijer DH, 2017, A Novel Approach for Custom Three-Dimensional Printing of a Zirconia Root Analogue Implant by Digital Light Processing. *Clin Oral Implants Res*, 28(6):668–70. DOI: 10.1111/clr.12859.
36. Zhu W, Li J, Leong YJ*, et al.*, 2015, 3D-Printed Artificial Microfish. *Adv Mater*, 27(30):4411–7. DOI: 10.1002/adma.201501372.
37. Fu X, Xia B, Ji B*, et al.*, 2019, Flow Controllable Three-Dimensional Paper-Based Microfluidic Analytical Devices Fabricated by 3D Printing Technology. *Anal Chim Acta*, 1065:64–70. DOI: 10.1016/j.aca.2019.02.046.
38. Tao J, Zhang J, Du T*, et al.*, 2019, Rapid 3D Printing of Functional Nanoparticle-Enhanced Conduits for Effective Nerve Repair. *Acta Biomater*, 90:49–59. DOI: 10.1016/j.actbio.2019.03.047.
39. Osman RB, van der Veen AJ, Huiberts D*, et al.*, 2017, 3D-Printing Zirconia Implants; A Dream or a Reality? An *in vitro* Study Evaluating the Dimensional Accuracy, Surface Topography and Mechanical Properties of Printed Zirconia Implant and Discs. *J Mech Behav Biomed Mater*, 75:521–8. DOI: 10.1016/j.jmbbm.2017.08.018.
40. Park C, Han YD, Kim HV*, et al.*, 2018, Double-Sided 3D Printing on Paper Towards Mass Production of Three-Dimensional Paper-Based Microfluidic Analytical Devices (3D-muPADs). *Lab Chip*, 18(11):1533–8. DOI: 10.1039/c8lc00367j.
41. Bianco P, Robey PG, 2001, Stem Cells in Tissue Engineering. *Nature*, 414:4.
42. Ma X, Liu J, Zhu W*, et al.*, 2018, 3D Bioprinting of Functional Tissue Models for Personalized Drug Screening and *in vitro* Disease Modeling. *Adv Drug Deliv Rev*, 132:235–51. DOI: 10.1016/j.addr.2018.06.011.
43. Anwar S, Singh GK, Miller J*, et al.*, 2018, 3D Printing is a Transformative Technology in Congenital Heart Disease. *JACC Basic Transl Sci*, 3(2):294–312. DOI: 10.1016/j.jacbts.2017.10.003.
44. Kadry H, Wadnap S, Xu C*, et al.*, 2019, Digital Light Processing (DLP) 3D-Printing Technology and Photoreactive Polymers in Fabrication of Modified-Release Tablets. *Eur J Pharm Sci*, 135:60–7. DOI: 10.1016/j.ejps.2019.05.008.
45. Soman P, Kelber JA, Lee JW*, et al.*, 2012, Cancer Cell

Migration Within 3D Layer-By-Layer Microfabricated Photocrosslinked PEG Scaffolds with Tunable Stiffness. *Biomaterials*, 33(29):7064–70. DOI: 10.1016/j.biomaterials.2012.06.012.

46. Peery AF, Crockett SD, Murphy CC*, et al.*, 2019, Burden and Cost of Gastrointestinal, Liver, and Pancreatic Diseases in the United States: Update 2018. *Gastroenterology*, 156(1):254–72, e211. DOI: 10.1053/j.gastro.2018.08.063.
47. Zhu W, Qu X, Zhu J*, et al.*, 2017, Direct 3D Bioprinting of Prevascularized Tissue Constructs with Complex Microarchitecture. *Biomaterials*, 124:106–15. DOI: 10.1016/j.biomaterials.2017.01.042.
48. Ma X, Qu X, Zhu W*, et al.*, 2016, Deterministically Patterned Biomimetic Human iPSC-Derived Hepatic Model Via Rapid 3D Bioprinting. *Proc Natl Acad Sci U S A*, 113(8):2206–11. DOI: 10.1073/pnas.1524510113.
49. Petersen TH, Calle EA, Zhao L*, et al.*, 2010, Tissue-Engineered Lungs for *in vivo* Implantation. *Science*, 329:5.
50. Horvath L, Umehara Y, Jud C*, et al.*, 2015, Engineering an *in vitro* Air-Blood Barrier by 3D Bioprinting. *Sci Rep*, 5:7974. DOI: 10.1038/srep07974.
51. Dean D, Jonathan W, Siblani A*, et al.*, 2012, Continuous Digital Light Processing (cDLP): Highly Accurate Additive Manufacturing of Tissue Engineered Bone Scaffolds. *Virtual Phys Prototyp*, 7(1):13–24. DOI: 10.1080/17452759.2012.673152.
52. Lim KS, Levato R, Costa PF*, et al.*, 2018, Bio-Resin for High Resolution Lithography-Based Biofabrication of Complex Cell-Laden Constructs. *Biofabrication*, 10(3):034101. DOI: 10.1088/1758-5090/aac00c.
53. Ma X, Dewan S, Liu J*, et al.*, 2019, 3D Printed Micro-Scale Force Gauge Arrays to Improve Human Cardiac Tissue Maturation and Enable High Throughput Drug Testing. *Acta Biomater*, 95:319–27. DOI: 10.1016/j.actbio.2018.12.026.
54. Koffler J, Zhu W, Qu X*, et al.*, 2019, Biomimetic 3D-Printed Scaffolds for Spinal Cord Injury Repair. *Nat Med*, 25(2):263–9. DOI: 10.1038/s41591-018-0296-z.
55. Mourino V, Boccaccini AR, 2010, Bone Tissue Engineering Therapeutics: Controlled Drug Delivery in Three-Dimensional Scaffolds. *J R Soc Interface*, 7(43):209–27. DOI: 10.1098/rsif.2009.0379.
56. Seitz H, Rieder W, Irsen S*, et al.*, 2005, Three-Dimensional Printing of Porous Ceramic Scaffolds for Bone Tissue Engineering. *J Biomed Mater Res B Appl Biomater*, 74(2):782–8. DOI: 10.1002/jbm.b.30291.
57. Gao G, Cui X, 2016, Three-Dimensional Bioprinting in Tissue Engineering and Regenerative Medicine. *Biotechnol Lett*, 38(2):203–11. DOI: 10.1007/s10529-015-1975-1.
58. Scaglione MS, Kliethermes S, Cao G, *et al.*, 2015, The Epidemiology of Cirrhosis in the United States A Population-based Study. *Orig Artic*, 49:7.
59. Cheung DY, Duan B, Butcher JT, 2015, Current Progress in Tissue Engineering of Heart Valves: Multiscale Problems, Multiscale Solutions. *Expert Opin Biol Ther*, 15(8):18.
60. Nguyen AH, Marsh P, Schmiess-Heine L*, et al.*, 2019, Cardiac Tissue Engineering: State-of-the-art Methods and Outlook. *J Biol Eng*, 13:57. DOI: 10.1186/s13036-019-0185-0.
61. Liu J, He J, Liu J*, et al.*, 2019, Rapid 3D Bioprinting of *in vitro* Cardiac Tissue Models Using Human Embryonic Stem Cell-Derived Cardiomyocytes. *Bioprinting*, 13: e00040. DOI: 10.1016/j.bprint.2019.e00040.
62. Ma ZLY, Yang Y, Wang J, *et al.*, 2019, Research Progress and Prospects of Tissue Engineering Scaffolds for Spinal Cord Injury Repair and Protection. *Regen Med*, 14(9):887–98.
63. Ashammakhi N, Kim H, Ehsanipour A*, et al.*, 2019, Regenerative Therapy for Spinal Cord Injury. *Tissue Eng Part B Rev*. DOI: 10.1089/ten.TEB.2019.0182.
64. Duan B, Hockaday LA, Kang KH*, et al.*, 2013, 3D Bioprinting of Heterogeneous Aortic Valve Conduits with Alginate/Gelatin Hydrogels. *J Biomed Mater Res A*, 101(5):1255–64. DOI: 10.1002/jbm.a.34420.
65. Pedde RD, Mirani B, Navaei A*, et al.*, 2017, Emerging Biofabrication Strategies for Engineering Complex Tissue Constructs. *Adv Mater*, 29(19):e1606061. DOI: 10.1002/adma.201606061.
66. Amir-Aslani A, Mangematin V, 2010, The Future of Drug Discovery and Development: Shifting Emphasis Towards Personalized Medicine. *Technol Forecast Soc Change*, 77(2):203–17. DOI: 10.1016/j.techfore.2009.09.005.
67. Trenfield SJ, Awad A, Goyanes A*, et al.*, 2018, 3D Printing Pharmaceuticals: Drug Development to Frontline Care. *Trends Pharmacol Sci*, 39(5):440–51. DOI: 10.1016/j.tips.2018.02.006.
68. Mateen R, Ali MM, Hoare T, 2018, A Printable Hydrogel Microarray for Drug Screening Avoids False Positives Associated with Promiscuous Aggregating Inhibitors. *Nat Commun*, 9(1):602. DOI: 10.1038/s41467-018-02956-z.
69. Fan Y, Nguyen DT, Akay Y*, et al.*, 2016, Engineering a Brain Cancer Chip for High-throughput Drug Screening. *Sci Rep*, 6:25062. DOI: 10.1038/srep25062.
70. Zhang YS, Yue K, Aleman J*, et al.*, 2017, 3D Bioprinting for Tissue and Organ Fabrication. *Ann Biomed Eng*, 45(1):148–63. DOI: 10.1007/s10439-016-1612-8.
71. 2015, First 3D-Printed Pill. *Nat Biotechnol*, 33(10):1014.

DOI: 10.1038/nbt1015-1014a.

72. Economidou SN, Lamprou DA, Douroumis D, 2018, 3D Printing Applications for Transdermal Drug Delivery. *Int J Pharm*, 544(2):415–24. DOI: 10.1016/j.ijpharm.2018.01.031.
73. Tao J, Xu X, Wang S*, et al.*, 2019, Polydiacetylene-Nanoparticle-Functionalized Microgels for Topical Bacterial Infection Treatment. *ACS Macro Lett,* 8:563–8. DOI: 10.1021/acsmacrolett.9b00196.
74. Yang Y, Du T, Zhang J*, et al.*, 2017, A 3D-Engineered Conformal Implant Releases DNA Nanocomplexs for Eradicating the Postsurgery Residual Glioblastoma. *Adv Sci (Weinh)*, 4(8):1600491. DOI: 10.1002/advs.201600491.
75. Xu X, Tao J, Wang S*, et al.*, 2019, 3D Printing of Nerve Conduits with Nanoparticle-Encapsulated RGFP966. *Appl Mater Today*, 16:247–56. DOI: 10.1016/j.apmt.2019.05.014.
76. Kotz F, Arnold K, Bauer W*, et al.*, 2017, Three-Dimensional Printing of Transparent Fused Silica Glass. *Nature*, 544(7650):337-9. DOI: 10.1038/nature22061.

REVIEW ARTICLE

Solvent-based Extrusion 3D Printing for the Fabrication of Tissue Engineering Scaffolds

Bin Zhang[1], Rodica Cristescu[2], Douglas B. Chrisey[3], Roger J. Narayan[1]*

[1]Joint Department of Biomedical Engineering, University of North Carolina and North Carolina State University, Raleigh, NC 27606, USA

[2]National Institute for Lasers, Plasma and Radiation Physics, Lasers Department, P.O. Box MG-36, Bucharest-Magurele, Romania

[3]Department of Physics and Engineering Physics, Tulane University, New Orleans, LA, USA

Abstract: Three-dimensional (3D) printing has been emerging as a new technology for scaffold fabrication to overcome the problems associated with the undesirable microstructure associated with the use of traditional methods. Solvent-based extrusion (SBE) 3D printing is a popular 3D printing method, which enables incorporation of cells during the scaffold printing process. The scaffold can be customized by optimizing the scaffold structure, biomaterial, and cells to mimic the properties of natural tissue. However, several technical challenges prevent SBE 3D printing from translation to clinical use, such as the properties of current biomaterials, the difficulties associated with simultaneous control of multiple biomaterials and cells, and the scaffold-to-scaffold variability of current 3D printed scaffolds. In this review paper, a summary of SBE 3D printing for tissue engineering (TE) is provided. The influences of parameters such as ink biomaterials, ink rheological behavior, cross-linking mechanisms, and printing parameters on scaffold fabrication are considered. The printed scaffold structure, mechanical properties, degradation, and biocompatibility of the scaffolds are summarized. It is believed that a better understanding of the scaffold fabrication process and assessment methods can improve the functionality of SBE-manufactured 3D printed scaffolds.

Keywords: Solvent-based extrusion 3D printing, Ink materials, Ink rheology, Fabrication process parameters, Tissue scaffolds

***Corresponding Author:** Roger J. Narayan, Joint Department of Biomedical Engineering, University of North Carolina and North Carolina State University, Raleigh, NC 27606, USA; roger_narayan@unc.edu

Received: May 30, 2019; ***Accepted:*** December 2, 2019; ***Published Online:*** January 17, 2020

Citation: Zhang B, Cristescu R, Chrisey DB, *et al.,* 2020, Solvent-based extrusion 3D printing for the fabrication of tissue engineering scaffolds. *Int J Bioprint*, 6(1):211. DOI: 10.18063/ijb.v6i1.211

1 Introduction

3D printing, which is also referred as additive manufacturing, is a process in which a scaffold architecture is initially designed with computer-aided design (CAD) file and subsequently fabricated in a layer-by-layer manner[1]. 3D printing can overcome the limitations of traditional scaffold fabrication methods in terms of scaffold interconnectivity and reproducibility[2-5]. SBE 3D printing is one of the most popular 3D printing techniques. The biomaterials are placed in solvents to create inks; these inks are extruded from nozzles as filaments in layer-by-layer manner to form the scaffold structure[6-10]. The currently utilized ink biomaterials are natural polymers, synthetic polymers, ceramics, and their combinations. SBE 3D printing has been performed with or without

cells to create tissue scaffolds for heart valve tissue[11,12], bone tissue[13,14], cartilage tissue[15], blood vessel[16], and skin tissue[17]. Recently, a concept study has described building a scaffold with simultaneous control over multiple biomaterial inks in the desired combination to create biomimetic and functional scaffolds that closely mimic natural tissue[18]. Despite these advances, the lack of feasible inks, particularly bio-composite ink, prevents the clinical use of current SBE 3D printed scaffolds. Scaffolds with appropriate levels of filament uniformity cannot easily be obtained; in addition, there is a poor fidelity between the structures of printed scaffolds and the computer models of these structures[11,19].

In this review paper, the biomaterials used in SBE 3D printing of TE scaffolds are considered. The ink rheology, cross-linking mechanisms, and processing parameters are described. The SBE structure, mechanical properties, biodegradation mechanisms, and biocompatibility, of 3D printed scaffolds, are also discussed. This paper also provides an overview of SBE 3D printing for TE applications and discussed printing-related factors. Hopefully this paper will provide guidance to 3D printing researchers, which facilitates improvements of scaffold design and reproducibility.

2 SBE 3D printing types in TE

The SBE 3D printing technique involves extruding a continuous filament of ink containing biomaterials with or without cells through a nozzle to form 3D woodpile structures in a layer-by-layer manner. The SBE 3D printer includes a three-axis position system, print head, and print platform. The print head is moved to appropriate locations on the build platform by the three-axis position system; inks are extruded from the syringe on the print head in the X, Y, and Z directions[9,10,20]. The printed filament resolution is dependent on the print head nozzle diameter, which can be varied in the range of 10–1000 μm. As shown in **Figure 1A-C**, SBE 3D printing can be classified as pneumatic driven, piston-driven, and screw-driven based 3D printing. In pneumatic-driven based printing, the inks are forced through the nozzle by control over the compressive air pressure. In the piston and screw-driven based 3D printing, inks are extruded by regulating the motor rotation speed. Among these three classifications of SBE 3D printing approaches, pneumatic-driven based 3D printing is more suitable for printing ink containing cells since the sterilized air can minimize contamination[21,22]. Piston and screw-driven based 3D printing can provide larger deposition forces compared with pneumatic-driven based 3D printing;

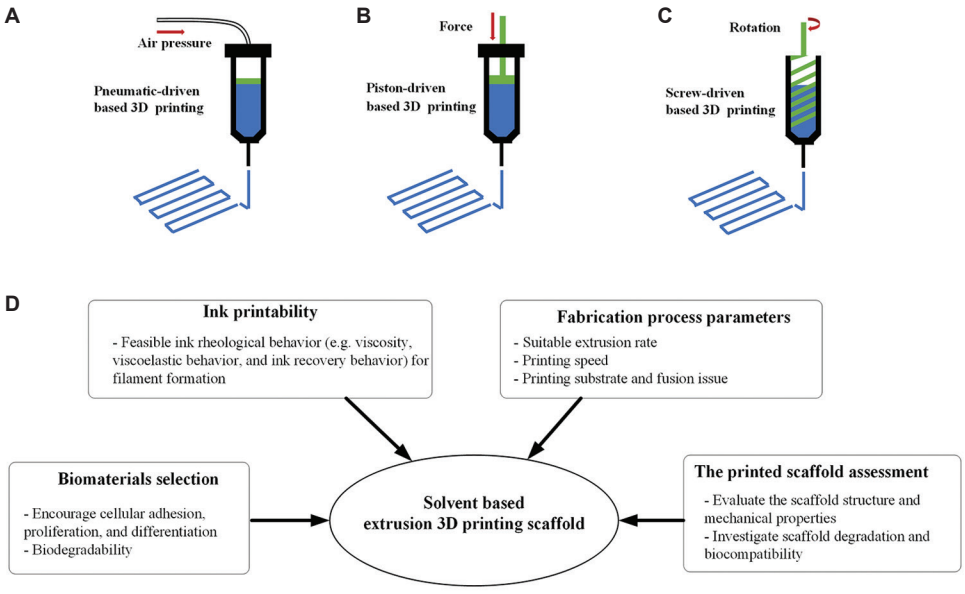

Figure 1. SBE 3D printing types, pneumatic-driven based 3D printing (A); piston-driven based 3D printing (B); screw-driven based 3D printing (C); a schematic showing the factors that influence SBE 3D printing.

these approaches are compatible with the printing of relatively high viscosity inks. However, screw-driven based 3D printing is not suitable for the printing of cell-laden inks since the shear stress generated on the blade may cause cell damage[23,24].

There is a wide variability among different tissues and organs in terms of their material composition and mechanical properties[25-27]. As such, functionalization of 3D scaffolds is dependent on material and mechanical parameters and should be tailored according to these parameters as appropriate. For the development of such scaffolds with SBE 3D printing, several factors should be considered (summarized in **Figure 1D**). These include (a) biomaterial selection for the ink, (b) investigation of the ink rheological behavior, (c) printing process parameters, and (d) assessment of printed scaffold regarding structure, mechanical properties, degradation, and biocompatibility.

3 Ink biomaterials for SBE 3D printing in TE

3.1 Ink materials with cells for SBE 3D printing

Biomaterials used in scaffold fabrication are mixed with solvents to create the liquid feedstock for SBE 3D printing. **Table 1** summarizes the use of SBE 3D printing with or without living cells for TE. Biomaterials used with living cells in scaffold fabrication should not only provide an appropriate environment for cell survival but also should be compatible with the printing process. The formulated biomaterial solution is often called a bioink and the processing approach is referred as bioprinting. The most commonly used biomaterials for bioprinting are hydrogels (either natural or synthetic hydrogels); these biomaterials can provide mild aqueous environment to the cells during the printing process. The hydrogels used in SBE 3D printing with cells includes alginate, hyaluronic acid, collagen, gelatin, and silk[12,17,28-30].

Duan *et al*.[12] formulated hydrogel inks with hyaluronic acid and gelatin; they incorporated human aortic valve interstitial cells (HAVICs) within these inks for 3D bioprinting of heart valve conduits. An increase in the gelatin concentration resulted in a lower ink stiffness and a higher viscosity; these parameters facilitated cell spreading and maintenance of a better HAVIC fibroblastic phenotype. They described the dependence of the bioprinting accuracy on the hydrogel concentration; optimization of the ink concentration enable the fabrication of a heart valve shape that matches the original design. Wüst *et al*.[31] evaluated a combination of alginate and gelatin with various amounts of hydroxyapatite (HA); human mesenchymal stem cells (hMSCs) mixed into the hydrogel/HA inks survived the printing process. The *in vitro* results show high cell viability, with an 85% cell viability rate after 3 days. The elastic modulus of the alginate-gelatin composite discs increased with the HA concentration. However, the ink became more viscous as the HA concentration was increased; as such, it is difficult to print HA-containing inks. They indicated that control of the tip temperature affected the viscosity of the bioink; increasing the temperature can convert the ink to liquid form, eliminating the clogging issues at the dispenser tips.

Notably, more viscous inks require larger pressures for extrusion from the nozzle; as such, cells in the bioinks are exposed to process-induced forces (i.e., shear stress). The deformation of the cell membrane can occur if the applied force is too high. As such, the shear stress is a key factor that needs to be evaluated during bioprinting. Blaeser *et al*.[32] developed a fluid dynamics model and performed *in vitro* experiments to understand shear stress at the nozzle site. The results show that the generated shear stress is affected by the hydrogel ink viscosity, extrusion pressure, and nozzle dimensions. Mouse fibroblasts can exhibit cell viability of 96% if exposed to shear stress of <5 KPa; viability is decreased to 90% and 75% for the shear stress of 5–10 kPa and more than 10 KPa, respectively.

3.2 Ink materials without cells for SBE 3D printing

The cells do not need to be placed within the inks. The printed scaffolds can serve as a support structure to facilitate tissue regeneration on the inherent recovery properties of the tissue. Direct ink writing (DIW) is a common applied method for printing inks that do not contain

Table 1. The summary of tissue scaffold fabrication using SBE 3D printing

	SBE 3D printing types	Ink materials	Ink rheology properties	Cross-linking mechanisms	Printing process parameters	Scaffold characterization methods	Biological outcomes	Reference
Printing with cells	Pneumatic-driven based 3D printing	Alginate, nanocellulose and human chondrocyte mixed in D-mannitol solvent	Ink shear viscosity was measured at the applied shear rate from 0.01 to 1000s^{-1}. Oscillation shear testing was performed to define the linear viscoelastic region.	$CaCl_2$ solution bath	Print speed was at 20 mm/s	The optimal ink was selected by the measurement of the filament width from microscopy images of the printed scaffold.	Human chondrocyte printed with the nanocellulose based ink and the cell viability of 86% after 3D culture for 7 days.	[15]
	Pneumatic-driven based 3D printing	Hyaluronic acid, gelatin and HAVIC mixed in cell culture medium	Ink shear viscosity was measured at applied shear stress from 1 to 1000 Pa. The elastic modulus of various concentration hydrogels inks was measured.	UV light	No specific mentioned	The printing accuracy was determined by evaluating the measured area and the design.	Increasing gelatin concentration facilitated cell spreading and better maintained HAVIC phenotype.	[12]
	Piston-driven based 3D printing	Alginate, gelatin, and hMSCs with different concentration HA mixed in PBS	The viscosity of inks with different HA concentration was at the shear rate from 0.0001 to 100 s−1. Oscillatory shear tests over a temperature ramp from 50 to 10°C to investigate the gel point.	$CaCl_2$ solution bath	Print speed was 2 mm/s and extrusion rate was 0.45×10^{-3} mm mm^{-1}	HA enabled the visualization of the patterns using micro-CT.	hMSCs survived the printing process and showed high cell viability of 85% living cells after three days of subsequent *in vitro* culture.	[31]
Printing without cells	Pneumatic-driven based 3D printing	PLA and a bioactive CaP glass dissolved in chloroform	CaP glass improved ink viscosity, but no ink rheology test was involved.	Solvent evaporation	The print speed was 3 mm/s	Scaffold pores size and porosity were accessed from the SEM image and micro-CT generated structure to compare with the theoretical values. The compressive modulus of printed scaffolds with different patterns was evaluated by uniaxial compression testing.	The glass particles increased roughness, hydrophilicity, and mechanical property of scaffolds. CaP glass improved MSCs adhesion.	[35]

(Contd...)

Table 1. (*Continued*)

SBE 3D printing types	Ink materials	Ink rheology properties	Cross-linking mechanisms	Printing process parameters	Scaffold characterization methods	Biological outcomes	Reference
Pneumatic-driven based 3D printing	PCL, HA, and CNT dissolved in dichloromethane	CNT concentration was adjusted to achieve an optimum viscosity between 2.5 and 7 Pa.s.	Solvent evaporation	No specific mentioned	The compressive modulus of printed scaffolds with different CNT concentrations was evaluated by uniaxial compression testing.	HA improved the bioactivity, there was good cell adhesion and spreading at the scaffold surface *in vitro*.	[36]
Pneumatic-driven based 3D printing	PCL, PLGA, and HA particles mixed in dichloromethane.	The optimal viscosity of 30–35 Pa·s was reached.	Solvent evaporation	The print speed was 15 cm/s, and extrusion rates were as 275 cm^3/h	The compressive modulus of printed scaffolds was evaluated by uniaxial compression testing.	Supported cell viability and proliferation and induced osteogenic differentiation of hMSCs *in vitro* and rapidly integrated with the tissue *in vivo*.	[13]

HAVIC: Human aortic valve interstitial cells, PLA: Polylactic acid, MSCs: Mesenchymal stem cells, PCL: Polycaprolactone, HA: Hydroxyapatite, CNT: Carbon nanotubes, PLGA: Poly (lactic-glycolic acid), SBE: Solvent-based extrusion, TE: Tissue engineering, hMSCs: Human mesenchymal stem cells

cells. Ghosh *et al*.[33] printed tissue scaffolds and microvascular networks using the DIW technique; they fabricated a scaffold with a silk fibroin solution ink; the extruded filament was deposited in a methanol-rich reservoir for crystallization. *In vitro* studies suggest that the scaffolds supported hMSC adhesion and growth as well as higher chondrogenic differentiation under chondrogenic conditions. Miranda *et al*.[34] used the DIW technique to produce scaffolds with precise porous features using concentrated TCP and HA inks with suitable viscoelastic properties. The 3D printed ceramic scaffolds have shown promising results for potential use in bone tissue repair; their application is limited due to their brittleness. The incorporation of a polymer material with a ceramic ink is a promising approach to overcome this limitation. The combination of polymer and ceramic components can also mimic the organic and inorganic components of natural bone tissue. Sun *et al*.[16] developed scaffolds composed of a gradient array of silk/HA, which supported the cocultures of hMSCs and human mammary microvascular endothelial cells (hMMECs). The histology results indicate that the hMSCs and hMMECs form intricate networks of extracellular matrix within the 3D scaffolds.

Some synthetic polymers are not water-soluble and must be mixed with organic solvents to form solutions; these polymers can often provide better mechanical strength than natural polymers. Considering the toxicity of many organic solvents, cells may not be incorporated within synthetic polymer-laden inks. Several synthetic polymers have been used in SBE 3D printing, including polycaprolactone (PCL), polylactic acid (PLA), poly (lactic-glycolic acid) (PLGA), and their copolymers. Serra *et al*.[35] used PCL and bioactive CaP glass to fabricate 3D scaffolds with orthogonal and displaced double-layer patterns. Their results indicate that scaffolds containing CaP glass particles exhibited increased roughness and hydrophilicity. The preliminary cell response of these materials was studied with MSCs; this study revealed that CaP glass improved cell adhesion. Gonçalves *et al*.[36] fabricated scaffolds out of composites containing PCL, nano-HA, and

carbon nanotubes (CNT). The CNT improved the mechanical behavior of the scaffolds. The *in vitro* results showed that HA improved bioactivity; good cell adhesion and spreading were noted on the scaffold surface. Although the use of SBE 3D printing to create polymer/ceramic composites is promising for TE applications, only a few studies to this point have investigated the ink printability and processing parameters. Additional studies should be performed to understand optimization of the ink rheology, processing parameters, and cross-linking mechanisms for fabrication of SBE scaffolds.

3.3 Ink rheological behavior in SBE 3D printing

The biomaterial ink solution should have appropriate rheology since the printed structure is prone to collapse if the viscosity of the solution is low. Inks with the non-Newtonian flow and shear thinning behavior are preferred. In shear thinning, high shear rate causes the viscosity of the material solutions to decrease so that it easily flows through the needle. The cells within the ink can influence ink rheology; they can be seen as "non-soluble" microparticles suspended in the solution. Ning *et al*.[37] investigated the influence of various types of cells and cell density on the viscosity of alginate ink. The results reveal that the viscosity of pure alginate ink was higher than those of inks containing three types of cells. As the cell density in the alginate inks is increased, a reduction in viscosity can be obtained. The results suggest that cells containing cytoplasm can be treated as a fluid with low viscosity; as such, the interactions among cells likely act as lubricants and reduce the viscosity[38]. Dávila and d'Ávila[39] formulated laponite/alginate inks without cells and analyzed the ink rheology in terms of viscosity, viscoelasticity behavior, and ink recovery behavior. As the laponite concentration increased from 0 to 6 wt%, an increase in viscosity was noted at the same shear rate (**Figure 2A**). Higher laponite concentrations causes strong shear-thinning behaviors. Understanding the viscoelastic behavior of the ink through evaluation of storage and loss modulus values can determine if the material behaves more like a "viscous flow" or "elastic gel." **Figure 2B** shows the oscillation shear test results of laponite/alginate inks; by increasing the concentration of laponite particles, the gap between storage modulus and loss modulus is increased. In addition, the ink recovery behavior was also investigated to mimic the ink extrusion process from the nozzle. **Figure 2C** shows the results of viscosity recovery studies. It was observed that the ink viscosity recovered almost instantaneously when a high shear load was removed; this result

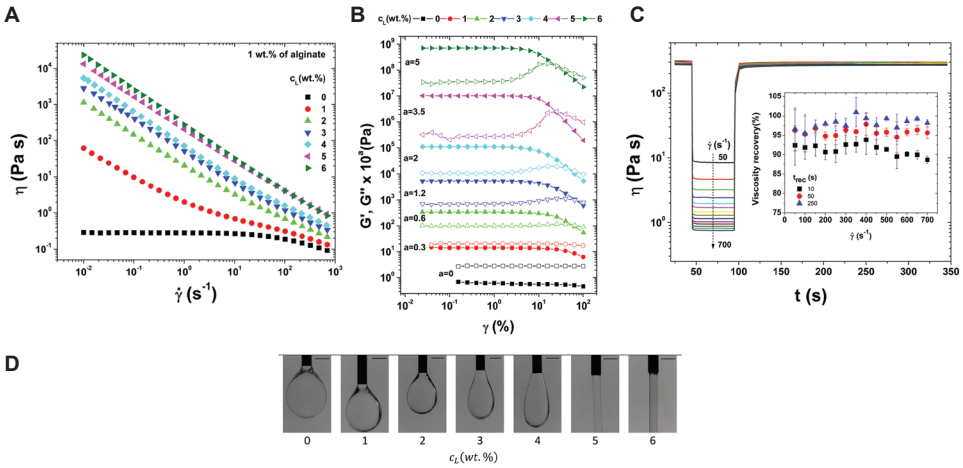

Figure 2. The relationship between viscosity (η) and shear rate ($\dot{\gamma}$) for the inks with 1 wt% alginate and a laponite concentration (cL) between 0 and 6 wt% (A); storage modulus (G') (elastic modulus) and loss modulus (G'') (viscous modulus) as a function of strain (γ) (B); viscosity as a function of the time (t) for the ink recovery test (C); microscopy images of the extrusion of alginate/laponite inks with the laponite between 0 and 6 wt%. The scale bar is 1 mm (D)[39].

is associated with elastic energy stored by the alginate chains. As shown in **Figure 2D**, filament formation with several concentrations of laponite was evaluated; filaments were formed at laponite concentrations greater than 5 wt%. The ink solution with higher viscosity is relatively more difficult to flow or spread; this phenomenon can serve to maintain the printed filament shape.

3.4 Ink cross-linking mechanisms for SBE 3D printing

Apart from increasing the ink concentration[40] and adding ceramic nanoparticles[39], ink cross-linking is a method to improve the ink elastic modulus and facilitate filament formation. Particularly in the case of a hydrogel-based ink, the cross-linking procedure can facilitate the transition from solution to gel. The most common used cross-linking procedures include ionic, covalent, thermal, and photo-cross-linking. Ionic cross-linking occurs when a water-soluble and charged polymer undergoes cross-linking with an ion of opposite charge[38]. It is an important mechanism in bioprinting since it enables mild and instant gelation of hydrogel bioinks. The cross-linking solution can be mixed, immersed, or sprayed with the ink during the printing process. Freeman and Kelly[41] investigated alginate ink stiffness by varying the calcium chloride ($CaCl_2$) crosslinking ratio. The results indicate that the spatial microenvironment was found to have a significant effect on the differentiation of MSCs within the alginate bioinks; stiffer regions of the printed construct preferentially supported osteogenesis over adipogenesis. Chung *et al*.[42] incorporated gelatin within an alginate solution; the alginate/gelatin scaffold showed better print resolution than the alginate scaffold after $CaCl_2$-crosslinking. In addition, alginate hydrogels can form covalent crosslinking through reacting with poly (ethylene glycol)-diamine[43]. Liu and Li[40] combined a covalent cross-linking polyacrylamide and ionic cross-linking k-carrageenan to synthesize the k-carrageenan/polyacrylamide double-network hydrogels. Their results showed that newly synthesized hydrogels displayed high elastic modulus values and biological functionality[44]. Ouyang *et al*.[45] studied thermal cross-linking by investigating the influence of printing temperature on ink printability and the viability of embryonic stem cells. They defined the bioink printability based on the printing of a square shape. The temperature was shown to affect the gelation degree. Samples at 30°C were proper gelatin; on the other hand, 25°C resulted in over gelation. It should be noted that gels formed by thermal cross-linking usually lack sufficient mechanical strength; furthermore, the incorporated cells would be sensitive to temperature changes.

Photo-cross-linking is the photoinduced formation of a covalent bond between macromolecules to form a cross-linked network with illuminated light. Ultraviolet (UV) light is commonly used for polymer cross-linking[38,46]. Schuurman *et al*.[47] investigated the stiffness of gelatin methacrylate after exposure to various UV light doses. The results shows that compressive modulus increases with UV exposure time. Hyaluronic acid is a material that is commonly used for cartilage tissue repair due to its structural and biological properties. However, unmodified hyaluronic acid exhibits poor stability. To solve this issue, photo-cross-linkable dextran derivates[48] or acrylate pluronic[30] were added to improve the mechanical properties and printability of hyaluronic acid ink. The incorporated chondrocytes showed good compatibility with the formulated inks and high cell viabilities. They indicate that the photo-cross-linking procedure can be used with cell-containing inks since light exposure is a minimally invasive process.

3.5 The processing parameters for SBE 3D printing

In addition to the ink material, ink rheology, and cross-linking mechanism, the processing parameters also affect the performance of the SBE 3D printing process. The processing parameters in SBE 3D printing include the extrusion rate, needle-moving speed, substrate, and parameters of the scaffold. The extrusion rate can be affected by several factors, including the ink rheology,

extrusion pressure, and needle parameters. The ink velocity alongside the needle ($V_{z(nozzle)}$). and the corresponding extrusion rate ($Q_{z(\text{extrusion})}$). follow the power-law equation; these parameters can be calculated using Equation 3.1 and 3.2[49]:

$$V_{z(nozzle)} = \int_{r}^{R} \gamma dr = \left(\frac{n}{n+1}\right)\left(\frac{\Delta P}{2KL}\right)^{\frac{1}{n}}\left[1-\left(\frac{r}{R}\right)^{\frac{n+1}{n}}\right] \quad 3.1$$

$$Q_{z\ (extrusion)} = \int_{0}^{R} 2\pi R V_Z dr = \left(\frac{\Delta P R}{2KL}\right)^{\frac{1}{n}}\left(\frac{n\pi R^3}{3n+1}\right) \quad 3.2$$

In this equation, K is the consistency index, and n is the power-law index. K is associated with the magnitude of the viscosity, and n defines the viscosity behavior; $n < 1$ for a shear-thinning ink[49]. As shown in **Figure 3A**, R is the needle radius, L is the length of the needle, and ΔP is the extrusion pressure drop along the needle. Equation 3.1 represents the velocity along the needle length; this equation shows that the velocity distribution of printed inks inside the needle is not constant. The parameter $V_{z(nozzle)}$ reaches a maximum in the core of the needle and is zero at the needle wall. Equation 3.2 shows that the extrusion rate is associated with the extrusion pressure and needle radius. The filaments are formed depending on the movement of the needle in the XY plane. The printed filament can be quantitively described; it can be simplified as a cylindrical object by neglecting the spreading of the ink. There is a relationship between the extrusion rate and the printed filament speed $V_{nozzle(xy)}$ within a certain period of time. The relationship among these parameters is represented in Equation 3.3[38].

$$V_{\text{nozzle(xy)}} = \frac{4Q_{\text{z(extrusion)}}}{\pi D^2} \quad 3.3$$

In this equation, D is the inner diameter of the applied syringe. The equation indicates that the printed filament diameter is proportional to the extrusion rate at a constant printing speed $V_{nozzle(xy)}$. Ideally, the printed filament diameter should be the same as the nozzle diameter by manipulating the printing speed and extrusion rate within a defined range. If the printing speed higher than the range, the printed filament will be stretched; the filament diameter will subsequently decrease. If the printing speed lower than the range, ink accumulation will occur and the filament diameter will increase.

The substrate can affect filament formation. As shown in **Figure 3B**, two filaments were formed with different contact angle values on the substrate; the structure of a filament with a large contact angle value can be maintained. On the other hand, a small contact angle value can improve the stability of the scaffold. In most cases, the substrate (e.g., glass) can have large contact angles with the filament. By coating the substrate with a thin layer of one or more chemicals (e.g., polyethyleneimine), the substrate properties can be modified to decrease the contact angle[38,50]. Meanwhile, the pore geometry in the Z direction is more determined by the ink rheology, needle dimensions, and needle movement distance in the Z direction. In **Figure 3 (C)**, Δh is caused by two adjacent filament layers that vertically fusion together. Since the scaffold is formed in a layer-by-layer manner, a dripping ink will form at the needle tip if the distance between the needle tip and the substrate is larger; this process interrupts the continuity of filament formation. If the needle tip is too close to the substrate, the extruded filament will be scratched by the needle; as a result, the filament diameter will be increased.

Appropriate maintenance of the shape of the extruded filament is necessary to support the structure without collapsing. He *et al*.[19] studied ink printability by investigating filament printing of the first layer and optimized printing parameters. As shown in **Figure 4A**, they indicate that an overlapping problem may occur when printing filaments with different angle orientations. This problem can result in material accumulation at the overlap site and cause uneven layer heights. Furthermore, diffusion should be considered when designing scaffold. As shown in **Figure 4B**, the lattice structures with various pore width (D_L) values were compared. The results showed that diffusion between two adjacent lines on the same layer could cause overlapping when the D_L was1 mm; when the D_L was 4 mm, the extent of diffusion was much less.

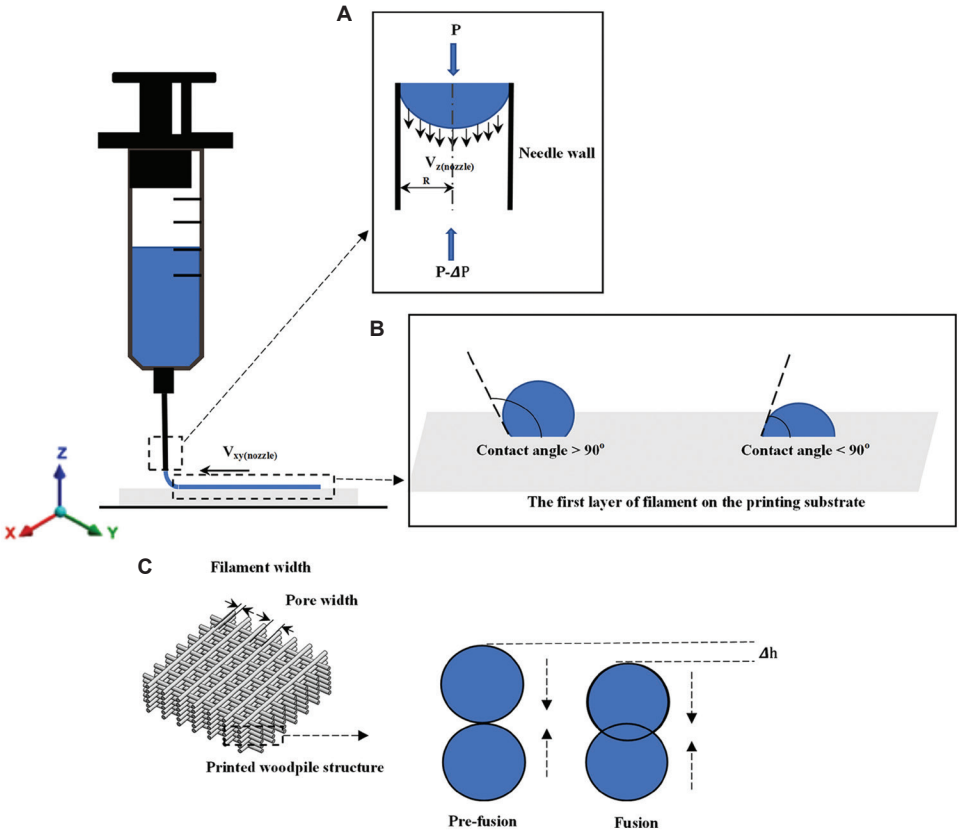

Figure 3. The schematic of ink flow inside the printing needle (A); the first layer of filament formation on the substrate (B); the fusion process of two filament layers in the vertical direction within the printed woodpile structure (C).

4 SBE 3D printed scaffold assessment

4.1 SBE 3D printed scaffold structure and mechanical properties

The solvents used in SBE 3D printing can cause scaffold shrinkage after drying; shrinkage can result in changes to the scaffold structural and mechanical properties. The 3D printed scaffold structures need to be evaluated before use *in vitro* or *in vivo*. There is no standardized method to quantify the difference between the theoretical CAD design and the printed structure. A common evaluation approach involves the measurement of the printed filament diameter and the filament distance from microscopy or SEM images. He *et al*.[19] developed a method to measure the intersection area formed by filaments in microscopy images (**Figure 4C**). They found that the area of the rectangle (A_{Re}) obtained from experiments was much smaller than the theoretical rectangle area (A_{Rt}). They also investigated the relationship between filament distance and diffusion rate (φ). Micro-computed tomography (micro-CT) can also be used to evaluate the scaffold pore dimensions, porosity, and pore interconnectivity. Hockaday *et al*.[11] performed surface deviation analysis by micro-CT imaging of SBE 3D printed valve scaffolds with inner diameters of 22, 17, and 12 mm. The results of this study indicate that the printing accuracy decreased as the scaffold geometric size was reduced.

The SBE 3D printed scaffold should have appropriate mechanical properties (e.g., stiffness) that match with those of the host tissue. Natural polymer and synthetic polymers are often combined with bioactive materials to achieve higher mechanical strength and better biological activity. Serra *et al*.[35] fabricated scaffolds with two types of geometries using two groups of materials, namely PLA/PEG and PLA/PEG/bioactive CaP.

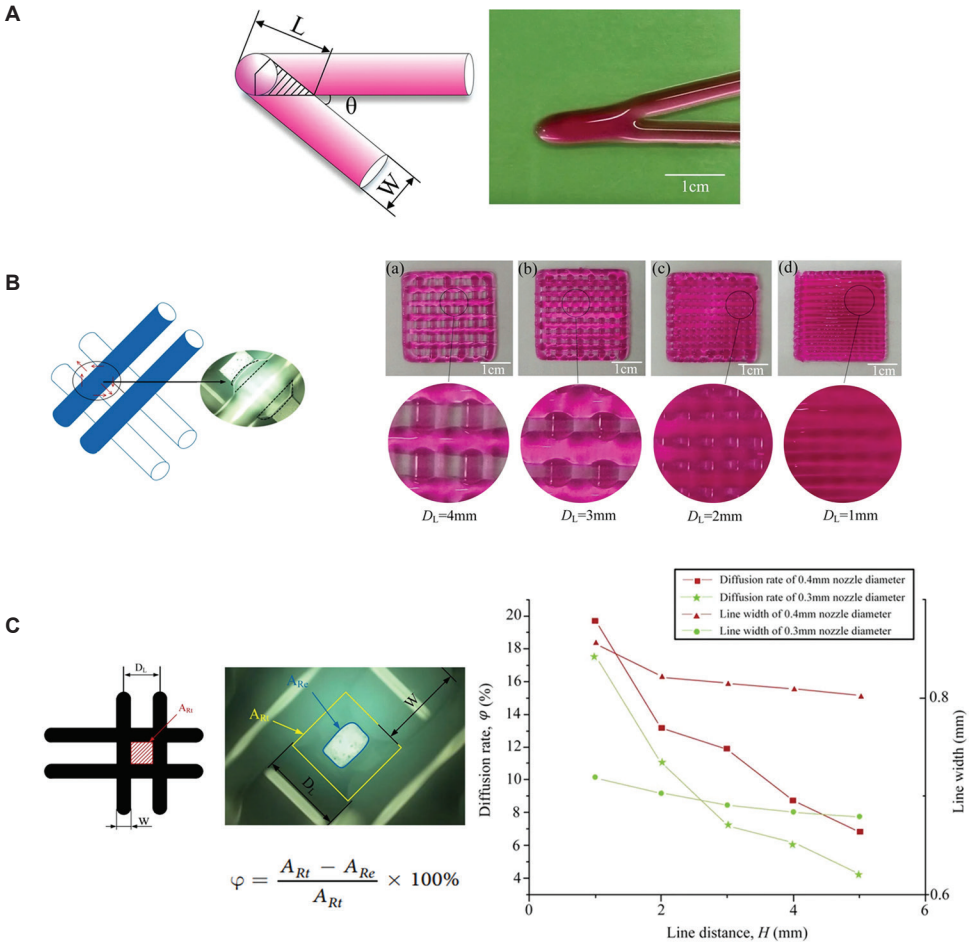

Figure 4. The schematic of overlap area in acute angle printing (A); the ink diffusion and fusion on the same layer when the D_L was at 1-4 mm (B); the comparison of lattice area from theory and experiment as well as the relationship among line distance, line width, and diffusion rate (C)[19].

The results indicate that the compressive modulus of scaffolds with bioactive CaP was higher than those without bioactive CaP for both scaffold geometries. Jakus *et al*.[13] formulated inks with PCL/PLGA/nano-HA mixtures; the printed scaffolds had hyperelastic characteristics. The results of the axial compressive loading showed that the scaffolds remained compliant and elastic; they underwent cycles of up to 25% compression without permanent deformation. Although scaffolds fabricated with SBE 3D printing have shown some success for bone tissue repair, the mechanical properties of the scaffolds are currently inferior to those of human cortical bone. Several studies tried to solve this problem by reinforcing the material. Srivas *et al*.[51] produced porous polymer/Ti6Al4V scaffolds using SBE 3D printing; the porosity and pore size of the printed scaffolds were assessed using micro-CT scanning. The results indicate that the scaffold exhibited less drying shrinkage. The compressive strength and elastic modulus values were 39.58±4.56 MPa and 450±7.21 MPa, respectively. Lacroix[52] applied a computational method to investigate the fluid dynamic environment within the micro-CT reconstructed scaffolds at the pore level. Their results indicate that the 3D printed scaffold samples did not replicate the CAD design; the generated fluid velocity and fluid shear stress magnitude for the 3D printed scaffold samples were up to 5 times higher than those for the CAD design. The variability among the 3D printed samples was also evaluated. These studies indicate that inspection methods should be used to understand the

structure, mechanical properties, and mechanical properties of the printed scaffolds.

4.2 SBE 3D printed scaffold degradation and biocompatibility

Degradation and biocompatibility are important parameters that affect the use of SBE 3D printed scaffolds for tissue repair. The degradation rate of scaffold material should be controllable, allowing the scaffold to be gradually replaced by an extracellular matrix that is released by nearby cells. The degradation rate can be manipulated by optimizing the cell/hydrogel ratio. Lowering the cell density and increasing the hydrogel level can extend the degradation time. Controlling the cross-linking procedure is another approach for optimizing the degradation rate[53]. A slower degradation rate can also be obtained by increasing the degree of cross-linking in the polymer[54,55]. Mixing the polymer with other polymers can also alter the polymer degradation rate[15,56,57]. Collagen, gelatin, and alginate hydrogel constructs were printed with human corneal epithelial cells incubated with a medium containing sodium citrate to obtain degradation-controllable cell-laden tissue constructs. The results indicate that the degradation time of the bioprinting constructs can be controlled by altering the mole ratio of sodium citrate to sodium alginate. The results of this study showed that the printed cells exhibited a higher proliferation rate and greater cytokeratin-3 expression[58].

For cell-free scaffolds, the degradation rate can be controlled by incorporating various combinations of hydrophobic and hydrophilic synthetic polymers[59-61]. Bioceramics can provide a range of degradation rates; in addition, these materials are capable of stimulating biomineralization for bone tissue repair[62,63]. Kolan *et al*.[64] plotted PCL/bio-glass composite scaffolds with and without the presence of hydrogel; the biodegradation rate was investigated by soaking the scaffold in the culture medium. A consistently higher weight loss was noted over one week for PCL/bio-glass scaffolds printed with hydrogel in comparison to those printed without hydrogel. The combination of biodegradables material with ceramics or polymers has also been investigated[65,66]. For example, Wong *et al*.[66] developed a biodegradable composite composed of PCL and magnesium; they indicated that magnesium hydroxide was formed during the degradation of magnesium microparticles. This process may help to neutralize the pH since acidic by-products are produced during PCL degradation. The scaffolds containing magnesium microparticles exhibited low scaffold degradation rates; in addition, the elastic modulus of the composite scaffolds showed no differences after a 2-month immersion period. The biological results showed significantly higher specific ALP activity and upregulation of bone-related markers in the Mg/PCL scaffold than in the pure PCL scaffold.

5 Summary and future perspective

Despite the remarkable achievements of SBE 3D printing in TE, challenges remain that have prevented the translation of 3D printed scaffolds for clinical applications. First, new types of biomaterials, particularly bio-composite materials, would facilitate the clinical use of SBE 3D printing. The use of a single type of material is currently not able to produce a suitable environment for more than one functional cell type. The use of bio-composite materials in an organized pattern that matches the biodegradability, biocompatibility, and mechanical properties of natural tissue may be a more effective approach to create a suitable environment for more than one functional cell type[67].

Second, the ink rheology and processing parameters should be adjusted carefully so that multiple biomaterials and cell types can be simultaneously processed during scaffold fabrication[18]. The ink should exhibit a shear-thinning behavior and recover quickly after the extrusion from the nozzle. The filament formation process should be evaluated to confirm that the printed filament diameter is close to the needle diameter. The processing parameters should be investigated to confirm the scaffold stackability. In addition, the shear stress that the cell experiences should be evaluated. A cell damage model should be developed to investigate the cell damage caused

by shear stress, which is induced by cell-cell and cell-material interactions during the printing process.

Third, there is a difference between the scaffold CAD model and SBE 3D printed scaffold after drying due to the solvent-based process; these variations also affect scaffold reproducibility. These differences can lead to unexpected variations affecting mechanical stimuli and cellular responses[68]. Micro-CT technology can be used to evaluate the scaffold pore size, porosity, and interconnectivity. Computational modeling is a cost-effective method, which can predict the mechanical stimuli that are detected by cells under *in vitro* or *in vivo* settings. Computational modeling methods and biological experiments can be used together to better understand the correlations among scaffold design, mechanical stimuli, and tissue regeneration performance[69,70].

The SBE 3D printing process begins with scaffold design, followed by biomaterial/cell ink formulation, scaffold manufacturing, scaffold culture, and implantation. The use of SBE 3D printing technologies for scaffold fabrication with or without cells remains fraught with many challenges. The ink biomaterials, ink rheology, processing parameters, and cross-linking mechanism affect the results of SBE 3D printing. Although encouraging results have been obtained from SBE 3D printing, challenges remain concerning the properties of current biomaterials, incorporation of multiple materials and cells, and poor reproducibility of the 3D printed scaffolds. Addressing these challenges will facilitate clinical translation and commercialization of SBE 3D printing.

Conflicts of interest

The authors declare that they have no conflicts of interest.

Acknowledgments

This work was supported by a grant of the Ministry of Research and Innovation, CNCS – UEFISCDI, Project Number PNIII-P4-ID-PCE-2016-0884 within PNCDI III, the Charles M. Vest National Academy of Engineering Grand Challenges for Engineering International Scholarship Program, and US National Science Foundation Award #1762202.

References

1. Gross BV, Erkal JL, 2014, Evaluation of 3d Printing and its Potential Impact on Biotechnology and the Chemical Sciences. *Anal. Chem.*, 86:3240–53.
2. Do AV, Khorsand B, Geary SM, *et al*., 2015, 3D Printing of Scaffolds for Tissue Regeneration Applications. *Adv Healthc Mater*, 4(12):1742–62. DOI: 10.1002/adhm.201500168.
3. Wüst S, Müller R, Hofmann S, 2011, Controlled Positioning of Cells in Biomaterials Approaches towards 3D Tissue Printing. *J Funct Biomater*, 2(3):119–54. DOI: 10.3390/jfb2030119.
4. Gloria A, Russo T, De Santis R, *et al*., 2009, 3D Fiber Deposition Technique to Make Multifunctional and Tailor-made Scaffolds for Tissue Engineering Applications. *J Appl Biomater Biomech*, 7(3):141–52.
5. Malda J, Woodfield TB, van der Vloodt F, *et al*., 2005, The Effect of PEGT/PBT Scaffold Architecture on the Composition of Tissue Engineered Cartilage. *Biomaterials*, 26(1):63–72. DOI: 10.1016/j.biomaterials.2004.02.046.
6. Melchels FP, Tonnarelli B, Olivares AL, *et al*., 2011, The Influence of the Scaffold Design on the Distribution of Adhering Cells After Perfusion Cell Seeding. *Biomaterials*, 32(11):2878–84. DOI: 10.1016/j.biomaterials.2011.01.023.
7. Phillippi JA, Miller E, Weiss L, *et al*., 2008, Microenvironments Engineered by Inkjet Bioprinting Spatially Direct Adult Stem Cells Toward Muscle-and Bone-like Subpopulations. *Stem Cells*, 26(1):127–34. DOI: 10.1634/stemcells.2007-0520.
8. Woodfield T, Van Blitterswijk CA, De Wijn J, *et al*., 2005, Polymer Scaffolds Fabricated with Pore-size Gradients as a Model for Studying the Zonal Organization within Tissue-engineered Cartilage Constructs. *Tissue Eng*, 11(9-10):1297–311. DOI: 10.1089/ten.2005.11.1297.
9. Gao, F., Xu Z, Liang Q, *et al*., 2018, Direct 3D Printing of High Strength Biohybrid Gradient Hydrogel Scaffolds for Efficient Repair of Osteochondral Defect. *Adv Funct Mater*, 28(13):1706644. DOI: 10.1002/adfm.201706644.
10. Trachtenberg JE, Placone JK, Smith BT, *et al*., 2017, Extrusion-based 3D Printing of Poly (Propylene Fumarate) Scaffolds with Hydroxyapatite Gradients. *J Biomater Sci Polym Ed*, 28(6):532–54. DOI: 10.1080/09205063.2017.1286184.
11. Hockaday L, Kang KH, Colangelo NW, *et al*., 2012, Rapid 3D Printing of Anatomically Accurate and Mechanically

Heterogeneous Aortic Valve Hydrogel Scaffolds. *Biofabrication*, 4(3):035005. DOI: 10.1088/1758-5082/4/3/035005.

12. Duan B, Kapetanovic E, Hockaday LA, *et al*., 2014, Three-dimensional Printed Trileaflet Valve Conduits Using Biological Hydrogels and Human Valve Interstitial Cells. *Acta Biomater*, 10(5):1836–46. DOI: 10.1016/j.actbio.2013.12.005.
13. Jakus AE, Rutz AL, Jordan SW, *et al*., 2016, Hyperelastic "Bone": A Highly Versatile, Growth Factor-free, Osteoregenerative, Scalable, and Surgically Friendly Biomaterial. *Sci Transl Med*., 8(358):358ra127. DOI: 10.1126/scitranslmed.aaf7704.
14. Gonçalves RM, Pereira AC, Pereira IO, *et al*., 2015, Macrophage Response to Chitosan/poly-(γ-glutamic Acid) Nanoparticles Carrying an Anti-inflammatory Drug. *J Mater Sci*, 26(4):167. DOI: 10.1007/s10856-015-5496-1.
15. Markstedt K, Mantas A, Tournier I, *et al*., 2015, 3D Bioprinting Human Chondrocytes with Nanocellulose-alginate Bioink for Cartilage Tissue Engineering Applications. *Biomacromolecules*, 16(5):1489–96. DOI: 10.1021/acs.biomac.5b00188.
16. Sun L, Parker ST, Syoji D, *et al*., 2012, Direct-Write Assembly of 3D Silk/Hydroxyapatite Scaffolds for Bone Co-Cultures. Adv Healthc Mater, 1(6):729–35. DOI: 10.1002/adhm.201200057.
17. Lee W, Debasitis JC, Lee VK, *et al*., 2009, Multi-layered Culture of Human Skin Fibroblasts and Keratinocytes Through Three-dimensional Freeform Fabrication. *Biomaterials*, 30(8):1587–95. DOI: 10.1016/j.biomaterials.2008.12.009.
18. Liu W, Zhang YS, Heinrich MA, *et al*., 2017, Rapid Continuous Multimaterial Extrusion Bioprinting. *Adv Mater*, 29(3):1604630.
19. He Y, *et al*., 2016, Research on the Printability of Hydrogels in 3D Bioprinting. *Sci Rep*, 6:29977.
20. Lewis JA, Gratson GM, 2004, Direct Writing in Three Dimensions. *Mater Today*, 7(7-8):32-39.
21. Jang TS, Jung HD, Pan HW, *et al*., 2018, 3D Printing of Hydrogel Composite Systems: Recent Advances in Technology for Tissue Engineering. *Int J Bioprint*, 4(1):126.
22. Ozbolat IT., 2016, 3D Bioprinting: Fundamentals, Principles And Applications. Academic Press, London.
23. Derakhshanfar S, Mbeleck R, Xu K, *et al*., 2018, 3D Bioprinting for Biomedical Devices and Tissue Engineering: A Review of Recent Trends and Advances. *Bioact Mater*, 3(2):144–56. DOI: 10.1016/j.bioactmat.2017.11.008.
24. Placone JK, Engler AJ, 2018, Recent Advances in Extrusion-Based 3D Printing for Biomedical Applications. *Adv Healthc Mater*, 7(8):e1701161. DOI: 10.1002/adhm.201701161.
25. Schaefer D, Martin I, Jundt G, *et al*., 2002, Tissue-engineered Composites for the Repair of Large Osteochondral Defects. *Arthritis Rheum*, 46(9):2524–34.
26. Chen J, Chen H, Li P, *et al*., 2011, Simultaneous Regeneration of Articular Cartilage and Subchondral Bone *in vivo* Using MSCs Induced by a Spatially Controlled Gene Delivery System in Bilayered Integrated Scaffolds. *Biomaterials*, 32(21):4793–805. DOI: 10.1016/j.biomaterials.2011.03.041.
27. Schaefer D, Martin I, Shastri P, *et al*., 2000, *In vitro* Generation of Osteochondral Composites. *Biomaterials*, 21(24):2599–606. DOI: 10.1016/s0142-9612(00)00127-7.
28. Schacht K, Jungst T, Schweinlin M, *et al*., 2015, Biofabrication of Cell-loaded 3D Spider Silk Constructs. *Angew Chem Int Ed*, 54(9):2816–20. DOI: 10.1002/anie.201409846.
29. Gao G, Yonezawa T, Hubbell K, *et al*., 2015, Inkjet-bioprinted Acrylated Peptides and PEG Hydrogel with Human Mesenchymal Stem Cells Promote Robust Bone and Cartilage Formation with Minimal Printhead Clogging. *Biotechnol J*, 10(10):1568–77. DOI: 10.1002/biot.201400635.
30. Müller M, Becher J, Schnabelrauch M, *et al*., 2015, Nanostructured Pluronic Hydrogels as Bioinks for 3D Bioprinting. *Biofabrication*, 7(3):035006. DOI: 10.1088/1758-5090/7/3/035006.
31. Wüst S, Godla ME, Müller R, *et al*., 2014, Tunable Hydrogel Composite with Two-step Processing in Combination with Innovative Hardware Upgrade for Cell-based Three-dimensional Bioprinting. *Acta Biomater*, 10(2):630–40. DOI: 10.1016/j.actbio.2013.10.016.
32. Blaeser A, Campos DF, Puster U, *et al*., 2016, Controlling Shear Stress in 3D Bioprinting is a Key Factor to Balance Printing Resolution and Stem Cell Integrity. *Adv Healthc Mater*, 5(3):326–33. DOI: 10.1002/adhm.201500677.
33. Ghosh S, Parker ST, Wang X, *et al*., 2008, Direct-write Assembly of Microperiodic Silk Fibroin Scaffolds for Tissue Engineering Applications. *Adv Funct Mater*, 18(13):1883–9. DOI: 10.1002/adfm.200800040.
34. Miranda P, Pajares A, Saiz E, *et al*., 2008, Mechanical Properties of Calcium Phosphate Scaffolds Fabricated by Robocasting. *J Biomed Mater Res Part A*, 85(1):218–27. DOI: 10.1002/jbm.a.31587.
35. Serra T, Planell JA, Navarro M, 2013, High-resolution PLA-based Composite Scaffolds Via 3-D Printing Technology. *Acta Biomater*, 9(3):5521–30. DOI: 10.1016/j.actbio.2012.10.041.
36. Gonçalves EM, Oliveira FJ, Silva RF, *et al*., 2016, Three-dimensional Printed PCL-hydroxyapatite Scaffolds Filled

with CNTs for Bone Cell Growth Stimulation. *J Biomed Mater Res Part B*, 104(6):1210–9. DOI: 10.1002/jbm.b.33432.

37. Ning L, Guillemot A, Zhao J, *et al*., 2016, Influence of Flow Behavior of Alginate Cell Suspensions on Cell Viability and Proliferation. *Tissue Eng Part C*, 22(7):652–62. DOI: 10.1089/ten.tec.2016.0011.
38. Chen DX, Glaser, C, 2019, Extrusion Bioprinting of Scaffolds for Tissue Engineering Applications. Springer, Cham.
39. Dávila JL, d'Ávila MA, 2019, Rheological Evaluation of Laponite/alginate Inks for 3D Extrusion-based Printing. *Int J Adv Manuf Technol*, 101(1-4):675–86. DOI: 10.1007/s00170-018-2876-y.
40. Liu S, Li L, 2016, Recoverable and Self-healing Double Network Hydrogel Based on κ-Carrageenan. *ACS Appl Mater Interfaces*, 8(43):29749–58. DOI: 10.1021/acsami.6b11363.
41. Freeman FE, Kelly DJ, 2017, Tuning Alginate Bioink Stiffness and Composition for Controlled Growth Factor Delivery and to Spatially Direct MSC fate Within Bioprinted Tissues. *Sci Rep*, 7(1):17042. DOI: 10.1038/s41598-017-17286-1.
42. Chung JH, Naficy S, Yue Z, *et al*., 2013, Bio-ink Properties and Printability for Extrusion Printing Living Cells. *Biomater Sci*, 1(7):763–73. DOI: 10.1039/c3bm00012e.
43. Donderwinkel I, van Hest JC, Cameron NR, 2017, Bio-inks for 3D Bioprinting: Recent Advances and Future Prospects. *Polym Chem*, 8(31):4451–71. DOI: 10.1039/c7py00826k.
44. Li H, Tan C, Li L, 2018, Review of 3D Printable Hydrogels and Constructs. *Mater Des*, 159:20–38. DOI: 10.1016/j.matdes.2018.08.023.
45. Ouyang L, Yao R, Zhao Y, *et al*., 2016, Effect of Bioink Properties on Printability and Cell Viability for 3D Bioplotting of Embryonic Stem Cells. *Biofabrication*, 8(3):035020. DOI: 10.1088/1758-5090/8/3/035020.
46. Knowlton S, Yenilmez B, Anand S, *et al*., 2017, Photocrosslinking-based Bioprinting: Examining Crosslinking Schemes. *Bioprinting*, 5:10–8. DOI: 10.1016/j.bprint.2017.03.001.
47. Schuurman W, Levett PA, Pot MW, *et al*., 2013, Gelatin-methacrylamide Hydrogels as Potential Biomaterials for Fabrication of Tissue-engineered Cartilage Constructs. *Macromol Biosci*, 13(5):551–61. DOI: 10.1002/mabi.201200471.
48. Pescosolido L, Schuurman W, Malda J, *et al*., 2011, Hyaluronic Acid and Dextran-based Semi-IPN Hydrogels as Biomaterials for Bioprinting. *Biomacromolecules*, 12(5):1831–8. DOI: 10.1021/bm200178w.
49. Morrison F, 2001, Understanding Rheology. Oxford University Press, New York.
50. You F, Wu X, Chen X, 2017, 3D Printing of Porous Alginate/gelatin Hydrogel Scaffolds and Their Mechanical Property Characterization. *Int J Polym Mater Polym Biomater*, 66(6):299–306. DOI: 10.1080/00914037.2016.1201830.
51. Srivas PK, Kapat K, Dadhich P, *et al*., 2017, Osseointegration Assessment of Extrusion Printed Ti6Al4V Scaffold Towards Accelerated Skeletal Defect Healing Via Tissue In-growth. *Bioprinting*, 6:8–17. DOI: 10.1016/j.bprint.2017.04.002.
52. Campos Marin A, Lacroix D, 2015, The Inter-sample Structural Variability of Regular Tissue-engineered Scaffolds Significantly Affects the Micromechanical Local Cell Environment. *Interface Focus*, 5(2):20140097. DOI 10.1098/rsfs.2014.0097.
53. Colosi C, Shin SR, Manoharan V, *et al*., 2016, Microfluidic Bioprinting of Heterogeneous 3D Tissue Constructs Using Low-viscosity Bioink. *Adv Mater*, 28(4):677–84. DOI: 10.1002/adma.201503310.
54. Jeon O, Song SJ, Lee KJ, *et al*., 2007, Mechanical Properties and Degradation Behaviors of Hyaluronic Acid Hydrogels Cross-linked at Various Cross-linking Densities. *Carbohydr. Polym*, 70(3):251–7. DOI: 10.1016/j.carbpol.2007.04.002.
55. Jia W, Gungor-Ozkerim PS, Zhang YS, *et al*., 2016, Direct 3D Bioprinting of Perfusable Vascular Constructs Using a Blend Bioink. *Biomaterials*, 106:58–68. DOI: 10.1016/j.biomaterials.2016.07.038.
56. Duan B, Hockaday LA, Kang KH, *et al*., 2013, 3D Bioprinting of Heterogeneous Aortic Valve Conduits with Alginate/gelatin Hydrogels. *J Biomed Mater Res*, 101(5):1255–64. DOI: 10.1002/jbm.a.34420.
57. Rutz AL, Hyland KE, Jakus AE, *et al*., 2015, A Multimaterial Bioink Method for 3D Printing Tunable, Cell-Compatible Hydrogels. *Adv Mater*, 27(9):1607–14. DOI: 10.1002/adma.201405076.
58. Wu Z, Su X, Xu Y, *et al*., 2016, Bioprinting Three-dimensional Cell-laden Tissue Constructs with Controllable Degradation. *Sci Rep*, 6:24474. DOI: 10.1038/srep24474.
59. Ragaert K, Maeyaert G, Martins CI, *et al*., 2014, Bulk Compounding of PCL-PEO Blends for 3D Plotting of Scaffolds for Cardiovascular Tissue Engineering. *J Mater Sci Eng*, 3(1):136. DOI: 10.4172/2169-0022.1000136.
60. Remya K, Chandran S, Mani S, *et al*., 2018, Hybrid Polycaprolactone/Polyethylene Oxide Scaffolds with Tunable Fiber Surface Morphology, Improved Hydrophilicity and Biodegradability for Bone Tissue Engineering Applications. *J Biomater Sci*, 29(12):1444–62. DOI: 10.1080/09205063.2018.1465664.
61. Lyons JG, Blackie P, Higginbotham CL, 2008, The Significance of Variation in Extrusion Speeds and Temperatures on a PEO/PCL Blend Based Matrix for Oral

Drug Delivery. *Int J Pharm*, 351(1–2):201–8. DOI: 10.1016/j.ijpharm.2007.09.041.

62. Kuo M, Yen S, 2002, The Process of Electrochemical Deposited Hydroxyapatite Coatings on Biomedical Titanium at Room Temperature. *Mater Sci Eng C*, 20(1):153–60. DOI: 10.1016/s0928-4931(02)00026-7.
63. Murugan R, Ramakrishna S, 2005, Development of Nanocomposites for Bone Grafting. *Compos Sci Technol*, 65(15-16):2385–406.
64. Kolan K, Liu Y, Baldridge J, *et al*., 2017, Solvent Based 3D Printing of Biopolymer/Bioactive Glass Composite and Hydrogel for Tissue Engineering Applications. *Procedia CIRP*, 65:38–43. DOI: 10.1016/j.procir.2017.04.022.
65. Zheng Y, Gu X, Witte F, 2014, Biodegradable Metals. *Mater Sci Eng*, 77:1–34.
66. Wong HM, Wu S, Chu PK, *et al*., 2013, Low-modulus Mg/PCL Hybrid Bone Substitute for Osteoporotic Fracture Fixation. *Biomaterials*, 34(29):7016–32. DOI: 10.1016/j.biomaterials.2013.05.062.
67. Ning L, Chen X, 2017, A Brief Review of Extrusion-based Tissue Scaffold Bio-printing. *Biotechnol J*, 12(8):1600671. DOI: 10.1002/biot.201600671.
68. Marin AC, 2016, *In silico* Study of the Mechanisms of Cell Deposition into 3D Rapid Prototyping Scaffolds Under *in vitro* Hydrodynamic Conditions. Thesis. University of Sheffield.
69. Melchels FP, Bertoldi K, Gabbrielli R, *et al*., 2010, Mathematically Defined Tissue Engineering Scaffold Architectures Prepared by Stereolithography. *Biomaterials*, 31(27):6909–16. DOI: 10.1016/j.biomaterials.2010.05.068.
70. Grayson WL, Fröhlich M, Yeager K, *et al*., 2010, Engineering Anatomically Shaped Human Bone Grafts. *Proc Natl Acad Sci*, 107(8):3299–304. DOI: 10.1073/pnas.0905439106.

RESEARCH ARTICLE

Extrusion-Based Bioprinting through Glucose-Mediated Enzymatic Hydrogelation

Enkhtuul Gantumur, Masaki Nakahata, Masaru Kojima and Shinji Sakai*

Department of Materials Engineering Science, Graduate School of Engineering Science, Osaka University, Toyonaka, Osaka 560-8531, Japan

Abstract: We report an extrusion-based bioprinting approach, in which stabilization of extruded bioink is achieved through horseradish peroxidase (HRP)-catalyzed cross-linking consuming hydrogen peroxide (H_2O_2) supplied from HRP and glucose. The bioinks containing living cells, HRP, glucose, alginate possessing phenolic hydroxyl (Ph) groups, and cellulose nanofiber were extruded to fabricate 3D hydrogel constructs. Lattice- and human nose-shaped 3D constructs were successfully printed and showed good stability in cell culture medium for over a week. Mouse 10T1/2 fibroblasts enclosed in the printed constructs remained viable after 7 days of culture. It was also able to switch a non-cell-adhesive surface of the printed construct to cell-adhesive surface for culturing cells on it through a subsequent cross-linking of gelatin possessing Ph moieties. These results demonstrate the possibility of utilizing the presented cross-linking method for 3D bioprinting.

Keywords: Enzymatic hydrogelation, Horseradish peroxidase, Glucose, Alginate, Cellulose nanofiber, Bioink, Extrusion-based bioprinting

***Corresponding Author:** Shinji Sakai, Department of Materials Engineering Science, Graduate School of Engineering Science, Osaka University, Toyonaka, Osaka 560-8531, Japan; sakai@cheng.es.osaka-u.ac.jp

Received: November 18, 2019; ***Accepted:*** January 02, 2020; ***Published Online:*** January 21, 2020

Citation: Gantumur E, Nakahata M, Kojima M, *et al*., 2020, Extrusion-based bioprinting through glucose-mediated enzymatic hydrogelation. *Int J Bioprint*, 6(1):250. DOI: 10.18063/ijb.v6i1.250.

1 Introduction

Fabrication of three-dimensional (3D) tissues has been a subject of interest in the fields of tissue engineering and regenerative medicine for over the past decades. The classic biofabrication techniques, such as solid or soft material-based scaffolding[1-3] and self-assembling of cell sheets or spheroids[4], have limitations to mimic the structure and function of the natural tissues that are well-organized with multicellular population, a variety of extracellular matrix, growth factors, and bioactive compounds[5]. Recent trend in the fields is 3D bioprinting,[6-8] which enables the deposition of living cells with biomaterials (i.e., bioinks) at micrometer precision to replicate the microarchitecture of targeted tissue[9-11]. Besides, the available bioprinting strategies[12] including inkjet-based[13,14], laser-assisted[15,16], and stereolithography-based[17,18], extrusion-based bioprinting[19] is the most extensively adopted strategy due to its simplicity, printing precision, and a variety of applicable biomaterials. In extrusion bioprinting, viscous solutions are extruded from a nozzle as inks on a substrate surface based on the digital design. The extruded inks must be stabilized into solid hydrogels before spreading for getting the constructs with designed shapes. In general, the stabilization is accomplished through the cross-linking of polymers in the inks resulting in hydrogelation. Various cross-linking methods have been applied to the extrusion bioprinting[20,21].

To fabricate a structure having a complicated structure like natural tissues, we believe that it

is desirable to use multiple materials that give a function suitable for each part and multiple cross-linking systems suitable for each material. Many attempts have been made to develop cross-linking methods which can exert powerful influences on printability, mechanical properties, and cell compatibility of hydrogels. Even today, it is desired to develop a novel bioprinting system that can be achieved by a biocompatible cross-linking process without using toxic substances because it will further enlarge the potential of bioprinting in the fields of tissue engineering and regenerative medicine. The existing cross-linking pathways in bioprinting include physical and chemical cross-linking that rely on external stimuli, such as temperature, ions, or light[22,23]. More recently, enzymatic reactions have newly attracted attention as mild and cell-friendly cross-linking methods for 3D bioprinting[24]. Specifically, bioinks containing horseradish peroxidase (HRP) that has a function to catalyze the conjugation of phenol and aniline derivatives by consuming hydrogen peroxide (H_2O_2) have been used for printing cell-laden microparticles[25], 3D hydrogel constructs[26-28], or patterned hydrogels for cell immobilization[29] using inkjet or extrusion-based bioprinting. Despite the advantage of a wide range of material choices, a major consideration in this reaction system is a way of supplying H_2O_2. To print a 3D hydrogel construct with living cells, the exposure time or the concentration of H_2O_2 should be at non-cytotoxic level and harmless to the activity of the enzyme itself[30]. In the previous studies, H_2O_2 was mixed into an aqueous bath solution[25,26], a hydrogel substrate[29], or another ink[27] to achieve the rapid hydrogelation when it was contacted with the ink containing HRP. Furthermore, there was an approach that uses air containing H_2O_2 instead of an aqueous H_2O_2 solution to control its concentration at the ppm level[28]. All of these approaches are the direct supply of H_2O_2, which might cause inhomogeneity of the resultant hydrogel network as well[31].

Recently, we have developed a way to supply H_2O_2 indirectly to this enzymatic reaction in the presence of reducing sugars, such as glucose, galactose, and mannose[32,33]. In this system, the redox reactions between thiol groups in HRP and formed disulfide bond gradually generate H_2O_2 by consuming reducing sugar under aerobic conditions. It was confirmed that living cells can be enclosed/cultured inside or on the surface of resultant hydrogel with high cell viability and proliferation. Herein, we utilized glucose-mediated enzymatic reaction for extrusion-based bioprinting as a comixable cross-linker with living cells to expand its potential application. Our bioink contains living cells, HRP, a supporting material, polymer possessing phenolic hydroxyl (Ph) groups (Polymer-Ph), and reducing sugar (**Figure 1**). Alginate and glucose were chosen as a representative polymer chain and reducing sugar. In a preliminary study of the application of the cross-linking system, we realized that a drawback of the system was a non-instantaneous hydrogelation of deposited ink. A possible approach to suppress a dispersion of the deposited ink was an enhancement of the viscosity of ink. To enhance the viscosity of ink and the shape fidelity of printed constructs until the stabilization through the enzyme-mediated

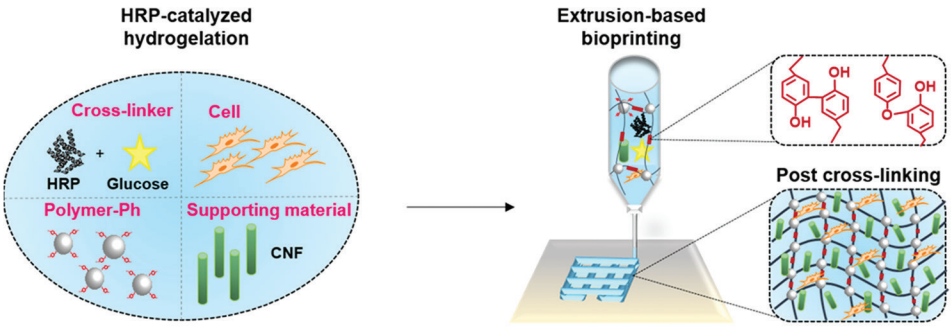

Figure 1. Schematic of extrusion-based bioprinting through glucose-mediated enzymatic hydrogelation.

cross-linking, a dispersion of cellulose nanofibers (CNF) was incorporated as a supporting material. CNF has already made an impact in the field of bioprinting due to its outstanding shear thinning and mechanical properties[34]. The combination of alginate and CNF has been previously used for bioink and separately treated with calcium ions for postcross-linking[35-37]. In this study, the cross-linker (i.e., enzyme and glucose) mixed in the bioink led to a slow hydrogelation during and the following printing step while CNF supported well the stability of complex construct. In addition to the printability, the cell behavior inside or on the surface of gelatin-coated hydrogel was investigated to ensure the cell compatibility of the proposed method.

2 Materials and methods

2.1 Materials

Sodium alginate (Kimica I-1G, high content of guluronic acid and molecular weight, 70 kDa), gelatin (type B from bovine skin), and CNF suspension (Rheocrysta I-2SX, dry CNF content, 2 w/v%) were purchased from Kimica (Tokyo, Japan), Kewpie (Tokyo, Japan), and DKS Co. Ltd. (Kyoto, Japan). HRP (200 units/mg), D-glucose, and *N*-hydroxysulfosuccinimide (NHS) were obtained from FUJIFILM Wako Pure Chemical Corporation (Osaka, Japan). Water-soluble carbodiimide (WSCD) and tyramine hydrochloride were purchased from Peptide Institute (Osaka, Japan) and Chem-Impex International (Wood Dale, IL, USA), respectively. 3-(4-hydroxyphenyl) propionic acid and rhodamine (Rho) were purchased from Tokyo Chemical Industry (Tokyo, Japan). Alginate (Alg-Ph, 1.4×10^{-4} mol-Ph/g) and gelatin (Rho-Gel-Ph, 1.5×10^{-4} mol-Ph/g) derivatives possessing Ph groups were synthesized by conjugating tyramine hydrochloride using NHS and WSCD, as previously reported[38,39]. Mouse 10T1/2 fibroblast cells were provided by Riken Cell Bank (Ibaraki, Japan) and cultured in Dulbecco's Modified Eagle's Medium (DMEM, Nissui, Tokyo, Japan) supplemented with 10% fetal bovine serum at 37°C in 5% CO_2.

2.2 Ink preparation and rheological characterization

Phosphate-buffered saline (PBS, pH 7.4) containing Alg-Ph (0.5 w/v%), HRP (100 units/mL), and D-glucose (44 mg/mL) was prepared. As a supporting material, CNF (autoclaved at 121°C for 20 min, 0.5~1.5 w/v%) was added. The rheological properties of the prepared bioinks were analyzed using a rheometer (HAAKE MARS III, Thermo Fisher Scientific, MA, USA) with a parallel plate of 20 mm radius at 25°C, immediately after mixing. Dynamic viscoelasticity measurement was performed at a constant shear strain of 1% and the gap between the parallel plate and the stage was set to 1 mm.

2.3 Bioprinting procedure

The prepared inks were printed using a software-assisted 3D printer (Reprap Prusa i3, HIC Technology Co. Ltd., Hong Kong, China) modified to have one syringe connected to a syringe pump. The inks were extruded from a 27-gauge stainless needle at 22 mm/s onto the stage moving at 22 mm/s to build lattice- (20×21 mm^2, thickness 1 mm, 10 layers) and a human nose-shaped (12×15 mm^2, thickness 7 mm, 70 layers at maximum) 3D hydrogel constructs. The thickness of a layer was set at 0.1 mm. The bioprinting process was carried out at room temperature and the obtained constructs were rested at room temperature for 2 h after printing to let the postcross-linking.

2.4 Swelling of hydrogel in medium

PBS containing Alg-Ph (0.5 w/v%), HRP (100 units/mL), D-glucose (44 mg/mL), and CNF (1.5 w/v%) was poured into PDMS mold and rested at room temperature for 2 h to obtain disk-shaped hydrogel with 15 mm in diameter. The resultant hydrogels were then soaked in DMEM. The medium was changed every day. The diameter of the specimen was measured using the software Image J (National Institutes of Health, USA).

2.5 Cell behavior in hydrogel

10T1/2 cells were suspended in PBS containing Alg-Ph (0.5 w/v%), HRP (100 units/mL),

D-glucose (44 mg/mL), and CNF (1.5 w/v%) at 5 × 10^5 cells/mL, as a bioink. The cell-laden lattice-shaped constructs were printed in a safety cabinet and kept in an incubator until the complete cross-linking. As a non-printed hydrogel, the mixture solution was poured into 24-well plate at 0.25 mL/well. The resultant hydrogels were incubated in DMEM at 37°C. After 1 day and 7 days of incubation, the cells in hydrogels were stained with Calcein-AM (live cells) and propidium iodide (dead cells) for the observation using a fluorescence microscope (BZ-9000, Keyence Corp., Osaka, Japan).

2.6 Switching hydrogel surface

Lattice-shaped hydrogel construct was printed first using the selected ink on a culture dish with a surface covered with 1.0% agarose gel. After post-cross-linking, the hydrogel construct was soaked in a solution containing Rho-Gel-Ph (1.0 w/v%) for overnight at 37°C. Then, the construct was rinsed well with PBS to remove

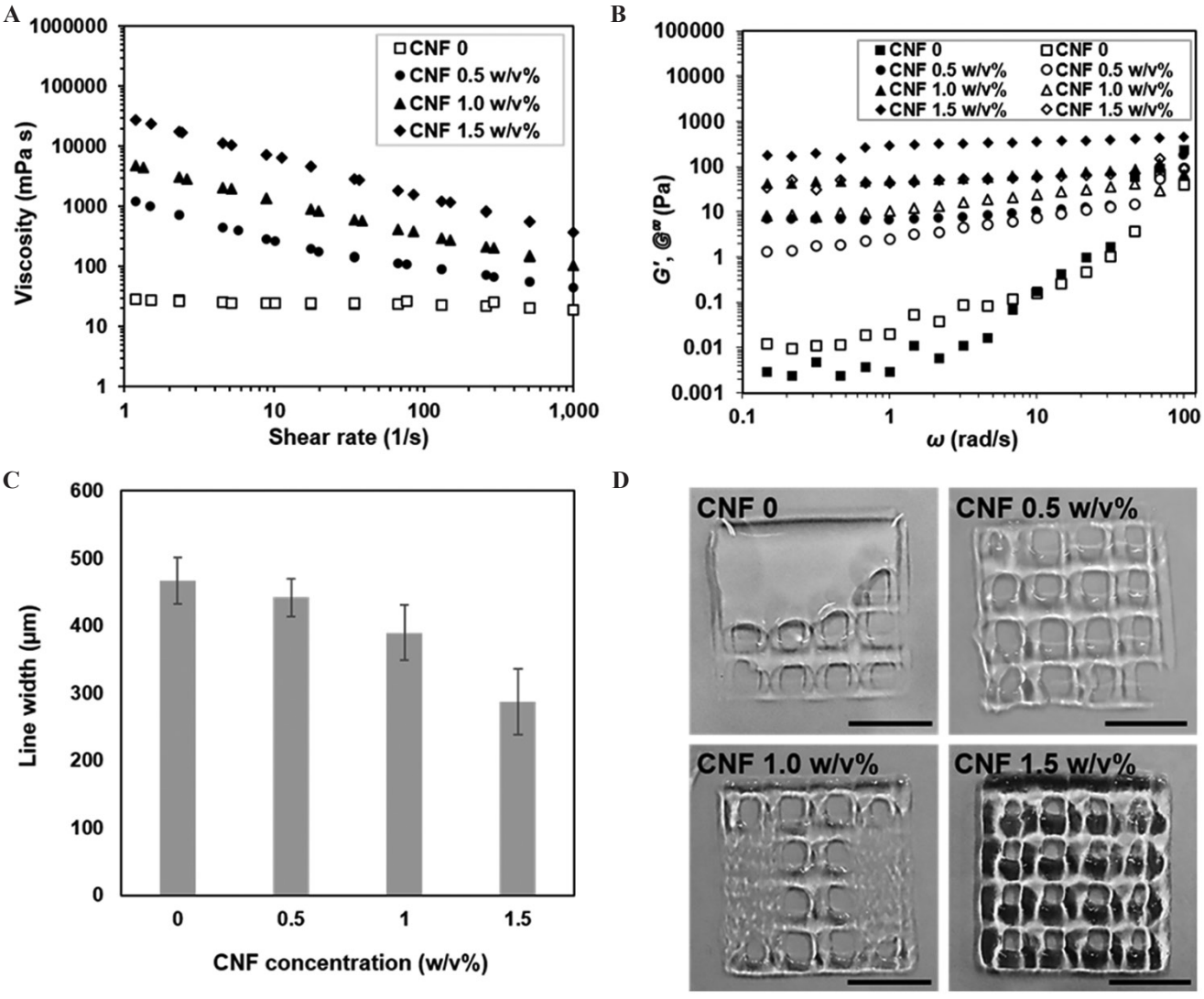

Figure 2. Rheological properties and printability of inks containing different concentrations of CNF: (A) Viscosity changes at various shear rates. (B) Storage modulus, G' (closed symbols) and loss modulus, G'' (open symbols) as a function of angular frequency. (C) Width measurement of the printed lines. Data are mean ± SD (n = 6). (D) Printed lattice-shaped constructs. Scale bars: 1 cm.

the non-cross-linked Rho-Gel-Ph. Subsequently, 10T1/2 cells were seeded at 1×10^4 cells/cm^2 and incubated in DMEM at 37°C.

3 Results and discussion

3.1 Characterization and printability of inks

To determine the optimal printing condition of CNF and alginate-based ink, the variable concentrations of CNF (from 0 to 1.5 w/v%) and the fixed concentration of Alg-Ph (0.5 w/v%) were mixed to prepare four different inks. The concentrations of HRP (100 units/mL) and glucose (44 mg/mL) were determined based on the previous findings in terms of gelation time[32,33]. Comparing to the direct supply of H_2O_2 as an aqueous solution[38], the gelation time of this method is much longer and that makes it possible to mix all the ink components at the same time. **Figure 2A** shows the viscosity changes of the prepared inks at various shear rates. The ink non-containing CNF (CNF 0) has low zero-shear viscosity at the beginning of cross-linking resulting in a poor shape fidelity during the printing (**Figure 2D**). The viscosity of Alg-Ph solution gradually increased with increasing the concentration of incorporated CNF. As already known[35], the shear-thinning property of the ink containing CNF was confirmed by showing high viscosity at low shear rates and low viscosity at high shear rates. Dynamic viscoelastic measurements in **Figure 2B** also show that the storage modulus (G') and loss modulus (G'') substantially increased with a higher proportion of CNF in the ink. These rheological responses of the prepared inks were in agreement with the printing resolution indicated by the widths of printed lines (**Figure 2C**). The inks with higher viscosities improved the printing resolution. Then, the high printing resolution gave nicely printed lattice-shaped hydrogel construct (**Figure 2D**). Based on the results, the ink containing 1.5 w/v% CNF was selected from the prepared inks as an appropriate ink for printing. Incorporating more high concentration of CNF into the ink caused nozzle clogging.

Once an optimal concentration of CNF incorporated in the ink was determined, a more complex construct was printed. It was previously noted that CNF can mimic the bulk collagen matrix for cartilage tissue[40]. Thus, the hydrogel construct resembling human nose, which is one of the cartilage tissues was successfully printed using the selected ink. Even during up to 20 min of printing procedure and slow cross-linking process, the printed construct maintained its shape without collapsing (**Figure 3A**). In addition, if it is required to let the cross-linking more slowly for longer printing procedure, the concentrations of HRP and glucose can be decreased[32,33]. After cross-linked through glucose-mediated HRP-catalyzed reaction, the printed human nose construct became mechanically stable and showed elastic deformation after squeezing (**Figure 3B**).

Furthermore, the stability of hydrogel after cross-linking in cell culture medium was examined before evaluating the cell behavior inside it. The diameters of disk-shaped hydrogels obtained using the selected ink increased <15% when compared with their initial sizes for the first 2 days of soaking in medium. After that, the changes in the size of hydrogels were barely noticeable and stayed stable during the 8 days of soaking (**Figure 4**). Taken together the results from rheology, printability, and stability, it is possible to print complex and stable hydrogel constructs with good shape fidelity using the proposed ink and the cross-linking method.

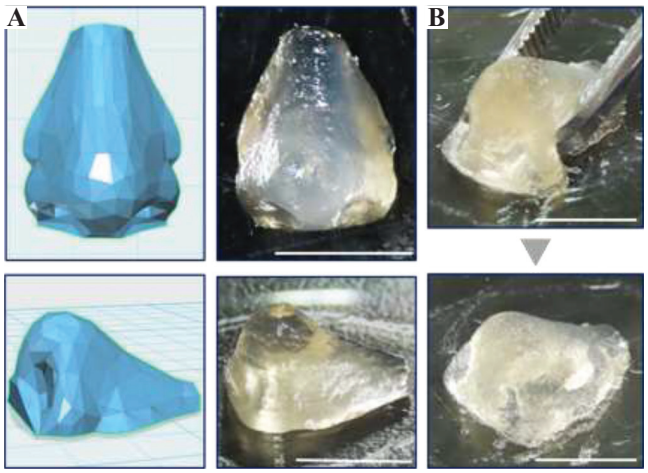

Figure 3. Printed human nose construct based on blueprint (A) before and (C) after postcross-linking. Scale bars: 1 cm.

3.2 Cell behavior in the printed construct

To ensure the feasibility of applying the proposed bioink and cross-linking method for printing living cells, the cell-laden lattice-shaped constructs were prepared. Mouse 10T1/2 fibroblasts were chosen as a model cell line for the cell studies. As non-printed hydrogels for comparison, the hydrogels were prepared in cell culture well plate using the same bioink. As shown in **Figure 5**, the homogeneous distributions of viable cells were observed in both non-printed (50.1 ± 0.4% viability, n=3) and printed hydrogels (54.1 ± 0.6% viability, n=3) after 1 day of culture. These similar cell viabilities indicate that there were no harmful effects on the cells by printing with the proposed cross-linking method. Moreover, the printed construct stably maintained its shape and dimension even after 7 days of culture in the presence of cells. The cell viability in the construct (56.0 ± 2.4%, n = 3) at day 7 was found to be higher than that in the non-printed hydrogel (44.3 ± 2.5%, n=3). The reason of this difference in cell viability may be due to the different internal architecture of the printed and non-printed bulk hydrogel. It was reported that the internal geometrical features of cell enclosed hydrogel have influence on cell fate[41]. However, the decreases of cell density in both hydrogels were observed. This is most likely attributed to the dead cells that were not stained due to the cell

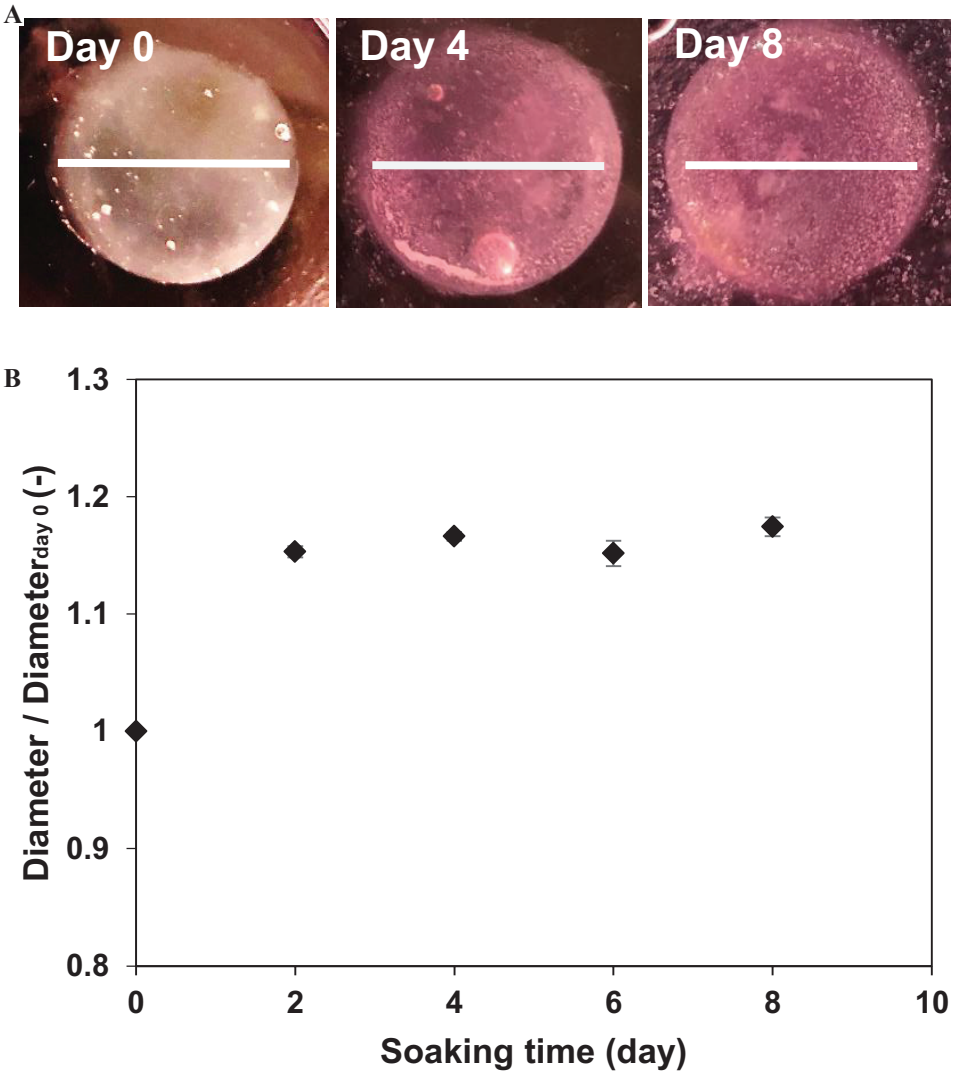

Figure 4. (A) Photographs of disk-shaped hydrogels after soaking in cell culture medium for 0, 4, and 8 days. Scale bars: 1.5 cm. (B) Change in diameter of hydrogels. Data are mean ± SD (n = 3).

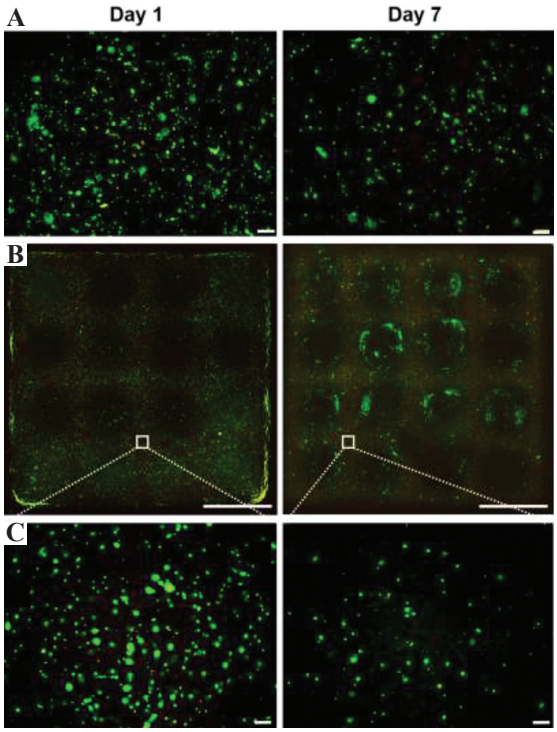

Figure 5. Fluorescence images of 10T1/2 cells cultured in (A) non-printed and (B, C) printed hydrogels for 1 and 7 days at different magnifications. Live and dead cells show green and red fluorescence, respectively. Scale bars: (A), (C) 200 μm and (B) 5 mm.

lysis. The possible reason for cell death might be the mechanical stress from the high concentration of CNF incorporated in the hydrogels during the mixing procedure and the culture time. In the previous study that also used CNF for the extrusion system, low cell viability (<70%) for human chondrocytes, which has different morphology than our model cell line, was reported. It could be considered as one of the drawbacks of using CNF for bioink[35]. Although it is out of the scope of this paper, CNF-based bioinks may be more suitable for the regeneration of cartilage tissues than the other tissues[40,42]. Besides this effect of CNF on cells, the proposed hydrogelation method can be utilized for 3D bioprinting of living cells.

3.3 Switchable construct surface

3D-printed hydrogel constructs can also be used as scaffolds for cell culture[43,44]. Since it is well-known that alginate has no binding site for cell adhesion[45], we made an attempt to switch the surface of a printed construct for cell culture. Taking advantage of the possibility to cross-link various polymers through the same enzymatic reaction, Gel-Ph was selected as a coating

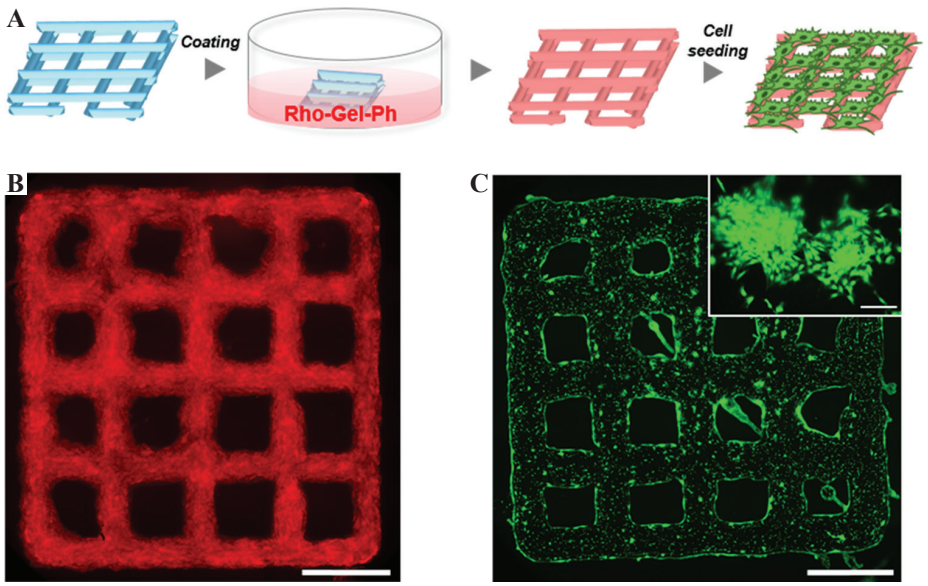

Figure 6. (A) Workflow of switching hydrogel surface after printing and postcross-linking. Fluorescence images of (B) printed lattice-shaped hydrogel after coating and (C) 10T1/2 cells cultured on the hydrogel for 2 days. The image (scale bar: 200 μm) in upper right corner shows the sign of cell elongation. Scale bars: (B) and (C) 5 mm.

material due to its ability to promote cell adhesion and proliferation. The lattice-shaped construct obtained using the selected ink was soaked in a solution containing rhodamine-labeled Gel-Ph (1.0 w/v%, Rho-Gel-Ph) right after printing (**Figure 6A**). Due to the remaining HRP and glucose, Gel-Ph can be cross-linked with non-cross-linked Ph moieties in the hydrogel. After 1 day of soaking, the entire surface of the lattice-shaped construct had a strong signal of red fluorescence derived from Rho-Gel-Ph, which indicates the successful coating process (**Figure 6B**). Subsequently, 10T1/2 cells were seeded on the construct to confirm the switched culture surface. As shown in **Figure 6C**, the cells adhered to and elongated on the entire surface of the construct. These results demonstrate that it is possible to switch non-cell-adhesive surface of the printed construct to cell-adhesive surface with a simple procedure. Moreover, the ability to modify the surface with desired materials through the proposed method enables to design functionalized 3D construct for individual applications.

4 Conclusions

We demonstrated the feasibility of utilizing glucose-mediated enzymatic hydrogelation for extrusion-based bioprinting. The cross-linking of Alg-Ph and CNF-based bioink through HRP-catalyzed reaction that consumes H_2O_2 generated by HRP and glucose enabled to print 3D cell-laden construct with good shape fidelity. The cell-laden construct was successfully cultured for 7 days without collapsing. In addition to the potency of printing with living cells, it was also demonstrated that the printed construct can be used as a scaffold for cell culture after coated with Gel-Ph through the same cross-linking method. Overall, the proposed method advances the ability of bioprinting with living cells with a mild and cell compatible cross-linking.

Acknowledgments

This work was supported by the Japan Society for the Promotion of Science (JSPS) KAKENHI Grant Numbers 15H04194, 16H02423, 17H03472, 18H01797 and Grand-In-Aid for JSPS Fellows 18J11601.

Conflicts of interest

There are no conflicts of interest to declare.

References

1. An J, Teoh JEM, Suntornnond R, *et al.*, 2015, Design and 3D Printing of Scaffolds and Tissues. *Engineering*, 1(2):261–8. DOI 10.15302/J-ENG-2015061.
2. Liu F, Mishbak H, Bartolo P, *et al.*, 2019, Hybrid Polycaprolactone/Hydrogel Scaffold Fabrication and In-process Plasma Treatment Using PABS. *Int J Bioprint*, 5(1):174. DOI: 10.18063/ijb.v5i1.174.
3. Yang Y, Wang G, Liang H, *et al.*, 2019, Additive Manufacturing of Bone Scaffolds. *Int J Bioprint*, 5(1):148. DOI: 10.18063/ijb.v5i1.148.
4. Zhuang P, Sun AX, An J, *et al.*, 2018, 3D Neural Tissue Models: From Spheroids to Bioprinting. *Biomaterials*, 154:113–33. DOI: 10.1016/j.biomaterials.2017.10.002.
5. Mironov V, Trusk T, Kasyanov V, *et al.*, 2009, Biofabrication: A 21st Century Manufacturing Paradigm. *Biofabrication*, 1(2):022001. DOI: 10.1088/1758-5082/1/2/022001.
6. Mir TA, Nakamura M, Iwanaga S, *et al.*, 2019, Biofabrication Offers Future Hope for Tackling Various Obstacles and Challenges in Tissue Engineering and Regenerative Medicine: A Perspective, *Int J Bioprint*, 5(1):153. DOI: 10.18063/ijb.v5i1.153.
7. Ng WL, Chua CK, Shen YF, *et al.*, 2019, Print Me an Organ! Why We are not There Yet. *Prog Polym Sci*, 97:101145. DOI: 10.1016/j.prog-polymsci.2019.101145.
8. Lee JM, Sing SL, Zhou M, *et al.*, 2018, 3D Bioprinting Processes: A Perspective on Classification and Terminology. *Int J Bioprint*, 4(2):151. DOI: 10.18063/ijb.v4i2.151.
9. Murphy SV, Atala A, 2014, 3D Bioprinting of Tissues and Organs. *Nat Biotechnol*, 32(8):773–85. DOI: 10.1038/nbt.2958.
10. Du X, 2018, 3D Bio-Printing Review. *Mater Sci Eng*, 301(1):012023. DOI: 10.1088/1757-899X/301/1/012023.
11. Heinrich MA, Liu W, Jimenez A, *et al.*, 2019, 3D Bioprinting: From Benches to Translational Applications. *Small*, 15(23):1805510. DOI: 10.1002/smll.201805510.
12. Lee JY, An J, Chua CK, *et al.*, 2017, Fundamentals and Applications of 3D Printing for Novel Materials. *Appl Mater Today*, 7:120–33. DOI: 10.1016/j.apmt.2017.02.004.
13. Nakamura K, Nishiyama Y, Henmi C, *et al.*, 2008, Ink

Jet Three-dimensional Digital Fabrication for Biological Tissue Manufacturing: Analysis of Alginate Microgel Beads Produced by Ink Jet Droplets for Three Dimensional Tissue Fabrication. *J Imaging Sci Technol*, 52(6):060201. DOI: 10.2352/J.ImagingSci.Technol.(2008)52:6(060201).

14. Arai K, Iwanaga S, Toda H, *et al.*, 2011, Three-Dimensional Inkjet Biofabrication Based on Designed Images. *Biofabrication*, 3(3):034113. DOI: 10.1088/1758-5082/3/3/034113.
15. Sorkio A, Koch L, Koivusalo L, *et al.*, 2018, Human Stem Cell Based Corneal Tissue Mimicking Structures Using Laser-Assisted 3D Bioprinting and Functional Bioinks. *Biomaterials*, 171:57–71. DOI: 10.1016/j.biomaterials.2018.04.034.
16. Kérourédan O, Hakobyan D, Rémy M, *et al.*, 2019, *In Situ* Prevascularization Designed by Laser-assisted Bioprinting: Effect on Bone Regeneration. *Biofabrication*, 11(4):045002. DOI: 10.1088/1758-5090/ab2620.
17. Sakai S, Kamei H, Mori T, *et al.*, 2018, Visible Light-Induced Hydrogelaton of an Alginate Derivative and Application to Stereolithographic Bioprinting Using a Visible Light Projector and Acic Red. *Biomacromolecules,* 19(2):672–9. DOI: 10.1021/acs.biomac.7b01827.
18. Lam T, Dehne T, Krüger JP, *et al.*, 2019, Photopolymerizable Gelatin and Hyaluronic Acid for Stereolithographic 3D Bioprinting of Tissue-Engineered Cartilage. *J Biomed Mater Res B,* 107(8):2649–57. DOI: 10.1002/jbm.b.34354.
19. Zhuang P, Ng WL, An J, *et al.*, 2019, Layer-By-Layer Ultraviolet Assisted Extrusion-Based (UAE) Bioprinting of Hydrogel Constructs with High Aspect Ratio for Soft Tissue Engineering Applications. *Plos One*, 14(6):e0216776. DOI: 10.1371/journal.pone.0216776.
20. Placone JK, Engler AJ, 2018, Recent Advances in Extrusion-Based 3D Printing for Biomedical Applications. *Adv Healthc Mater,* 7(8):e1701161. DOI: 10.1002/adhm.201701161.
21. Tai C, Bouissil S, Gantumur E, *et al.*, 2019, Use of Anionic Polysaccharides in the Development of 3D Bioprinting Technology. *Appl Sci,* 9(13):2596. DOI: 10.3390/app9132596.
22. Hölzl K, Lin S, Tytgat L, *et al.*, 2016, Bioink Properties Before, During and After 3D Bioprinting. *Biofabrication*, 8(3):032002. DOI: 10.1088/1758-5090/8/3/032002.
23. Ji S, Guvendiren M, *et al.*, 2017, Recent Advances in Bioink Design for 3D Bioprinting of Tissues and Organs. *Front Bioeng Biotechnol*, 5:23. DOI: 10.3389/fbioe.2017.00023.
24. Das S, Pati F, Choi YJ, *et al.*, 2015, Bioprintable, Cell-Laden Silk Fibroin-Gelatin Hydrogel Supporting Multilineage Differentiation of Stem Cells for Fabrication of Three-Dimensional Tissue Constructs. *Acta Biomater*, 11:233–46. DOI: 10.1016/j.actbio.2014.09.023.
25. Sakai S, Yamamoto Y, Enkhtuul G, *et al.*, 2017, Inkjetting Plus Peroxidase-Mediated Hydrogelation Produces Cell-laden, Cell-Sized Particles with Suitable Characters for Individual Applications. *Macromol Biosci*, 17(5):1600416. DOI: 10.1002/mabi.201600416.
26. Arai K, Tsukamoto Y, Yoshida H, *et al.*, 2016, The Development for Cell-Adhesive Hydrogel for 3D Printing. *Int J Bioprinting*, 2(2):44–53. DOI: 10.18063/IJB.2016.02.002.
27. Sakai S, Ueda K, Gantumur E, *et al.*, 2018, Drop-on-Drop Multimaterial 3D Bioprinting Realized by Peroxidase-Mediated Cross-Linking. *Macromol Rapid Commun*, 39(3):1700534. DOI: 10.1002/marc.201700534.
28. Sakai S, Mochizuki K, Qu Y, *et al.*, 2018, Peroxidase-Catalyzed Microextrusion Bioprinting of Cell-Laden Hydrogel Constructs in Vaporized Ppm-Level Hydrogen Peroxide. *Biofabrication*, 10(4):045007. DOI: 10.1088/1758-5090/aadc9e.
29. Gantumur E, Kimura M, Taya M, *et al.*, 2020, Inkjet Micropatterning Through Horseradish Peroxidase-mediated Hydrogelation for Controlled Cell Immobilization and Microtissue Fabrication. *Biofabrication*, 12(1):011001. DOI: 10.1088/1758-5090/ab3b3c.
30. Sakai S, Nakahata M, *et al.*, 2017, Horseradish Peroxidase Catalyzed Hydrogelation for Biomedical, Biopharmaceutical, and Biofabrication Applications. *Chem Asian J*, 12(24):3098–109. DOI: 10.1002/asia.201701364.
31. Moriyama K, Minamihata K, Wakabayashi R, *et al.*, 2014, Enzymatic Preparation of a Redox-Responsive Hydrogel for Encapsulating and Releasing Living Cells. *Chem Commun*, 50(44):5895–8. DOI: 10.1039/c3cc49766f.
32. Gantumur E, Sakai S, Nakahata M, *et al.*, 2017, Cytocompatible Enzymatic Hydrogelation Mediated by Glucose and Cysteine Residues. *ACS Macro Lett*, 6(5):485–8. DOI: 10.1021/acsmacrolett.7b00122.
33. Gantumur E, Sakai S, Nakahata M, *et al.*, 2019, Horseradish Peroxidase-Catalyzed Hydrogelation Consuming Enzyme-Produced Hydrogen Peroxide in the Presence of Reducing Sugars. *Soft Matter*, 15(10):2163–9. DOI: 10.1039/c8sm01839a.
34. Athukoralalage SS, Balu R, Dutta NK, *et al.*, 2019, 3D Bioprinted Nanocellulose-Based Hydrogels for Tissue Engineering Applications: A Brief Review. *Polymers*, 11(5):898. DOI: 10.3390/polym11050898.
35. Markstedt K, Mantas A, Tournier I, *et al.*, 2015, 3D Bioprinting Human Chondrocytes with Nanocellulose-Alginate Bioink for Cartilage Tissue Engineering Application. *Biomacromol*,

16(5):1489–96. DOI: 10.1021/acs.biomac.5b00188.

36. Leppiniemi J, Lahtinen P, Paajanen A, *et al.*, 2017, 3D-Printable Bioactivated Nanocellulose-Alginate Hydrogels. *ACS Appl Mater Interfaces*, 9(26):21959–70. DOI: 10.1021/acs.ami.7b02756.
37. Ojansivu M, Rashad A, Ahlinder A, *et al.*, 2019, Wood-Based Nanocellulose and Bioactive Glass Modified Gelatin-Alginate Bioinks for 3D Bioprinting of Bone Cells. *Biofabrication*, 11(3):035010. DOI: 10.1088/1758-5090/ab0692.
38. Sakai S, Kawakami K, *et al.*, 2007, Synthesis and Characterization of Both Ionically and Enzymatically Cross-linkable Alginate. *Acta Biomater*, 3(4):495–501. DOI: 10.1016/j.actbio.2006.12.002.
39. Sakai S, Hirose K, Taguchi K, *et al.*, 2009, An Injectable, In Situ Enzymatically Gellable, Gelatin Derivative for Drug Delivery and Tissue Engineering. *Biomaterials*, 30(20):3371-7. DOI: 10.1016/j.biomaterials.2009.03.030.
40. Nguyen D, Hägg DA, Forsman A, *et al.*, 2017, Cartilage Tissue Engineering by the 3D Bioprinting of iPS Cells in a Nanocellulose/Alginate Bioink. *Sci Reports*, 7(1):658. DOI: 10.1038/s41598-017-00690-y.
41. Wang L, Xu M, Luo L, *et al.*, 2018, Iterative Feedback Bio-printing-derived Cell-laden Hydrogel Scaffolds with Optimal Geometrical Fidelity and Cellular Controllability. *Sci Rep*, 8(1):2802. DOI: 10.1038/s41598-018-21274-4.
42. Piras CC, Fernandez-Prieto S, De Borggraeve WM, *et al.*, 2017, Nanocellulosic Materials as Bioinks for 3D Bioprinting. *Biomater Sci*, 5(10):1988–92. DOI: 10.1039/c7bm00510e.
43. Xu W, Zhang X, Yang P, *et al.*, 2019, Surface Engineered Biomimetic Inks Based on UV Cross-Linkable Wood Biopolymers for 3D Printing. *Appl Mater Interfaces*, 11(13):12389–400. DOI: 10.1021/acsami.9b03442.
44. Ajdary R, Huan S, Ezazi NZ, *et al.*, 2019, Acetylated Nanocellulose for Single-Component Bioinks and Cell Proliferation on 3D-Printed Scaffolds. *Biomacromol*, 20(7):2770–8. DOI: 10.1021/acs.biomac.9b00527.
45. Sarker B, Singh R, Silva R, *et al.*, 2014, Evaluation of Fibroblasts Adhesion and Proliferation on Alginate-Gelatin Crosslinked Hydrogel. *Plos One*, 9(9):e107952. DOI: 10.1371/journal.pone.0107952.

RESEARCH ARTICLE

Pilot Study of the Biological Properties and Vascularization of 3D Printed Bilayer Skin Grafts

Yige Huyan, Qin Lian*, Tingze Zhao, Dichen Li, Jiankang He

State Key Laboratory for Manufacturing System Engineering, School of Mechanical Engineering, Xi'an Jiaotong University, Xi'an, China

Abstract: The skin is the largest human organ, and defects in the skin with a diameter greater than 4 cm do not heal without treatment. Allogeneic skin transplantation has been used to allow wound healing, but many grafts do not survive after implantation, due to multiple complications in the procedure. In the present study, the vascularization of three-dimensional (3D) printed full-thickness skin grafts was investigated. Dermal-epithelial grafts were transplanted into a nude mouse model to evaluate integration with the host tissue and the extent of wound healing. To create microvessels in the skin grafts, a bilayer structure consisting of human dermal fibroblasts, keratinocytes, and microvascular endothelial cells was designed and fabricated using an extruded 3D printer. Human dermal fibroblasts and human microvascular endothelial cells were mixed with gelatin-sodium alginate composite hydrogel as the dermis, and human keratinocytes were mixed with gel as the epithelium. Confocal imaging allowed visualization of the location of the cells in the double-layer skin grafts. A full-thickness wound was created on the backs of nude mice and then covered with a double-layer skin graft. Various groups of mice were tested. Animals were euthanized and tissue samples collected after specified time points. Compared with the control group, wound contraction improved by approximately 10%. Histological analysis demonstrated that the new skin had an appearance similar to that of normal skin and with a significant degree of angiogenesis. The results of the immunohistochemical analysis demonstrated that the transplanted cells survived and participated in the healing process.

Keywords: Three-dimensional printing, Bilayer skin graft, Gelatin-alginate complex hydrogel, Vascularization

***Corresponding Author:** Qin Lian, State Key Laboratory for Manufacturing System Engineering, School of Mechanical Engineering, Xi'an Jiaotong University, Xi'an, China; lqiamt@mail.xjtu.edu.cn

Received: November 11, 2019; ***Accepted:*** January 02, 2020; ***Published Online:*** January 21, 2020

Citation: Huyan Y, Lian Q, Zhao T, *et al*., 2020, Pilot study of the biological properties and vascularization of 3D printed bilayer skin grafts. *Int J Bioprint*, 6(1):246. DOI: 10.18063/ijb.v6i1.246

1 Introduction

As the largest human organ, skin[1] protects the body from poisons, pathogens, microorganisms, and other invaders. It can also regulate homeostasis of body fluids, regulate body temperature, immune monitoring, and self-healing, in addition to, physiological functions such as external sensory stimulation. Human skin consists of epidermis and dermis[2]. The epidermis is the outermost layer of the skin, of which 90 – 95% of cells are keratinocytes. The dermis lies between the epidermis and subcutaneous tissue, consisting principally of fibroblasts[3].

At present, large-area skin defects and chronic skin injury remain major problems in clinics[4]. Autologous skin transplantation is limited by donor insufficiency, and allografts suffer immune rejection. Tissue-engineered skin is an effective solution[5]. It can be used not only as a skin substitute in the clinic but also as an infiltration and screening model for basic research. Great progress has been made in the study of tissue-engineered

skin[6-11]. A variety of commercial tissue-engineered skins have been used clinically[12]. However, the majority of these products are designed for timely coverage and to promote wound healing, being unable to satisfy every function of the skin. An ideal tissue-engineered skin would exhibit no toxicity or immune rejection, have normal color, include accessory structures, vessels, and nerves, while demonstrating flexibility and appropriate mechanical strength, and able to exchange material and energy[13-15]. Vascularization of tissue-engineered implants is a key issue that restricts the development of tissue-engineered skin products[16]. At present, tissue-engineered skin has no vascular structure, its nutritional supply principally relies on osmosis, and hence the thickness is limited. The epidermis is unable to receive sufficient nutrients quickly when the skin thickness is >1 mm, causing partial exfoliation and necrosis of the epidermis.

In the present study, a 3D-printed artificial skin was fabricated which included vascular features and through a series of *in vitro* tests, the cell-hydrogel hybrid material printed by an extrusion printing process was evaluated. The rate of survival of keratinocytes, fibroblasts, and endothelial cells was found to be >90%. In addition, the bilayer skin construct was evaluated *in vivo* by detecting the integration of bilayer skin transplantation with host tissue in a nude mouse model. Nude mice are appropriate in the study of wound healing because they do not suffer immune rejection. In this experiment, a full-thickness wound was created on the back of nude mice. The degree of wound healing contraction rate of mice was close to 90%[9], significantly different from that of human wounds. However, the nude mouse model exhibited the ability to support the engineered skin transplantation, in addition to allowing measurement of the structural differences between transplanted and normal skin following wound healing. Wound contraction is a part of the normal healing process, but when it is too large, it may lead to dysfunction or esthetic problems in the wounds of patients. The purpose of this study was to compare the *in vivo* response of a number of tissue-engineered skin grafts with different cellular components to non-transplanted skin grafts and to demonstrate that the tissue-engineered skin graft with vascular endothelial cells is significantly better in wound healing.

2 Materials and methods

2.1 Construction of 3D printed bilayer skin graft

2.1.1 Cell culture and hydrogel preparation

Normal human dermal fibroblasts (NHDFs), human dermal microvascular endothelial cells (HMVECs), and normal human epidermal keratinocytes (NHEKs) were purchased from American type culture collection (ATCC), and maintained and subcultured in accordance with the supplier's protocol. NHDFs were maintained in Dulbecco's Modified Eagle's Medium (DMEM) supplemented with 10% fetal bovine serum (FBS) and 1% antibiotic/antimycotic solution, HMVEC in Roswell Park Memorial Institute (RPMI) 1640 medium supplemented with 10% FBS, and 1% antibiotic/antimycotic solution and NHEKs in Iscove's Modified Dulbecco's Medium (IMDM) supplemented with 10% FBS, and 1% antibiotic/antimycotic solution. Cells were incubated at 37°C in 5% CO_2.

Sodium alginate (Sigma-Aldrich) and gelatin (Sigma-Aldrich) were dissolved in deionized water, heated in a water bath at 37°C, and then stirred with a magnetic stirrer at 80 rpm for 24 h. The gelatin-sodium alginate composite hydrogel solution with 4% (w/v) sodium alginate concentration and 10% (w/v) gelatin concentration was prepared.

2.1.2 Cytotoxicity assay

The hydrogel constructs created in this study were composed of 10% gelatin and 4% sodium alginate. The constructs were placed in DMEM at a 1:10 volume ratio so as to prepare extracts and cultured at 37°C for 24 h[17]. An improved cell counting kit-8 (CCK-8) cytotoxicity assay (Dojin, Japan) was used to determine cell activity, in accordance with the manufacturer's instructions. NHDFs were plated into the wells of a 96-well plate at a density of 5000 cells per well. Hydrogel extracts were added and incubated with the cells in a humidified atmosphere containing 5% CO_2 at 37°C for 24 h, 48 h, and 72 h. Cells without

hydrogel extract constituted the control. 10 µl CCK-8 solutions were added to each well of the plate and incubated at 37°C for 4 h. Absorbance at a wavelength of 450 nm was measured using a microplate reader. All results are presented as optical density (OD) values minus the absorbance of blank wells. The distribution of cells was observed using fluorescence microscopy.

2.1.3 3D bioprinter

A custom-built extruded 3D printing equipment consisted of a control system, a mechanism for motion, and feed and nozzle systems (**Figure 1**). The main body of the equipment was placed on an ultra-clean platform. The mechanism providing motion comprised a gantry with four spindles able to move independently in the Z direction. The effective printing range was 100 × 100 × 100 mm, with a repeatable precision of 0.05 mm. The feed system was a pneumatic pump.

2.1.4 Live and dead assay

NHDFs were mixed with 10% gelatin and 4% sodium alginate composite hydrogel solution at a cell density of 1×10^6 cells/ml. The combination of cells and hydrogel was used to print the 3D structure, which was then cultured in a CO_2 incubator at 5% CO_2, 37°C[18], and evaluated using live and dead staining of the cells on days 1, 4, and 7. Cell growth was observed using a Laser Confocal Microscope (Nikon A1). Live cells appeared green and dead cells red.

2.1.5 Bioprinting of 3D printed bilayer skin graft

NHEKs and a mixture of NHDFs and HMVECs which ratio was 1:1 were separately mixed with 10% gelatin and 4% sodium alginate composite hydrogel solution at each cell density of 1×10^6 cells/ml. A layer of NHEK-hydrogel mixture measuring 20 × 20 × 0.5 mm was printed under the printing pressure 0.15 MPA and move speed 15 mm/s in 25°C, representing the epidermal layer of the full-thickness skin, and an additional layer 20 × 20 × 0.5 mm was printed using the mixture of NHDFs, HMVECs, and hydrogel as the dermal layer of full-thickness skin (**Figure 2**).

The printed skin grafts were cultured *in vitro* for 1 day before transplantation. The coculture

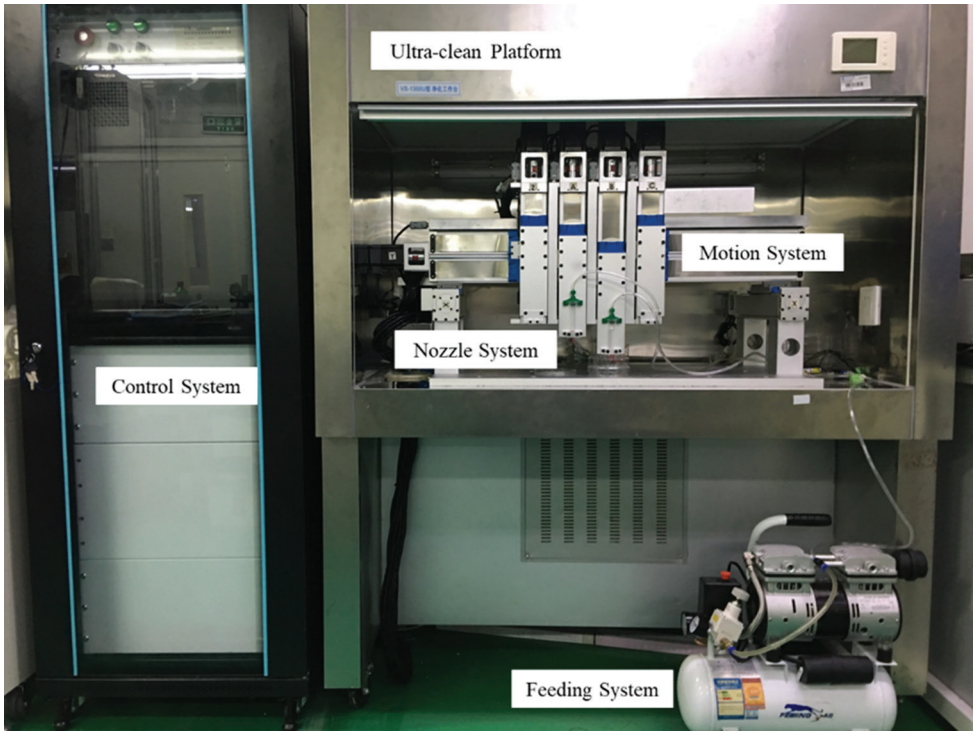

Figure 1. The extruded three-dimensional printing equipment consists of control, motion, feed, and nozzle systems. The main body of the equipment was placed on an ultra-clean platform.

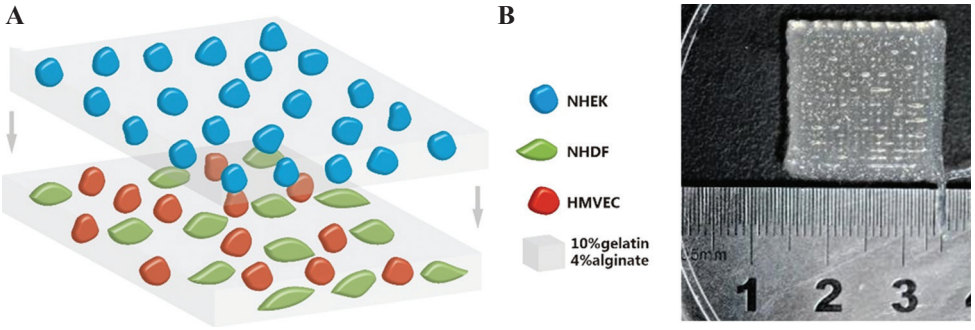

Figure 2. (A) Schematic diagram of transplantable printed skin. The top layer consisted of keratinocytes and gel and the bottom layer fibroblasts, microvascular endothelial cells and gel. (B) A macroscopic image of the printed skin graft.

medium used *in vitro* was the mixed solution of DMEM: IMDM:RPMI = 1:1:1.

2.2 Characterization of the *in vitro* 3D printed bilayer skin graft

NHEKs were labeled with cell Tracker™ Blue 7-amino-4-chloromethylcoumarin dye, in accordance with the manufacturer's protocol. Briefly, the culture medium was removed and pre-warmed cell Tracker Blue (5 μM of blue dye in 2 ml of serum free media) added and incubated for 15 min at 37°C[19]. The dye was then removed and the cells incubated with fresh culture medium at 37°C for 30 min. The medium was again removed and the cells washed with phosphate-buffered solution (PBS) labeled cells pass the dye to daughter cells but not adjacent cells. NHDFs were labeled with cell Tracker™ Green 5-chloromethylfluorescein diacetate dye and HMVECs with cell Tracker™ Red CMTPX dye. The labeling procedure was the same in each case.

2.3 Characterization of the *in vivo* 3D printed bilayer skin graft

2.3.1 Animal surgery

Thirty-two male nude mice were purchased from the SPF Animal Room, Experimental Animal Center of Xi'an Jiaotong University. All experiments had been approved by the Institutional Animal Care and Use Committee of the Ethics Committee of Xi'an Jiaotong University Health Science Center, China. Surgical procedures and post-operative animal care used sterilized instruments and the procedures were strictly sterile. Mice were anesthetized with ketamine (40–90 mg/kg) and xylazine (5–10 mg/kg) by intraperitoneal injection before surgery. The region for skin grafting was sterilized with iodophor and 75% ethanol. A full-thickness skin incision, 20 × 20 mm, approximately 1 mm deep, was created on the backs of the nude mice with ophthalmic scissors[20]. The wounds represented approximately 30–40% of the back of each animal. An aseptic gauze pad was used to halt bleeding of the wound and prevent blood loss exceeding 10–15% of total animal blood volume during surgery. All animals were divided into four groups of eight nude mice each. The printed skin graft was placed within wound so that it completely filled the defect in the experimental group of nude mice. The wound was not grafted in the control group. Tegaderm (3M, London, ON, Canada, http://www.3m.com) was placed over the wound to protect the wound site and maintain a moist environment[21] (**Figure 3**). After surgery, the animals were placed in an aseptic Individual ventilated cage (IVC) containing sterile surgical gauze. The Tegaderm was in place for 8 – 10 days to ensure that the printed skin had grafted to the tissues of the mice. During this period, infection and the dressings were monitored at least twice per day. The mice were monitored until the experiment had completed, at which time the animals were euthanized and tissue samples collected. Tissues were fixed in 4% paraformaldehyde and then analyzed histologically and with immunohistochemistry.

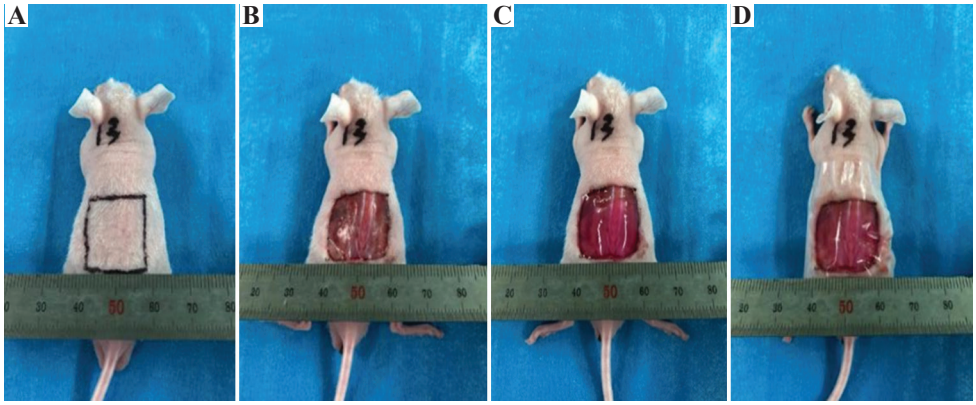

Figure 3. The surgical procedure involved establishing a full-thickness skin wound and transplantation. (A) Marking of the wound incision lines; (B) establishment of a full-thickness skin wound; (C) placement of the printed skin graft; (D) covering by Tegaderm.

2.3.2 Wound contraction

Mice were photographed on the day of surgery and at the end of the experiment. A ruler was placed next to the wound to ensure wounds matched the graft size. The area of the wound at each time point was measured using ImageJ software[22]. The percentage of wound contraction was defined as follows:

wound contraction = (1 − wound area at end point/wound area at surgery) × 100%[23].

2.3.3 Histology

Tissue samples were harvested at specified times, including the regenerated and contracted skin. The tissue samples were embedded in paraffin wax and cut into 6 μm-thick slices with a microtome then stained with hematoxylin and eosin (H&E)[24]. The samples were sealed with a glass coverslip and the growth and scar formation of the regenerated skin evaluated by light microscopy, including the formation of microvessels and other skin accessories, and epidermal differentiation. The thickness of the regenerated skin, including the epidermis and dermis, was measured through cross-sectional staining.

2.3.4 Immunohistochemistry

Tissue sections for immunohistochemistry (IHC) were dewaxed in xylene and hydrated in a decreasing gradient of ethanol concentrations (100%, 95%, 70%, 50%, and 0%). Samples were boiled for 15 min in an antigen retrieval solution consisting of 10 mM sodium citrate, 0.05% polysorbate 20, pH 6.0, cooled for 30 min and washed with 1 × PBS to recover the antigens. The tissue samples were placed in 100 μl normal goat serum and incubated at room temperature for 1 h. An appropriate primary antibody (CD31 YM6277 Immunoway, and CK10 YM6622 Immunoway) diluted in PBS (1: 500) was added to each sample and incubated overnight at 4°C. The samples were washed 5 times with PBS for 5 min each to remove unbound antibody. The samples were incubated with a secondary antibody diluted in PBS (1: 500) for 30 min. The samples were washed in accordance with previously published procedures[25] then incubated with DAB. The samples were mounted with neutral chewing gum and covered with a coverslip. Finally, staining was observed using a light microscope.

2.4 Statistical analysis

All quantitative data were calculated as arithmetic means and standard deviations. A student's *t*-test was used to compare the skin transplantation samples and control groups at the different time periods. $P < 0.05$ was considered statistically significant.

3 Results

3.1 Cytotoxicity assay

Cytotoxicity evaluation was conducted using a CCK-8 assay to directly determine the effect of the gelatin-alginate composite on the activity of NHDF cells. As shown in **Figure 4**, there

was no significant difference in OD between the experimental and control groups, indicating that the extract had no inhibitory effect on cell growth ($P < 0.05$). Relative growth rate (RGR) was calculated according to the measured OD value. The RGR was between 92.0% and 98.3%, indicating that cytotoxicity was Grade 0 or 1, which is conventionally considered as noncytotoxic.

3.2 Live and dead assay

Confocal microscopy was used to scan cell printed constructs over approximately 1250 × 1250 × 300 μm. The results in **Figure 5** demonstrate that the human dermal fibroblasts grew well and were evenly distributed within the gelatin-alginate composite hydrogel. The cell survival rate was maintained at >90% by day 7, indicating that the composite hydrogel fulfilled the demands required of a material for printing cells.

3.3 Cell tracking and observation

The results of fluorescent cell tracking are presented in **Figure 6**. Keratinocytes labeled in blue were located on the top layer of the double-layered skin-printed graft, and microvascular endothelial cells and fibroblasts labeled red and green, respectively, were evenly distributed on the bottom layer of a double layer skin graft. *In vitro* culture and observation continued until 7 days after printing. It was observed that the double-layer skin graft maintained normal skin structure, with no apparent microangiogenesis observed, probably due to the lack of the required conditions, such as the inclusion of growth factors in the *in vitro* culture conditions.

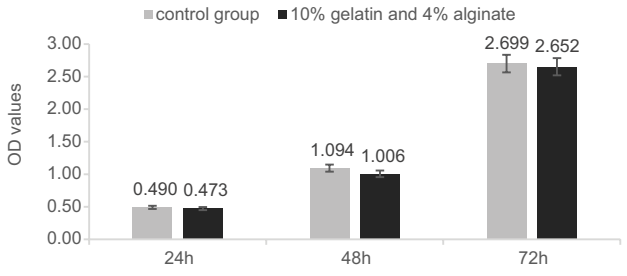

Figure 4. CCK-8 cytotoxicity assay used to assess the cytotoxicity of the hydrogel over 24 h, 48 h, and 72 h on NHDFs.

3.4 Wound contraction

The wound contraction results are displayed in **Figure 7**. Compared with the size of the wound on the day of surgery, the contraction rate due to the printed skin grafting group (**Figure 7A**) was 79 ± 6% at 4 weeks. In the blank (**Figure 7D**) and control groups (**Figure 7B and C**), wound contraction was larger than that in the printed skin graft group. After 4 weeks, the wound contraction rate in controls with no endothelial cells was 81 ± 10%, 85 ± 7% in the acellular controls, and 90 ± 5% in the blank group. One week after surgery, there was no significant difference in wound contraction between the printed skin grafting group and two control groups which were no endothelial cells and no cells, but the wound area gradually decreased with time. Four weeks after surgery, the wound contraction rate in the printed skin grafting group was significantly lower than that in the blank group and cell-free control group ($P < 0.05$). There was no significant difference in wound contraction between the printed skin

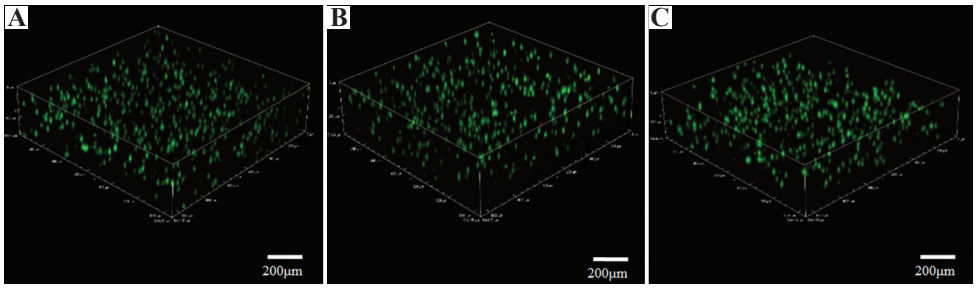

Figure 5. Three-dimensional images of printed cells after live/dead staining. A, B, and C represent cells 1, 4, and 7 days after printing, respectively. Green staining indicates cell survival. Sample dimensions were 1265 μm (length) × 1265 μm (width) × 305 μm (height).

transplantation group and the control group without endothelial cells.

3.5 Histology

H&E staining of the different groups 4 weeks after surgery is displayed in **Figure 8**. Histological analysis demonstrated that the printed skin graft group correctly contained all the graft components, with epidermal and dermal structures that were intact. Growth of the printed skin graft group was significantly better than those of the control groups. First, there was significant angiogenesis in the dermis, while there were barely any microvessels in the other groups. Second, the epidermal layer thickness of this group was also significantly greater than the others, a difference that was significant.

3.6 Immunohistochemistry

Immunohistochemical staining of CD31 4 weeks after surgery is shown in **Figure 9**. These results further confirm the histological observations that the printed skin graft group not only exhibited significant angiogenesis but also that the microvascular-derived cells that were derived from the printed microvascular endothelial cells, confirming that the printed skin graft was capable of growing efficiently and promoting its integration with the mouse tissues and regeneration of blood vessels. **Figure 10** displays immunohistochemical staining of Cytokeratin 10(CK10) 4 weeks after surgery. CK10 identifies the spinous layer of the epidermis and represents one of its major components. Epidermal growth of the printed skin grafting group was significantly greater than those of the control group, with a spinous layer that was significantly thickened.

4 Discussion

The principal purpose of this study was to evaluate the capability of printed skin transplantation to act as a full-thickness skin graft in a full-thickness skin defect model in nude mice. Bioprinting as a highly automated, advanced manufacturing technology[7], has potential to build tissue-engineered skin with pigment[26] and sweat glands

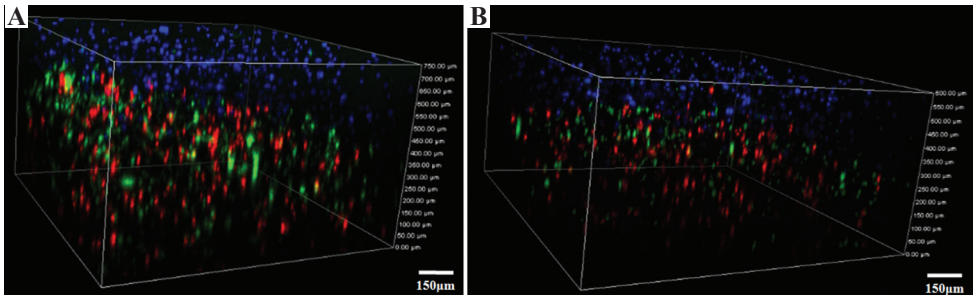

Figure 6. Fluorescent cell tracking in the double skin grafts on the (A) day 1 and (B) day 7 after printing, respectively. Keratinocytes are labeled blue, microvascular endothelial cells red, and fibroblasts green.

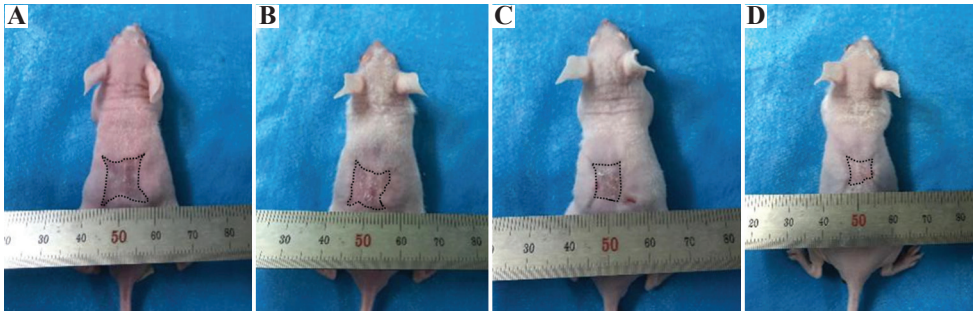

Figure 7. Gross observation of the mice after 4 weeks. A represents the printed skin graft, B is the control group without endothelial cells, C is the control group with no cells, and D is the blank group.

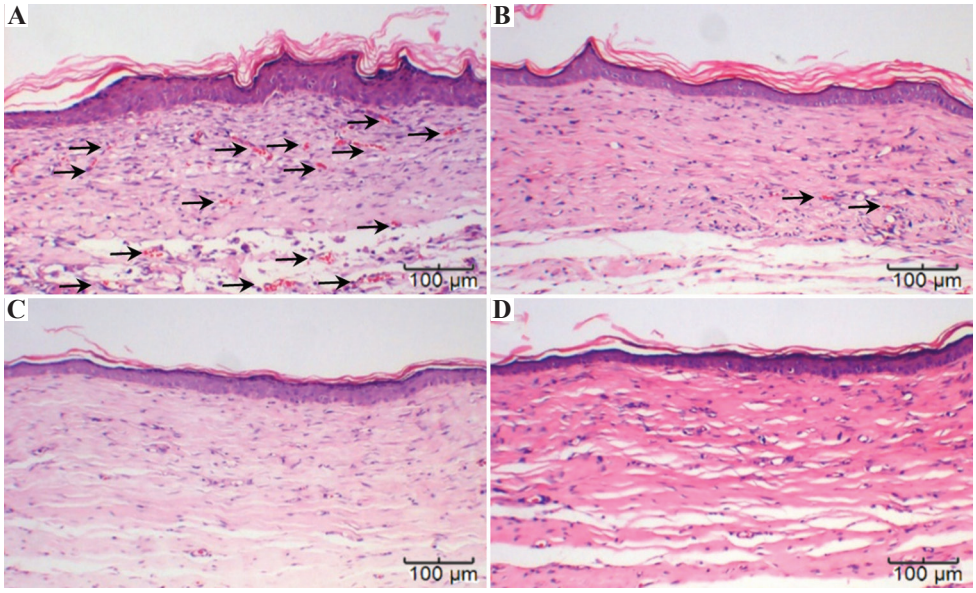

Figure 8: H&E staining of (A) the printed skin graft group with three types of cell; (B) the control group without endothelial cells; (C) the acellular control group; and (D) the blank group.

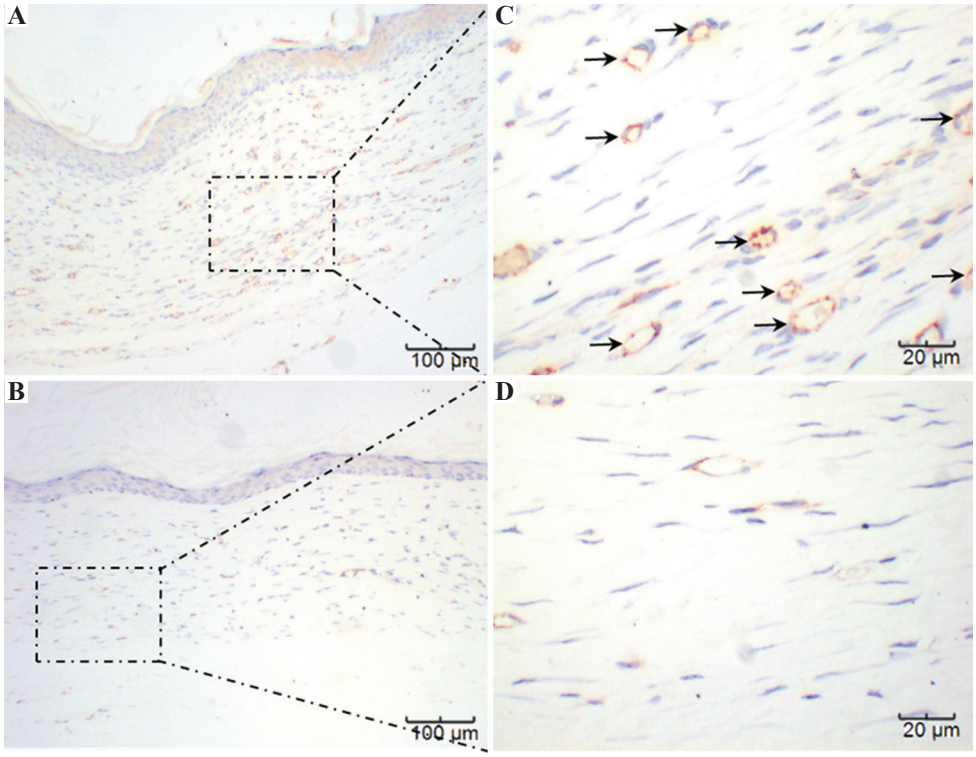

Figure 9. A and C represent the printed skin graft group, at ×100 and ×400, respectively. B and D represent the control group, at ×100 and ×400, respectively. Because there was no significant difference between the three control groups, only one set is displayed. The microvessels marked as brown in A and C can be clearly seen, while visible in B and D only sparsely.

regeneration[27]. Furthermore, to solve the problems of cell survival and differentiation within the grafts, prevascularization of the scaffold has become a potential strategy[28]. Here, we use direct writing

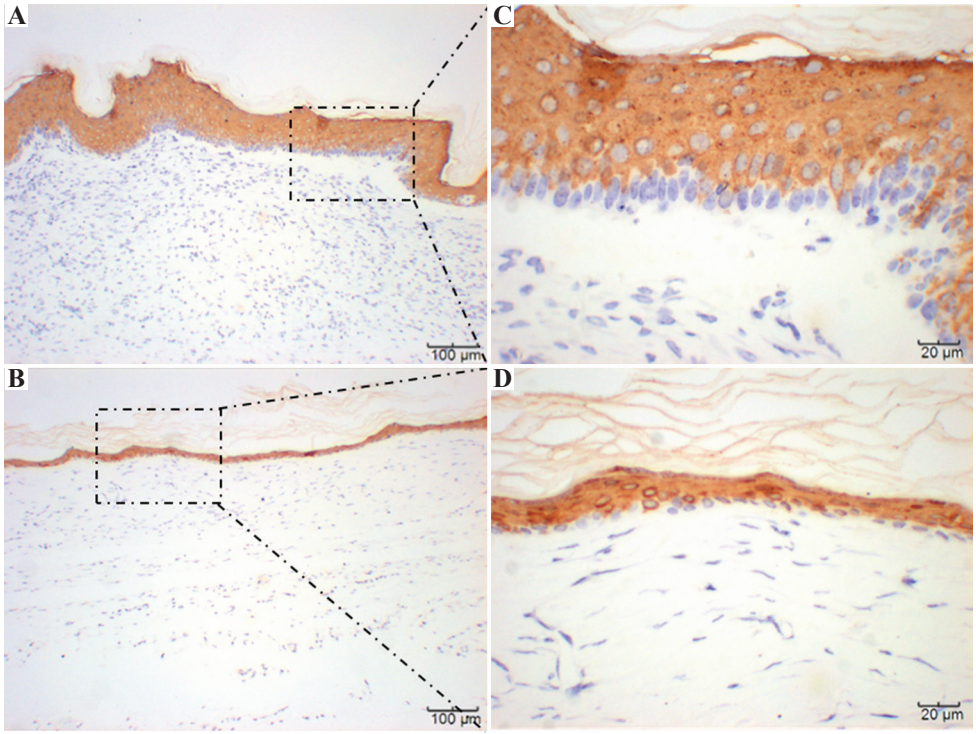

Figure 10. Immunohistochemical staining of CK10. A and C represent the printed skin graft group with HMVECs. B and D represent the control group without HMVECS.

(DW) technology to make a prevascularized skin grafts. First, we developed a composite hydrogel material suitable for printing and transplanting, namely, 10% gelatin and 4% sodium alginate[29]. Gelatin has excellent biocompatibility but is difficult to print directly at a temperature suitable for cells, while sodium alginate has good performance for printing, but cells can survive within it, they do not function physiologically. We discovered a ratio for the hybrid material that fulfilled both print performance and biocompatibility. The cytotoxicity test results demonstrated good biocompatibility of the composite. In addition, after printing, rather than cross-linking the sodium alginate with calcium ions, an innovative step was to cross-link the gelatin with only the transglutaminase[29], causing the construct to gradually lose sodium alginate later during culture. In addition, the porosity of the construct increased, allowing greater cell growth and function.

Before performing the animal experiments, we conducted a series of *in vitro* experiments to observe the performance of the printed skin grafts. A live and dead assay demonstrated that the cells survived well in the material. Fluorescence cell tracking indicated that the double-layer skin graft cultured *in vitro* was able to maintain the printed skin structure over time, with the epidermal and dermal layers clearly demarcated and fibroblasts and microvascular endothelial cells evenly distributed on the bottom layer. However, due to the limitations of the culture conditions, only nutrients derived from the culture medium were present *in vitro*, quite different from normal physiological conditions and so no microvascular formation was observed. As the duration of culture continued, the graft gradually degraded, suggesting that this hybrid hydrogel was an ideal scaffold material[30].

Wound contraction is a normal part of the healing process[31], which depends on the age of the animal, wound size, and many other parameters[32]. Typically, observed wound contraction in human adults is between 20% and 40%, compared with approximately 90% in other mammals such as mice[33]. Excessive wound contraction leads to joint contracture, local dysfunction, and esthetic problems[34]. In this study, we found that printing

skin grafts on full-thickness wounds in nude mice improved the degree of wound shrinkage. Wound contraction in the cell groups (printed skin transplantation group and non-endothelial control group) improved to varying degrees compared with the other two groups (cell-free control and blank control groups). However, we did not observe a decrease in wound contraction over time, due to tissue remodeling into normal tissue. The possible reason is that the post-operative observation time was not long enough, but we believe that printing double-layer skin grafts would effectively improve wound contraction in long-term applications.

Histological observations showed that the skin grafts formed epidermal and dermal layers 14 days after surgery, and microvessels are formed, mainly due to the microvascular endothelial cells within the printed skin grafts. In addition, due to the *in vivo* environment providing appropriate stimulation, unlike the *in vitro* environment, such as the presence of relevant growth factors, the printed cells in the skin graft underwent functional phenotypic remodeling. We can be certain that the printed microvascular endothelial cells were involved in the formation of the microvessels during tissue regeneration, but mouse cells may also participate in the repair process through migration or other mechanisms. The majority of other studies have used collagen or other materials as extracellular matrix[35]. Sodium alginate and gelatin were used in the present study. The good healing response of the animal model and results of histology establish that the use of this hybrid material can achieve excellent results, forming tissue similar to physiological tissue. Microvessel is one of the most important skin appendages[36]. No other appendages such as hair follicles[37], sweat glands,[38] or nerves were observed in this study. We speculate that generation of these appendages may require inclusion of additional components or cells in the printed skin graft. A design that is more rational and closer to the physiological tissue is also required.

5 Conclusions

A gelatin-alginate composite mixed with three skin-specific cell types was manufactured using direct writing (DW) technology and implanted for the repair of damaged skin on the back of mice in this study. The DW cell-printing process developed by our lab achieved more than a 90% cell survival rate for all three skin-specific cell types and facilitated the manufacture of a bilayer structure which integrated with host tissue within a wound. Animal experimental results indicate that the composite constructs with or without cells can assist skin wound healing, but constructs with cells had the clear advantage of microvessels regeneration. Four weeks after surgery, the constructs containing cells had an approximately 10% increase in wound contraction compared to the other groups, promoting microvessels and skin tissue regeneration, as demonstrated by histological and immunohistochemical analysis.

Acknowledgments

This work was supported by grants from the Science and Technology Projects of PLA (BWS17J036, 18-163-13-ZT-003-011-01) and the National Natural Science Foundation of China (51835010 and 51375371). We thank Health Science Center of Xi'an Jiaotong University for animal experiments, as well as Mr Linian Zhou for his hard work of printing experiments and Mz Lin Gao of histology analysis.

References

1. Rognoni E, Walko G, 2019, The Roles of YAP/TAZ and the Hippo Pathway in Healthy and Diseased Skin. *Cells*, 8(5):E411. DOI: 10.3390/cells8050411.
2. Prost-Squarcioni C, 2006, Histology of Skin and Hair Follicle. *Med Sci (Paris)*, 22(2):131–7. DOI: 10.1051/medsci/2006222131.
3. Bernerd F, 2005, Human Skin Reconstructed *in vitro* as a Model to Study the Keratinocyte, the Fibroblast and Their Interactions: Photodamage and Repair Processes. *J Soc Biol*, 199(4):313–20.
4. Kim SW, Choi SH, Kim JT*, et al.*, 2015, An Additional Option for Split-Thickness Skin Graft Donors: The Previous Free Flap Sites. *Ann Plast Surg*, 75(6):634–6. DOI: 10.1097/SAP.0000000000000143.
5. Wei LG, Chang HI, Wang Y*, et al.*, 2019, A Gelatin/Collagen/Polycaprolactone Scaffold for Skin Regeneration. *PeerJ*,

7:e6358. DOI: 10.7717/peerj.6358.

6. Han XX, Courseaus J, Khamassi J*, et al.*, 2018, Optimized Vascular Network by Stereolithography for Tissue Engineered Skin. *Int J Bioprinting*, 4(2):17. DOI: 10.18063/IJB.v4i2.134.
7. Ng WL, Chua CK, Shen YF, 2019, Print Me An Organ! Why We Are Not There Yet. *Prog. Polym Sci*, 97:45. DOI: 10.1016/j.progpolymsci.2019.101145.
8. Liu F, Liu C, Chen QH*, et al.*, 2018, Progress in Organ 3D Bioprinting. *Int J Bioprinting*, 4(1):15. DOI: 10.18063/IJB.v4i1.128.
9. An J, Teoh JEM, Suntornnond R*, et al.*, 2015, Design and 3D Printing of Scaffolds and Tissues. *Engineering*, 1(2):261–8. DOI: 10.15302/j-eng-2015061.
10. Choudhury D, Anand S, Naing MW, 2018, The Arrival of Commercial Bioprinters Towards 3D Bioprinting Revolution! *Int J Bioprinting*, 4(2):20. DOI: 10.18063/IJB.v4i2.139.
11. Zhuang P, Sun AX, An J*, et al.*, 2018, 3D Neural Tissue Models: From Spheroids to Bioprinting. *Biomaterials*, 154:113–33. DOI: 10.1016/j.biomaterials.2017.10.002.
12. Chong C, Wang Y, Fathi A*, et al.*, 2019, Skin Wound Repair: Results of a Pre-clinical Study to Evaluate Electropsun Collagen-Elastin-PCL Scaffolds as Dermal Substitutes. *Burns*, 45(7):1639–48. DOI: 10.1016/j.burns.2019.04.014.
13. Kandhasamy S, Arthi N, Arun RP*, et al.*, 2019, Synthesis and Fabrication of Novel Quinone-Based Chromenopyrazole Antioxidant-Laden Silk Fibroin Nanofibers Scaffold for Tissue Engineering Applications. *Mater Sci Eng C Mater Biol Appl*, 102:773–87. DOI: 10.1016/j.msec.2019.04.076.
14. Baltazar T, Merola J, Catarino C*, et al.*, 2019, Three Dimensional Bioprinting of a Vascularized and Perfusable Skin Graft Using Human Keratinocytes, Fibroblasts, Pericytes, and Endothelial Cells. *Tissue Eng Part A*, 12. DOI: 10.1089/ten.tea.2019.0201.
15. Ng WL, Yeong WY, 2019, The Future of Skin Toxicology Testing Three-Dimensional Bioprinting Meets Microfluidics. *Int J Bioprinting*, 5(2.1):44–54. DOI: 10.18063/ijb.v5i2.1.237.
16. Wang JH, Chen J, Kuo SM*, et al.*, 2019, Methods for Assessing Scaffold Vascularization *In Vivo*. *Methods Mol Biol*, 1993:217–26. DOI: 10.1007/978-1-4939-9473-1_17.
17. Li Y, Lu H, Gu Y*, et al.*, 2017, Enhancement of NK Cells Proliferation and Function by Shikonin. *Immunopharmacol Immunotoxicol*, 39(3):124–30. DOI: 10.1080/08923973.2017.1299174.
18. Zhou S, Cui Z, Urban J, 2011, Dead Cell Counts During Serum Cultivation are Underestimated by the Fluorescent Live/Dead Assay. *Biotechnol J*, 6(5):513–8. DOI: 10.1002/biot.201000254.
19. Kuppan P, Sethuraman S, Krishnan UM, 2017, *In Vitro* Co-Culture of Epithelial Cells and Smooth Muscle Cells on Aligned Nanofibrous Scaffolds. *Mater Sci Eng C Mater Biol Appl*, 81:191–205. DOI: 10.1016/j.msec.2017.07.050.
20. Yanez M, Rincon J, Dones A*, et al.*, 2015, *In Vivo* Assessment of Printed Microvasculature in a Bilayer Skin Graft to Treat Full-Thickness Wounds. *Tissue Eng Part A*, 21(1-2):224–33. DOI: 10.1089/ten.TEA.2013.0561.
21. Nye R, Robinia K, Peterson P*, et al.*, 2018, Efficacy of a Nitric Oxide Dressing in Decreasing Bacterial Counts on Human Skin. *J Wound Care*, 27(7):S19–25. DOI: 10.12968/jowc.2018.27.Sup7.S19.
22. Garcia M, Escamez MJ, Carretero M*, et al.*, 2007, Modeling Normal and Pathological Processes Through Skin Tissue Engineering. *Mol Carcinog*, 46(8):741–5. DOI: 10.1002/mc.20327.
23. Yannas IV, Tzeranis DS, So PTC, 2017, Regeneration of Injured Skin and Peripheral Nerves Requires Control of Wound Contraction, not Scar Formation. Wound Repair Regen, 25(2):177–91. DOI: 10.1111/wrr.12516.
24. Feldman AT, Wolfe D, 2014, Tissue Processing and Hematoxylin and Eosin Staining. Methods Mol Biol, 1180:31–43. DOI: 10.1007/978-1-4939-1050-2_3.
25. Ferringer T, 2015, Immunohistochemistry in Dermatopathology. *Arch Pathol Lab Med*, 139(1):83–105. DOI: 10.5858/arpa.2014-0075-RA.
26. Ng WL, Qi JTZ, Yeong WY, *et al*., 2018, Proof-of-Concept: 3D Bioprinting of Pigmented Human Skin Constructs. *Biofabrication*, 10(2):025005. DOI: 10.1088/1758-5090/aa9e1e.
27. Huang S, Yao B, Xie J, *et al*., 2016, 3D Bioprinted Extracellular Matrix Mimics Facilitate Directed Differentiation of Epithelial Progenitors for Sweat Gland Regeneration. *Acta Biomater*, 32: 170–7. DOI: 10.1016/j.actbio.2015.12.039.
28. Kim BS, Kwon YW, Kong JS, *et al*., 2018, 3D Cell Printing of *In Vitro* Stabilized Skin Model and *In Vivo* Pre-Vascularized Skin Patch Using Tissue-Specific Extracellular Matrix Bioink: A Step Towards Advanced Skin Tissue Engineering. *Biomaterials*, 168:38–53. DOI: 10.1016/j.biomaterials.2018.03.040.
29. Chen H, Xing X, Tan H, *et al*., 2017, Covalently Antibacterial Alginate-Chitosan Hydrogel Dressing Integrated Gelatin Microspheres Containing Tetracycline Hydrochloride for Wound Healing. *Mater Sci Eng C Mater Biol Appl*, 70:287–95. DOI: 10.1016/j.msec.2016.08.086.
30. Nezhad ZM, Poncelet A, Fervaille C, *et al*., 2019, Comparing

the Host Reaction to CorMatrix and Different Cardiac Patch Materials Implanted Subcutaneously in Growing Pigs. *Thorac Cardiovasc Surg*, 67(1):44–9. DOI: 10.1055/s-0037-1607332.

31. Limandjaja GC, van den Broek LJ, Breetveld M, *et al*., 2018, Characterization of *In Vitro* Reconstructed Human Normotrophic, Hypertrophic, and Keloid Scar Models. *Tissue Eng Part C Methods*, 24(4):242–53. DOI: 10.1089/ten.TEC.2017.0464.
32. Walmsley GG, Hu MS, Hong WX, *et al*., 2015, A Mouse Fetal Skin Model of Scarless Wound Repair. *J Vis Exp*, 95:52297. DOI: 10.3791/52297.
33. Tranquillo RT, Murray JD, 1993, Mechanistic Model of Wound Contraction. *J Surg Res*, 55(2):233–47. DOI: 10.1006/jsre.1993.1135.
34. Oosterwijk AM, Mouton LJ, Schouten H, *et al*., 2017, Prevalence of Scar Contractures After Burn: A Systematic Review. *Burns*, 43(1):41–9. DOI: 10.1016/j.burns.2016.08.002.
35. Lee V, Singh G, Trasatti J P, *et al*., 2014, Design and Fabrication of Human Skin by Three-Dimensional Bioprinting. *Tissue Eng Part C Methods*, 20(6):473–84. Doi: 10.1089/ten.TEC.2013.0335.
36. Lee MS, Ahmad T, Lee J, *et al*., 2017, Dual Delivery of Growth Factors with Coacervate-Coated Poly(Lactic-Co-Glycolic Acid) Nanofiber Improves Neovascularization in a Mouse Skin Flap Model. *Biomaterials*, 124:65–77. Doi: 10.1016/j.biomaterials.2017.01.036.
37. Lalley AL, Boyce ST, 2019, Fabrication of Chimeric Hair Follicles for Skin Tissue Engineering. *Methods Mol Biol*, 1993:159–79. DOI: 10.1007/978-1-4939-9473-1_13.
38. Brandenburger M, Kruse C, 2019, Fabrication of a Co-Culture System with Human Sweat Gland-Derived Cells and Peripheral Nerve Cells. *Methods Mol Biol*, 1993:139–48. DOI: 10.1007/978-1-4939-9473-1_11.

RESEARCH ARTICLE

Bioprinting of Multimaterials with Computer-aided Design/Computer-aided Manufacturing

J. M. Lee, S. L. Sing, W. Y. Yeong*

Singapore Centre for 3D Printing, School of Mechanical and Aerospace Engineering, Nanyang Technological University, Singapore

Abstract: Multimaterials deposition, a distinct advantage in bioprinting, overcomes material's limitation in hydrogel-based bioprinting. Multimaterials are deposited in a build/support configuration to improve the structural integrity of three-dimensional bioprinted construct. A combination of rapid cross-linking hydrogel has been chosen for the build/support setup. The bioprinted construct was further chemically cross-linked to ensure a stable construct after print. This paper also proposes a file segmentation and preparation technique to be used in bioprinting for printing freeform structures.

Keywords: Three-dimensional bioprinting, Bioprinting, Hydrogel, Three-dimensional printing, Rapid prototyping, Additive manufacturing, Computer-aided design, Support structure generation

***Corresponding Author:** W. Y. Yeong, Singapore Centre for 3D Printing, School of Mechanical and Aerospace Engineering, Nanyang Technological University, Singapore; wyyeong@ntu.edu.sg

Received: August 11, 2019; ***Accepted:*** January 03, 2020; ***Published Online:*** January 22, 2020

Citation: Lee JM, Sing SL, Yeong WY, 2020, Bioprinting of multimaterials with computer-aided design/computer-aided manufacturing. *Int J Bioprint*, 6(1):245. DOI: 10.18063/ijb.v6i1.245.

1 Introduction

Bioprinting can be considered as a derivative technique that has evolved from three-dimensional (3D) printing, also known as additive manufacturing[1-3]. Through computer assistive technology, different bioprinting techniques can be integrated together for multimaterial printing. Material jetting and material extrusion are two technologies that have been commonly used in bioprinting due to the ease of setup. Moreover, these processes are relatively biocompatible as opposed to other additive manufacturing technologies. In material jetting bioprinting, biomaterials, cells, and growth factors are dispensed as droplets[4-7]. Comparatively, the material extrusion setup uses a combination of an automated robotic system for controlling platform movement and a dispensing system for deposition of cell-hydrogel constructs in forms of either strands or droplets[8-17]. In addition, valves can be placed at the nozzle to create droplets by regulating the flow of the hydrogel within the syringe[18].

2 Limitations of bioprinting in forming structural stable construct

Hydrogels[19], commonly used as vehicles for cell delivery in bioprinting, are high water content polymers with hydrophilic polymer chains that can be cross-linked to form 3D matrices[20]. Naturally derived hydrogels, such as collagen, gelatin, hyaluronic acid, chitosan, alginate, and cellulose, are used for tissue engineering and in bioprinting[21-23]. However, the naturally derived polymers have certain drawbacks including relatively weak mechanical property, fast degradation, and sometimes may cause allergic reactions[21,23]. Materials that are used for bioprinting are usually limited by their

viscosity and gelling speed, hence reducing the process window to bioprint freeform biological structures[24]. Different bioprinting strategies have been used to overcome such material-based limitation for bioprinting freeform constructs[25]. One such strategy is through the use of support materials that help assist in forming structural integrity for the build materials.

2.1 Support structure generation in additive manufacturing

The use of build/support configuration is prevalent in 3D printing. 3D printing technologies, such as inkjet printing[26-28], and material extrusion such as fused deposition modeling make use of multimaterials to differentiate the part from the support materials[29,30]. The software involved has the capability to generate the support structures needed for the part and to assign a secondary material to the supports. Using materials of different properties, the supports can be removed preferentially during post-processing[31].

In general, the purpose for support structure in additive manufacturing is to provide structural integrity where regions of object display overhanging or floating features. Support structure generation in additive manufacturing can be distinguished according to the density difference between build and support parts. For instance, support structure generation for metal powder bed fusion and stereolithography (STL) is designed as struts[32]. Comparatively, support material can

Table 1. Comparison of the current technology for multimaterial deposition and support structure generation across additive manufacturing technologies.

Material	Form	AM technologies		Multimaterial deposition	Support structure generation	Function of support structure
Metal	Powder	Powder bed fusion[40-43]	Selective laser melting	×	Struts	- Support floating and overhanging objects - Melt pool heat dissipation - Prevent thermal warping prevention
			Electron-beam melting	×		
		Directed energy deposition[44]	LENS	✓	NA	
Polymer	Powder	Powder bed fusion[45-47]	Selective laser sintering	×	NA	
	Powder	Binder jetting[45-47]	Indirect inkjet printing (Binder 3DP)	✓	NA	
	Liquid, photopolymer	Material jetting[45,47]	Polyjet/inkjet printing	✓	Partially or fully encapsulate build part	- Support floating and overhanging objects
	Solid, thermoplastic	Material extrusion[45,47]	Filament deposition modeling	✓	Lattice scaffolding structures	- Support weight imbalance
	Liquid, hydrogel		Bioprinting	✓	Partially or fully encapsulate build part	- Support floating and overhanging objects - Improve print fidelity
	Liquid, photopolymer	Vat polymerization[45,47]	Stereolithography	✓	Struts	- Support floating and overhanging objects

LENS: Laser engineered net shaping

be generated to partially or fully encapsulate the 3D-printed part commonly used in material jetting and material extrusion techniques[33,34]. Support structures are also generated in response to include technology-specific consideration. For instance, the support structure in selective laser melting[35-38] or electron-beam melting[39] functions is strategically placed to improve heat dissipation and prevent print jobs from thermal warping[32].

The prevalence of multimaterial deposition and build/support printing configuration has been demonstrated across additive manufacturing technologies (**Table 1**). With an increase interest in multimaterial bioprinting for use in build-support configuration, it is imperative to develop a systematic framework for file processing method in multimaterial bioprinting. Considerations in segmenting computer-aided design (CAD) files for bioprinting are also discussed in the following section.

2.2 Use of build/support strategies in bioprinting

Bioprinting allows the deposition of heterogeneous materials and cells in a controlled manner to form an engineered construct that recaptures the complexities of native tissues[25,48,49]. The capability of depositing multimaterial in bioprinting is in line with build/support strategies commonly found in 3D printing. Increasing research interest lies in bioprinting cell-hydrogel materials using a build/support configuration[4,50-56]. In build/support configuration, support materials are used to provide mechanical strength to hold the structure giving the overall form for the engineered construct. In many cases, these materials are eventually removed from the printed constructed (i.e., sacrificial). On the other hand, cells and/or hydrogels (build materials) provide the functional components in the bioprinted construct.

Such printing strategy can be either vat-based or sequential printing of build/support materials (**Figure 1**). In such build/support configuration, the

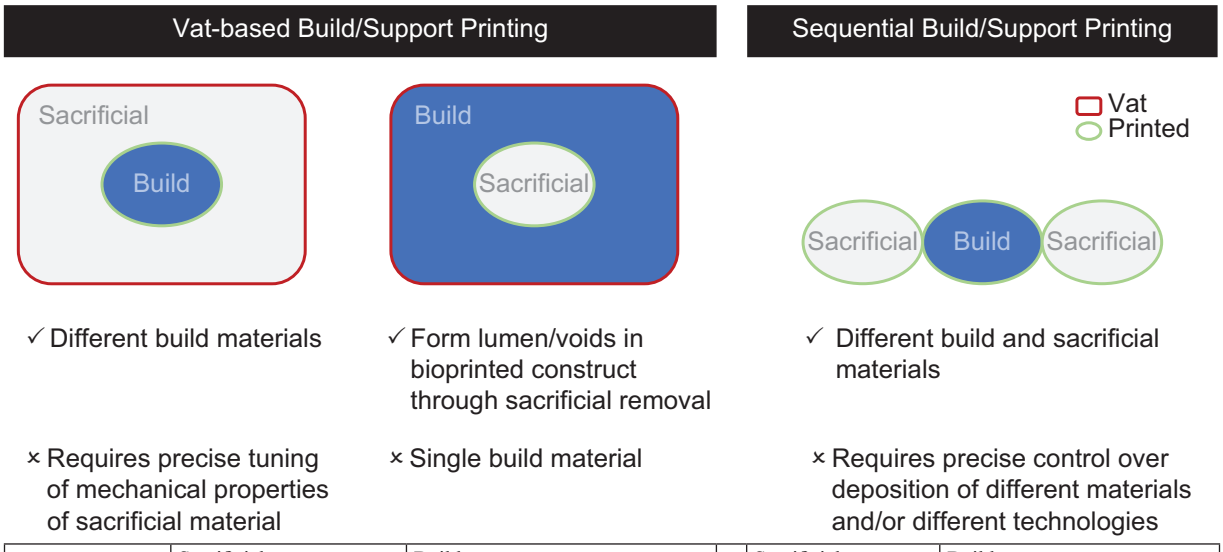

	Sacrificial	Build		Sacrificial	Build
Natural	- Alginate[4] - Collagen[4,47] - Gelatin[47,55,56]	- Gelatin and derivatives[46] - Collagen[56] - Alginate[47,56] - Fibrinogen[47] - HA[47,56] - Spheroids[55] - Dextran and derivatives[57]		- HA and derivatives[44]	- HA and derivatives[44,52,54] - Gelatin and derivatives[44,52,54] - Fibrinogen[54] - Alginate[51] - Atelocollagen[52] - dECM[58]
Synthetic	- Pluronic F127[46] - PEO and derivatives[57]			- Pluronic F127[54] - PCL[46,51,52,54,58] - PLGA[52]	

Figure 1. Schematic illustration on the different configurations in build/support printing.

support material can be a temporary scaffold[57,58] that is either manually remove or dissolved away (i.e., sacrificial); while support material such as poly(epsilon-caprolactone) and poly(lactic-co-glycolic acid) thermoplastic provides mechanical integrity and eventually degrades through biological process[9,15,59-62]. Pluronic F127 and gelatin are commonly used in vat-based build/support printing such that bioink containing cells are extruded and embedded within the vat of support material[55].

Optimizing build orientation and topology of support structure aims at reducing support material usage and total build time. Algorithms have been developed to design tool path for strategically positioning build parts, minimizing support material wastage, and decreasing both build and post-processing time[34,66]. In this article, a novel file processing method is introduced. In brief, CAD files used for bioprinting are segmented into different sections. Build or support material printing reaches a certain z-layer before the printhead is changed for the alternating materials.

3 Methodology

3.1 File preparation

A series of CAD segmentation method is used in the novel approach in preparing CAD files for bioprinting. This method has several advantages such as (i) improve structural stability of bioprinted construct, (ii) deposit multimaterial, (iii) optimize overall printing time, and (iv) overcome machine limitations. Overview of the novel approach as compared to conventional file segmentation approach is illustrated in **Figure 2**.

To assess the functionality of the novel file segmentation approach, two models are demonstrated (i) freestanding coil (15 mm) and (ii) left ventricle wall. Regenhu bioprinter with multi-printhead channels is used for the printing.

3.2 Synthesis of gelatin methacrylate

All materials are purchased from Sigma-Aldrich unless otherwise stated. Gelatin methacrylate (GelMA) was synthesized as previously described with slight modification[67]. About 10% w/v Gelatin Type A (porcine skin) was dissolved in 1× phosphate-buffered saline (PBS) (Vivantis) stirred at 600 rpm keeping temperature at 60°C for 1 h. Methacrylate anhydride was added at 1.4% v/v dropwise into the solution and the reaction is continued for 2 h at 50°C. The reaction is quenched by adding pre-warmed 1× PBS at 40°C. The mixture was transferred into dialysis tubing (MWCO: 12400) for dialysis in distilled water for 4 days at 40°C. Finally, the solution was lyophilized for 7 days to obtain pure GelMA and was stored at −20°C until further use.

3.3 Preparation of bioink (build and support material)

The build material contains 5% w/v Gelatin Type A, 5% w/v GelMA, and 2% w/v sodium alginate which were dissolved in 1× PBS. Photoinitiator containing 10% w/v 2-Hydroxy-4′-(2-hydroxyethoxy)-2-methylpropiophenone (Sigma-Aldrich) was dissolved in ethanol and added to the mixture of build material at 0.02% v/v. The support material consists of Pluronic F-127 and 1 M calcium chloride dissolved in 10 mM HEPES buffer.

4 Results and discussion

Hydrogels that rapidly cross-link are chosen as the complimentary pairs in a build/support configuration[25]. As such, build material comprising gelatin methacrylate and sodium alginate is coupled with support material comprising of Pluronic F127/calcium chloride. Primary cross-linking occurs when alginate is in contact with $CaCl_2$ from the support material. Pluronic F127 comprises a hydrophobic core conjugated with hydrophilic segments at the two ends[68]. However, Pluronic F127 has weak mechanical properties specifically with rapid dissolution when in contact with aqueous media or biological fluid. Hence, it is essential to ensure that support material is structurally stable before secondary polymerization of GelMA without being dissolved. A layer of alginate hydrogel is formed between the build/support interface that acts as a barrier to slow the

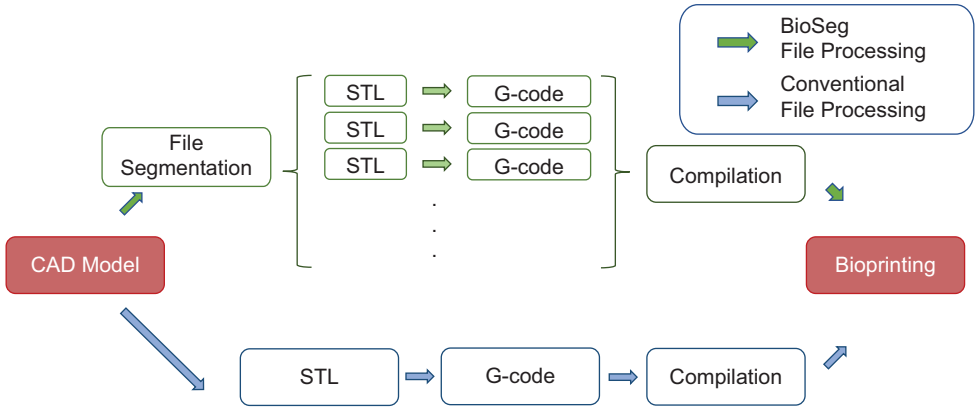

Figure 2. Process flow for file preparation for bioprinting, comparing between the two different file processing methods.

rate of dissolution, providing sufficient time before secondary cross-linking through ultraviolet (UV) cross-linking of GelMA.

4.1 Freestanding coil

The coil is designed with both materials interlacing each other, as shown in **Figure 3A**. The segments in red and gray regions correspond to the build and support material, respectively.

As the coil has materials overlapping each other at multipoints, the CAD model was sliced into different segments to be fabricated, **Figure 3B**. The prepared CAD file is then fabricated using both the conventional and new proposed file preparation methods. The fabricated coils are shown in **Figure 4**.

Comparing the two file processing methods, each file preparation method has its respective consideration factors, as shown in **Table 2.** As conventional file processing approach deposits different materials according to each z-layer, the printing process is significantly longer as compared to the printing files that have been segmented using BioSeg file processing. The BioSeg files minimize time required to interchange between different printheads. Such printing approach first completes the print of a single material until critical parameters such as material instability and height limitation of printhead are reached before switching to the alternative material. One distinct advantage of processing CAD models for bioprinting is to improve on the design freedom of printed construct. For instance, it has been found

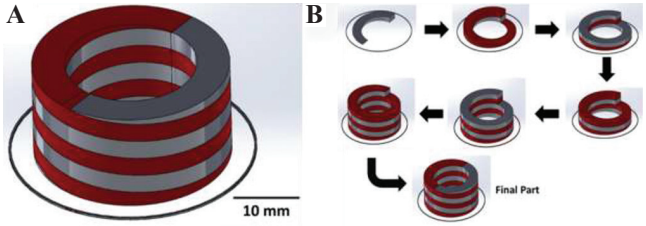

Figure 3. Freestanding coil computer-aided design (CAD) model (A) multimaterial (Red: Build material and gray: Support material) CAD model, (B) slicing of CAD files into segments.

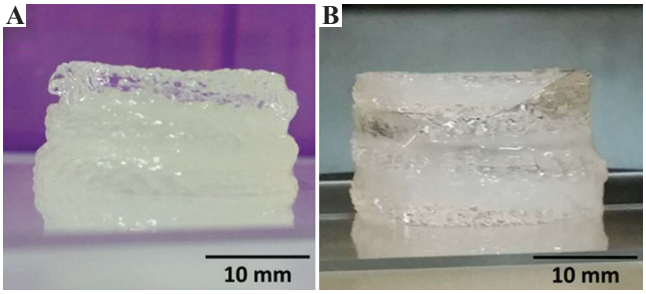

Figure 4. Coil fabricated using (A) conventional file processing, (B) BioSeg file processing.

that intrinsic staircase features are observed in filament deposition modeling[45]. These features arise from (i) the basic structure of a filament and (ii) processing of 3D CAD files using STL format. The use of STL format for 3D printing requires the deposition of material in a planar form, layer by layer. Using BioSeg method of printing, materials can be divided into smaller fragments and will not be restricted by the layer-by-layer printing of STL format.

Table 2. Consideration factors and comparison between the different file processing methods.

Intentional spacing	BioSeg file processing	Conventional file processing
Consideration factors	Bioprinter's compatibility issues Axis of movement Height of platform Distance between printed model and print head Material's compatibility issues Curing mechanism of build material Stability of material prior to curing Interaction between different materials	Material's compatibility issues Curing mechanism of build material Stability of material prior to curing Interaction between different materials
Advantages	Shorten printing duration Greater design of freedom in depositing build material	Straightforward process

4.2 Left ventricle

A model of the heart's left ventricle is fabricated to show the capability of proposed new method for realistic bioprinting applications. Based on the file segmentation criteria, the current model does not require fragmenting the CAD model into smaller part files. The 3D CAD images of the structure fabricated, together with the generated support structure, are shown in **Figure 5**.

The printed construct was cured under exposure of UV lamp before support material removal by washing with cold water. The curvature of the left ventricle printed was present even without the support structure, as shown in **Figure 5C**.

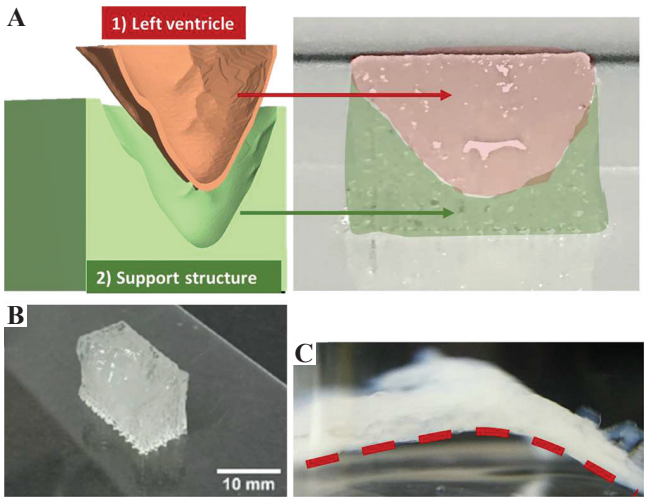

Figure 5. Three-dimensional image of the left ventricle (A) computer-aided design model with build (red) and support (green) materials corresponding with the respective red and green area of printed construct, (B) side profile of printed construct, (C) curvature of printed left ventricle preserved after support material removal (top view, curvature mapped with red dotted line).

5 Conclusion

Multimaterial deposition is of increasing interest in bioprinting for improving print fidelity in 3D bioprinting. Specifically, the use of build and support materials has been demonstrated in several researches to build engineered tissue constructs with structural stability. The study on support material generation and print path optimization is of great relevance for bioprinting as demonstrated across other additive manufacturing technologies.

Material selection is imperative in a build/support printing setup for building biological constructs with shape fidelity. Build materials have been chosen to facilitate cross-linking at different degrees. The first degree of cross-linking uses hydrogel with rapid gelation mechanism (sodium alginate and calcium chloride) to provide partial mechanical stability before fully cross-linking the printed construct through the formation of chemical bonds between polymer chains (gelatin methacrylate).

In this paper, we have also demonstrated a proof of concept to highlight the novelty in file segmentation for multimaterial deposition in bioprinting. This method can be used to fully utilize the tool changing capabilities of bioprinter to print multimaterials at a reduced print time. Considerations in terms of machine and materials

compatibility are needed when adopting such file segmentation method across different bioprinter setup. Fragmenting CAD models and printing 3D bioprinted models into small section invoke novel bioprinting approaches for structures that are more organic and closer to nature. Future studies may include cells in the build material printing to study cell responses with the improved BioSeg file processing method.

Acknowledgment

This research is supported by the National Research Foundation, Prime Minister's Office, Singapore under its Medium-Sized Centre funding scheme and by NTU startup grant.

Conflicts of interest

There are no conflicts of interest to declare.

References

1. Zhuang P, Sun AX, An J, *et al*., 2018, 3D Neural Tissue Models: From Spheroids to Bioprinting. *Biomaterials*, 154:113–133. DOI: 10.1016/j.biomaterials.2017.10.002.
2. Ng WL, Chua CK, Shen YF, 2019, Print Me An Organ! Why We Are Not There Yet. *Prog Polym Sci*, 97:101145. DOI: 10.1016/j.progpolymsci.2019.101145.
3. Kolan KCR, Semon JA, Bromet B, *et al*., 2019, Bioprinting with Human Stem Cells-Laden Alginate-gelatin Bioink and Bioactive Glass for Tissue Engineering. *Int J Bioprint*, 5:13. DOI: 10.18063/ijb.v5i2.2.204.
4. Xu T, Zhao W, Zhu JM, *et al*., 2013, Complex Heterogeneous Tissue Constructs Containing Multiple Cell Types Prepared by Inkjet Printing Technology. *Biomaterials*, 34:130–139. DOI: 10.1016/j.biomaterials.2012.09.035.
5. Guillemot F, Guillotin B, Fontaine A, *et al.*, 2011, Laser-assisted Bioprinting to Deal with Tissue Complexity in Regenerative Medicine. *MRS Bull*, 36:1015–1019. DOI: 10.1557/mrs.2011.272.
6. Lee YB, Polio S, Lee W, *et al.*, Bio-printing of Collagen and VEGF-Releasing Fibrin Gel Scaffolds for Neural Stem Cell Culture. *Exp Neurol*, 223:645–652. DOI: 10.1016/j.expneurol.2010.02.014.
7. Skardal A, Mack D, Kapetanovic E, *et al.*, 2012, Bioprinted Amniotic Fluid-derived Stem Cells Accelerate Healing of Large Skin Wounds. *Stem Cells Transl Med*, 1:792–802. DOI: 10.5966/sctm.2012-0088.
8. Ozbolat IT, Hospodiuk M, 2016, Current Advances and Future Perspectives in Extrusion-based Bioprinting. *Biomaterials*, 76:321–343. DOI: 10.1016/j.biomaterials.2015.10.076.
9. Lee H, Ahn S, Bonassar LJ, *et al*., 2013, Cell-laden Poly(varepsilon-Caprolactone)/Alginate Hybrid Scaffolds Fabricated by an Aerosol Cross-Linking Process for Obtaining Homogeneous Cell Distribution: Fabrication, Seeding Efficiency, and Cell Proliferation and Distribution. *Tissue Eng Part C Methods*, 19:784–793. DOI: 10.1089/ten.tec.2012.0651.
10. Billiet T, Gevaert E, De Schryver T, *et al*., 2014, The 3D Printing of Gelatin Methacrylamide Cell-laden Tissue-engineered Constructs with High Cell Viability. *Biomaterials*, 35:49–62. DOI: 10.1016/j.biomaterials.2013.09.078.
11. Duan B, Hockaday LA, Kang KH, *et al*., 2013, 3D Bioprinting of Heterogeneous Aortic Valve Conduits with Alginate/Gelatin Hydrogels. *J Biomed Mater Res A*, 101:1255–1264. DOI: 10.1002/jbm.a.34420.
12. Fedorovich NE, Wijnberg HM, Dhert WJ, *et al*., 2011, Distinct Tissue Formation by Heterogeneous Printing of Osteo and Endothelial Progenitor Cells. *Tissue Eng Part A*, 17:2113–2121. DOI: 10.1089/ten.tea.2011.0019.
13. Huang Y, He K, Wang X, 2013, Rapid Prototyping of a Hybrid Hierarchical Polyurethane-Cell/Hydrogel Construct for Regenerative Medicine. *Mater Sci Eng C Mater Biol Appl*, 33:3220–3229. DOI: 10.1016/j.msec.2013.03.048.
14. Ozbolat IT, Chen H, Yu Y, 2014, Development of "Multi-Arm Bioprinter" for Hybrid Biofabrication of Tissue Engineering Constructs. *Robot. Comput. Integr. Manuf*, 30:295–304. DOI: 10.1016/j.rcim.2013.10.005.
15. Shim JH, Lee JS, Kim JY, *et al*., 2012, Bioprinting of a Mechanically Enhanced Three-dimensional Dual Cell-Laden Construct for Osteochondral Tissue Engineering Using a Multi-Head Tissue/Organ Building System. *J Micromech Microeng*, 22:085014. DOI: 10.1088/0960-1317/22/8/085014.
16. Snyder JE, Hamid Q, Wang C, *et al*., 2011, Bioprinting Cell-laden Matrigel for Radioprotection Study of Liver by Pro-drug Conversion in a Dual-tissue Microfluidic Chip. *Biofabrication*, 3:034112. DOI: 10.1088/1758-5082/3/3/034112.
17. Visser J, Peters B, Burger TJ, *et al*., 2013, Biofabrication of Multi-material Anatomically Shaped Tissue Constructs. *Biofabrication*, 5:035007. DOI: 10.1088/1758-5082/5/3/035007.
18. Lee W, Lee V, Polio S, *et al*., 2009, Three-dimensional Cell-hydrogel Printer Using Electromechanical Microvalve for Tissue Engineering. In: Solid-State Sensors, Actuators and Microsystems Conference, 2009. TRANSDUCERS 2009,

pp. 2230-2233. DOI: 10.1109/sensor.2009.5285591.

19. Zhuang P, Ng WL, An J, *et al*., Layer-by-layer Ultraviolet Assisted Extrusion-based (UAE) Bioprinting of Hydrogel Constructs with High Aspect Ratio for Soft Tissue Engineering Applications. *PLoS One*, 14:e0216776. DOI: 10.1371/journal.pone.0216776.
20. Peppas NA, Hilt JZ, Khademhosseini A, *et al*., 2006, Hydrogels in Biology and Medicine: From Molecular Principles to Bionanotechnology. *Adv Mater*, 18:1345-1360. DOI: 10.1002/adma.200501612.
21. O'Brien FJ, 2011, Biomaterials and Scaffolds for Tissue Engineering. *Mater Today*, 14:88–95.
22. Place ES, Evans ND, Stevens MM, 2009, Complexity in Biomaterials for Tissue Engineering. *Nat Mater*, 8:457–470.
23. Hubbell JA, 1995, Biomaterials in Tissue Engineering. *Nat Biotech*, 13:565–576.
24. Malda J, Visser J, Melchels FP, *et al.*, 2013, 25th Anniversary Article: Engineering Hydrogels for Biofabrication. *Adv. Mater*, 25:5011–5028. DOI: 10.1002/adma.201302042.
25. Lee JM, Yeong WY, 2016, Design and Printing Strategies in 3D Bioprinting of Cell-Hydrogels: A Review. *Adv Healthc Mater*, 5:2856–2865. DOI: 10.1002/adhm.201600435.
26. Takagi D, Lin W, Matsumoto T, *et al.*, 2019, High-precision 3D Inkjet Technology for Live Cell Bioprinting. *Int J Bioprint*, 5:208. DOI: 10.18063/ijb.v5i2.208.
27. Tan HW, Tran T, Chua CK, 2016, A Review of Printed Passive Electronic Components Through Fully Additive Manufacturing Methods. *Virtual Phys Prototyp*, 11:271–288. DOI: 10.1080/17452759.2016.1217586.
28. Saengchairat N, Tran T, Chua CK, 2017, A Review: Additive Manufacturing for Active Electronic Components. *Virtual Phys Prototyp*, 12:31–46. DOI: 10.1080/17452759.2016.1253181.
29. Yap YL, Yeong WY, 2015, Shape Recovery Effect of 3D Printed Polymeric Honeycomb. *Virtual Phys Prototyp*, 10:91–99.
30. Francis V, Jain PK, 2016, Experimental Invesitgations on Fused Deposition Modelling of Polymer-layered Silicate Nanocomposite. *Virtual Phys Prototyp*, 11:109–121. DOI: 10.1080/17452759.2016.1172431.
31. Meisel N, Williams C, 2015, An Investigation of Key Design for Additive Manufacturing Constraints in Multimaterial Three-Dimensional Printing. *J Mech Des*, 137:111406. DOI: 10.1115/1.4030991.
32. Gan MX, Wong CH, 2016, Practical Support Structures for Selective Laser Melting. *J Mater Processing Technol*, 238:474–484. DOI: 10.1016/j.jmatprotec.2016.08.006.
33. Rodgers LM, 2012, Extrusion-based Additive Manufacturing Process with Part Annealing. Google Patents.
34. Barnett E, Gosselin C, 2015, Weak Support Material Techniques for Alternative Additive Manufacturing Materials. *Addit Manufac*, 8:95–104. DOI: 10.1016/j.addma.2015.06.002.
35. Yap CY, Chua CK, Dong ZL, *et al.*, 2015, Review of Selective Laser Melting: Materials and Applications. *Appl Phys Rev*, 2:041101.
36. Loh LE, Chua CK, Yeong WY, *et al.*, 2015, Numerical Investigation and an Effective Modelling on the Selective Laser Melting (SLM) Process with Aluminium Alloy 6061. *Int J Heart Mass Transfer*, 80:288–300. DOI: 10.1016/j.ijheatmasstransfer.2014.09.014.
37. Sun Z, Tan X, Tor SB, *et al*., 2018, Simultaneously Enhanced Strength and Ductility for 3D-printed Stainless steel 316L by Selective Laser Melting. *NPG Asia Mater*, 10:127–136. DOI: 10.1038/s41427-018-0018-5.
38. Li Y, Zhou K, Tan P, *et al*., 2018, Modeling Temperature and Residual Stress Fields in Selective Laser Melting. *Int J Mech Sci*, 136:24–35.
39. Tan X, Kok Y, Tan YJ, *et al.*, 2015, Graded Microstructure and Mechanical Properties of Additive Manufactured Ti–6Al–4V Via Electron Beam Melting. *Acta Mater*, 97:1–16. DOI: 10.1016/j.actamat.2015.06.036.
40. Yu WH, Sing SL, Chua CK, *et al*., 2019, Influence of Re-melting on Surface Roughness and Porosity of AlSi10Mg Parts Fabricated by Selective Laser Melting. *J Alloys Compd*, 792:574–581. DOI: 10.1016/j.jallcom.2019.04.017.
41. Yu WH, Sing SL, Chua CK, *et al*., 2019, Particle-Reinforced Metal Matrix Nanocomposites Fabricated by Selective Laser Melting: A State of the Art Review. *Prog Mater Sci*, 104:330–379. DOI: 10.1016/j.pmatsci.2019.04.006.
42. Kuo CN, Chua CK, Peng PC, *et al.*, 2020, Microstructure Evolution and Mechanical Property Response via 3D Printing Parameter Development of Al–Sc Alloy. *Virtual Phys Prototyp*, 15:120–129. DOI: 10.1080/17452759.2019.1698967.
43. Tey CF, Tan X, Sing SL, *et al*., Additive Manufacturing of Multiple Materials by Selective Laser Melting: Ti-alloy to Stainless Steel via a Cu-alloy Interlayer. *Addit. Manufact*, 31:100970. DOI: 10.1016/j.addma.2019.100970.
44. Tan JHK, Sing SL, Yeong WY, 2020, Microstructure Modelling for Metallic Additive Manufacturing: A Review. *Virtual Phys Prototyp*, 15:87–105. DOI: 10.1080/17452759.2019.1677345.
45. Lee JY, Tan WS, An J, *et al.*, 2016, The Potential to Enhance Membrane Module Design with 3D Printing Technology. *J Membr Sci*, 499:480–490.
46. Yuan S, Shen F, Chua CK, *et al*., 2019, Polymeric Composites for Powder-based Additive Manufacturing: Materials and

Applications. *Prog Polym Sci*, 91:141–168. DOI: 10.1016/j.progpolymsci.2018.11.001.

47. Lee JY, An J, Chua CK, 2017, Fundamentals and Applications of 3D Printing for Novel Materials. *Appl Mater Today*, 7:120–133.
48. Horváth L, Umehara Y, Jud C, *et al*., Engineering an *in vitro* air-blood barrier by 3D bioprinting. *Sci Rep*, 5:7974.
49. Merceron TK, Burt M, Seol YJ, *et al.*, 2015, A 3D Bioprinted Complex Structure for Engineering the Muscle-tendon Unit. *Biofabrication*, 7:035003. DOI: 10.1088/1758-5090/7/3/035003.
50. Miller JS, Stevens KR, Yang MT, *et al.*, 2012, Rapid Casting of Patterned Vascular Networks for Perfusable Engineered Three-dimensional Tissues. *Nat. Mater*, 11:768–774. DOI: 10.1038/nmat3357.
51. Wüst S, Godla ME, Müller R, *et al*., 2014, Tunable Hydrogel Composite with Two-step Processing in Combination with Innovative Hardware Upgrade for Cell-based Three-dimensional Bioprinting. *Acta Biomater*, 10:630–640. DOI: 10.1016/j.actbio.2013.10.016.
52. Skardal A, Zhang J, McCoard L, *et al*., 2010, Photocrosslinkable Hyaluronan-Gelatin Hydrogels for Two-Step Bioprinting. *Tissue Eng Part A*, 16:2675–2685. DOI: 10.1089/ten.tea.2009.0798.
53. Blaeser A, Campos DF, Puster U, *et al*., 2016, Controlling Shear Stress in 3D Bioprinting is a Key Factor to Balance Printing Resolution and Stem Cell Integrity. *Adv Healthc Mater*, 5:326–333. DOI: 10.1002/adhm.201500677.
54. Kolesky DB, Truby RL, Gladman AS, *et al*., 3D Bioprinting of Vascularized, Heterogeneous Cell-laden Tissue Constructs. *Adv Mater*., 26:3124–3130. DOI: 10.1002/adma.201305506.
55. Hinton TJ, Jallerat Q, Palchesko RN, *et al.*, 2015, Three-dimensional Printing of Complex Biological Structures by Freeform Reversible Embedding of Suspended Hydrogels. *Sci Adv*, 1:e1500758. DOI: 10.1126/sciadv.1500758.
56. Wu W, DeConinck A, Lewis JA, 2011, Omnidirectional Printing of 3D Microvascular Networks. *Adv Mater*, 23:H178.
57. An J, Teoh JE, Suntornnond R, *et al*., 2015, Design and 3D Printing of Scaffolds and Tissues. *Engineering*, 1:261–268.
58. Liu F, Mishbak H, Bartolo PJ, 2019, Hybrid Polycaprolactone/Hydrogel Scaffold Fabrication and in-process Plasma Treatment Using PABS. 5:1–9.
59. Schuurman W, Khristov V, Pot MW, *et al*., 2011, Bioprinting of Hybrid Tissue Constructs with Tailorable Mechanical Properties. *Biofabrication*, 3:021001. DOI: 10.1088/1758-5082/3/2/021001.
60. Shim JH, Kim JY, Park M, *et al*., 2011, Development of a Hybrid Scaffold with Synthetic Biomaterials and Hydrogel Using Solid Freeform Fabrication Technology. *Biofabrication*, 3:034102. DOI: 10.1088/1758-5082/3/3/034102.
61. Pati F, Jang J, Ha DH, *et al.*, 2014, Printing Three-dimensional Tissue Analogues with Decellularized Extracellular Matrix Bioink. Nat Commun, 5:3935. DOI: 10.1038/ncomms4935.
62. Kang HW, Lee SJ, Ko IK, *et al*., 2016, A 3D Bioprinting System to Produce Human-scale Tissue Constructs with Structural Integrity. *Nat. Biotechnol*, 34:312–319. DOI: 10.1038/nbt.3413.
63. Skylar-Scott MA, Uzel SG, Nam LL, *et al.*, 2019, Biomanufacturing of Organ-specific Tissues with High Cellular Density and Embedded Vascular Channels. *Sci Adv*, 5:eaaw2459. DOI: 10.1126/sciadv.aaw2459.
64. Lee A, Hudson AR, Shiwarski DJ, *et al.*, 2019, 3D Bioprinting of Collagen to Rebuild Components of the Human Heart. *Science*, 365:482–487. DOI: 10.1126/science.aav9051.
65. Luo G, Yu Y, Yuan Y, *et al*., 2019, Freeform, Reconfigurable Embedded Printing of All-aqueous 3D Architectures. *Adv Mater*, 31:1904631. DOI: 10.1002/adma.201904631.
66. Mirzendehdel AM, Suresh K, 2016, Support Structure Constrained Topology Optimization for Additive Manufacturing. *Comput. Aided Des*, 81:1–13. DOI: 10.1016/j.cad.2016.08.006.
67. Nichol JW, Koshy ST, Bae H, *et al*., 2010, Cell-laden Microengineered Gelatin Methacrylate Hydrogels. *Biomaterials*, 31:5536–5544. DOI: 10.1016/j.biomaterials.2010.03.064.
68. Akash MS, Rehman K, 2015, Recent Progress in Biomedical Applications of Pluronic (PF127): Pharmaceutical Perspectives. *J Control Release*, 209:120–138. DOI: 10.1016/j.jconrel.2015.04.032.

RESEARCH ARTICLE

Hydrolytic Expansion Induces Corrosion Propagation for Increased Fe Biodegradation

Cijun Shuai[1,2,3], Sheng Li[1], Shuping Peng[4], Youwen Yang[2], Chengde Gao[1]*

[1]State Key Laboratory of High-Performance Complex Manufacturing, College of Mechanical and Electrical Engineering, Central South University, Changsha 410083, China

[2]Institute of Bioadditive Manufacturing, Jiangxi University of Science and Technology, Nanchang 330013, China

[3]Shenzhen Institute of Information Technology, Shenzhen 518172, China

[4]The Key Laboratory of Carcinogenesis of the Chinese Ministry of Health, Xiangya Hospital, Central South University, Changsha, 410008, China

Abstract: Fe is regarded as a promising bone implant material due to inherent degradability and high mechanical strength, but its degradation rate is too slow to match the healing rate of bone. In this work, hydrolytic expansion was cleverly exploited to accelerate Fe degradation. Concretely, hydrolyzable Mg_2Si was incorporated into Fe matrix through selective laser melting and readily hydrolyzed in a physiological environment, thereby exposing more surface area of Fe matrix to the solution. Moreover, the gaseous hydrolytic products of Mg_2Si acted as an expanding agent and cracked the dense degradation product layers of Fe matrix, which offered rapid access for solution invasion and corrosion propagation toward the interior of Fe matrix. This resulted in the breakdown of protective degradation product layers and even the direct peeling off of Fe matrix. Consequently, the degradation rate for Fe/Mg_2Si composites (0.33 mm/y) was significantly improved in comparison with that of Fe (0.12 mm/y). Meanwhile, Fe/Mg_2Si composites were found to enable the growth and proliferation of MG-63 cells, showing good cytocompatibility. This study indicated that hydrolytic expansion may be an effective strategy to accelerate the degradation of Fe-based implants.

Keywords: Hydrolytic expansion, Biodegradation, Fe-based implants, Selective laser melting, Cytocompatibility

***Corresponding Author:** Chengde Gao, State Key Laboratory of High-Performance Complex Manufacturing, College of Mechanical and Electrical Engineering, Central South University, Changsha 410083, China; gaochengde@csu.edu.cn.

Received: November 12, 2019; ***Accepted:*** January 2, 2020; ***Published Online:*** January 23, 2020

Citation: Shuai C, Li S, Peng S, *et al*., 2020, Hydrolytic expansion induces corrosion propagation for increased Fe biodegradation. *Int J Bioprint*, 6(1):248. DOI: 10.18063/ijb.v6i1.248

1 Introduction

Due to natural degradability, favorable mechanical properties, and acceptable biocompatibility, biodegradable metals have been extensively highlighted for fabricating bone implants over the past years[1-3]. Iron (Fe), which can corrode in the physiological environment, is considered as a typical biodegradable metal. Fe is especially attractive in load-bearing applications due to its high mechanical strength. The applications of Fe as bone implants have been validated by animal experiments and no acute inflammatory reaction, systemic, or local toxicity were reported, indicating good biocompatibility[4-7]. However, Fe still stays intact *in vivo* even after 6 months, which indicates that a fast corrosion rate is urgently demanded[8].

To increase the corrosion rate of Fe, lots of researches, for example, alloying, surface treatment, and new fabrication process have been carried out[9]. Hermawan *et al*. added manganese (Mn) into Fe to reduce the corrosion potentials of Fe, thereby increasing the corrosion rates[10]. Subsequently,

Schinhammer *et al*. introduced palladium (Pd) into Fe−Mn alloy and found that Pd accelerated Fe degradation through micro-galvanic corrosion[11]. Zhou *et al*. prepared silicon carbide (SiC) thin films on the Fe surface through sandblasting treatment[12]. They found that surface morphology, surface composition, and surface area of Fe were changed, causing higher weight loss. Moravej *et al*. fabricated Fe implants by electroforming and evaluated the degradation behavior *in vitro*[13]. This process increased structural defects of Fe, which was responsible for the fast corrosion. These Fe-based implants exhibit a faster degradation rate than Fe in the physiological environment. However, as the degradation proceeds, corrosion products will gradually accumulate on the substrate, forming dense protective layers due to their low solubility. This inevitably impedes or even insulates the contact between the solution and the matrix, resulting in a slow degradation at the later stage of degradation[12].

Magnesium silicide (Mg_2Si) is a common biomaterial with favorable biocompatibility, and both of silicon (Si) and magnesium (Mg) are essential elements in the human body, as reported by Jiang *et al*.[14] Due to the high chemical activity, Mg_2Si can rapidly react with H_2O, releasing expansive gases[15]. This prompts us to contemplate that if Mg_2Si is introduced into the Fe matrix, the rapid hydrolysis of Mg_2Si will expose more area of Fe matrix to the physiological environment. More importantly, the escaped gases resulted from Mg_2Si hydrolysis may penetrate the dense degradation product layers, which is expected to solve the above-mentioned problem induced by dense degradation product layers, thereby endowing the Fe-based implant a rapid degradation throughout the degradation process.

In this work, hydrolyzable Mg_2Si was cleverly exploited to accelerate Fe degradation. Fe/Mg_2Si composites were prepared through selective laser melting process, which was also known as one kind of three-dimensional (3D) printing techniques[16,17]. Moving laser can irradiate powder bed with a rapid solidification rate compared with traditional method[18,19], which was beneficial for ensuring the relative phase stability of samples, which may be due to the rapid melting and solidification process (with a cooling rate of $10^3 – 10^6$°C/s), as pointed out by Yu *et al*.[20] Moreover, Dadbakhsh *et al*. stated that selective laser melting possessed an exceptional flexibility to manufacture composites with a uniform dispersion of secondary phase due to laser-based and layer-by-layer natures, simultaneous powder metallurgy[21-23]. Besides, selective laser melting is well known for the capability of directly preparing 3D parts with precise shape[24-29]. This paper aimed to present a systematic study that investigated the degradability of selective laser melting derived Fe/Mg_2Si composites based on their composition variation. The microstructure and mechanical properties of the composites were investigated for bone implant applications. In addition, cytocompatibility was also systematically evaluated. This study covered processes of 3D printing technologies, property evaluations of printed implants, interactions of MG-63 cells, the composites, etc.

2 Materials and methods

2.1 Materials

Fe powder with a purity of 99.9% was purchased from Wuxi Sairui metal powder manufacturing Co., Ltd. (Jiangsu, China). The powder particle size was characterized by laser particle analyzer (Malvern 3000, UK). Mg_2Si powder was obtained from Shanghai Xianxin New Material Technology Co., Ltd. The Mg_2Si powder was milled to get a small particle size at a speed of 200 rpm for 3 h in a planetary ball mill, and the stainless steel ball to powder ratio was 1:1. Subsequently, Mg_2Si powder with different mass ratio (0, 0.3, 0.6, 0.9, and 1.2 wt.%) was mixed with Fe powder using mechanical stirring followed by milling at a speed of 200 rpm for 60 min after optimization of the main parameters of mixing time and rotation rate. These mixing parameters were beneficial for relatively better powder mixing performance[30,31].

2.2 Sample preparation

Fe/Mg_2Si composites were prepared by a selective laser melting system, which was composed of a laser melting platform, control system, and lifting

platform[32,33]. The specific laser melting procedure was as follows: (1) Fe/Mg_2Si powders were put on the laser melting platform; (2) Fe/Mg_2Si powders was selectively melted by laser beam; (3) after laser melting, a descending height was achieved through the lifting platform; (4) the steps of (1) – (3) were continually repeated until the Fe/Mg_2Si composites were completely prepared; and (5) an air compressor was used for scrubbing samples and removing residual powder. In this study, the laser scan rate of 24 mm/s, layer thickness of 100 μm, and laser power of 90 W were used as the melting parameters for good formality during experiments.

2.3 Microstructural characterization

Fe/Mg_2Si composites were mechanically polished, thereafter ultrasonically cleaned in ethanol. After etching in 4% HNO_3 alcohol solution for 40 s, the metallographic microstructure of Fe/Mg_2Si composites was observed using an Olympus optical microscope (PMG-3, Japan). The surface morphology was characterized by a XL-30FEG scanning electron microscopy (SEM, Philips, the Netherlands), and the elemental compositions were determined by energy-dispersive X-ray spectroscopy (EDS). The phase analysis of Fe/Mg_2Si composites was performed by a Siemens X-ray diffractometer (XRD, D5000, Germany) with a scanning speed of 8/min from 20° to 90° of scattering angles.

2.4 Mechanical tests

The mechanical properties of Fe/Mg_2Si composites were determined by compression, bending, and hardness tests. The compression tests were performed on a Zhongluchang Universal Tester (Model WDW-10H, China) at a strain rate of 0.05 mm/s according to the ASTM E9-09 standard[34]. The prepared Fe/Mg_2Si samples were circular cylinder with a diameter of 8 mm and a height of 12 mm. As all the samples were ductile, compression strength was determined by the stress at a strain of 30%[34]. Three-point bending tests were performed at a speed of 0.05 mm/s on the Zhongluchang Universal Tester (Model WDW-10H, China). The span of the bending tests was 12 mm between the two supporting points. Hardness tests were carried out using micro-indentation tester (Shanghai Taiming Optical Instrument Co. Ltd., China) with a dwell time of 10 s. For each group, at least four measurements were carried out to acquire accurate average values.

2.5 Electrochemical tests

The electrochemical behaviors of Fe/Mg_2Si composites were tested by an IM6 electrochemical workstation (Zahner, Germany) in simulated body fluid (SBF) at 37°C. The SBF with a pH of 7.4 contained 8.035 $g \cdot L^{-1}$ NaCl, 0.225 $g \cdot L^{-1}$ KCl, 0.311 $g \cdot L^{-1}$ $MgCl_2 \cdot 6H_2O$, 0.231 $g \cdot L^{-1}$ $K_2HPO_4 \cdot 3H_2O$, 6.118 $g \cdot L^{-1}$ $(CH_2OH)_3CNH_2$, 0.355 $g \cdot L^{-1}$ $NaHCO_3$, 0.292 $g \cdot L^{-1}$ $CaCl_2$, and 0.072 $g \cdot L^{-1}$ Na_2SO_4[2,35]. The typical three-electrode cell, containing the saturated calomel electrode (SCE, reference electrode), the sample (working electrode), and the platinum electrode (auxiliary electrode), was used to perform electrochemical tests. The potentiodynamic polarization curves of samples were obtained at a rate of 0.25 mV/s (−1200 – 100 mV) in SBF. The corrosion current density (I_{corr}) of samples was calculated by tafel extrapolation of the anodic and cathodic part of the polarization curves. Afterward, the I_{corr} was converted into the electrochemical corrosion rates based on the ASTM G59 standard[36,37]. The surface morphologies of the samples were examined using a Wyko NT9100 optical profiler (VEECO, USA) and the surface roughness value (*Ra*) was simultaneously acquired by the average standard deviation of height values.

2.6 Immersion tests

The immersion tests of Fe/Mg_2Si composites were performed to study the degradation behavior, including corrosion rates, corrosion morphologies, and surface composition. The immersion tests were carried out in SBF[38]. According to the ASTM-G31-72, Fe/Mg_2Si samples with an exposed surface (cm^2) to SBF (ml) ratio of 1:15 were separately immersed at 37°C[3,39]. After immersion for 21 days, the samples were first rinsed with deionized water and ethanol, and then dried in hot air. The cross-sectional morphologies were observed using SEM.

Meanwhile, the composition analysis of corrosion products was performed by EDS. The degradation rates of samples were calculated according to the methods in the literature[35].

2.7 Cytocompatibility tests

Human osteosarcoma cell line (MG-63) from the American Type Culture Collection was adopted to evaluate the cytocompatibility of samples according to the indirect contact method[4,40]. The MG-63 cells were first cultured in Dulbecco's Modified Eagle's Medium (DMEM) with 100 U/ml penicillin, 100 mg/ml streptomycin, and 10% fetal bovine serum at 37°C under a humidified atmosphere of 5% CO_2. The Fe/Mg_2Si samples were immersed in DMEM for 3 days with a surface area/solution ratio of 1.25 (cm^2/ml) at 37°C according to the ISO 10993-12[1]. Subsequently, the supernatant fluid was withdrawn and centrifuged for preparing the extract. For fluorescence staining assay, MG-63 cells were incubated in the extracts of different concentrations (25, 50, and 100%) with DMEM as the control group (extract concentration of 0%) for 1, 2, and 3 days, respectively. The MG-63 cells were subsequently stained by ethidium homodimer-1 reagents and calcein-AM for 18 min, and finally rinsed twice using phosphate-buffered solution. To observe the living cells, the cells were fixed on glasses and checked using a BX60 Fluorescence Microscope (Olympus, Japan). The number of living cells was estimated by ImageJ software according to the fluorescent images. To evaluate the viability of MG-63 cells in the extracts of different concentrations (0, 25, 50, and 100%), CCK-8 tests were performed for 1, 2, and 3 days, respectively. After culture for the scheduled time, 10 μL CCK-8 solutions (5 mg/ml) were added to the cell culture medium. Then, the absorbance was gained by a microplate reader (BioRad, USA) at 450 nm. Cell viability was calculated since it was positively correlated with the absorbance[41].

2.8 Statistical analysis

Experimental data were presented as mean ± standard deviation. Symbol "*" indicates a significant difference ($P < 0.05$).

3 Results and discussion

3.1 Powder characterization and sample preparation

The used powders in this study are depicted in **Figure 1A-F**. SEM images in **Figure 1A,B** indicated that both Fe and Mg_2Si powders had an irregular shape and the latter exhibited smaller particle sizes than the former. The particle size distribution of Fe powder was further measured by a laser particle analyzer. It is shown in **Figure 1A** that the particle size of Fe powder was mainly between 12 and 30 μm and the average value was 27.1 ± 0.5 μm. Meanwhile, fine Mg_2Si particles were evenly distributed in Fe powder in **Figure 1C**, which enabled Mg_2Si to fully exert its roles in the composite. Besides, XRD patterns in **Figure 1E** showed that the only detectable phase was α-Fe with BCC structure and the (110) crystal plane had the highest intensity due to the preferred crystalline orientation. For Mg_2Si powder, the Mg_2Si phase was identified by main diffraction peaks at 24.2°, 40.1°, and 47.3° corresponding to (111), (220), and (311) diffraction planes, respectively, as illustrated in **Figure 1E**. EDS analysis in **Figure 1F** showed that Fe and Mg_2Si powders were composed of Fe and Mg, Si elements, respectively, which indicated higher purity of the powders. The mixed powders of Fe and Mg_2Si were scanned by laser according to the computer-aided design model to prepare composites, as illustrated in **Figure 1G**. It could be found that the prepared composites have uniformly distributed porous structures with a diameter of 0.8 mm. The porous structures of composites would not only accelerate Fe degradation through the increase of surface area in contact with SBF but also promote nutrient transport through the interconnected architecture.

3.2 Microstructure

The microstructural features of Fe/Mg_2Si composites are presented in **Figure 2**. It is shown in **Figure 2A,E** that the Fe/0.3Mg_2Si had a compact microstructure without original powder particles. Meanwhile, a small amount of Mg_2Si could be discernible, as evidenced by EDS

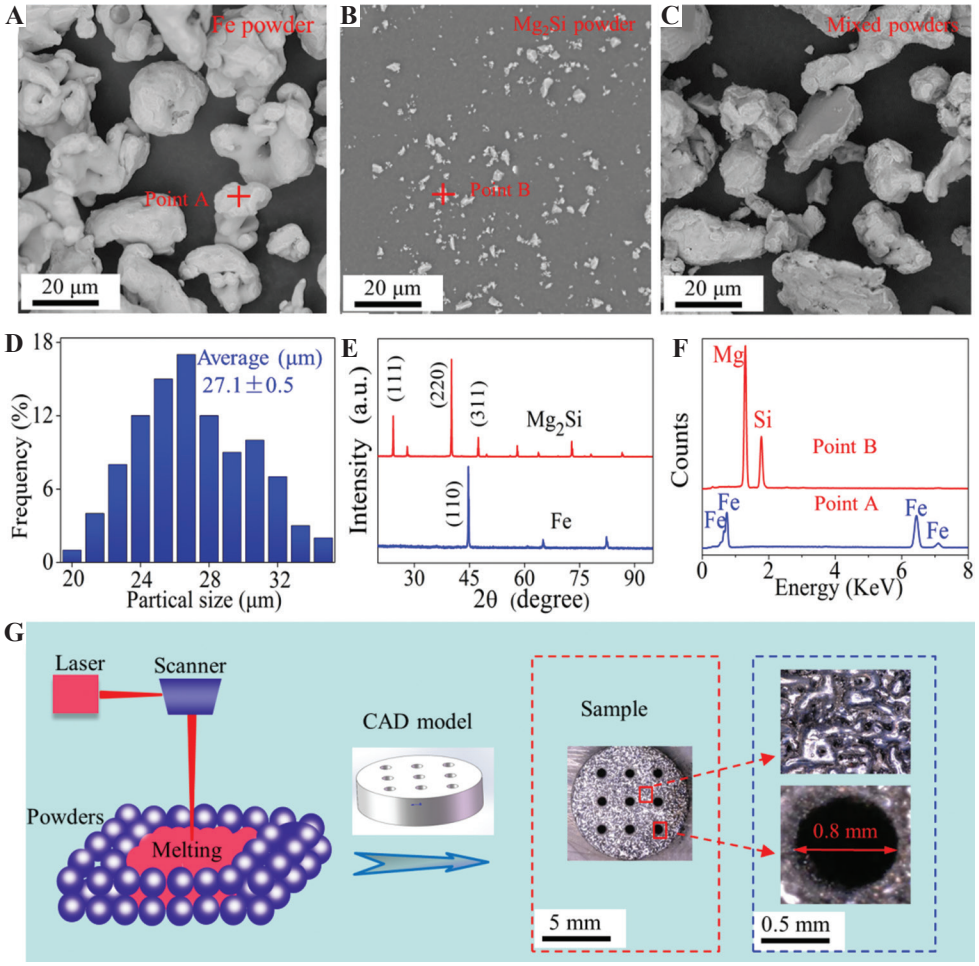

Figure 1. (A-C) The morphologies, (D) particle size distribution, (E) XRD patterns, and (F) EDS analysis of Fe and/or Mg_2Si powders. (G) Schematic illustration of the laser melting process for sample preparation. The prepared composites had a uniformly distributed porous structure (the pore diameter of 0.8 mm).

analysis in **Figure 2I**. Fe/0.6Mg_2Si in **Figure 2B,F** exhibited similar microstructural features with Fe/0.3Mg_2Si except for a slightly higher Mg_2Si content. Fe/0.9Mg_2Si in **Figure 2C,G** showed two distinct phases in the microstructure, in which the black phase was Mg_2Si and the grey phase was Fe matrix. Moreover, Fe/0.9Mg_2Si also showed the uniformly distributed Mg_2Si within the matrix. Therefore, it was reasonably expected that the Fe/Mg_2Si composite would possess uniform bulk property. However, when the additional content of Mg_2Si was 1.2 wt.%, micropores were found, as exhibited in **Figure 2D,H**. The micropores may be caused by interconnected Mg_2Si by EDS analysis **Figure 2J,K** as a result of the inhomogeneous distribution. The interconnected Mg_2Si tended to merge and form large clusters, which hindered the bonding of liquid Fe, leading to micropores. Micropores as microstructure defects may become stress concentration points, resulting in deteriorated mechanical properties and local corrosion, especially in the corrosive physiological environment containing chloride ion. This was similar to other studies on the microstructural features of Fe/ceramic composites[34].

The water contact angles of Fe/Mg_2Si composites as well as Fe are shown in **Figure 3a**. The sequence of water contact angle from low to high was: Fe/1.2Mg_2Si (60.11 ± 2.1°) < Fe/0.9Mg_2Si (61.08 ± 1.8°) < Fe/0.6Mg_2Si (62.95 ± 2.2°) < Fe/0.3Mg_2Si (65.24 ± 2.5°) < Fe (68.74 ± 3.1°). Usually, the smaller the

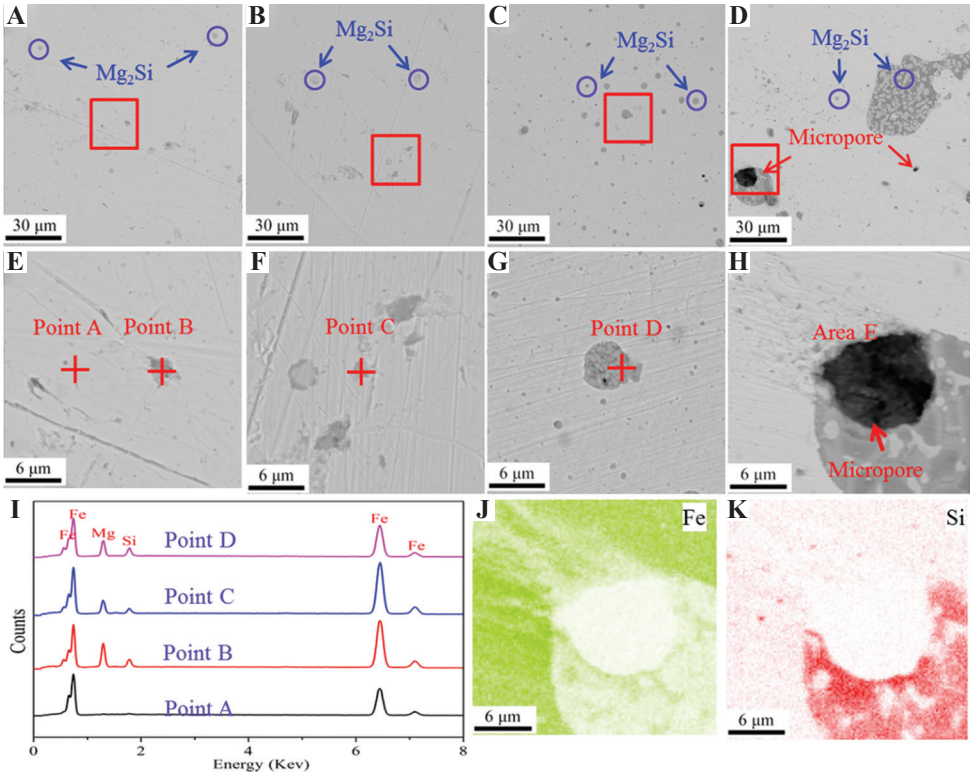

Figure 2. Low- and high-magnification SEM images of (A,E) Fe/0.3Mg_2Si, (B,F) Fe/0.6Mg_2Si, (C,G) Fe/0.9Mg_2Si, and (D,H) Fe/1.2 Mg_2Si composites and corresponding EDS analysis of (I) point A-D and (J,K) area E.

contact angle is, the better the hydrophilicity will be. This indicated that Fe/Mg_2Si had stronger hydrophilicity than Fe. It is considered that high hydrophilicity is of significance for bone implants, which contributes to corrosion attack in the physiological environment[38].

The XRD patterns of Fe/Mg_2Si composites are given in **Figure 3B**. It could be found from the figure that the detectable phase was α-Fe for all the Fe/Mg_2Si composites, which was similar to that of Fe powder in **Figure 1E**. Moreover, there were no obvious changes in the peak positions and relative intensities. The Mg_2Si peaks could not be found for all the samples, which attributed to the low contents. The metallographic micrographs of Fe/Mg_2Si composites are presented in **Figure 3C**. It was seen that Fe/0.3Mg_2Si exhibited flexuous grain boundaries with grain sizes ranging from 5 to 45 μm (average grain size of 29.8 ± 2.1 μm). The Fe/0.6Mg_2Si consisted of grain sizes ranging from 5 to 35 μm and its average grain size was 23.7 ± 1.5 μm. The grains of Fe/0.9Mg_2Si were obviously refined with an average grain size of 18.6 ± 1.2 μm. The grains of Fe/1.2Mg_2Si also exhibited a smaller size (average grain size of 21.1 ± 1.8 μm) in comparison with Fe/0.3Mg_2Si. However, the micropores on surfaces of Fe/1.2Mg_2Si were discernible due to the relatively large amounts of Mg_2Si.

3.3 Mechanical properties

Functionally speaking, the compression strength of bone implants was thought to be an important indicator since bones need to be strong enough to survive normal activities[42]. In this study, the compression strength of Fe/Mg_2Si composites is depicted in **Figure 4A**. It could be found that the compression strength gradually decreased (230 ± 15, 202 ± 20, 172 ± 12, 130 ± 10, and 88 ± 6 MPa for Fe, Fe/0.3Mg_2Si, Fe/0.6Mg_2Si, Fe/0.9Mg_2Si, and Fe/1.2Mg_2Si, respectively). The decreased compression strength could be attributed to the distributions and amounts of Mg_2Si, which may cause defects in the microstructure, as evidenced

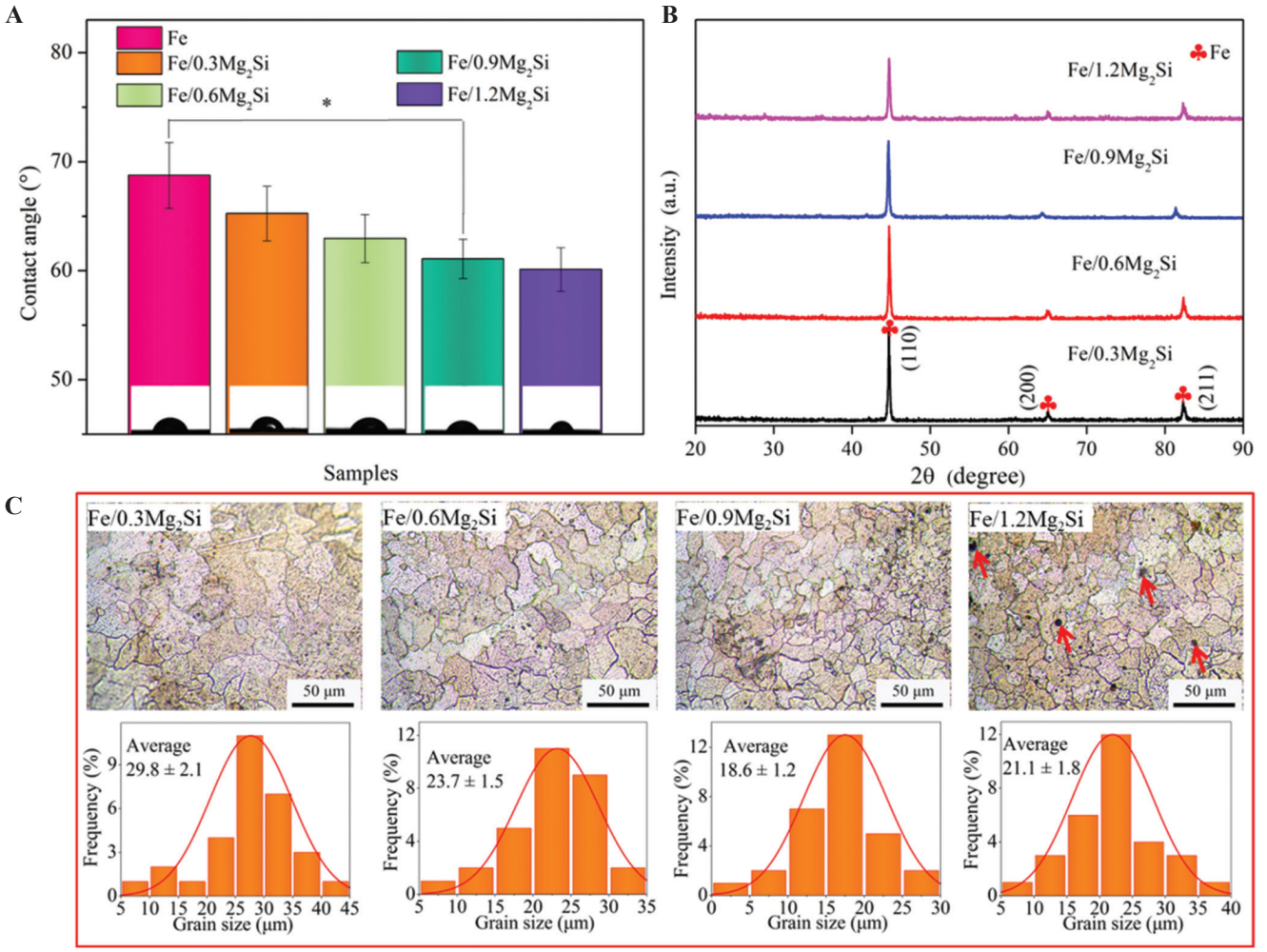

Figure 3. (A) Water contact angles, (B) XRD patterns, and (C) metallographic micrographs with corresponding grain size distributions of Fe/Mg_2Si composites. The micropores in the Fe/Mg_2Si composites were marked by red arrows.

in **Figure 2**. This phenomenon was similar to the previous study on the effects of hydroxyapatite on the compression strength of Fe-hydroxyapatite composite[43]. It was worth noting that the compression strength of human compact bone was between 90 and 170 MPa[44], which implied that the Fe/Mg_2Si composites still could provide adequate mechanical support for load-bearing applications. The modulus of fabricated Fe/Mg_2Si composites with the increasing Mg_2Si contents is shown in **Figure 4B**. It could be found from **Figure 4B** that the modulus gradually decreased with the increase in Mg_2Si. This phenomenon may be related to the increasing amount and dispersion patterns of the additive. Increasing Mg_2Si tended to form agglomerates and voids in the microstructure. Besides, the reduced modulus was also closely related to porous structures fabricated by selective laser melting. The modulus in this study could greatly alleviate biomechanical mismatch during the new bone remodeling process, thereby eliminating the problem of stress shielding between bone and implants. In addition, it is shown in **Figure 4C** that the sequence of bending strength from high to low was: Fe > Fe/0.3Mg_2Si > Fe/0.6Mg_2Si > Fe/0.9Mg_2Si > Fe/1.2Mg_2Si composite, which was consistent with the sequence of the compression strength.

In addition, the measured hardness by micro-indentation tester is exhibited in **Figure 4D**. It could be found that the hardness of Fe/0.9Mg_2Si sample (145 ± 9 HV) was higher than other

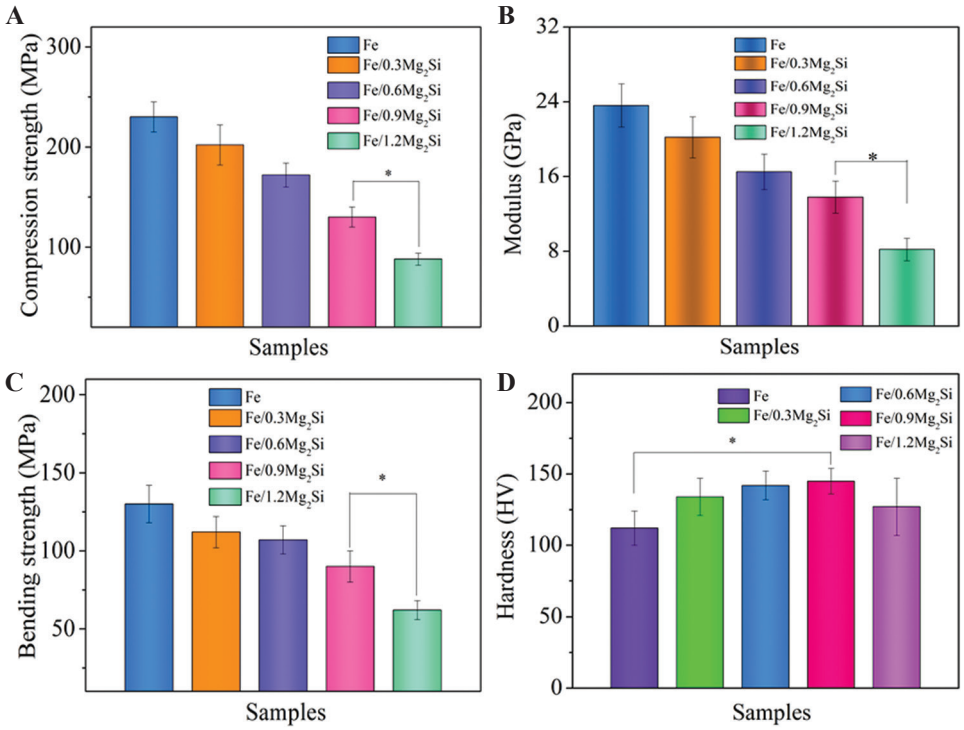

Figure 4. (A) Compression strength, (B) elastic modulus, (C) bending strength, and (D) hardness of Fe/Mg_2Si composites with Fe as a control group. *$P < 0.05$.

samples (112 ± 12, 134 ± 13, 142 ± 10, and 127 ± 20 HV for Fe, Fe/0.3Mg_2Si, Fe/0.6Mg_2Si, and Fe/1.2Mg_2Si, respectively). It was also worthy to note that a decrease in hardness was observed in Fe/1.2Mg_2Si. Both too high amount and uneven distribution of Mg_2Si would merge and hinder the liquid Fe phase bonding, leading to the formation of micropores, thereby reducing the hardness of Fe/1.2Mg_2Si composite. This was also evidenced by the large standard deviation in **Figure 4D**.

3.4 Electrochemical behaviors

Potentiodynamic polarization curves were useful tools to measure the instantaneous corrosion of samples. The polarization curves of Fe/0.3Mg_2Si, Fe/0.6Mg_2Si, Fe/0.9Mg_2Si, and Fe/1.2Mg_2Si composites with Fe as a control group are shown in **Figure 5A** and I_{corr} was determined from abscissa of intersection from tafel extrapolation. I_{corr} for Fe, Fe/0.3Mg_2Si, Fe/0.6Mg_2Si, Fe/0.9Mg_2Si, and Fe/1.2Mg_2Si was 12.58 ± 3.5, 19.95 ± 4.2, 27.54 ± 4.7, 39.81 ± 4.6, and 50.11 ± 4.9 μA/cm^2, respectively. The increase in I_{corr} indicated aggravated corrosion of composites with the addition of Mg_2Si. Meanwhile, a higher I_{corr} corresponded to worse corrosion resistance and a higher electrochemical corrosion rate. According to **Figure 5B**, the average electrochemical corrosion rates of Fe, Fe/0.3Mg_2Si, Fe/0.6Mg_2Si, Fe/0.9Mg_2Si, and Fe/1.2Mg_2Si were determined as 0.15, 0.24, 0.33, 0.48, and 0.61 mm/y, respectively, indicating that the addition of Mg_2Si accelerated Fe corrosion. The extent of metal corrosion on the surface after potentiodynamic polarization tests could be characterized by corrosion morphology. The stronger the corrosion was, the more severe the surface damage was. The surface profiles of Fe/0.3Mg_2Si, Fe/0.6Mg_2Si, Fe/0.9Mg_2Si, and Fe/1.2Mg_2Si with Fe as a control group were observed by an optical profiler and depicted in **Figure 5C-G**, in which red meant surface with large height and blue meant deep depression caused by corrosion. Besides, the calculated surface roughness value (*Ra*) is shown in **Figure 5H**. It could be found that there were obvious differences between the surface profiles of Fe/Mg_2Si and Fe. Fe remained relatively intact and most surfaces

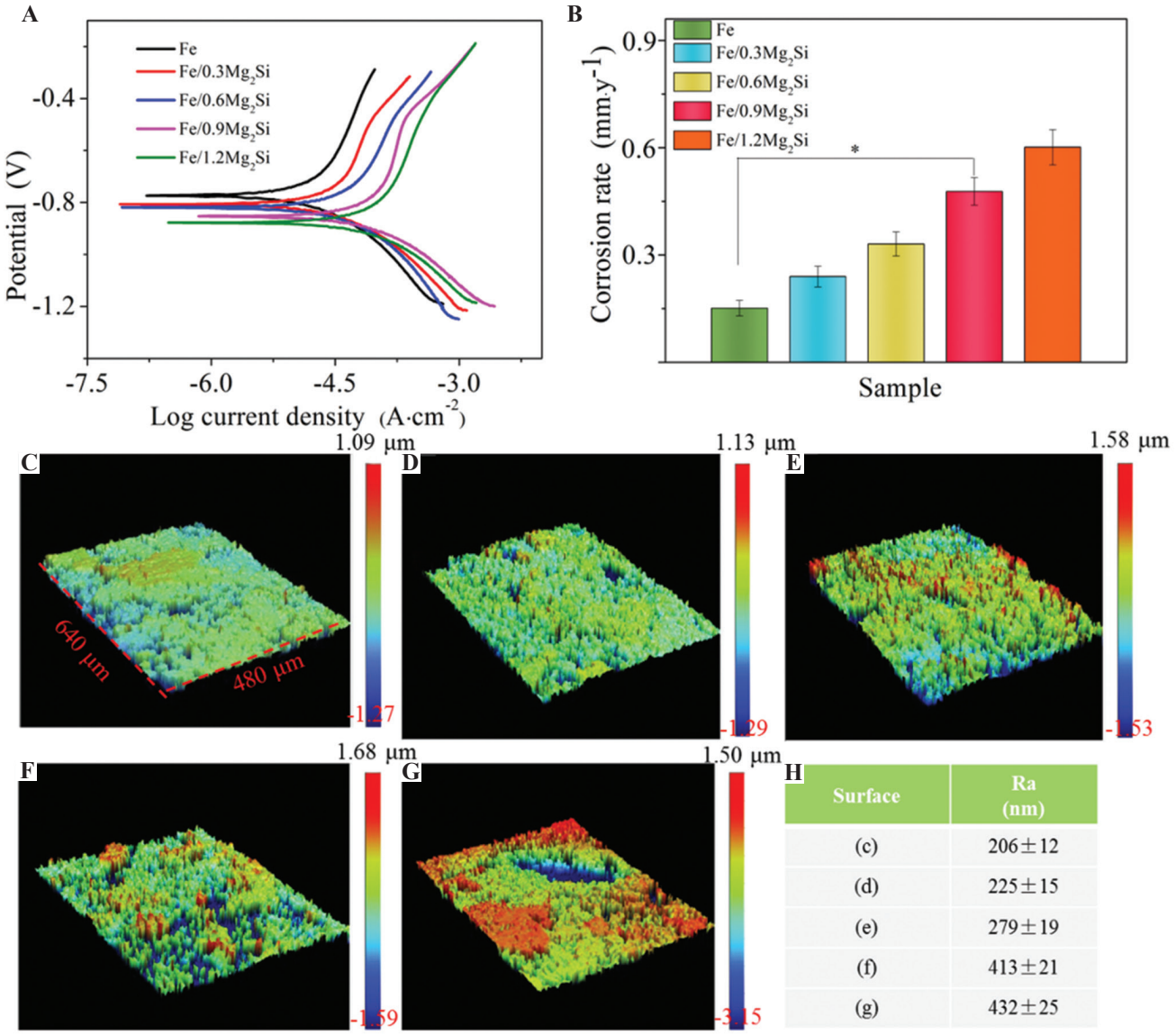

Figure 5. (A) Potentiodynamic polarization curves of Fe/Mg_2Si composites with Fe as a control group and (B) the corresponding electrochemical corrosion rates determined from tafel extrapolation. The representative surface profiles of (C) Fe, (D) Fe/0.3Mg_2Si, (E) Fe/0.6Mg_2Si, (F) Fe/0.9Mg_2Si, (G) Fe/1.2Mg_2Si, and (H) average surface roughness (*Ra*).

were even and smooth after polarization tests. Fe/0.3Mg_2Si presented a relatively smooth surface with a *Ra* value of 225 ± 15 nm. Enhanced corrosion of Fe/0.6Mg_2Si brought about an increase in *Ra* value of 279 ± 19 nm. Fe/0.9Mg_2Si revealed relatively rough surface morphologies with a high *Ra* value of 413 ± 21 nm. Fe/1.2Mg_2Si was characterized by inhomogeneous corrosion with a *Ra* value of 432 ± 25 nm and corrosion holes.

3.5 Immersion tests

The corrosion morphologies of Fe/Mg_2Si and Fe surface after immersion tests for 21 days in SBF at 37°C are depicted in **Figure 6**. The surface of Fe was corroded and a few corrosion products were present on its surface, as shown in **Figure 6A**. Fe/0.3Mg_2Si and Fe/0.6Mg_2Si in **Figure 6B,C** suffered relatively severe corrosion in comparison with that of Fe. Fe/0.9Mg_2Si and Fe/1.2Mg_2Si

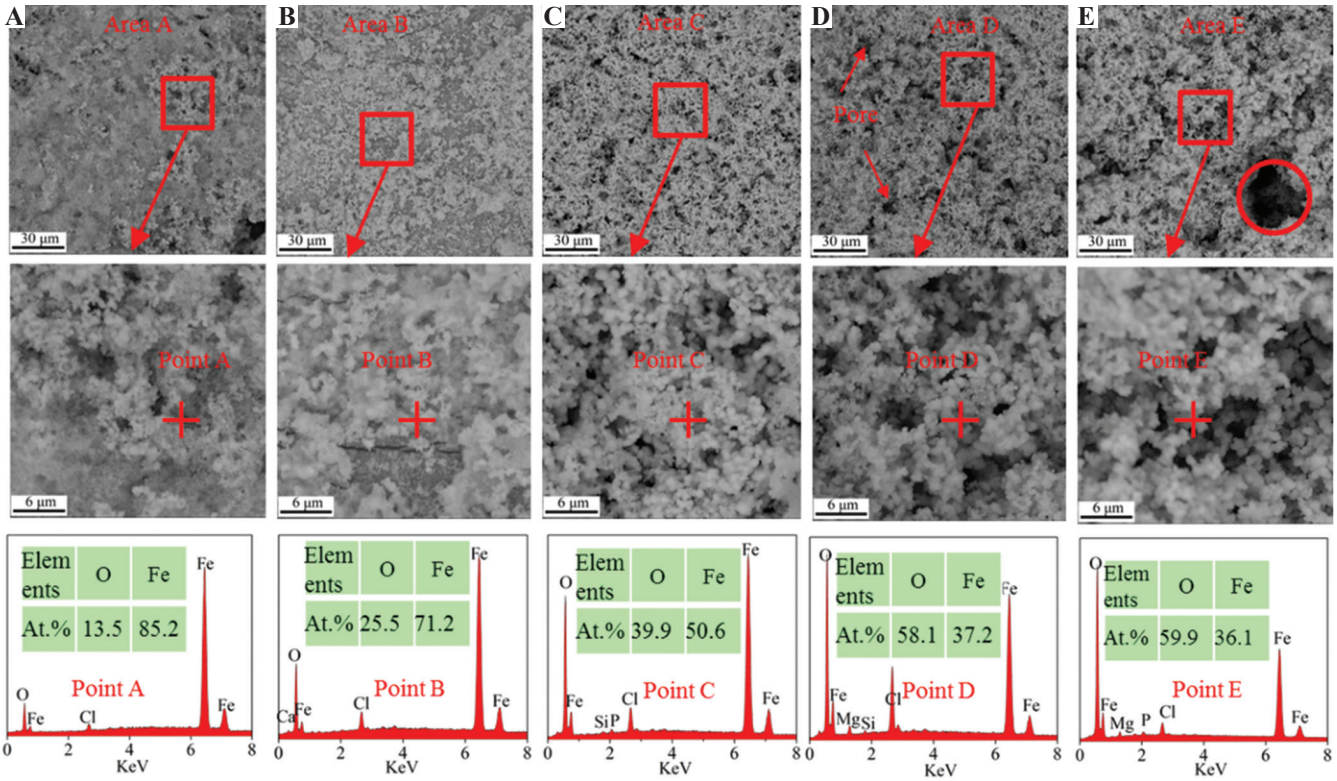

Figure 6. The surface morphologies of (A) Fe, (B) Fe/0.3Mg_2Si, (C) Fe/0.6Mg_2Si, (D) Fe/0.9Mg_2Si, and (E) Fe/1.2Mg_2Si at low- and high-magnifications after 21 days immersion in SBF. EDS analysis of corrosion products was performed to reveal the elemental ratios of O/Fe.

suffered the most severe corrosion, as evidenced by the existence of many more corrosion products in **Figure 6D,E**. Moreover, a few pores were present in the corrosion layers, which indicated that the corrosive SBF penetrated into the matrix through the degradation of product layers. In other words, the corrosion products were not as passive as that of Fe. Meanwhile, EDS analysis of corrosion products revealed that the elemental ratio of O/Fe became higher with the increase of Mg_2Si, also indicating that Fe corrosion was more severe. However, local corrosion was found for Fe/1.2Mg_2Si, as evidenced by the circle in **Figure 6E**, which may deteriorate the mechanical properties during the degradation process. Local corrosion for Fe/1.2Mg_2Si may be closely related to the presence of micropores in its microstructure.

To gain insight into the corrosion process of Fe/Mg_2Si composites in SBF, their cross-sectional morphologies after 21 days of immersion were investigated by SEM and the elemental compositions were analyzed by EDS (**Figure 7**). It could be found from **Figure 7A** that there were dense degradation product layers on Fe matrix, and the interface between Fe matrix and the degradation product layers was obvious. The dense degradation product layers provided good protection effects on Fe in SBF, which inhibited corrosion propagation toward the interior of Fe matrix. The introduction of Mg_2Si significantly changed the cross-sectional morphology of Fe. For Fe/0.3Mg_2Si, cracks were present in the degradation of product layers in **Figure 7B**, which promoted SBF penetration. For Fe/0.6Mg_2Si, the degradation of product layers was more porous and loose than that of Fe/0.3Mg_2Si, as shown in **Figure 7C**. For Fe/0.9Mg_2Si and Fe/1.2Mg_2Si in **Figure 7D,E**, the degradation of product layers had many tiny and narrow openings exposed toward the outside surface. In addition, EDS analysis of Points A, B, and C in **Figure 7D,E** indicated that the gray region was Fe matrix and the black region was the degradation products containing O, Fe, and Si. The presence of these

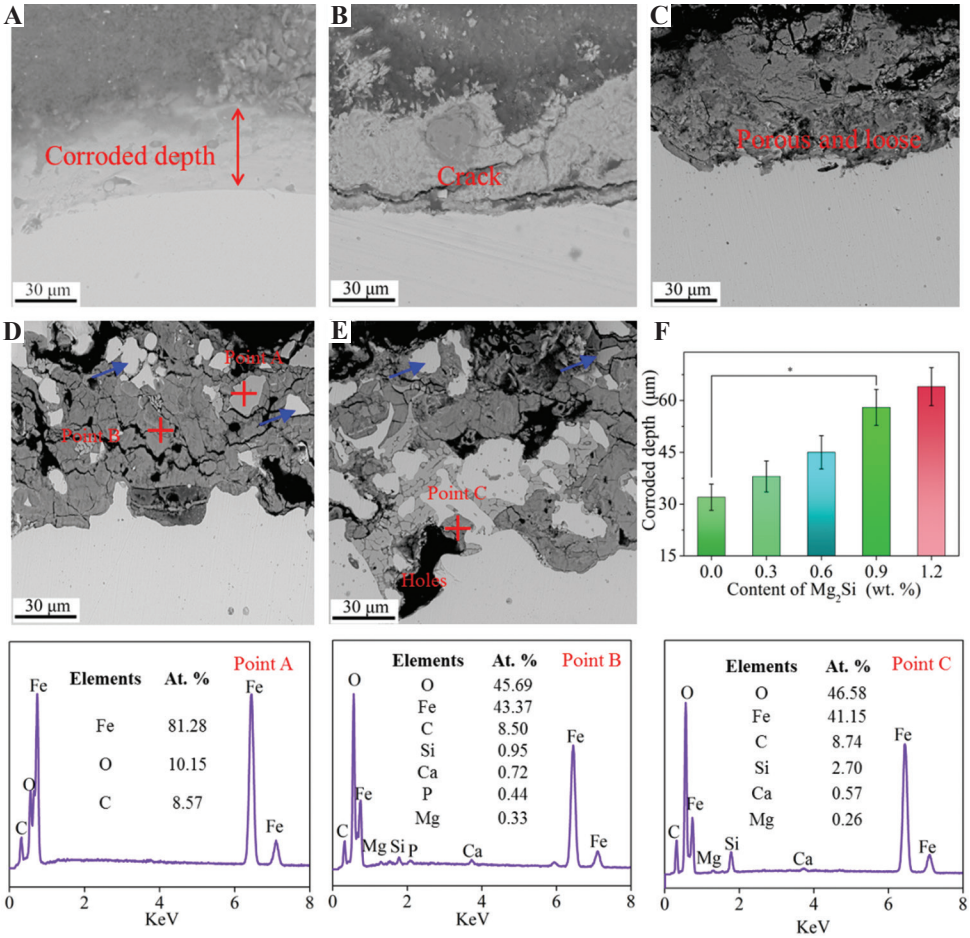

Figure 7. SEM images showing the typical cross-sectional morphologies of (A) Fe, (B) Fe/0.3Mg_2Si, (C) Fe/0.6Mg_2Si, (D) Fe/0.9Mg_2Si, (E) Fe/1.2Mg_2Si with corresponding EDS analysis of Points A, B, and C. (F) Corroded depth of Fe/Mg_2Si composites with Fe as the control group. *$P < 0.05$. The direct peeling off of Fe matrix was marked by arrows.

elements further confirmed the corrosion of Fe and the hydrolysis of Mg_2Si. Besides, a small amount of Ca and P was also detected, which was beneficial to the recovery of bone tissue since these elements were important components of new bone. Interestingly, some of the un-corroded Fe was surrounded by the corrosion products and fell off the matrix, as marked by the arrow in **Figure 7D,E**. This indicated that the solution had penetrated into the interior of Fe matrix, which greatly accelerated the degradation rate of Fe matrix during the corrosion process. It could be reasonably expected that these corrosion would start with hydrolyzed Mg_2Si and then propagated along the grain boundary direction so that the matrix would continuously corrode and peel off. As a result, Fe/Mg_2Si composites possessed a larger corroded depth than Fe, as shown in **Figure 7F**. This was especially important for Fe, since its slow corrosion rate did not match the growth rate of new bone, which would seriously hamper bone repair. In this study, it was noteworthy that Mg_2Si not only accelerated the initial corrosion of Fe but also broke down the protective degradation product layers, thereby maintaining a rapid corrosion rate.

The calculated degradation rates of Fe/Mg_2Si composites with that of Fe as a control group after immersion for 21 days in SBF are exhibited in **Figure 8A**. It could be found that the degradation rates of the Fe/Mg_2Si composites (0.15 ± 0.013, 0.21 ± 0.015, 0.31 ± 0.021, and 0.33 ± 0.030 mm/y for Fe/0.3Mg_2Si, Fe/0.6Mg_2Si, Fe/0.9Mg_2Si, and Fe/1.2Mg_2Si, respectively) were obviously

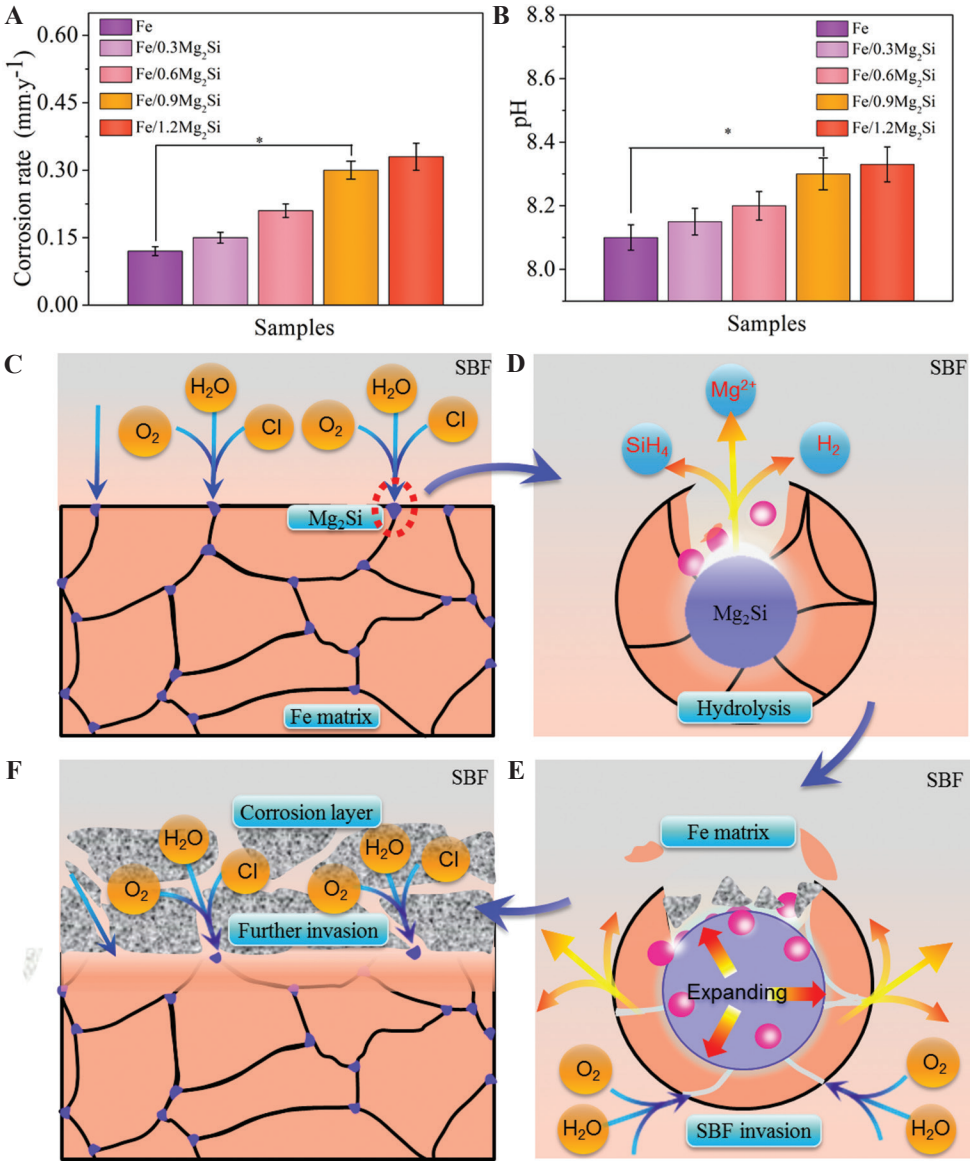

Figure 8. (A) Degradation rates determined by immersion tests and (B) the corresponding pH of Fe/Mg_2Si composites with Fe as a control group in SBF for 21 days. Schematic diagrams of degradation mechanism for Fe/Mg_2Si composites: (C) initial corrosion reaction, (D) Mg_2Si hydrolysis to expose more surface to SBF, (E) hydrolysate escaping from Fe matrix and offering access to SBF, and (F) corrosion propagation as a result of the broken down degradation product layers.

higher than that of Fe (0.12 ± 0.011 mm/y) and the degradation rate increased with the increasing content of Mg_2Si in the composites. This trend was explained by the decomposition of Mg_2Si in the SBF through a chemical reaction with H_2O[45,46]. It should be stated that the degradation rates of Fe/0.9Mg_2Si and Fe/1.2Mg_2Si composites were among 0.2 – 0.5 mm/y, which was a suitable degradation rate to match the restoration process of new bone[2,47]. These results accorded well with that of electrochemical tests. However, it should be remembered that the addition of 1.2 wt% Mg_2Si into the Fe matrix led to a significant decline in mechanical properties. As a result, further increase in the contents of Mg_2Si may be undesirable, especially considering the load-bearing capacity during bone repair. Besides, the pH of Fe/Mg_2Si composites and Fe after immersion for 21 days showed the same trend with the degradation rates, as depicted in **Figure 8B**. The high pH values of

Fe/Mg_2Si composites were caused by the rapid degradation of the Fe matrix.

As biodegradable composites, the degradation rate needs to be consistent with the healing rate of the defect bones to allow a gradual transfer of load to the new bone and to avoid the long-term negative effects of permanent implants. After exposure to physiological environment, Fe degraded in a manner of oxygen absorption corrosion mode, producing degradation products as follows:

$$2Fe \rightarrow 2Fe^{2+} + 4e^- \quad (1)$$

$$O_2 + 2H_2O + 4e^- \rightarrow 4OH^- \quad (2)$$

$$2Fe + 2H_2O + O_2 \rightarrow 2Fe(OH)_2\downarrow \quad (3)$$

$$Fe^{2+} \rightarrow Fe^{3+} + e^- \quad (4)$$

$$Fe^{3+} + 3OH^- \rightarrow Fe(OH)_3\downarrow \quad (5)$$

$$Fe(OH)_2 + 2Fe(OH)_3 \rightarrow Fe_3O_4\downarrow + 4H_2O \quad (6)$$

Reactions between Fe^{2+} from anodic oxidation and other anions in physiological environment could simultaneously occur[39,48]:

$$3Fe^{2+} + 2PO_4^{3-} + 8H_2O \rightarrow Fe_3(PO_4)_2\cdot 8H_2O\downarrow \quad (7)$$

Degradation products, such as $Fe(OH)_2$, $Fe(OH)_3$, Fe_3O_4, and $Fe_3(PO_4)_2\cdot 8H_2O$, were almost insoluble in the physiological environment[49,50]. As a result, the degradation products would deposit on Fe matrix and form dense product layers, as shown in **Figure 7A**, significantly reducing the degradation rates. In this study, Mg_2Si with high chemical activity was introduced into the Fe matrix and it would be readily hydrolyzed according to Equation (8):

$$Mg_2Si + 4H_2O \rightarrow 2Mg(OH)_2 + SiH_4\uparrow \quad (8)$$

The generated gas (SiH_4) would escape from the matrix and then diffuse into the solution, which destroyed the accumulated degradation product layers. Once the protective layers were broken down, the corrosive solution would quickly infiltrate and induce Fe corrosion. More importantly, the generated SiH_4 underwent further hydrolysis:

$$SiH_4 + 2H_2O \rightarrow SiO_2 + 4H_2\uparrow \quad (9)$$

This also aggravated the damage to degradation product layers and hindered the accumulation of the degradation product layers, further enlarging the access of corrosive solution to the matrix. Meanwhile, the produced silicon dioxide (SiO_2) acted as a cathode site, and then galvanic corrosion occurred between SiO_2 and Fe matrix due to the different corrosion potentials.

Based on this corrosion mode, the hydrolysis of Mg_2Si would, on the one hand, create vacancies in the matrix, exposing more surface of Fe to the solution during the initial immersion. On the other hand, the produced gases by the hydrolysis had an expansive effect, which cracked the degradation product layers as well as Fe matrix, and brought about the breakdown of degradation product layers, thereby contributing to the corrosion propagation toward the interior of the matrix. As a result, the degradation product layers became porous, loose and easily detached from the matrix, resulting in peeling off of corrosion products or even Fe matrix, as evidenced in **Figure 7D,E**. Moreover, since Mg_2Si was homogeneously distributed in the Fe matrix, fast and macroscopical corrosion would occur throughout the matrix. This corrosion mechanism was first proposed and verified in this study, which fundamentally solved the problem that corrosion product accumulation hindered the degradation. It should be noted that the generated gases by the hydrolysis of Mg_2Si would be carried away by the circulating blood in the human body, which would not produce obvious side effects.

3.6 Cytocompatibility

Cytocompatibility tests using MG-63 cells were taken to evaluate the biological safety of Fe/0.9Mg_2Si composite. Fluorescent images in extracts were taken to investigate the growth of MG-63 cells, as exhibited in **Figure 9A-D**. It could be found that there was no obvious difference in cell morphologies after 72 h of exposure to different extracts. The average cell number was estimated by ImageJ software according to the fluorescent images in **Figure 9E**, which showed no significant difference. Besides, cell viability was

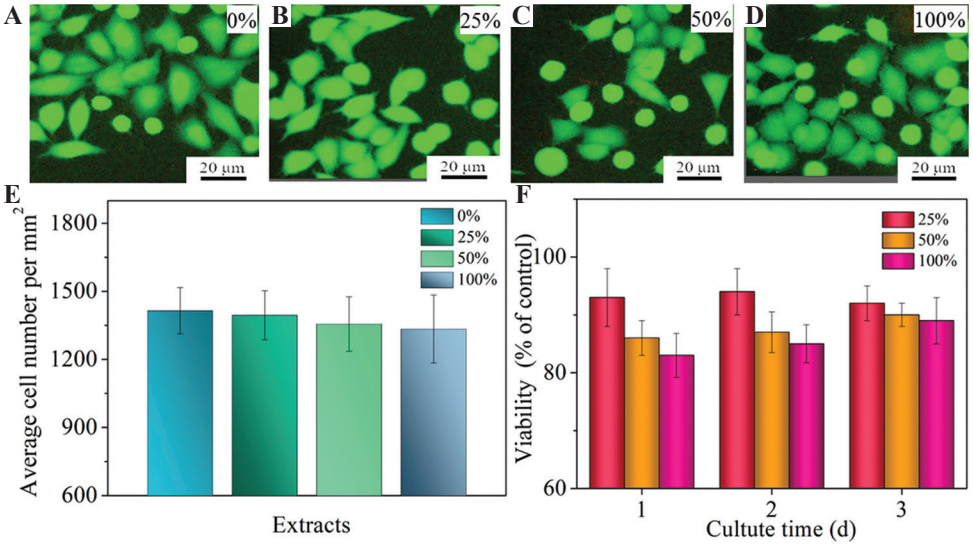

Figure 9. Cytocompatibility of Fe/0.9Mg_2Si composite: fluorescent images of different concentrations of extract: (A) 0%, (B) 25%, (C) 50%, and (D) 100%, respectively, (E) average MG-63 cell number per mm^2 in different concentrations of extracts (25, 50, and 100%, respectively) measured by ImageJ software; (F) MG-63 cell viability after incubation in different concentrations of extracts (25, 50, and 100%, respectively) for 1, 2, and 3 days.

further investigated, and the results are depicted in **Figure 9F**. It was found that cell viability decreased with the increase in concentrations of extract at 1 and 2 days. Meanwhile, there was no statistical significance in the cell viability of Fe/0.9Mg_2Si composite in comparison with the control group. However, on day 3, cell viability of 50 and 100% extracts became approximately identical as that of the control group (0% extract). Moreover, during 3 days of incubation, cell viability was all above 70%, indicating no cytotoxicity of Fe/Mg_2Si composites according to the ISO10993-5[51].

4 Conclusions

In this study, Fe/Mg_2Si composites were successfully fabricated by selective laser melting to accelerate degradation for biomedical applications. The effects of Mg_2Si on microstructure, mechanical properties, and corrosion behaviors of Fe were systematically studied.

(1) Fe/Mg_2Si composites had similar microstructure, in which Mg_2Si was easily discernible with the increase in Mg_2Si content. However, when the additional content of Mg_2Si was 1.2 wt.%, micropores were found.

(2) The addition of Mg_2Si led to a decrease in compression strength, but their compression strength was in the range of compact bone (90 – 170 MPa). The hardness of Fe/0.9Mg_2Si composite (145 HV) was higher than other samples (112, 134, 142, and 127 HV for Fe, Fe/0.3Mg_2Si, Fe/0.6Mg_2Si, and Fe/1.2Mg_2Si, respectively). A slight decrease was found after adding Mg_2Si to 1.2 wt% may be caused by micropores in the microstructure.

(3) Electrochemical tests revealed accelerated corrosion behaviors for Fe/Mg_2Si composites. This was due to the hydrolysis of Mg_2Si, resulting in more matrix exposure to SBF. Immersion tests showed that corrosion occurred in the interior of Fe/Mg_2Si composites with porous and loose corrosion product layers. This induced corrosion propagation toward the interior of the Fe matrix and bulk Fe matrix may peel off. As a result, Fe/Mg_2Si composites exhibited high degradation rates (higher than 0.30 mm/year). *In vitro*, MG-63 cell tests confirmed the good cytocompatibility Fe/Mg_2Si composites. These results collectively showed that hydrolytic expansion was an effective strategy to accelerate the degradation of Fe-based implants for bone applications.

Acknowledgments

This study was supported by the following funds: (1) The Natural Science Foundation of China (51705540, 51935014, 51905553, 81871494, 81871498); (2) Hunan Provincial Natural Science Foundation of China (2018JJ3671, 2019JJ50774, 2019JJ50588); (3) JiangXi Provincial Natural Science Foundation of China (20192ACB20005); (4) Guangdong Province Higher Vocational Colleges and Schools Pearl River Scholar Funded Scheme (2018); (5) The Open Sharing Fund for the Large-scale Instruments and Equipments of Central South University; and (6) The Project of Hunan Provincial Science and Technology Plan (2017RS3008).

References

1. Gao C, Yao M, Li S, *et al*., 2019, Highly Biodegradable and Bioactive Fe-Pd-Bredigite Biocomposites Prepared by Selective Laser Melting. *J Adv Res*, 20:91–104. DOI: 10.1016/j.jare.2019.06.001.
2. Shuai C, Li S, Peng S, *et al*., 2019, Biodegradable Metallic Bone Implants. *Mater Chem Front*, 3(1):544–62. DOI: 10.1039/C8QM00507A.
3. Yang YY, He C, Dianyu E, *et al*., 2019, Mg Bone Implant: Features, Developments and Perspectives. *Mater Design*, 185:108259. DOI: 10.1016/j.matdes.2019.108259.
4. Gao C, Yao M, Shuai C, *et al*., 2019, Nano-SiC Reinforced Zn Biocomposites Prepared Via Laser Melting: Microstructure, Mechanical Properties and Biodegradability. *J Mater Sci Tech*, 35:2608–17. DOI: 10.1016/j.jmst.2019.06.010.
5. Shuai C, Yang W, He C, *et al*., 2019, A Magnetic Micro-Environment in Scaffolds for Stimulating Bone Regeneration. *Mater Des*, 185:108275. DOI: 10.1016/j.matdes.2019.108275.
6. Wang G, Qi F, Yang W, *et al*., 2019, Crystallinity and Reinforcement in Poly-L-Lactic Acid Scaffold Induced by Carbon Nanotubes. *Advances in Polymer Technology*, 2019:10. DOI: 10.1155/2019/8625325.
7. He S, Yang S, Zhang Y, *et al*., 2019, LncRNA ODIR1 Inhibits Osteogenic Differentiation of hUC-MSCs Through the FBXO25/H2BK120ub/H3K4me3/OSX axis. *Cell Death Dis*, 10:1–16. DOI: 10.1038/s41419-019-2148-2.
8. Zivic F, Grujovic N, Pellicer E, *et al*., 2018, Biodegradable Metals as Biomaterials for Clinical Practice: Iron-Based Materials, Biomaterials in Clinical Practice. Springer, Berlin. pp. 225–80. DOI: 10.1007/978-3-319-68025-5_9.
9. Deng Y, Yang Y, Gao C, *et al*., 2018, Mechanism for Corrosion Protection of β-TCP Reinforced ZK60 Via Laser Rapid Solidification. *Int J Bioprint*, 4(1):27–41. DOI: 10.18063/IJB.v4i1.124.
10. Hermawan H, Dubé D, Mantovani D, 2007, Development of Degradable Fe-35Mn Alloy for Biomedical Application. *Adv Mater Res*, 15:107–12. DOI: 10.4028/www.scientific.net/AMR.15-17.107.
11. Schinhammer M, Steiger P, Moszner F, *et al*. 2013, Degradation Performance of Biodegradable FeMnC (Pd) Alloys. *Mater Sci Eng C*, 33:1882–93. DOI: 10.1016/j.msec.2012.10.013.
12. Zhou J, Yang Y, Alonso Frank M, *et al*., 2016, Accelerated Degradation Behavior and Cytocompatibility of Pure Iron Treated with Sandblasting. *ACS Appl Mater Interfaces*, 8:26482–92. DOI: 10.1021/acsami.6b07068.
13. Moravej M, Purnama A, Fiset M, *et al*., 2010, Electroformed Pure Iron as a New Biomaterial for Degradable Stents: *In Vitro* Degradation and Preliminary Cell Viability Studies. *Acta Biomater*, 6:1843–51. DOI: 10.1016/j.actbio.2010.01.008.
14. Jiang W, Wang J, Yu W, *et al*., 2019, *In Situ* Formation of a Gradient Mg2Si/Mg Composite with Good Biocompatibility. *Surf Coat Technol*, 361:255–62. DOI: 10.1016/j.surfcoat.2018.12.107.
15. Sikora-Jasinska M, Paternoster C, Mostaed E, *et al*., 2017, Synthesis, Mechanical Properties and Corrosion Behavior of Powder Metallurgy Processed Fe/Mg2Si Composites for Biodegradable Implant Applications. *Mater Sci Eng C*, 81(2):511–21. DOI: 10.1016/j.msec.2017.07.049.
16. Lee JY, An J, Chua CK, 2017, Fundamentals and Applications of 3D Printing for Novel Materials. *Appl Mater Today*, 7:120–33. DOI: 10.1016/j.apmt.2017.02.004.
17. An J, Teoh JEM, Suntornnond R, *et al*., 2015, Design and 3D Printing of Scaffolds and Tissues. *Engineering*, 1:261–68. DOI: 10.15302/J-ENG-2015061.
18. Sing SL, Huang S, Yeong WY, 2020, Effect of Solution Heat Treatment on Microstructure and Mechanical Properties of Laser Powder Bed Fusion Produced Cobalt-28chromium-6molybdenum. *Mater Sci Eng A*, 769:138511. DOI: 10.1016/j.msea.2019.138511.
19. Nasab MH, Giussani A, Gastaldi D, *et al*., 2019, Effect of Surface and Subsurface Defects on Fatigue Behavior of AlSi10Mg Alloy Processed by Laser Powder Bed Fusion (L-PBF). *Metals*, 9:1063. DOI: 10.3390/met9101063.
20. Yu W, Sing S, Chua C, *et al*., 2019, Particle-Reinforced Metal Matrix Nanocomposites Fabricated by Selective Laser Melting: A State of the Art Review. *Prog Mater Sci*,

104:330-379. DOI: 10.1016/j.pmatsci.2019.04.006.

21. Dadbakhsh S, Mertens R, Hao L, *et al*., 2019, Selective Laser Melting to Manufacture "*In Situ*" Metal Matrix Composites: A Review. *Adv Eng Mater*, 21:1801244. DOI: 10.1002/adem.201801244.
22. Hariharan K, Arumaikkannu G, 2016, Structural, Mechanical and *In Vitro* Studies on Pulsed Laser Deposition of Hydroxyapatite on Additive Manufactured Polyamide Substrate. *Int J Bioprint*, 2:85–94. DOI: 10.1016/S0021-9290(06)83793-0.
23. Lepowsky E, Tasoglu S, 2018, 3D Printing for Drug Manufacturing: A Perspective on the Future of Pharmaceuticals. *Int J Bioprint*, 4:119. DOI: 10.18063/IJB.v4i1.119.
24. Yap CY, Chua CK, Dong ZL, *et al*., 2015, Review of Selective Laser Melting: Materials and Applications. *Appl Phys Rev*, 2:041101. DOI: 10.1063/1.4935926.
25. Loh LE, Chua CK, Yeong WY, *et al*., 2015, Numerical Investigation and an Effective Modelling on the Selective Laser Melting (SLM) Process with Aluminium Alloy 6061. *Int J Heat Mass Transfer*, 80:288–300. DOI: 10.1016/j.ijheatmasstransfer.2014.09.014.
26. Sun Z, Tan X, Tor SB, *et al*. 2018, Simultaneously Enhanced Strength and Ductility for 3D-Printed Stainless Steel 316L by Selective Laser Melting. *NPG Asia Materials*, 10:127. DOI: 10.1038/s41427-018-0018-5.
27. Li Y, Zhou K, Tan P, *et al*., 2018, Modeling Temperature and Residual Stress Fields in Selective Laser Melting. *Int J Mech Sci*, 136:24–35. DOI: 10.1016/j.ijmecsci.2017.12.001.
28. Yu W, Sing SL, Chua CK, *et al*., 2019, Influence of Re-Melting on Surface Roughness and Porosity of AlSi10Mg Parts Fabricated by Selective Laser Melting. *J Alloys Compd*, 792:574–81. DOI: 10.1016/j.jallcom.2019.04.017.
29. Kuo C, Chua C, Peng P, *et al*., 2019, Microstructure Evolution and Mechanical Property Response Via 3D Printing Parameter Development of Al-Sc alloy. *Virtual Phys Prototyp*, 15:1–10. DOI: 10.1080/17452759.2019.1698967.
30. Vanarase AU, Muzzio FJ, 2011, Effect of Operating Conditions and Design Parameters in a Continuous Powder Mixer. *Powder Technol*, 208:26–36. DOI: 10.1016/j.powtec.2010.11.038.
31. Portillo PM, 2008, Quality by Design for Continuous Powder Mixing. Rutgers University-Graduate School, New Brunswick.
32. Shuai C, Zan J, Yang Y, *et al*., 2019, Surface Modification Enhances Interfacial Bonding in PLLA/MgO Bone Scaffold. *Mater Sci Eng C*, 108:110486. DOI: 10.1016/j.msec.2019.110486.
33. Shuai C, Xu Y, Feng P, *et al*., 2019, Antibacterial Polymer Scaffold Based on Mesoporous Bioactive Glass Loaded with *In Situ* Grown Silver. *Chem Eng J*, 374:304–15. DOI: 10.1016/j.cej.2019.03.273.
34. Wang S, Xu Y, Zhou J, *et al*., 2017, *In Vitro* Degradation and Surface Bioactivity of Iron-Matrix Composites Containing Silicate-Based Bioceramic. *Bioact Mater*, 2:10–18. DOI: 10.1016/j.bioactmat.2016.12.001.
35. Shuai C, Li S, Wang G, *et al*., 2019, Strong Corrosion Induced by Carbon Nanotubes to Accelerate Fe Biodegradation. *Mater Sci Eng C*, 104(5):109935. DOI: 10.1016/j.msec.2019.109935.
36. Wang H, Zheng Y, Li Y, *et al*., 2017, Improvement of *In Vitro* Corrosion and Cytocompatibility of Biodegradable Fe Surface Modified by Zn Ion Implantation. *Appl Surf Sci*, 403(12):168–76. DOI: 10.1016/j.apsusc.2017.01.158.
37. Shuai C, Cheng Y, Yang Y, *et al*., 2019, Laser Additive Manufacturing of Zn-2Al Part for Bone Repair: Formability, Microstructure and Properties. *J Alloys Comp*, 798:606–15. DOI: 10.1016/j.jallcom.2019.05.278.
38. Cheng J, Liu B, Wu Y, *et al*., 2013, Comparative *In Vitro* Study on Pure Metals (Fe, Mn, Mg, Zn and W) as Biodegradable Metals. *J Mater Sci Tech*, 29:619–27. DOI: 10.1016/j.jmst.2013.03.019.
39. Shuai C, Liu G, Yang Y, *et al*., 2019, Functionalized BaTiO3 Enhances Piezoelectric Effect Towards Cell Response of Bone Scaffold. *Colloids Surf*, 3:110587–94. DOI: 10.1016/j.colsurfb.2019.110587.
40. Feng P, Kong Y, Yu L, *et al*., 2019, Molybdenum Disulfide Nanosheets Embedded with Nanodiamond Particles: Co-Dispersion Nanostructures as Reinforcements for Polymer Scaffolds. *Appl Mater Today*, 17:216–26. DOI: 10.1016/j.apmt.2019.08.005.
41. Prakasam M, Locs J, Salma-Ancane K, *et al*., 2017, Biodegradable Materials and Metallic Implants a Review. *J Funct Biomater*, 8:44. DOI: 10.3390/jfb8040044.
42. Gao C, Peng S, Feng P, *et al*., 2017, Bone Biomaterials and Interactions with Stem Cells. *Bone Res*, 5:17059. DOI: 10.1038/boneres.2017.59.
43. Dehestani M, Adolfsson E, Stanciu LA, 2016, Mechanical Properties and Corrosion Behavior of Powder Metallurgy Iron-Hydroxyapatite Composites for Biodegradable Implant Applications. *Mater Des*, 109:556–69. DOI: 10.1016/j.matdes.2016.07.092.
44. Kato K, Ochiai S, Yamamoto A, *et al*., 2013, Novel Multilayer Ti Foam With Cortical Bone Strength and Cytocompatibility. *Acta Biomater*, 9:5802–09. DOI:

10.1016/j.actbio.2012.11.018.

45. Panemangalore DB, Shabadi R, Tingaud D, *et al*., 2019, Biocompatible Silica-Based Magnesium Composites. *J Alloys Comp,* 772(15):49–57. DOI: 10.1016/j.jallcom.2018.09.060.
46. Zhang Y, Wang L, Sun W, *et al*., 2019, Membrane Technologies for Li+/Mg2+ Separation From Salt-Lake Brines and Seawater: A Comprehensive Review. *J Ind Eng Chem,* 81:7–23. DOI: 10.1016/j.jiec.2019.09.002.
47. Bowen PK, Shearier ER, Zhao S, *et al*., 2016, Biodegradable Metals for Cardiovascular Stents: From Clinical Concerns to Recent Zn-Alloys. *Adv Healthc Mater*, 5:1121–40. DOI: 10.1002/adhm.201501019.
48. Shuai C, Yang Y, Feng P, *et al*., 2018, A Multi-Scale Porous Scaffold Fabricated by a Combined Additive Manufacturing and Chemical Etching Process for Bone Tissue Engineering. *Int J Bioprint*, 4:133. DOI: 10.18063/IJB.v4i2.133.
49. Gorejová R, Haverová L, Oriňaková R, *et al*., 2019, Recent Advancements in Fe-Based Biodegradable Materials for Bone Repair. *J M Sci*, 54(12):1913–47. DOI: 10.1007/s10853-018-3011-z.
50. Jin J, Tan Y, Liu R, *et al*., 2018, Synergy Effect of Attapulgite, Rubber, and Diatomite on Organic Montmorillonite-Modified Asphalt. *J Mater Civil Eng*, 31:04018388. DOI: 10.1061/(ASCE)MT.1943-5533.0002601.
51. Zhao Y, Jamesh MI, Li WK, *et al*., 2014, Enhanced Antimicrobial Properties, Cytocompatibility, and Corrosion Resistance of Plasma-Modified Biodegradable Magnesium Alloys. *Acta Biomater*, 10:544–56. DOI: 10.1016/j.actbio.2013.10.012.

RESEARCH ARTICLE

Graphene Oxide Induces Ester Bonds Hydrolysis of Poly-l-lactic Acid Scaffold to Accelerate Degradation

Cijun Shuai[1,2,3], Yang Li[1], Wenjing Yang[1], Li Yu[1], Youwen Yang[2], Shuping Peng[4,5], Pei Feng[1]*

[1]State Key Laboratory of High-Performance Complex Manufacturing, College of Mechanical and Electrical Engineering, Central South University, Changsha 410083, China

[2]Institute of Bioadditive Manufacturing, Jiangxi University of Science and Technology, Nanchang 330013, China

[3]Shenzhen Institute of Information Technology, Shenzhen 518172, China

[4]NHC Key Laboratory of Carcinogenesis and The Key Laboratory of Carcinogenesis and Cancer Invasion of the Chinese Ministry of Education, Xiangya Hospital, Central South University, Changsha, Hunan China

[5]Cancer Research Institute, School of Basic Medical Sciences, Central South University, Changsha, Hunan China

Abstract: Poly-l-lactic acid (PLLA) possesses good biocompatibility and bioabsorbability as scaffold material, while slow degradation rate limits its application in bone tissue engineering. In this study, graphene oxide (GO) was introduced into the PLLA scaffold prepared by selective laser sintering to accelerate degradation. The reason was that GO with a large number of oxygen-containing functional groups attracted water molecules and transported them into scaffold through the interface microchannels formed between lamellar GO and PLLA matrix. More importantly, hydrogen bonding interaction between the functional groups of GO and the ester bonds of PLLA induced the ester bonds to deflect toward the interfaces, making water molecules attack the ester bonds and thereby breaking the molecular chain of PLLA to accelerate degradation. As a result, some micropores appeared on the surface of the PLLA scaffold, and mass loss was increased from 0.81% to 4.22% after immersing for 4 weeks when 0.9% GO was introduced. Besides, the tensile strength and compressive strength of the scaffolds increased by 24.3% and 137.4%, respectively, due to the reinforced effect of GO. In addition, the scaffold also demonstrated good bioactivity and cytocompatibility.

Keywords: Poly-l-lactic acid scaffold, GO, Degradation property, Ester bonds hydrolysis

***Corresponding Author:** Pei Feng, State Key Laboratory of High-Performance Complex Manufacturing, College of Mechanical and Electrical Engineering, Central South University, Changsha 410083, China; fengpei@csu.edu.cn

Received: November 15, 2019; ***Accepted:*** January 02, 2020; ***Published Online:*** January 23, 2020

Citation: Shuai C, Li Y, Yang W, *et al*., 2020, Graphene oxide induces ester bonds hydrolysis of poly-l-lactic acid scaffold to accelerate degradation. *Int J Bioprint*, 6(1):249. DOI: 10.18063/ijb.v6i1.249

1 Introduction

Poly-l-lactic acid (PLLA) is a bone scaffold material[1,2], recognized by the US Food and Drug Administration (FDA) with good biocompatibility and bioabsorbability[3,4]. It can be first degraded into lactic acid in the human body, then decomposed into carbon dioxide and water by metabolism, and finally excreted without any harmful residue[5-7]. In addition, the elastic modulus of PLLA is close to that of human bone tissue compared to stainless steel, titanium alloy, etc., and can avoid stress shielding effect[8-10] whereas the degradation rate of PLLA is slow in the human body. It has been reported that PLLA needs a complete resorption time of 2 – 3 years[11], while new bone regeneration[12-14], usually takes 12 – 18 weeks[15]. The unmatched degradation rate of PLLA with new bone regeneration limits its further applications.

To accelerate the degradation of PLLA, Kang *et al*. blended collagen and PLLA, using collagen's natural fast degradability to accelerate degradation. Nevertheless, the introduction of collagen decreased the mechanical strength of the PLLA scaffold[16]. Considering that PLLA is formed by the linkage of ester bonds between lactic acid monomers, its degradation is first caused by the hydrolysis of the ester bond in the main chains and then decomposes into carbon dioxide and water[17]. PLLA is a hydrophobic material and is not beneficial for the intrusion of water molecules into its interior to break the ester bonds, making it difficult to degrade[18]. Therefore, promoting the contact between water molecules and the ester bond of PLLA is an effective method to accelerate the hydrolysis of ester bonds.

Graphene oxide (GO) is a two-dimensional lamellar structure with a large amount of oxygen-containing functional groups (such as –COOH and –OH) on its surface[19-22]. These functional groups can endow GO good hydrophilic property and water absorption capacity[23-26]. At the same time, the lamellar GO with large surface area is likely to form many interfaces with matrix, and these interfaces can be regarded as microchannels to facilitate water molecules to invade and induce the breaking of ester bonds. Besides, GO with excellent mechanical properties (Young's modulus >0.5 TPa, and tensile strength ~130 GPa) can be used as a reinforcing phase for scaffold[27,28]. In addition, it has also been reported that GO possessed good biocompatibility for cell adhesion and proliferation[29-31]. The current reports mainly utilized GO to improve the mechanical properties, thermal stability, and cytocompatibility of PLLA[32-35] whereas few studies focused on inducing ester bonds hydrolysis of PLLA scaffold by GO to accelerate degradation.

In this study, GO was introduced into PLLA to accelerate degradation, and three-dimensional porous PLLA/GO scaffolds were prepared by selective laser sintering (SLS)[36], which is an additive manufacturing method[37], and can realize the preparation of personalized scaffolds and interconnected porous structures compared to traditional fabrication methods[38-42]. Degradation properties of the PLLA scaffold containing different ratios of GO were studied by observation of degradation morphology and measurement of mass loss. Meanwhile, degradation mechanism was also analyzed. Besides, surface and fracture morphologies of the scaffold were also observed to further investigate the causes of changes in mechanical properties. In addition, bioactivity and cytocompatibility had also been evaluated by simulated body fluid (SBF) immersion and cell proliferation experiments, respectively.

2 Materials and methods

2.1 Materials and preparation

PLLA powders (Purity: tionigand inherent viscosity: 1.46 dl/g) were provided from Shenzhen Polymtek Biomaterial Co., Ltd. (Shenzhen, China). GO powders (purity > 98%) were obtained from Chengdu Organic Chemicals Co., Ltd. (Chengdu, China). The composition of phosphate-buffered solution (PBS) was NaCl, KCl, Na_2HPO2H_2O, and KH_2PO_4, which was provided from Sigma-Aldrich (Beijing, China). SBF was purchased from Qingdao Jieshang Biological Technology Co., Ltd. (Qingdao, China). Human osteoblast-like MG-63 cells were supplied from the American Type Culture Collection (ATCC, Rockville, MD).

Three-dimensional porous PLLA and PLLA/GO scaffolds with 0.3%, 0.6%, 0.9%, and 1.2% GO were prepared by SLS. The powders were evenly laid on the sintering platform and selectively sintered according to the pre-planned scaffold models, and the sintering platform would be lowered to a corresponding height when a layer of powders was sintered and then a layer of powders was applied again, sintering layer by layer, and finally obtaining the required scaffolds. The processing parameters were applied as follows: Spot size of 1.2 mm, laser power of 2.2 W, and laser scanning speed of 100 mm/min.

2.2 Characterization

Surface and fracture morphologies were observed by Phenom Scanning Electron Microscopy (FEI Co., USA), and energy-dispersive spectroscopy (EDS) was used to examine the elemental content

of various substances. The phase composition of the scaffolds was carried out from 500 cm^{-1} to 3500 cm^{-1} with LabRAM HR800 confocal micro Raman spectrometer (HORIBA Scientific Instruments & Systems, Paris, France). Three-dimensional surface morphologies of PLLA/GO samples with 0%, 0.3%, 0.6%, 0.9%, and 1.2% GO after degradation for 4 weeks were observed by laser confocal microscopy (Zeiss Co., Germany) and surface roughness (Ra, Rq, and Rz) date was calculated automatically.

2.3 Wettability

The water contact angles of PLLA and PLLA/GO samples (10 × 10 × 5 mm^3) with 0.3%, 0.6%, 0.9%, and 1.2% GO were measured by an Attension Theta Lite optical tensiometer (Biolin Scientific Co. Ltd., Stockholm, Sweden). The water absorption of the samples was measured to determine the water uptake ability. Five times were used to measure the water absorption rate for each different ratio sample. The mass of each sample was weighed as W_{dry} before immersing, and then the sample was immersed in the distilled water according to the pre-planned time and weighed as W_{wet}. The water absorption rate (W_{war}) was calculated by the following formula[43]:

$$W_{war} = \frac{W_{wet} - W_{dry}}{W_{dry}} \times 100\%$$

2.4 Degradation properties

Each sample with a size of 10 × 10 × 5 mm^3 was measured for initial weight as W_i and then placed in a test tube containing 20 mL of PBS solution (pH = 7.4) at 37°. for 1, 2, 3, and 4 weeks, respectively. After reaching the predetermined immersing time, the samples were taken out and washed with distilled water 3 times, and then dried in a dry box for 24 h and weighted as W_u. The surface morphological changes were evaluated by SEM. The weight loss percentage (W_L) of the samples was calculated by the following formula[44]:

$$W_L = \frac{W_i - W_u}{W_i} \times 100\%$$

2.5 Mechanical properties

The mechanical properties of the samples were evaluated by a universal testing machine (WD-D1, LTD, China). Compressive samples were cylindrical scaffolds with 10 mm of diameter and 5 mm of height; tensile samples were dumbbell scaffolds with a size of 12 × 4 × 2 mm^3. Different proportions of the samples were placed on the compression fixture and subjected to uniaxial compression with a crosshead speed of 0.5 mm/min at room temperature. Similarly, the samples were also placed on the stretching fixture and subjected to uniaxial tensile under the same conditions. Compressive strength and modulus, tensile strength and modulus were calculated through stress-strain curves, respectively. Six samples were tested for each point.

2.6 Bioactivity

PLLA/GO samples (10 × 10 × 5 mm^3) with 0%, 0.3%, 0.6%, 0.9%, and 1.2% GO were placed in 6-well culture plates, immersed in 10 ml SBF, and maintained at 37°C. Fresh SBF was changed every other day for up to 4 weeks. After incubation for various periods of time, the specimens were removed from the solution and rinsed with deionized water 3 times to remove any soluble inorganic ions. Then, the samples were dried in a dry box for 24 h for further characterization.

2.7 Cytocompatibility

Fluorescence staining experiment was carried out to qualitatively assess the cell proliferation of PLLA and PLLA/0.9 GO scaffolds with a size of 10 × 10 × 5 mm^3. Twenty microliters of MTT solution were added into cell culture plates for 3 h at 37°C after 1, 3, and 5 days of cell culture. Subsequently, 200 mL of dimethyl sulfoxide was taken into each plate to dissolve formazan crystals and staining cells were imaged using a phase-contrast light microscope. The CCK-8 assay was used to quantificationally assess cell proliferation. The samples were cleaned with PBS after being cultured for 1, 3, and 5 days. Afterward, CCK-8 reagent (Dojindo Laboratories, Kumamoto, Japan) was added into culture plates and cultured

for 2 h. Finally, the absorbance of the solution was measured by a microplate reader at 450 nm.

2.8 Statistical analysis

Data were expressed as mean value ± one standard deviation. The differences of measured data were taken to be significant for $P < 0.05$, sign * and ** denotes $P < 0.05$ and $P < 0.01$, respectively.

3 Results and discussion

3.1 Preparation of powders and scaffolds

The morphology of the powders and scaffolds is shown in **Figure 1**. PLLA powders presented oblong or spherical particles in **Figure 1A**, and particle size was approximately 120 μm. In **Figure 1B**, GO presented flaky structure and piece of diameter was approximately 40 μm. PLLA/GO composites are shown in **Figure 1C**, GO was evenly distributed between PLLA particles, and the particle size was obviously smaller compared to PLLA particles. PLLA and PLLA/GO scaffolds were prepared by SLS, as shown in **Figure 1D-F**. PLLA scaffold presented a white appearance with a diameter of 12 mm and a height of 9 mm. Similarly, PLLA/GO had the same shape and size, while the appearance was grayish-black. More importantly, these scaffolds possessed interpenetrating micropores. These pores mimicked the microporous structure of bone, which facilitated the transport of nutrients, the discharge of metabolic waste, and the adhesion and proliferation of cells[45,46]. Feng *et al*. prepared three-dimensional porous structure scaffold and confirmed that the porous structure is favorable for cell growth[47].

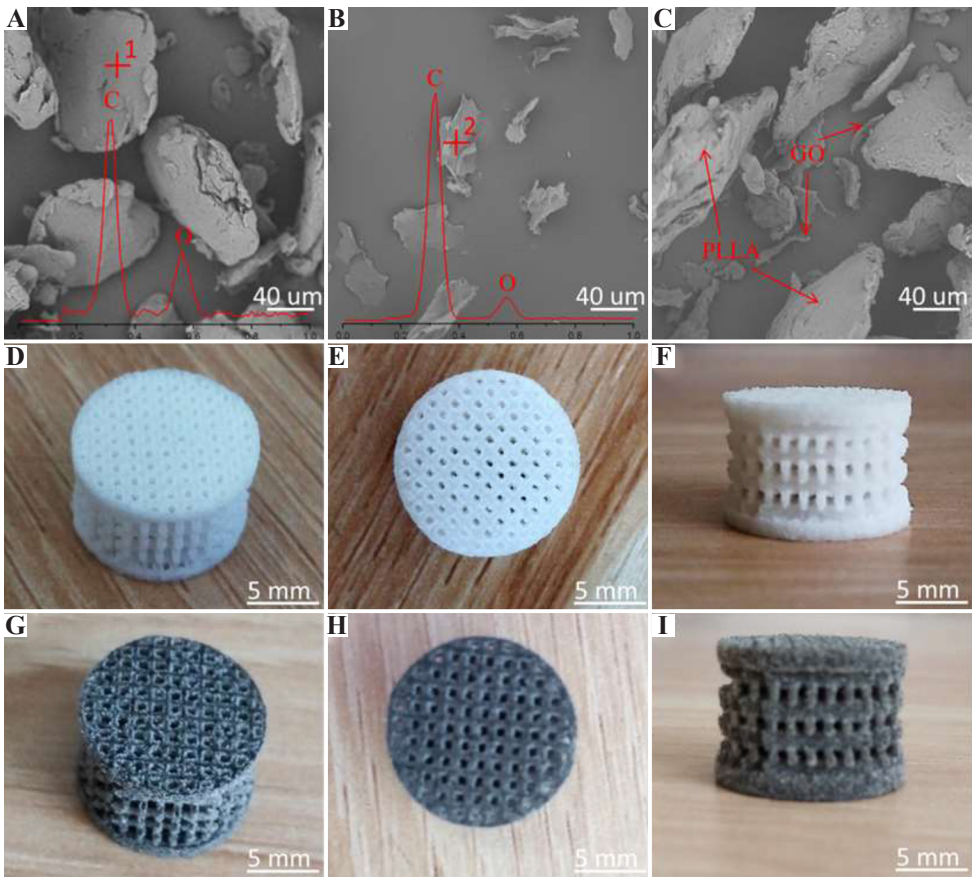

Figure 1. (A-C) SEM of PLLA, GO and PLLA/GO composite powders, (D-F) axis view, top view, and front view of the PLLA scaffold and (G-I) axis view, top view and front view of the PLLA/GO scaffold fabricated by SLS. PLLA and PLLA/GO scaffolds had similar shape sizes and interconnected porous structures.

3.2 Characterization

Raman spectroscopy was used to demonstrate the presence of GO in PLLA scaffolds and their interactions. As shown in **Figure 2A**, the Raman spectrum obtained for PLLA showed three obvious characteristic peaks at 871 cm^{-1}, 1451 cm^{-1}, and 2942 cm^{-1}. The PLLA/GO scaffold also showed three characteristic peaks in the same position. There were two new characteristic peaks appearing in the PLLA/GO spectra, representing the D (1330 cm^{-1}) and G (1544 cm^{-1}) peaks of GO, which confirmed the presence of GO in the PLLA matrix. To explore the interaction between PLLA and GO, the partial spectra in **Figure 2A** were magnified and showed, as shown in **Figure 2B**. The characteristic peaks at 1761 cm^{-1} were C=O stretch of PLLA. Interestingly, the C=O peak shifted to high wavenumber when GO was introduced into the PLLA scaffold, demonstrating the possibly interaction between PLLA and GO because of hydrogen bonding. Geng *et al*. also reported a similar conclusion[48].

Water contact angle measurement was used to detect the hydrophilic properties of PLLA and PLLA/GO scaffolds with 0.3%, 0.6%, 0.9%, and 1.2% GO. The water contact angle of PLLA was 88.98°, which indicated that it had poor hydrophilic properties. The water contact angle began to decrease when GO was introduced. Water contact angle continuously decreased with increasing GO content, indicating that GO was beneficial to improve the hydrophilic properties of the PLLA scaffold. To further explore the

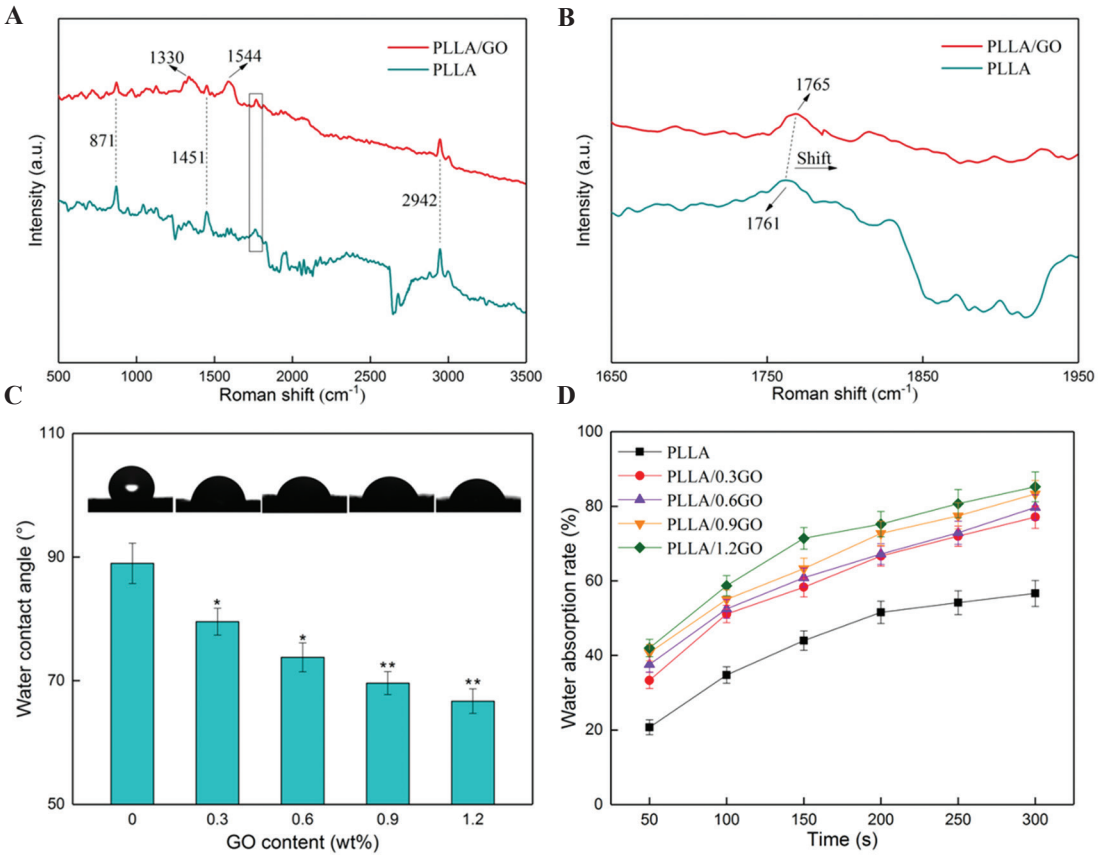

Figure 2. (A) Raman spectra of PLLA and PLLA/GO, and (B) partial magnification in spectra a. (C) Water contact angle of the PLLA scaffolds with 0%, 0.3%, 0.6%, 0.9%, and 1.2 wt % GO. (D) Water absorption rate of the PLLA scaffolds with 0%, 0.3%, 0.6%, 0.9%, and 1.2 wt % GO after immersing in aqueous solution for different time. GO was successfully introduced into the PLLA scaffold and interacted with PLLA. Hydrophilicity and water absorption capacity increased with increasing GO.

hydrophilic properties of scaffold, the water uptake of the scaffold was evaluated. The water absorption of the PLLA scaffold increased with the immersion time, while the slope of the increase in water absorption rate was decreased. Similarly, water absorption increased with the introduction of GO due to a large amount of hydrophilic groups on the surface of GO, which enhanced the water absorption capacity of scaffold.

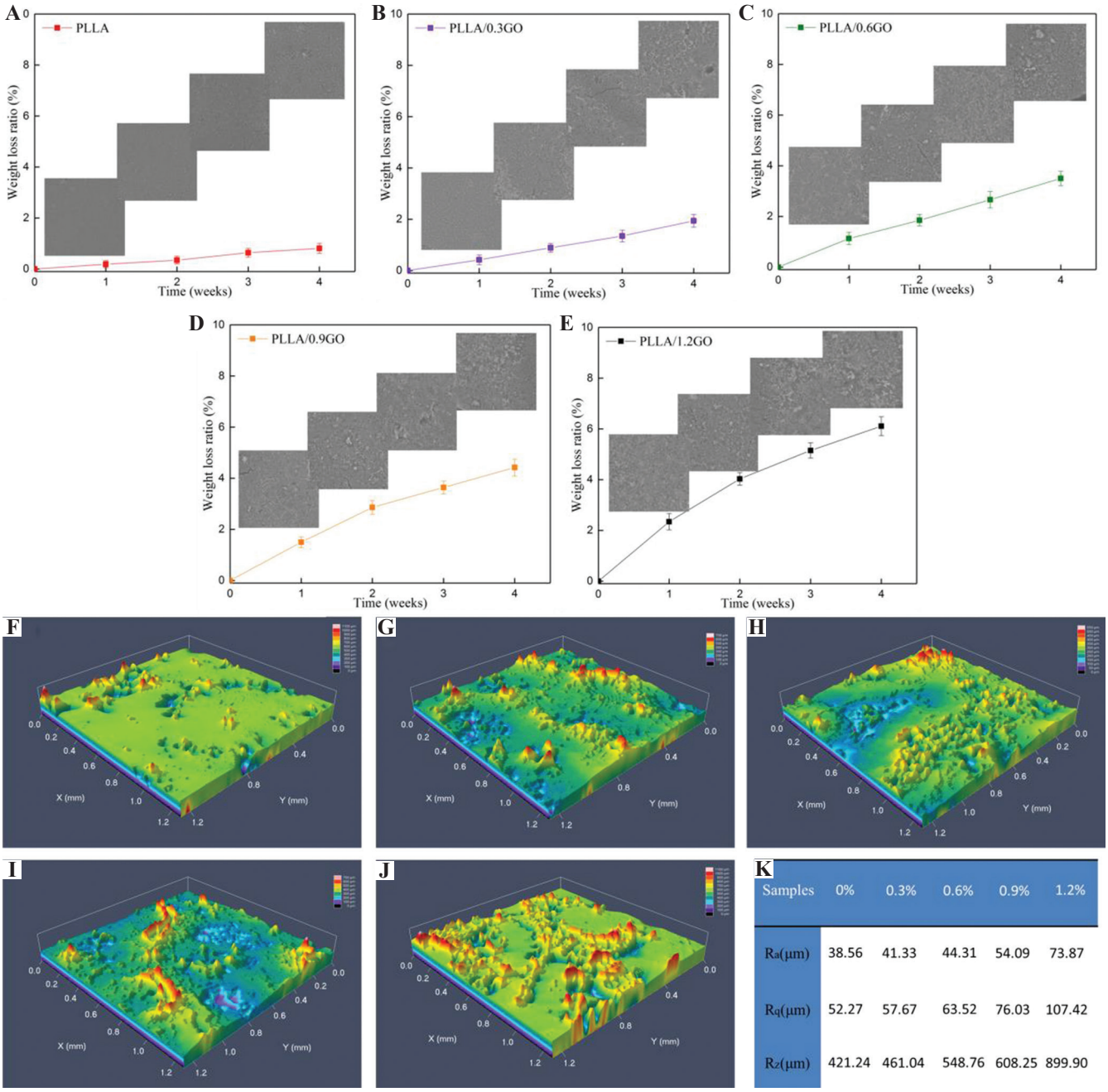

Figure 3. (A-E) The mass loss ratio and degradation morphology of PLLA scaffolds with 0%, 0.3%, 0.6%, 0.9%, and 1.2 wt % GO after immersing in PBS solution for 1, 2, 3, and 4 weeks, respectively. (F-J) Three-dimensional surface morphologies of PLLA/GO samples with 0%, 0.3%, 0.6%, 0.9%, and 1.2% GO after degradation for 4 weeks. (J) Surface roughness (Ra, Rq, and Rz) date of different ratios of PLLA/GO samples. Degradation of PLLA accelerated and surface roughness increased with increasing GO content.

3.3 Degradation properties

Degradation morphologies and mass loss of different proportions of PLLA/GO scaffolds are shown in **Figure 3A-E**. The surface of the PLLA sample did not change clearly after immersing in PBS for 1, 2, and 3 weeks (**Figure 3A**). When the immersing time was extended to 4 weeks, the surface of the sample became rough and surface roughness of Ra, Rq, and Rz was 38.56 μm, 52.27 μm, and 421.24 μm, respectively, and some precipitated particles appeared. Correspondingly, the mass loss of samples was measured to quantitatively assess the degree of degradation. It could be seen that PLLA had a small mass loss after 4 weeks of degradation and less than 1%. When 0.3% GO was introduced into PLLA, it could be seen that the surface of the PLLA/0.3 GO sample became rough after 1 week of soaking (**Figure 3B**). After 4 weeks of soaking, the surface began to appear degraded holes. As the GO content continued to increase, the surface of the samples became rougher and the quality loss also increased (**Figure 3C, D**). After soaking for 4 weeks, the surface of the PLLA/1.2 GO sample became rough with a Ra value of 73.87 μm, a Rq value of 107.42μm, and a Rz value of 899.90 μm and uneven, and the mass loss was close to 6%, indicating significant degradation and confirming that GO accelerated the degradation of PLLA (**Figure 3E**). Three-dimensional surface morphologies of PLLA/GO samples with 0%, 0.3%, 0.6%, 0.9%, and 1.2% GO after degradation for 4 weeks are shown in **Figure 3F-J**. It can be clearly seen that the surface of PLLA/GO samples after degradation became rougher as the GO content increased (**Figure 3K**).

3.4 Degradation mechanism

It was proved by the degradation of morphology and mass loss experiments that the introduction of GO could accelerate the degradation of PLLA. The explanation mechanism was also analyzed (**Figure 4**) as follows: First, the surface of GO contained a large number of oxygen-containing functional groups, and these functional groups had good hydrophilicity[49,50]. The introduction of GO

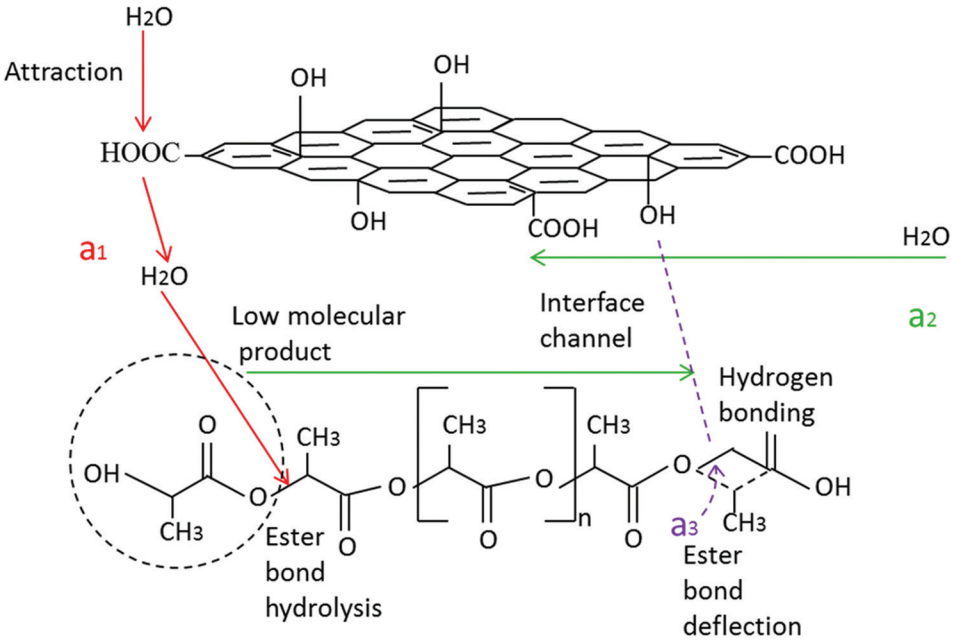

Figure 4. Schematic of GO promoting the degradation of PLLA. GO accelerated the degradation of PLLA could be divided into three parts. a_1: Hydrophilic GO attracted water molecules. a_2: The interface channels between GO and PLLA facilitated the intrusion of water molecules and discharged of degraded low molecular products. a_3: The hydrogen bonding between PLLA and GO induced the ester bond to deflect toward the interfaces, making the water molecules easily to attack the ester bond.

promoted the hydrophilic properties of the scaffold is demonstrated in **Figure 2**. Good hydrophilicity facilitated liquid intrusion into the scaffold. This process was described as a_1 and represented by the red line. Second, GO was a sheet-like structure with a large surface area and could form many interfaces with the PLLA matrix in the scaffold. These interfaces could be regarded as microchannels. On the one hand, the solution could enter the inside of the scaffold through the interface channels to promote the hydrolysis of ester bonds of the PLLA. On the other hand, these small molecule products produced by hydrolysis of the ester bond could also be discharged through the interface channels. This process was described as a_2 and was represented by the green line. Third, the oxygen-containing functional groups on the surface of GO could form hydrogen bond interaction with the ester bond of PLLA[51]. This interaction can induce the ester bond of PLLA to deflect toward the interface, promoting it be attacked by water molecules, thus accelerating the degradation of PLLA. This process was described as a_3 and was represented by the purple line.

3.5 Mechanical property

The compressive properties of samples containing different proportions of GO are presented in **Figure 5A and B**. The compressive strength of PLLA was 23.60 MPa, which was consistent with the report of Zhang[52]. The compressive strength was 37.51 MPa and increased by 58.9% when 0.3% GO was introduced. As the GO content continued to increase, the compressive strength gradually increased and reached a peak of 56.19 MPa when 0.9% GO was introduced. Nevertheless, when the content of GO increased from 0.9 wt% to 1.2 wt%, the compression strength of scaffolds decreased slightly from 56.19 MPa to 54.74 MPa. Similarly,

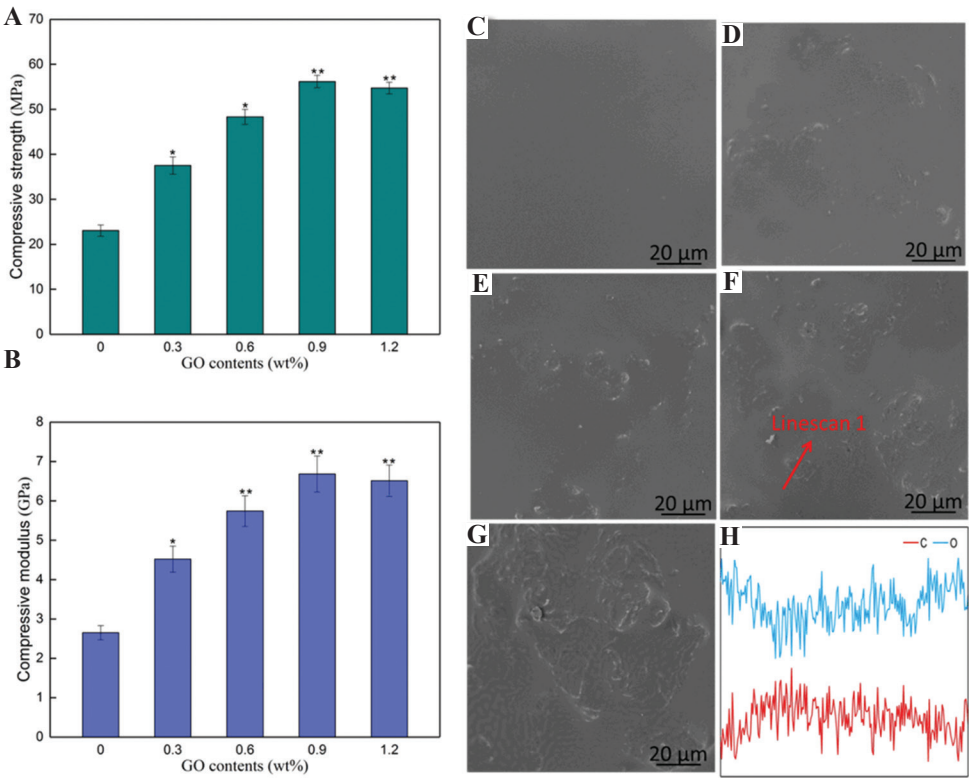

Figure 5. (A) Compressive strength and (B) compressive modulus of PLLA and PLLA/GO scaffolds with 0.3%, 0.6%, 0.9%, and 1.2 wt% GO. (C-G) Surface dispersion state of GO in PLLA substrate with 0%, 0.3%, 0.6%, 0.9%, and 1.2 wt% GO. (H) Linescan 1 showed the distribution of elements C and O. The compressive strength and modulus increased with increasing GO content, while there was a slight decrease when 1.2% GO was introduced. GO was uniformly dispersed in the PLLA matrix, but agglomerates formed when the GO content was further increased.

compression modulus also had a similar trend (**Figure 5B**). To investigate the cause of the change in compressive properties, the surface morphologies of the samples were observed by SEM, as shown in **Figure 5C-G**. The surface of PLLA was smooth and flat (**Figure 5C**), some flakes began to appear on the surface of the PLLA/0.3 GO sample (**Figure 5D**), and as the GO content continued to increase, more and more flakes appeared (**Figure 5E and F**). A large number of flakes were stacked together to form continuous agglomerates when 1.2% GO was introduced (**Figure 5G**). Red line scan 1 was used to distinguish the difference by penetrating the matrix and flakes (**Figure 5H**). In the direction of the line scan, the content of the C element first increased and then decreased. On the contrary, the content of the O element first decreased and then increased. The ratio of C to O elements proved that the flakes were GO. When the line scan 1 was moved from PLLA to GO, since the ratio of C to O in GO was higher than that of PLLA, so the C element rises. Then, when the line scan moved from GO to PLLA, the C element began to drop. The EDS of the powders in **Figure 1** also confirmed that the ratio of C to O in GO was larger than that in PLLA. The trend of the elements in the line scan 1 also confirmed that the flakes were GO. GO was a sheet-like structure with excellent mechanical strength, it could be used as a reinforcing phase to improve the compression properties of the scaffolds. However, when an excessive amount of GO was introduced, it was difficult to uniformly disperse and formed agglomerates, which formed defects in the matrix, resulting in a decrease in compressive strength.

The tensile strength and modulus of samples containing different GO ratios are measured and presented in **Figure 6A and B**. The tensile strength of PLLA was 16.90 MPa. As the GO content increased, the tensile strength also increased, but the tensile strength decreased when 1.2% GO was introduced. The compressive modulus was also increased first and then decreased. To explore the mechanism of tensile properties change, the fracture surface morphologies were analyzed by SEM. The fracture surface of PLLA was smooth with no obvious wrinkles, indicating that PLLA was brittle material (**Figure 6C**). Todo *et al*. also confirmed that the fracture mode of PLLA was brittle fracture[53]. When 0.3% GO was introduced, the fracture surface began to become rough and uneven (**Figure 6D**). GO sheets were embedded in the PLLA matrix when the content was increased to 0.6%, which was indicated by the red arrow (**Figure 6D**). When the GO content was further increased, more GO was embedded on the matrix, and the embedded GO could effectively transfer and consume external force, thereby increasing the tensile strength of the scaffolds. However, when the GO content was further increased, some of the GO sheets accumulated to form agglomeration, which weakened the enhancement of GO to PLLA, and thus the tensile strength and modulus decreased (**Figure 6G**).

3.6 Bioactivity

Good bioactivity is one of the required properties for bone scaffolds[54,55]. PLLA and PLLA/GO scaffolds with 0.3%, 0.6%, 0.9%, and 1.2 wt% GO were immersed in SBF for 4 weeks to assess bioactivity. There did not have a calcium-phosphorus layer appearing on the surface of PLLA after immersing in SBF, indicating that PLLA lacked good biological activity (**Figure 7A**). Zhou also has similar reports[56]. Calcium-phosphorus layer appeared on the surface of the sample when 0.3% GO was introduced into PLLA (**Figure 7B**). As the GO content continued to increase, there was more calcium-phosphorus layer on the surface of the sample, and the particle size was getting larger and larger (**Figure 7C-E**). Point 1 in **Figure 7E** was used to measure the elements of white particles by EDS, as shown in **Figure 7F**. There were Ca and P elements in the EDS map, which could prove that the white particles were the calcium-phosphorus layer. The surface of GO contained a large number of functional groups, such as –COOH and –OH[57-59]. These functional groups could adsorb Ca ions in SBF, and Ca ions could continue to adsorb PO_4 ions to nucleate and grow, thereby forming a calcium-phosphorus layer[60,61].

3.7 Cytocompatibility

Fluorescence staining experiment and CCK8 experiments were used to assess cell compatibility

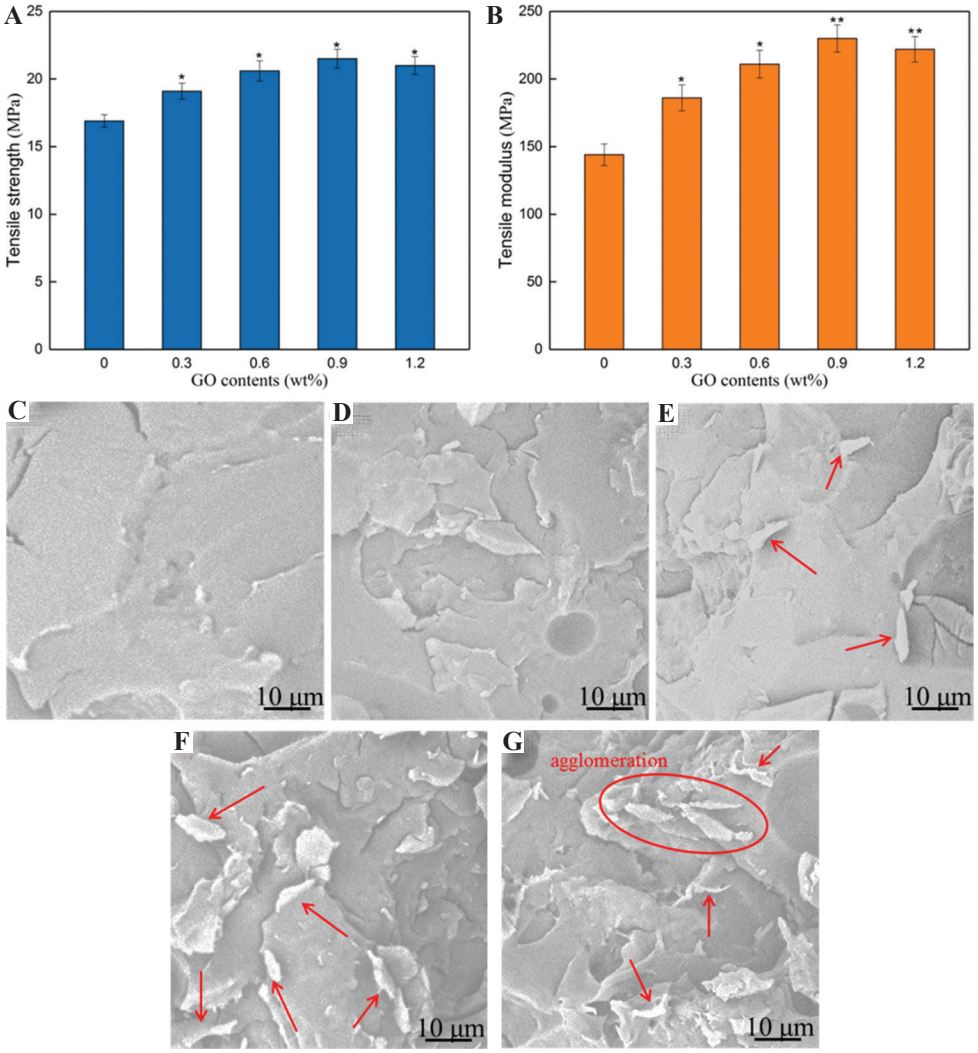

Figure 6. (A) Tensile strength and (B) tensile modulus of PLLA and PLLA/GO scaffolds with 0.3%, 0.6%, 0.9%, and 1.2 wt% GO. (C-G) Fracture morphology of GO in PLLA substrate with 0%, 0.3%, 0.6%, 0.9%, and 1.2 wt% GO. Tensile strength and modulus increased first and then decreased with increasing GO content. The fracture surface of PLLA was smooth, the introduction of GO rendered the fracture surface rough, and more GO was embedded in the PLLA matrix with the increase of GO.

by cultured on PLLA and PLLA/GO samples. MG63 cell was cultured on PLLA samples for 1 day, and the stained image is visualized in **Figure 8A**, living cells were dyed green by fluorescence, and showed spherical morphologies. The number of cells on PLLA/0.9 GO was more than that on PLLA after 1 day (**Figure 8B**). As the culture time of the cells on PLLA was extended, the number of cells was increasing (**Figure 8C and D**). After 5 days of culture, the cells on PLLA began to change from spherical to fusiform indicated by the red arrow. In contrast, cells on the PLLA/0.9 GO samples exhibited a more pronounced fusiform appearance compared to PLLA and covered almost the surface of the sample. CCK-8 experiment was used to qualitatively evaluate cytocompatibility. Compared to PLLA, the number of cells on PLLA/GO was higher than PLLA at any time (**Figure 8G**), indicating that the introduction of GO was beneficial to cell compatibility.

4 Conclusions

In this study, GO was introduced into PLLA to accelerate its degradation. PLLA/GO scaffolds were prepared by SLS and showed a three-dimensional

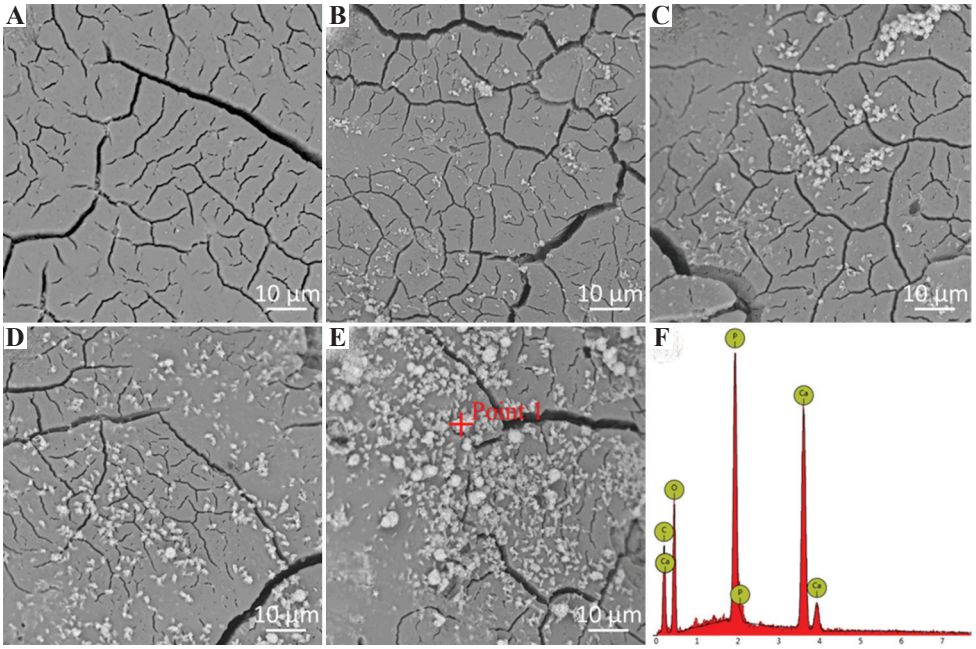

Figure 7. (A-F) Formation of a calcium-phosphorus layer of PLLA and PLLA/GO scaffolds with 0.3%, 0.6%, 0.9%, and 1.2 wt% GO after immersing in the SBF solution for 4 weeks. Samples containing GO possessed the ability of forming a calcium-phosphorus layer, while PLLA had no calcium-phosphorus layer formation.

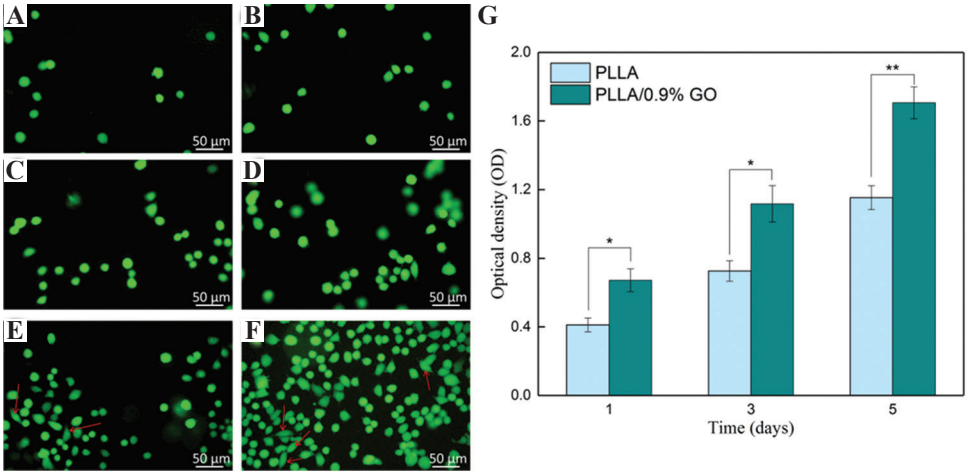

Figure 8. (A,C,E) The fluorescence staining of MG63 cells fostered on the PLLA scaffolds for 1, 3, and 5 days, (B,D,F) the fluorescence staining of MG63 cells fostered on the PLLA/0.9 GO scaffolds for 1, 3, and 5 days, respectively. (G) CCK-8 experiment of MG63 cells fostered on the PLLA and PLLA/0.9 GO scaffolds for 1, 3, and 5 days, respectively. Cells on PLLA/0.9 GO samples had better cell morphology and more cell number compared to PLLA.

porous structure. The introduction of GO increased the hydrophilicity and water absorption of the scaffolds, accelerated the breakage of the PLLA ester bonds. As a result, the surface of PLLA became rough and mass loss was increased from 0.81% to 6.11% after immersing for 4 weeks. Besides, the tensile strength was increased by 24.3% and compressive strength was also increased by 137.4%, respectively.

In addition, the scaffold also demonstrated good bioactivity and cytocompatibility. This study suggested that PLLA/GO scaffolds may be promising for bone tissue engineering.

Acknowledgments

This work was supported by the following funds: (1) The Natural Science Foundation of China (51935014, 51905553, 81871494, 81871498, 51705540); (2) Hunan Provincial Natural Science Foundation of China (2019JJ50774, 2018JJ3671, 2019JJ50588); (3) JiangXi Provincial Natural Science Foundation of China (20192ACB20005); (4) Guangdong Province Higher Vocational Colleges & Schools Pearl River Scholar Funded Scheme (2018); (5) The Open-End Fund for the Valuable and Precision Instruments of Central South University; (6) National Postdoctoral Program for Innovative Talents (BX201700291); (7) The China Postdoctoral Science Foundation (2018M632983); (8) The Project of Hunan Provincial Science and Technology Plan (2017RS3008); (9) The Project of State Key Laboratory of High-Performance Complex Manufacturing, Central South University; and (10) The Fundamental Research Funds for the Central Universities of Central South University (2019zzts141, CX20190197).

References

1. An J, Teoh JE, Suntornnond R, *et al.*, 2015, Design and 3D Printing of Scaffolds and Tissues. *Engineering*, 1:261–268.
2. Liu F, Mishbak H, Bartolo PJ, 2019, Hybrid Polycaprolactone/ Hydrogel Scaffold Fabrication and in-process Plasma Treatment Using PABS. *Int J Bioprint*, 5:174.
3. Cardoso, GB, Perea, GN, D'Avila, MA, *et al.*, 2011, Initial Study of Electrospinning PCL/PLLA Blends. *Adv Mater Phys Chem*, 1:94–98.
4. Saito Y, Minami K, Kobayashi M, *et al.*, 2002, New Tubular Bioabsorbable Knitted Airway Stent: Biocompatibility and Mechanical Strength. *J Thorac Cardiovasc Surg*, 123:161–167. DOI: 10.1067/mtc.2002.118503.
5. Shuai C, Yang W, He C, *et al.*, 2020, A Magnetic Micro-environment in Scaffolds for Stimulating Bone Regeneration. *Mater Des*, 185:108275. DOI: 10.1016/j.matdes.2019.108275.
6. Weng Y, Jin Y, Meng Q, *et al.*, 2013, Biodegradation Behavior of Poly (Butylene Adipate-co-terephthalate) (PBAT), Poly (Lactic Acid)(PLA), and their Blend under Soil Conditions. *Polym Test*, 32:918–926. DOI: 10.1016/j.polymertesting.2013.05.001.
7. Shuai C, Li Y, Feng P, *et al.*, 2019, Montmorillonite Reduces Crystallinity of Poly-l-lactic Acid Scaffolds to Accelerate Degradation. *Polym Adv Technol*, 30:2425–2435. DOI: 10.1002/pat.4690.
8. Tanaka M, Tanaka H, Hojo M, *et al.*, 2019, Change in Deformation/Fracture Behavior of Interface-controlled HAP/PLLA Composites by Hydrolysis, Proceedings of the 17th International Conference on Composite Materials, CD-ROM.
9. Yang Y, He C, Dianyu E, *et al.*, 2019, Mg Bone Implant: Features, Developments and Perspectives. *Mater Des*, 2019:108259.
10. Lee JH, Park TG, Park HS, *et al.*, 2003, Thermal and Mechanical Characteristics of Poly(L-lactic acid) Nanocomposite Scaffold. *Biomaterials*, 24:2773–2778. DOI: 10.1016/s0142-9612(03)00080-2.
11. Chen X, Wu X, Fan Z, *et al.*, 2018, Biodegradable Poly (Trimethylene carbonate-b-(L-lactide-ran-glycolide) Terpolymers with Tailored Molecular Structure and Advanced Performance. *Polym Adv Technol*, 29:1684–1696. DOI: 10.1002/pat.4272.
12. Shuai C, Yang Y, Feng P, *et al.*, 2018, A Multi-scale Porous Scaffold Fabricated by a Combined Additive Manufacturing and Chemical Etching Process for Bone Tissue Engineering. *Int J Bioprint*, 4:133. DOI: 10.18063/ijb.v4i1.133.
13. Shie MY, Fang HY, Lin YH, *et al.*, 2019, Application of Piezoelectric Cells Printing on Three-dimensional Porous Bioceramic Scaffold for Bone Regeneration. *Int J Bioprint*, 5:210. DOI: 10.18063/ijb.v5i2.210.
14. Yang Y, Wang G, Liang H, *et al.*, 2019, Additive manufacturing of bone scaffolds. *Int J Bioprint*, 5:184.
15. Ji JH, Park IS, Kim YK, *et al.*, 2015, Influence of Heat Treatment on Biocorrosion and Hemocompatibility of Biodegradable Mg-35Zn-3Ca Alloy. *Adv Mater Sci Eng*, 17:1–10. DOI: 10.1155/2015/318696.
16. Kang Y, Chen P, Shi X, *et al.*, 2018, Multilevel Structural Stereocomplex Polylactic Acid/collagen Membranes by Pattern Electrospinning for Tissue Engineering. *Polymer*, 156:250–260. DOI: 10.1016/j.polymer.2018.10.009.
17. Buwalda SJ, Dijkstra PJ, Calucci L, *et al.*, 2019, Influence of Amide versus Ester Linkages on the Properties of Eight-Armed PEG-PLA Star Block Copolymer Hydrogels. *Biomacromolecules*, 11:224–232. DOI: 10.1021/bm901080d.
18. Kontakis GM, Pagkalos JE, Tosounidis TI, *et al.*, 2007,

Bioabsorbable Materials in Orthopaedics. *Acta Orthop Belg*, 73:159–169.

19. Shuai C, Zan J, Yang Y, *et al*., 2019, Surface Modification Enhances Interfacial Bonding in PLLA/MgO Bone Scaffold. Mater Sci Eng C, 108:110486. DOI: 10.1016/j.msec.2019.110486.
20. Ding L, Wei Y, Wang Y, *et al.*, 2017, A Two-Dimensional Lamellar Membrane: MXene Nanosheet Stacks. *Angew Chem Int Ed Engl*, 56:1825–1829. DOI: 10.1002/anie.201609306.
21. Shen J, Hu Y, Shi M, *et al.*, 2009, Fast and Facile Preparation of Graphene Oxide and Reduced Graphene Oxide Nanoplatelets. *Chem Mater*, 21:3514–3520. DOI: 10.1021/cm901247t.
22. Wang G, Qi F, Yang W, *et al*., 2019, Crystallinity and Reinforcement in Poly-l-lactic Acid Scaffold Induced by Carbon Nanotubes. *Adv Polym Technol*, 2019:8625325.
23. Yoon OJ, Sohn IY, Kim DJ, *et al.*, Enhancement of Thermomechanical Properties of poly(D,L-lactic-co-glycolic acid) and Graphene Oxide Composite Films for Scaffolds. *Macromol Res*, 20:789–794. DOI: 10.1007/s13233-012-0116-0.
24. He S, Yang S, Zhang Y, Li X, *et al*., 2019, LncRNA ODIR1 Inhibits Osteogenic Differentiation of hUC-MSCs through the FBXO25/H2BK120ub/H3K4me3/OSX Axis. *Cell Death Dis*, 10:1–16. DOI: 10.1038/s41419-019-2148-2.
25. Depan D, Girase B, Shah JS, *et al.*, 2011, Structure-Process-Property Relationship of the Polar Graphene Oxide-mediated Cellular Response and Stimulated Growth of Osteoblasts on Hybrid Chitosan Network Structure Nanocomposite Scaffolds. *Acta Biomater*, 7:3432–3445. DOI: 10.1016/j.actbio.2011.05.019.
26. Xiong G, Luo H, Zuo G, *et al.*, Novel Porous Graphene Oxide and Hydroxyapatite Nanosheets-reinforced Sodium Alginate Hybrid Nanocomposites for Medical Applications. *Mater Charact*, 107:419–425. DOI: 10.1016/j.matchar.2015.07.016.
27. Chen J, Shi X, Ren L, *et al.*, 2016, Graphene Oxide/PVA Inorganic/Organic Interpenetrating Hydrogels with Excellent Mechanical Properties and Biocompatibility. *Carbon*, 111:18–27. DOI: 10.1016/j.carbon.2016.07.038.
28. Zhao X, Zhang Q, Chen D, *et al.*, 2010, Enhanced Mechanical Properties of Graphene-Based Poly(vinyl alcohol) Composites. *Macromolecules*, 44:2392–2392. DOI: 10.1021/ma200335d.
29. Wang K, Ruan J, Song H, *et al.*, 2011, Biocompatibility of Graphene Oxide. *Nanoscale Res Lett*, 6:1–8.
30. Gao C, Yao M, Shuai C, *et al.*, 2019, Nano-SiC Reinforced Zn Biocomposites Prepared via Laser Melting: Microstructure, Mechanical Properties and Biodegradability. *J Mater Sci Technol*, 35:2608–2617. DOI: 10.1016/j.jmst.2019.06.010.
31. Rodríguez-Lozano FJ, García-Bernal D, Aznar-Cervantes S, *et al.*, 2014, Effects of Composite Films of Silk Fibroin and Graphene Oxide on the Proliferation, Cell Viability and Mesenchymal Phenotype of Periodontal Ligament Stem Cells. *J Mater Sci Mater Med*, 25:2731–2741. DOI: 10.1007/s10856-014-5293-2.
32. Li W, Xu Z, Chen L, *et al.*, 2014, A Facile Method to Produce Graphene Oxide-g-poly (L-lactic acid) as an Promising Reinforcement for PLLA Nanocomposites. *Chem Eng J*, 237:291–299. DOI: 10.1016/j.cej.2013.10.034.
33. Zhang K, Zheng H, Liang S, *et al.*, 2016, Aligned PLLA Nanofibrous Scaffolds Coated with Graphene Oxide for Promoting Neural Cell Growth. *Acta Biomater*, 37:131–142. DOI: 10.1016/j.actbio.2016.04.008.
34. Pan LH, Kuo SH, Lin TY, *et al.*, 2017, An Electrochemical Biosensor to Simultaneously Detect VEGF and PSA for Early Prostate Cancer Diagnosis Based on Graphene Oxide/ssDNA/PLLA Nanoparticles. *Biosens Bioelectron*, 89:598–605. DOI: 10.1016/j.bios.2016.01.077.
35. Chen Q, Mangadlao JD, Wallat J, *et al.*, 2017, 3D Printing Biocompatible Polyurethane/Poly (Lactic Acid)/Graphene Oxide Nanocomposites: Anisotropic Properties. *ACS Appl Mater Interfaces*, 9:4015–4023. DOI: 10.1021/acsami.6b11793.
36. Yuan S, Shen F, Chua CK, *et al.*, 2019, Polymeric Composites for Powder-based Additive Manufacturing: Materials and Applications. *Prog Polym Sci*, 91:141–168. DOI: 10.1016/j.progpolymsci.2018.11.001.
37. Lee JY, An J, Chua CK, 2017, Fundamentals and Applications of 3D Printing for Novel Materials. *Appl Mater Today*, 7:120–133.
38. Zhuang P, Sun AX, An J, *et al.*, 2018, 3D Neural Tissue Models: From Spheroids to Bioprinting. *Biomaterials*, 154:113–133. DOI: 10.1016/j.biomaterials.2017.10.002.
39. Mir TA, Iwanaga S, Kurooka T, *et al.*, 2019, Biofabrication Offers Future Hope for Tackling Various Obstacles and Challenges in Tissue Engineering and Regenerative Medicine: A Perspective. *Int J Bioprint*, 5:153. DOI: 10.18063/ijb.v5i1.153.
40. Ng WL, Chua CK, Shen YF, 2019, Print me an Organ! Why we are not there yet. *Prog Polym Sci*, 97:101145. DOI: 10.1016/j.progpolymsci.2019.101145.
41. Lee JM, Sing SL, Zhou M, *et al.*, 2018, 3D Bioprinting Processes: A Perspective on Classification and Terminology. *Int J Bioprint*, 4:151. DOI: 10.18063/ijb.v4i2.151.

42. Zhuang P, Ng WL, An J, *et al.*, 2019, Layer-by-Layer Ultraviolet Assisted Extrusion-based (UAE) Bioprinting of Hydrogel Constructs with High Aspect Ratio for Soft Tissue Engineering Applications. *PLoS One*, 14:e0216776. DOI: 10.1371/journal.pone.0216776.
43. Lins LC, Wianny F, Livi S, *et al.*, Development of Bioresorbable Hydrophilic-hydrophobic Electrospun Scaffolds for Neural Tissue Engineering. *Biomacromolecules*, 17:3172–3187. DOI: 10.1021/acs.biomac.6b00820.
44. Gao C, Yao M, Li S, *et al.*, 2019, Highly Biodegradable and Bioactive Fe-Pd-Bredigite Biocomposites Prepared by Selective Laser Melting. *J Adv Res*, 20:91–104. DOI: 10.1016/j.jare.2019.06.001.
45. Wei G, Ma PX, 2004, Structure and Properties of Nano-Hydroxyapatite/Polymer Composite Scaffolds for Bone Tissue Engineering. *Biomaterials*, 25:4749–4757. DOI: 10.1016/j.biomaterials.2003.12.005.
46. Xia W, Chang J, 2010, Bioactive Glass Scaffold with Similar Structure and Mechanical Properties of Cancellous Bone. *J Biomed Mater Res Part B Appl Biomater*, 95:449–455. DOI: 10.1002/jbm.b.31736.
47. Feng P, Kong Y, Yu L, *et al.*, 2019, Molybdenum Disulfide Nanosheets Embedded with Nanodiamond Particles: Co-dispersion Nanostructures as Reinforcements for Polymer Scaffolds. *Appl Mater Today*, 17:216–226. DOI: 10.1016/j.apmt.2019.08.005.
48. Geng LH, Peng XF, Jing X, *et al.*, Investigation of Poly(l-lactic acid)/Graphene Oxide Composites Crystallization and Nanopore Foaming Behaviors via Supercritical Carbon Dioxide Low Temperature Foaming. *J Mater Res*, 31:348–359. DOI: 10.1557/jmr.2016.13.
49. Morales-Narváez E, Baptista-Pires L, Zamora-Gálvez A, *et al.*, 2017, Graphene-Based Biosensors: Going Simple. *Adv Mater*, 29:1604905. DOI: 10.1002/adma.201604905.
50. Kaniyoor A, Baby TT, Ramaprabhu S, 2010, Graphene Synthesis via Hydrogen Induced Low Temperature Exfoliation of Graphite Oxide. *J Mater Chem*, 20:8467–8460. DOI: 10.1039/c0jm01876g.
51. Eckhart KE, Holt BD, Laurencin MG, *et al.*, 2019, Covalent Conjugation of Bioactive Peptides to Graphene Oxide for Biomedical Applications. *Biomater Sci*, 7:3876–3885. DOI: 10.1039/c9bm00867e.
52. Zhang P, Wang BT, Gao D, *et al.*, The Study on the Mechanical Properties of Poly (Lactic Acid)/Straw Fiber Composites. *Appl Mech Mater*, 2012:312–315.
53. Todo M, Park SD, Arakawa K, *et al.*, 2006, Relationship between Microstructure and Fracture Behavior of Bioabsorbable HA/PLLA Composites. *Compos Part A Appl Sci Manuf*, 37:2221–2225. DOI: 10.1016/j.compositesa.2005.10.001.
54. Yang Y, He C, Dianyu E, *et al.*, 2019, Mg Bone Implant: Features, Developments and Perspectives. *Mater Des*, 185:108259. DOI: 10.1016/j.matdes.2019.108259.
55. Shuai C, Liu G, Yang Y, *et al.*, 2020, Functionalized $BaTiO_3$ Enhances Piezoelectric Effect towards Cell Response of Bone Scaffold. *Colloids Surf B Biointerfaces*, 185:110587. DOI: 10.1016/j.colsurfb.2019.110587.
56. Zhou Z, Liu L, Liu Q, *et al.*, 2012, Effect of Surface Modification of Bioactive Glass on Properties of Poly-L-Lactide Composite Materials. *J Macromol Sci Part B*, 51:1637–1646. DOI: 10.1080/00222348.2012.672295.
57. Alexa A, Rahnenführer J, Lengauer TR, 2006, Improved Scoring of Functional Groups from Gene Expression Data by Decorrelating GO Graph Structure. *Bioinformatics*, 22:1600–1607. DOI: 10.1093/bioinformatics/btl140.
58. Shuai C, Cheng Y, Yang Y, *et al.*, 2019, Laser Additive Manufacturing of Zn-2Al Part for Bone Repair: Formability, Microstructure and Properties. *J Alloys Compd*, 798:606–615. DOI: 10.1016/j.jallcom.2019.05.278.
59. Yang X, Li X, Ma X, *et al.*, 2014, Carbonaceous Impurities Contained in Graphene Oxide/Reduced Graphene Oxide Dominate their Electrochemical Capacitances. *Electroanalysis*, 26:139–146. DOI: 10.1002/elan.201300128.
60. Wang H, Zhao S, Xiao W, *et al.*, 2016, Influence of Cu Doping in Borosilicate Bioactive Glass and the Properties of its Derived Scaffolds. *Mater Sci Eng C*, 58:194–203. DOI: 10.1016/j.msec.2015.08.027.
61. Suntornnond R, An J, Chua CK, 2017, Roles of Support Materials in 3D Bioprinting-Present and Future. *Int J Bioprint*, 3:321–328. DOI: 10.18063/ijb.2017.01.006.

ORIGINAL ARTICLE

Matrix-Assisted Pulsed laser Evaporation-deposited Rapamycin Thin Films Maintain Antiproliferative Activity

Rodica Cristescu[1], Irina Negut[1], Anita Ioana Visan[1], Alexander K. Nguyen[2,4], Andrew Sachan[3], Peter L. Goering[4], Douglas B. Chrisey[5], Roger J. Narayan[2*]

[1]Department of Lasers, National Institute for Lasers, Plasma and Radiation Physics, P.O. Box MG-36, Bucharest-Magurele, Romania
[2]UNC/NCSU Joint Department of Biomedical Engineering, Raleigh, North Carolina, USA
[3]Wake Technical Community College, Raleigh, North Carolina, USA
[4]Center for Devices and Radiological Health, U.S. Food and Drug Administration, Silver Spring, Maryland, United States
[5]Department of Physics and Engineering Physics, Tulane University, New Orleans, LA, USA

Abstract: Matrix-assisted pulsed laser evaporation (MAPLE) has many benefits over conventional methods (e.g., dip-coating, spin coating, and Langmuir–Blodgett dip-coating) for manufacturing coatings containing pharmacologic agents on medical devices. In particular, the thickness of the coating that is applied to the surface of the medical device can be tightly controlled. In this study, MAPLE was used to deposit rapamycin-polyvinylpyrrolidone (rapamycin-PVP) thin films onto silicon and borosilicate optical glass substrates. Alamar Blue and PicoGreen studies were used to measure the metabolic health and DNA content of L929 mouse fibroblasts as measures of viability and proliferation, respectively. The cells on the MAPLE-deposited rapamycin-PVP surfaces exhibited 70.6% viability and 53.7% proliferation compared to a borosilicate glass control. These data indicate that the antiproliferative properties of rapamycin were maintained after MAPLE deposition.

Keywords: Rapamycin, Drug delivery, Matrix-assisted pulsed laser evaporation, Thin film

***Corresponding Author**: Roger J. Narayan, UNC/NCSU Joint Department of Biomedical Engineering, Raleigh, North Carolina, USA; roger_narayan@unc.edu; roger_narayan@unc.edu

Received: March 04, 2019; ***Accepted:*** May 16, 2019; ***Published Online:*** Janaury 30, 2020

Citation: Cristescu R, Negut I, Visan AI, *et al*., 2020, Matrix-assisted pulsed laser evaporation-deposited rapamycin thin films maintain antiproliferative activity. *Int J Bioprint*, 6(1):188. DOI: 10.18063/ijb.v6i1.188

1 Introduction

Rapamycin is a water-insoluble macrocyclic triene with antiproliferative properties used in multiple applications[1]. For example, rapamycin has been coated on the surfaces of endovascular stents to prevent neointimal hyperplasia, in which the proliferation of smooth muscle cells causes a reduction in the lumen of the vessel[2,3]. Another application of interest to the medical community is delivering rapamycin to the eye to prevent cell proliferation for the treatment of Sjögren's syndrome, neovascular age-related macular degeneration, diabetic macular edema, and prevention of corneal allograft rejection[4-7]. Shah *et al*. showed that rapamycin eye drops were able to increase tear secretion and affect genes associated with Sjogren's syndrome in male non-obese diabetic mice[8]. However, the use of eye drop solutions is associated with low bioavailability for delivery of the pharmacologic agent to the ocular tissue due to several issues

such as (a) blinking, (b) low corneal membrane permeability, (c) nasolacrimal drainage, (d) non-productive absorption through the conjunctiva, and (e) tearing[4]. Due to the aforementioned issues, the use of eye drop solutions is associated with a tear film residence time of 1–3 min and low bioavailability (1–3%)[4]. This limitation can be addressed with frequent dosing; however, frequent dosing is associated with low patient compliance and a high incidence of side effects[9]. Alternatively, rapamycin can be loaded onto contact lenses to improve drug bioavailability. The most straightforward mechanism to load a pharmacologic agent into contact lenses is by soaking a preformed contact lens in a solution containing the pharmacologic agent before use[10,11]. However, it is difficult to load high-molecular-weight pharmacologic agents within the bulk material of the contact lens by soaking. A coating approach that enables contact lenses to receive a uniform and ultrathin coating of a pharmacologic agent would enable therapeutic contact lenses to be efficiently produced.

Matrix-assisted pulsed laser evaporation (MAPLE) has many benefits over conventional methods for manufacturing coatings containing rapamycin or other pharmacologic agent-containing coatings (e.g., dip-coating, spin coating, and Langmuir–Blodgett dip-coating) such as the facile control of film thickness, roughness and uniformity, the deposition of thin films in a single "step"[12], and the maintenance of pharmacologic agent integrity. For example, poly(D, L) lactic acid/dexamethasone bilayer coatings deposited using MAPLE significantly reduced nitric oxide production in microglial cell cultures demonstrating that the biological function of dexamethasone is retained after the MAPLE process[13]. In addition, MAPLE was previously utilized for the coverage of non-planar substrates[14,15].

The MAPLE process involves laser evaporation of a frozen solution containing the pharmacologic agent in a matrix composed of a volatile solvent (**Figure 1**). Solvents used with MAPLE have a high vapor pressure and preferentially absorb the energy associated with laser wavelength[13]; the absorption of laser energy by the solvent matrix instead of the pharmacologic agent protects the agent from photodegradation. The laser ablation of the solvent matrix carries molecules of the pharmacologic agent into the vacuum where the high vapor pressure solvent is vaporized and

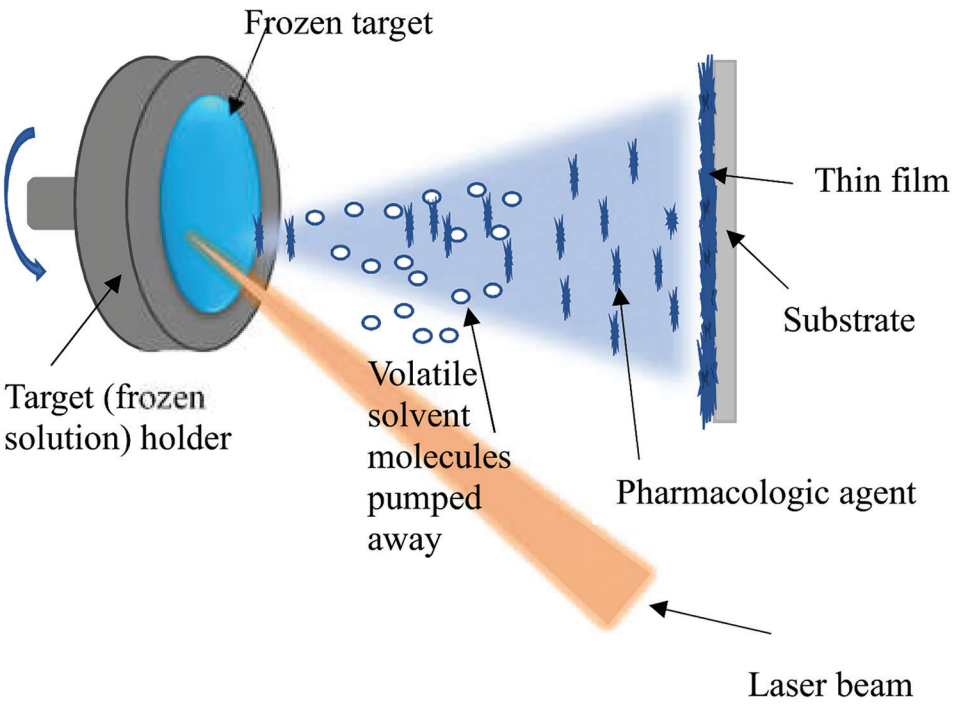

Figure 1. Schematic of the MAPLE process.

removed. Thus, the pharmacologic agent forms most of the molecules deposited onto the substrate.

In this study, MAPLE was used to deposit antiproliferative rapamycin-PVP thin films on glass and silicon (Si) substrates. Alamar Blue and PicoGreen assays were performed to measure the metabolic health and DNA content of L929 mouse fibroblasts as a measure of viability and proliferation, respectively. The results of this study indicate that the MAPLE-deposited rapamycin-PVP thin films successfully reduced cell viability and proliferation.

2 Materials and methods

Homogenous solutions consisting of polyvinylpyrrolidone (PVP), rapamycin, and dimethyl sulfoxide (DMSO) were prepared at room temperature by dissolving 40 mg of PVP in 4 mL DMSO, and then adding 1 mg rapamycin. Before each laser deposition, 3.5 mL of the freshly prepared solution was dropped using a syringe in a copper holder and frozen in liquid nitrogen (77 K) for 30 min. The cryogenic process was accomplished by plunging the target in a Dewar vessel, which was filled with liquid nitrogen. After freezing, the target holder was rapidly mounted inside the deposition chamber.

All MAPLE thin films were fabricated using a 248 nm wavelength KrF* excimer laser source (25 ns pulse duration, 10 Hz repetition rate). The laser was operated at the fluence of 200 mJ/cm^2 per pulse for 101,000 laser pulses. Both the target and substrate were rotated at a rate of 50 Hz during the coating process, while the laser beam was swept over the entire target surface at an incident angle of 45°. The target was maintained at cryogenic temperatures using direct contact with a cooling device connected to a liquid nitrogen reservoir by copper heat pipes. A laser beam homogenizer was used to produce a top-hat energy distribution and increase the deposition area on the substrate. All depositions were performed at a 10^{-1} Pa background pressure; a 5 cm substrate-to-target separation distance was used to deposit the MAPLE coatings.

One-side polished Si <100> and 10 × 10 mm^2 borosilicate optical glass pieces were used as substrates in this study. The substrates were ultrasonically cleaned using ethanol, air dried, then sterilized by exposing to germicidal UV-C radiation from a VL-115UV UV lamp (Vilber, Marne-la-Vallée, France) before deposition.

Rapamycin-PVP thin films were characterized using atomic force microscopy (AFM) and attenuated total reflectance Fourier-transform infrared (ATR-FTIR) spectroscopy. The AFM micrographs were collected in tapping mode using a hard tapping tip (~300 kHz Fo, k ~ 40 N/m) using an Asylum Research MFP-3D instrument (Goleta, CA). Thirty-two scans with a resolution of 4 cm^{-1} were collected using Thermo Fisher Nicolet iS50 FTIR spectroscopy bench with built-in diamond attenuated total reflection attachment.

Cell viability and proliferation were measured using Alamar Blue (Thermo Scientific, Grand Island, NY) and PicoGreen (Thermo Scientific, Grand Island, NY) assays, respectively. All reagents were purchased from Thermo Scientific unless otherwise noted. L929 mouse fibroblasts (ATCC, Manassas, VA) were cultured using RPMI media with 10% v/v fetal bovine serum in T-150 flasks. The medium used in the plate assays contained an additional 100 IU/mL penicillin and streptomycin (ATCC, Manassas, VA); antibiotics are necessary since UV sterilization would damage the rapamycin-PVP thin films.

Three each of the unsterilized MAPLE-deposited rapamycin-PVP-coated glass samples and 10-mm square glass coverslips (Ted Pella, Redding, CA) were placed into a 24-well plate and seeded with 3.1 × 10^4 cells/cm^2 using 0.5 mL of cell suspension. The plate was centrifuged at 50 g for 1 min then incubated overnight at 37°C, 5.0% CO_2, 95% RH for cell attachment.

Samples and control coverslips were transferred to a fresh 24-plate and 0.5 mL of 10% v/v Alamar Blue in-media was added; wells containing only 10% v/v Alamar Blue in-media were used as the assay blank. The plate was then incubated for 3 h. 100 µl of solution from each well were added to a 96-well plate in triplicate and read in a fluorescence plate reader (SpectraMAX Gemini EM, Molecular Devices, San Jose, CA) using 570 nm excitation and 585 nm emission wavelengths. The remaining dye solution was aspirated from the 24-well plate,

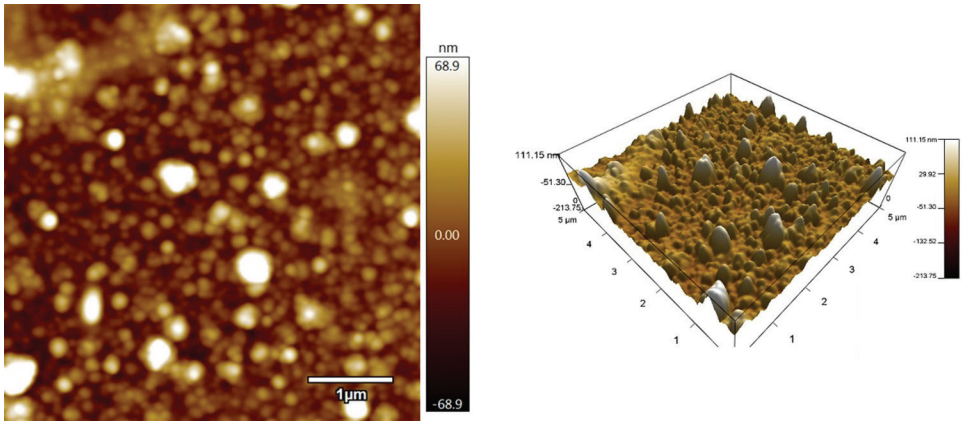

Figure 2. Representative atomic force micrograph of MAPLE-deposited rapamycin-PVP thin films on Si <100>.

replaced with 0.5 mL of the lysis buffer (0.2% v/v Triton X-100 in TE buffer), and then placed on a microplate shaker for 30 min. Plates were then stored at -70°C overnight to complete cell lysis. Cell lysates in the treatment well and control wells were transferred in triplicate to a 96-well plate. PicoGreen dye solution was prepared according to manufacturer instructions and 100 µL of the dye solution was added to each well. After 30 min of staining, the double-stranded DNA signal was read on a fluorescence plate reader at 460 nm excitation and 540 emission wavelengths. Measurements from each sample or blank were obtained in triplicate and averaged. Reported data are the averages and standard deviations of three independent replicate experiments. The results were deemed statistically significant for $P < 0.05$ using the two-tailed Student's *t*-test.

3 Results and discussion

AFM analysis showed a root-mean-square roughness of 23.150 nm; this value represents the overall mean magnitude of surface variations (**Figure 2**). The maximum and minimum measurements were 137.112 and −43.012 nm, respectively. Skewness that is associated with the lack of symmetry around the data point distribution curve was 1.71. Kurtosis, a measure of whether the data is more peaked (positive) or flat (negative) compared to a normal curve shape, was 4.28.

The roughness of the MAPLE-deposited rapamycin-PVP thin films onto silicon was much higher than that of uncoated Si[16]. In general, thin films with <600 nm thickness[17] tend to closely follow the topography of the substrate. The MAPLE-deposited rapamycin-PVP thin films show a morphology similar to that of other MAPLE-deposited structures[18].

The characteristic absorption bands of rapamycin are visible in both the MAPLE-coated rapamycin-PVP thin films and dropcast control coatings (**Figure 3**). This result confirms that the MAPLE deposition method has not significantly altered the chemical structure of rapamycin-PVP starting material. There is a close resemblance between the peaks found in the spectrum of MAPLE-deposited rapamycin-PVP thin film and dropcast coating. The bands at 2862 and 2945 cm^{-1} are attributed to C-H stretching vibrations from the macrocyclic groups in rapamycin[19]. The band centered at 1660 cm^{-1} that corresponds to the carbonyl groups of rapamycin is also present[20]. The bands centered at 1430 and 1366 cm^{-1} are assigned to the stretching and bending vibration of methylene; these bands are ascribed to methylene groups in rapamycin[21]. The broad peaks at 915 cm^{-1}[22,23] and 769 cm^{-1} are attributed to the borosilicate glass substrate[24].

Alamar Blue and PicoGreen assays were used to measure metabolic health and DNA content as a measure of viability and proliferation, respectively (**Figure 4**). MAPLE-deposited rapamycin-PVP glass chips were found to have 70.6% viability and 53.7% proliferation versus a similarly sized

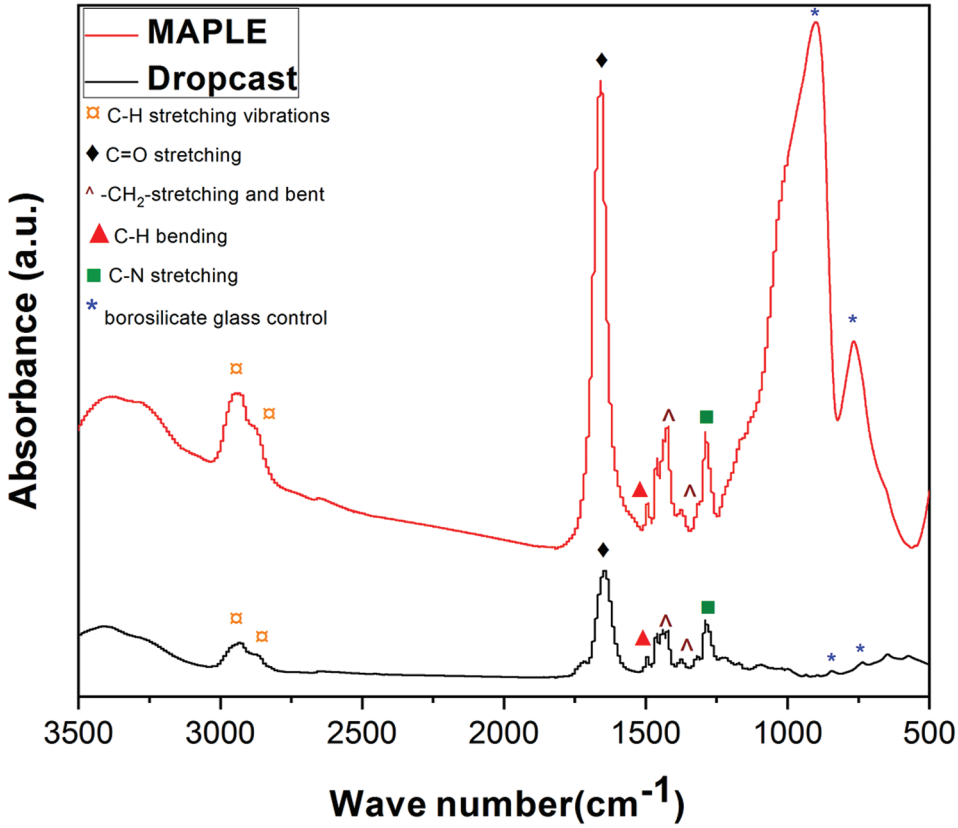

Figure 3. Typical Fourier transform infrared spectrum of MAPLE-deposited rapamycin-PVP thin film (red spectrum) and dropcast coating (black spectrum), respectively.

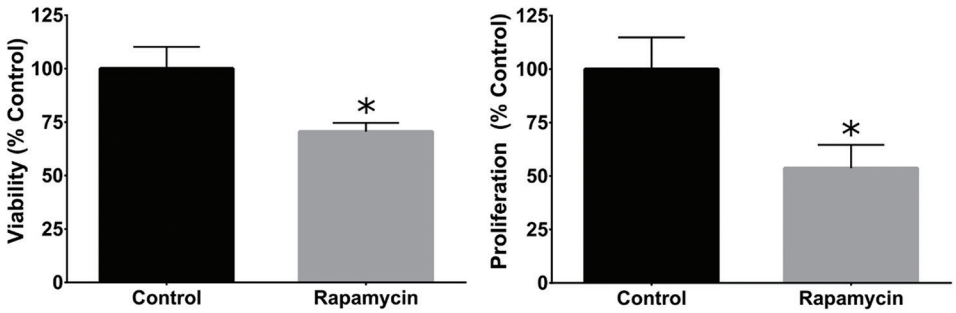

Figure 4. Reductions in proliferation (left) and cell viability (right) were observed in L929 fibroblasts cultured on borosilicate glass coated with rapamycin using MAPLE (rapamycin-PVP) versus untreated borosilicate glass (control). Values represent of $\bar{x} \pm SD$ $N = 3$ independent replicate experiments. Bars with asterisks are significantly different from the negative control ($P < 0.05$).

borosilicate glass control. Alamar Blue and PicoGreen experiments demonstrated reduced cell viability and proliferation, respectively, when grown on MAPLE-deposited rapamycin-PVP surfaces compared to borosilicate glass control ones.

4 Conclusions

Highly uniform rapamycin-PVP thin films were successfully deposited onto the surfaces of silicon and borosilicate optical glass substrates using MAPLE. The antiproliferative properties

of rapamycin were maintained after the MAPLE process; L929 mouse fibroblasts grown on MAPLE-deposited rapamycin-PVP thin films exhibited lower cell viability and proliferation rates than cells grown on borosilicate glass control surfaces. The MAPLE-fabricated thin films may have the potential use for preventing undesirable cell proliferation on the surfaces of medical devices such as therapeutic contact lenses. Further studies are underway to understand the *in vivo* attributes that may allow novel rapamycin release profiles from MAPLE-deposited thin films.

Acknowledgments

This work was supported by a grant of the Ministry of Research and Innovation, CNCS – UEFISCDI, Project Number PNIII-P4-ID-PCE-2016-0884 within PNCDI III and US National Science Foundation Award #1762202.

Disclaimer

The findings and conclusions in this paper have not been formally disseminated by the Food and Drug Administration and should not be construed to represent any agency determination or policy. The mention of commercial products, their sources, or their use in connection with material reported herein is not to be construed as either an actual or implied endorsement of such products by the Department of Health and Human Services.

References

1. National Center for Biotechnology Information. PubChem Database. Sirolimus, CID=5284616. Available from: https://www.pubchem.ncbi.nlm.nih.gov/compound/Sirolimus. [Last accessed on 2019 Dec 24].
2. Stefanini GG, Byrne RA, Windecker S, *et al*., 2017, State of the Art: Coronary Artery Stents Past, Present and Future. *Eurointervention*, 13:706–16. DOI: 10.4244/eij-d-17-00557.
3. Byrne RA, Stone GW, Ormiston J, *et al*., 2017, Coronary Balloon Angioplasty, Stents, and Scaffolds. *Lancet*, 390:781– 92. DOI: 10.1016/s0140-6736(17)31927-x.
4. Shah M, Edman MC, Janga SR, *et al*., 2017, Rapamycin Eye Drops Suppress Lacrimal Gland Inflammation in a Murine Model of Sjögren's Syndrome. *Invest Ophthalmol Vis Sci*, 58:372–85. DOI: 10.1167/iovs.16-19159.
5. Yagasaki R, Nakahara T, Ushikubo H, *et al*., 2014, Anti-angiogenic Effects of Mammalian Target of Rapamycin Inhibitors in a Mouse Model of Oxygen-induced Retinopathy. *Biol Pharm Bull,* 37:1838–42. DOI: 10.1248/bpb.b14-00487.
6. Krishnadev N, Forooghian F, Cukras C, *et al*., 2011, Subconjunctival Sirolimus in the Treatment of Diabetic Macular Edema. *Graefe's Arch Clin Exp Ophthalmol*, 249:1627–33. DOI: 10.1007/s00417-011-1694-9.
7. Olsen TW, Benegas NM, Joplin AC, *et al*., 1994, Rapamycin Inhibits Corneal Allograft Rejection and Neovascularization. *Arch Ophthalmol*, 112:1471–5. DOI: 10.1001/archopht.1994.01090230085026.
8. Yan ZC, Bai YJ, Tian Z, *et al*., 2011, Anti-proliferation Effects of Sirolimus Sustained Delivery Film in Rabbit Glaucoma Filtration Surgery. *Mol Vis*, 17:2495–506.
9. Maulvi FA, Soni TG, Shah DO, 2016, A Review on Therapeutic Contact Lenses for Ocular Drug Delivery. *Drug Deliv*, 23:3017–26. DOI: 10.3109/10717544.2016.1138342.
10. Phan CM, Subbaraman L, Jones L, 2014, Contact Lenses for Antifungal Ocular Drug Delivery: A Review. *Expert Opin Drug Deliv,* 11:537–46. DOI: 10.1517/17425247.2014.882315.
11. Carvalho IM, Marques CS, Oliveira RS, *et al*., 2015, Sustained Drug Release by Contact Lenses for Glaucoma Treatment A Review. *J Controlled Release*, 202:76–82. DOI: 10.1016/j.jconrel.2015.01.023.
12. Chrisey DB, McGill RA, Horwitz JS, *et al*., 2003, Novel Laser-based Deposition of Active Protein Thin Films. *Chem Rev*, 103:553–76.
13. Patz TM, Doraiswamy A, Narayan RJ, *et al*., 2007, Matrix Assisted Pulsed Laser Evaporation of Biomaterial Thin Films. *Mater Sci Eng C*, 27:514–22. DOI: 10.1016/j.msec.2006.05.039.
14. Cristescu R, Mihailescu IN, Jelinek M, *et al*., 2006, Functionalized Thin Films and Structures Obtained by Novel Laser Processing Issues. In: Kassing R, Petkov P, Kulisch W, *et al*., editors. Functionalized Properties of Nanostructured Materials. NATO Science Series by Springer, Series II: Mathematics. p211–26. DOI: 10.1007/1-4020-4594-8_15.
15. Sachan R, Jaipan P, Zhang J, *et al*., 2017, Printing Amphotericin B on Microneedles Using Matrix-assisted Pulsed Laser Evaporation. *Int J Bioprinting*, 3(2):147–57. DOI: 10.18063/ijb.2017.02.004.
16. Pandey K, Pandey PM, 2017, Chemically Assisted Polishing of Monocrystalline Silicon Wafer Si (100) by DDMAF. *Procedia Eng*, 184:178–84. DOI: 10.1016/j.proeng.2017.04.083.
17. Caio F, Moreau C, 2019, Influence of Substrate Shape and Roughness on Coating Microstructure in Suspension Plasma

Spray. *Coatings*, 9:746. DOI: 10.3390/coatings9110746.

18. Popescu-Pelin G, Fufă O, Popescu RC, *et al*., 2018, Lincomycin-embedded PANI-based Coatings for Biomedical Applications. *Appl Surf Sci*, 455:653–66. DOI: 10.1016/j.apsusc.2018.06.016.
19. Stead SO, McInnes SJP, Kireta S, *et al*., 2018, Manipulating Human Dendritic Cell Phenotype and Function with Targeted Porous Silicon Nanoparticles. *Biomaterials*, 155:92–102. DOI: 10.1016/j.biomaterials.2017.11.017.
20. Gandhi PJ, Murthy ZVP, Pati RK, 2011, Optimization of Process Parameters by Taguchi Robust Design Method for the Development of Nano-crystals of Sirolimus Using Sonication Based Crystallization. *Cryst Res Technol*, 47(1):53–72. DOI: 10.1002/crat.201100329.
21. Othman R, Vladisavljević GT, Nagy ZK, *et al*., 2016, Encapsulation and Controlled Release of Rapamycin from Polycaprolactone Nanoparticles Prepared by Membrane Micromixing Combined with Antisolvent Precipitation. *Langmuir*, 32(41):10685–93. DOI: 10.1021/acs.langmuir.6b03178.
22. Singh PK, Sah P, Meher JG, *et al*., 2016, Macrophage-targeted Chitosan Anchored PLGA Nanoparticles Bearing Doxorubicin and Amphotericin B Against Visceral Leishmaniasis. *RSC Adv*, 6:71705–18. DOI: 10.1039/c6ra06007b.
23. Jovanović Ž, Radosavljević A, Šiljegović M, *et al*., 2012, Structural and Optical Characteristics of Silver/poly(N–vinyl–2–pyrrolidone) Nanosystems Synthesized by γ–irradiation. *Radiat Phys Chem*, 81:1720–8. DOI: 10.1016/j.radphyschem.2012.05.019.
24. Nolan M, Perova TS, Moore RA, *et al*., 2000, Spectroscopic Investigations of Borosilicate Glass and its Application as a Dopant Source for Shallow Junctions. *J Electrochem Soc*, 147(8):3100–5. DOI: 10.1149/1.1393863.

INTERNATIONAL JOURNAL OF BIOPRINTING

ISSN (print): 2424-7723

ABOUT THE JOURNAL

International Journal of Bioprinting is a biannual, double-blind peer-reviewed, open access journal. This journal focuses on the use of 3D printing technology with materials that incorporate viable living cells or biological elements to produce tissue or biotechnological products. Further discourses and technological advancements in bioprinting are the goals behind acceptance of high-quality basic and applied research: from concept creation to fabrication of the bioprinting process, associated clinical applications as well as social implications.

Whioce Publishing, official publisher for the journal welcomes researchers to submit their papers relevant to bioprinting for consideration via **http://ijb.whioce.com/** For general enquiries and order for prints and reprints, please write in to **IJB@whioce.com** for a fast response.

SUBMIT YOUR PAPERS HERE

WHIOCE
PUBLISHING PTE. LTD.

ABOUT THE PUBLISHER

Whioce Publishing in Singapore is a registered publisher of excellent quality academic journals for an international readership. We deliver exceptional editorial support for the advancement and dissemination of scientific research by linking readers and researchers with networks and industries. We have ambitions to get our journals indexed in prominent databases such as EI, SCI, SSCI and AHCI, thereby aiming to be a first-class knowledge platform for researchers worldwide.

Whioce Publishing also engages in publishing e-books, organizing academic conferences and educational trainings, and providing translational services.

International Journal of Bioprinting is an
independent open access journal published
by Whioce Publishing Pte.Ltd.

WHIOCE PUBLISHING PTE. LTD.
PROVIDING
FIRST-CLASS SCIENTIFIC INFORMATION
FOR TOP SCHOLARS

Whioce Publishing Pte.Ltd.
7030 Ang Mo Kio Avenue 5
#04-15 Northstar@AMK
Singapore 569880
Tel: +65 65702707/65702718
Fax: +65 65702803

See **www.whioce.com/contact** for a full list of offices and contact information.

Whioce Publishing Pte.Ltd. is a company registered in Singapore (No. 201427293E), whose registered office is at 7030 Ang Mo Kio Avenue 5 #04-15 Northstar@AMK Singapore 569880